Incremental nonlinear control allocation for an aircraft with distributed electric propulsion

An application to the scaled flight demonstrator

P. de Heer

Master of Science Thesis

Cover image courtesy of Orange Aerospace B.V.

Delft University of Technology

Delft Center for Systems and Control

Incremental nonlinear control allocation for an aircraft with distributed electric propulsion

An application to the scaled flight demonstrator

Master of Science Thesis

For the degree of Master of Science in Systems and Control at Delft University of Technology

P. de Heer

October 12, 2021

Faculty of Mechanical, Maritime and Materials Engineering (3mE) · Delft University of Technology

The work in this thesis was supported by Royal Netherlands Aerospace Centre (NLR). Their cooperation is hereby gratefully acknowledged.

Abstract

To meet the demanding requirements on the environmental impact of aircraft, radically new aircraft concepts need to be developed. Within the NOVAIR project, Royal Netherlands Aerospace Centre (NLR) tests these new concepts on a Scaled flight demonstrator (SFD). Using an SFD allows for testing of dynamic and flight physical behavior of new aircraft concepts, which is difficult with more theoretical methods. Furthermore, by using an SFD, the risks associated with full-scale testing in terms of cost and time are minimized. One of the new concepts developed for the SFD is Distributed electric propulsion (DEP). Here, the two jet engines are replaced by six electric propellers. As these can be used actively for control, this results in an over-actuated system. These propellers interact with the aerodynamics of the wing resulting in Propulsion airframe interaction (PAI) effects. Although using the PAI effects for control has the potential to improve capabilities, efficiency and robustness of the aircraft, research into controllers using these effects actively is limited.

This thesis, therefore, presents a new control method including control allocation for the DEP-SFD aircraft, based on the nonlinear Incremental nonlinear dynamic inversion (INDI) controller. INDI enables controlling the nonlinear dynamics of the DEP aircraft over the complete flight envelope with one controller. By feeding back real-time sensor measurements, robustness to modeling errors and external disturbances is increased. Using the Incremental nonlinear control allocation (INCA) method, the full control authority of the DEP can be used. This technique enables taking into account nonlinear allocation relations and control effector interactions, while solving the control allocation real-time, which is key in actively using the PAI effects for control. The INCA method is used for two performance improvements: tracking performance and propeller power efficiency. To compensate for actuator dynamics, this thesis implements an Model predictive control (MPC) controller which results in improved tracking and higher efficiency. The performance of the controller was analyzed in simulation, where a reference square signal input on the roll angle was applied, while minimizing the sideslip angle and maintaining a steady altitude and velocity. The INCA controller with MPC is compared to a conventional INDI controller, showing a significant decrease in rise time from 2.46 s to 0.703 s with minimal tracking error. Furthermore, the effective bandwidth of the system was increased from 0.186 Hz to 0.663 Hz and the power consumption reduced by 6.3%. Modeling uncertainties, external disturbances and a propeller fault were introduced to verify the robustness of the controller. Finally, the reference altitude and velocity were varied, demonstrating controller performance over a large part of the flight envelope.

Contents

List of Figures

List of Tables

Acknowledgements

Firstly, I would like to thank my supervisor from the TU Delft Prof. Dr. Gleb Vdovin. Although his field of expertise is not in aircraft control, he guided me pleasantly through the process of this thesis, giving a much appreciated other perspective to my research. Also, I would like to thank Dr. Coen de Visser for giving me advice on the controller algorithms I use, which are developed in his research group.

Next to that, I would like to thank my daily supervisor Ir. Marijn Hoogendoorn from Royal Netherlands Aerospace Centre (NLR) for always supporting me and giving feedback for my thesis. I appreciate that you were always ready to help me with your knowledge or by setting me up with other people. Your advice of scoping and focusing shaped this thesis for a major part. Furthermore, I would like to thank all my other colleagues of my department at NLR for providing your advice or for just casuals talks. Although I had to work a lot from home due to the pandemic, I enjoyed my time at NLR a lot. As far as I experienced it, I think that your mentality of always being ready to help each other will make the SFD and DEP project successful for sure.

Apart from my supervisors and colleagues, I would like to thank my roommates Daan, Thijs and Lex for always being there for either a discussion regarding my thesis or any other issues I struggled with. Especially in a pandemic when working that much from home, you motivated me to work on my thesis. Also, I would like to thank my friends from S&C, my other friends in Delft and also the ones from Breda for supporting me and making my thesis time more enjoyable.

Lastly, I would like to thank my brother, sister, parents and the rest of my family for always being interested in what I was doing. Although this was not always easy for me to explain, I really enjoyed telling what I was doing. Also, I much appreciated you regularly checking in on me whether I was still doing well.

Besides all these amazing people, music kept me going throughout my thesis whether I was reading papers, programming or writing. Sometimes, theories were not understood immediately or code was not working the way it was intended. What I learned from this is to always keep going. It might not immediately lead to results, but just moving will always take you further. This feeling can be well summarized by a song quote given on the following page which motivated me to actually "keep moving".

Delft, University of Technology — P. de Heer
October 12, 2021

“If I can’t understand it, I’ll find another way. Keep moving, keep moving.”
— *Joshua Loyd-Watson, Thomas McFarland and Lydia Kitto*

Chapter 1

Introduction

This first chapter discusses the motivation behind the thesis project from which the research objective is defined. Finding methods to fulfill this research objective, relevant related work found in the literature review will be discussed. After that, deciding on which control methods to adopt in this thesis, the research questions will be specified. Following up, the thesis contributions will be given and lastly, this chapter concludes with an outline for this thesis.

1-1 Motivation and problem formulation

Current aircraft are 75% more fuel-efficient compared to the ones from the early jet age. Still, if no significant measures are taken, the amount of CO_2 emissions will triple by 2050. This is due to the growth of air transport, which historically doubles every fifteen years [1]. To reduce the environmental impact of aircraft, the European union (EU) developed the Clean Sky 2 program [2] which will soon be succeeded by the Clean Aviation program [1]. This program aims at reaching net-zero greenhouse gas emissions and a climate-neutral aviation system in Europe by 2050.

Given these continuously more demanding requirements on fuel consumption, noise and chemical emissions, radically new airplane concepts need to be developed, which show large potential for improvements. The development of these new concepts gives more uncertainty as less historical data is available. Flight testing with an Scaled flight demonstrator (SFD) forms a valuable addition to the common test methods of wind tunnel testing and numerical simulation. Especially for these new concepts, where only a small amount of data is available, an SFD can reduce the high uncertainty and risks associated with new designs. Here, full-scale testing will introduce high risks in terms of cost and time. Therefore, Royal Netherlands Aerospace Centre (NLR) works together in a consortium of four partners to validate the SFD approach. For this project, a 1:8.5 scale model of the Airbus A-320 is developed. This model allows for testing of dynamic and flight physical behavior of new propulsion concepts, which is the main advantage of using an SFD compared to traditional methods as wind tunnel testing or Computational fluid dynamics (CFD) analysis [3]. At this moment the SFD has performed taxi tests and is almost ready for the first flight test. A picture showing the SFD in the wind tunnel about half a year ago is given below.

Figure 1-1: The SFD in the wind tunnel for testing its aerodynamics before flight testing. [1]

The NOVAIR project aims at further developing the SFD of the Airbus A-320 by looking at new aircraft concepts. One of these new concepts is Distributed electric propulsion (DEP). In this configuration, the two jet engines of the Airbus A320 are replaced by six electric propellers, three on each wing. Similar projects developing this technology include the NASA Sceptor project for the NASA x-57 aircraft [4] and the NASA STTR project with a Cirrus SR22T scale model [5].

Key advantages of electric propulsion include compact packaging, scale-free sizing, higher power to weight density for the motor, relatively low control input lags and non-air breathing operation so that power is independent of altitude [5]. An important drawback of electric propulsion is that battery technologies have 60 to 100 times less energy per unit mass compared to typical aircraft fuels [6]. However, short-range missions can be very effective with electric propulsion and the extra advantages of using DEP potentially reduce the weight penalty of electric propulsion [4].

Integrating several smaller propellers over the wing results in coupling effects between the aerodynamics and propulsion, which are defined as Propulsion airframe interaction (PAI) effects [5]. An example of this interaction is the NASA X-57 aircraft where the slipstream of the propellers is used to increase the dynamic pressure over the wing, thus enhancing the lift [7]. As the electric propellers have lower control input lags compared to jet engines they can be used actively for control. An interesting effect regarding control is the interaction of the propeller slipstream on an aerodynamic surface which together with differential thrust produces extra control authorities. This enables improving the capabilities, efficiency and robustness of aircraft [8].

[1] This project has received funding from the Clean Sky 2 Joint Undertaking under the European Union's Horizon 2020 research and innovation programme under grant agreement No 717183 and 945583.

The control aspect of DEP is a subject that has received limited attention in research [5]. The concept of using propulsive systems for maneuvering derives from Propulsion-controlled aircraft (PCA). Here, the differential thrust of jet engines is used for yaw control allowing for reduction of the vertical tail size [9]. It is shown that the same principle holds for the NASA X-57 DEP aircraft, developing a dynamic model including PAI effects of this aircraft [10]. In this research, a simple Proportional-integral-derivative (PID) controller is used for directional control. Thrust mapping is employed to distribute the required thrust over the remaining propellers. In [11], a Linear time-invariant (LTI) state-space model was developed for the scale model of the Cirrus SR22T. As this model is linear, it can only describe the aircraft dynamics around a predefined operating point. A major shortcoming of this research is that the PAI effects are not taken into account, but the model rather forms a baseline for further development. It was realized in [11] that including the PAI effects is necessary for the design of a closed-loop control system for the DEP aircraft. This poses a significant challenge, as the PAI are hard to model and introduce nonlinear behavior and cross-couplings which are difficult to control efficiently [12].

Recently, flight testing was performed with a wingtip mounted electrical propulsion system using differential thrust for yaw control [13]. Identification of the coupling effects also showed a roll moment being applied, so that it is hypothesized that DEP can be used for both roll and yaw control. An important aspect to consider is that by introducing these extra control authorities, the DEP aircraft becomes over-actuated so that control allocation is required [14]. This also opens up the opportunity for Fault tolerant control (FTC) regarding the propellers. If one of them fails the others can compensate for this deficiency.

Previous research into the DEP aircraft in terms of control is thus limited, which forms a research gap this thesis aims to fill. Prior to this thesis, following the literature discussed above, the hypothesis was made that by incorporating the differential thrust and PAI effects into the controller design, performance in terms of reference tracking for the DEP aircraft can be improved. Introduction of these control authorities leads to an over-actuated system, so that a control allocation method needs to be developed which maximizes the performance. This method should take into account the cross-coupling between the different control inputs and airframe: the PAI effects. To prevent actuators from saturating, control input constraints will need to be implemented. As the extra control authorities can be used to increase the efficiency of the aircraft, this thesis will investigate a possible performance increase through finding control inputs that minimize power consumption. This will contribute to the goals of sustainable flight as discussed in the beginning of this introduction. Furthermore, over-actuated systems should be more robust to actuator faults, so that the opportunity of Fault tolerant control (FTC) in case of propeller failure will be explored. Finally, as the PAI effects are complicated to model and turbulence can affect the DEP aircraft, the proposed controller should be robust against modeling errors and disturbances. These goals can be formalized into the following problem formulation.

Design a reference tracking controller and control allocation method which enables to use all control authorities of the DEP aircraft as efficiently as possible while being robust against modeling errors, external disturbances and propeller failure over the complete operating range of the aircraft.

The aim of this thesis is, therefore, to constitute an important step in the development of control methods for the DEP aircraft by actively using the extra control authorities in the form of differential thrust and PAI effects. It should be noted that the main focus of this research is the implementation of the PAI effects in the controller, thereby showing the extra capabilities of DEP in terms of control. Therefore, this thesis can be seen as the framework to which more elaborate PAI models can be added. It is, therefore, important to find a control method that can easily be adapted when new aerodynamic information is available through for example CFD analysis or wind tunnel testing.

1-2 Related work

As discussed in the previous section, only limited attention has been paid to the control aspect of the DEP aircraft. This section will therefore discuss different suitable control techniques for over-actuated aircraft in general. It is based on the literature review completed before the start of this thesis work and will conclude with the outcomes from this literature review. Here the most applicable control technique was determined by looking at the requirements following from the research objective. For completeness, the requirements for the controller are listed below. The controller should be

- able to deal with the nonlinear dynamics of the aircraft and PAI effects so that it can control the DEP aircraft over the complete operating range,
- robust against modeling errors and external disturbances, especially considering that the PAI effects are hard to model,
- able to use all control authorities of the DEP aircraft to maximize tracking performance and efficiency which means that it performs control allocation taking into account actuator constraints,
- be real-time implementable[2], meaning that the underlying algorithms should not be computationally expensive.

The next two sections will discuss the different nonlinear control methods and control allocation techniques found in literature. Both conclude with the most suitable technique for the DEP aircraft. These methods form the starting point of this thesis, from where controllers designed specifically for the DEP aircraft will be developed.

1-2-1 Nonlinear control methods

In literature, different methods have been proposed for nonlinear aircraft control. These can be classified into two categories: linear and nonlinear controllers. Note that adaptive controllers were not considered in this research, as stability of these types of controllers cannot be guaranteed [16]. Linear controllers are based on linearizing the nonlinear aircraft model around different operating points. This gives a collection of LTI systems, where for each system a linear controller needs to be designed. The method was first developed for aircraft trajectory control which made it the industry standard [17]. To control the aircraft

[2]For fixed-wing aircraft the flight control system generally needs to run at 100 Hz [15]. Effects of sampling time will be discussed in more detail in Section 3-6.

over the complete operating range, gain scheduling techniques are employed. For this method, the controller is interpolated between the different operating points [18]. A problem with this method is that stability can only be guaranteed around the operating points and extensive simulation is required to ensure global performance.

Furthermore, it takes much time to design the controllers for all the different operating points. The controller design can be automated by finding optimal H_2 or H_∞ controllers using multi-modal and multi-objective tuning, optimizing for either the l_2 or l_∞ norm [19]. Using these formulations, controllers are synthesized which are robust to both modeling errors and disturbances. The method of H_∞ control can be further extended by using a Linear parameter varying (LPV) controller [20]. This type of controller is analogous to traditional gain scheduling, indexing a collection of linear systems. In contrast, this type of controller interpolates between the different LTI systems using predefined parameters and can thereby guarantee stability and performance over the complete operating range. A major downside of using control methods based on H_2 or H_∞ synthesis is that the modeling uncertainties need to be quantified beforehand. For the DEP aircraft, these are unknown especially considering the PAI effects, which makes it hard to correctly implement such a controller.

Secondly, the class of nonlinear controllers was considered. For aircraft control, either Nonlinear dynamics inversion (NDI) [17] or Backstepping (BKS) [21] can be used. NDI is based on the general feedback linearization method. For this method, the nonlinear dynamics are canceled out, so that the closed-loop dynamics are in linear form. Simple linear control techniques can then be employed to control the system. The BKS method uses Lyapunov functions to control the nonlinear system thereby guaranteeing stability. As the method is recursive, it can be used to design a single control law for cascaded systems [22]. As both these methods can deal with nonlinear dynamics they can be used to control the DEP aircraft over the complete flight envelope. A downside of both approaches is that they rely completely on the aircraft model so that robustness against modeling errors is inadequate. Therefore, the incremental counterparts for these methods called Incremental nonlinear dynamic inversion (INDI) [23] and Incremental backstepping (IBKS) [22] were proposed in literature. Both controllers are based on computing incremental control inputs. If sampled at a sufficient frequency, this allows for discarding part of the aircraft's model in the control law. These dynamics are then captured by sensor measurements. Relying less on the model and feeding back sensor measurements in the control law, makes both INDI and IBKS inherently robust to modeling errors and external disturbances. As for BKS, stability of the IBKS method is guaranteed through the use of Lyapunov functions. Still, implementation of filters for on sensor measurements and actuator dynamics will violate the Lyapunov assumptions [24]. Also, tuning of the IBKS method is less intuitive as compared to INDI, where for example a PID controller can be used to make the aircraft follow a reference trajectory. Based on these considerations regarding implementation of the controller, the choice was made to use the INDI controller as a basis for controller design of the DEP aircraft.

As active control of the propellers will not only influence the attitude of the aircraft, but also the altitude and velocity, both the translation and rotation of the aircraft need to be controlled. In [25], this controller is developed by designing an inner loop rotational controller and an outer loop translational controller. Using INDI for the dynamics relations, this controller is robust to modeling errors and external disturbances so that it forms the ideal foundation for controller development in this thesis

1-2-2 Control allocation

Following the fact that the DEP aircraft is over-actuated, a suitable control allocation technique needs to be determined. Such a technique, determines the required control input of all effectors. These effectors are either the control surfaces or propellers, which produce the required forces and moments. One simple method is called ganging where different control effectors are grouped into one [26]. As this leads to sub-optimal allocation, different other techniques were considered.

These techniques can be classified into two categories: linear and nonlinear allocation. The latter can take into account the nonlinear relationships of the control inputs on the nonlinear dynamics of the aircraft. Examples of these methods include nonlinear direct control allocation [27], modeling with piecewise linear functions [28] and nonlinear optimization using Nonlinear programming (NP). Although all these methods show a significant improvement in terms of performance, they are computationally demanding, so that they cannot run online [29].

Linear control allocation methods, therefore, form a more promising framework for implementation on the DEP aircraft. Common linear methods found in literature include weighted generalized inverse [26], redistributed pseudo-inverse [30] and daisy chaining [31]. The last two techniques can take into account control input constraints to prevent actuator saturation. Nevertheless, both suffer from the fact that optimal control allocation cannot be guaranteed. Another method proposed in [32] is direct allocation, which scales the control inputs on the attainable input set. Computing this set is computationally expensive, especially for problems with a large number of control inputs [26].

The linear control allocation problem can also be solved using an optimization problem defined as either Linear programming (LP) or Quadratic programming (QP). Different optimization problems can be defined, of which the mixed optimization shows the best performance in terms of solving time and numerical properties [33]. In this formulation, two objectives are defined. The first objective ensures that the control inputs produce the required control forces and moments and the second objective is introduced to find a unique solution to the allocation problem. Solving this optimization problem with the l_2 QP norm tends to distribute the control effort over more effectors. In contrast the l_1 LP norm will use the minimum amount of control effectors possible [34]. As for the DEP aircraft the aim is to use all control effectors to maximize tracking performance and efficiency, the l_2 norm seems more suitable.

A downside of these proposed methods is that actuator dynamics and effector interactions cannot be taken into account. The actuator dynamics can have a significant effect on the effector output, therefore leading to a discrepancy between the commanded and actual control input. A simple method to overcome this problem is by overdriving the actuators so that the actual value equals the commanded value [35]. A more advanced method can be found in the form of Model predictive control (MPC), where an optimization with future control horizon is used to compensate for the actuator dynamics. As constraints can be added to this optimization, actuator saturation can be taken into account by setting limits on the control input [36]. For the control effector interactions, these can be modeled as bilinear functions [37].

Note that this leads to a NP problem for which computational demand is high. An alternative method is proposed in [38], solving the control allocation incrementally using the same philosophy as for INDI and IBKS discussed in the previous section. This method is called Incremental nonlinear control allocation (INCA) and solves the mixed optimization incrementally at each sampling instant using QP, taking into account nonlinear relations and control effector interactions. As QP can be used because of the incremental nature of the controller, the allocation can be solved online. Also, actuator dynamics can be taken into account as the method uses real-time measurements of the effectors' output. Note that the INCA method cannot compensate for these dynamics, so that performance concerning these dynamics should be tested in simulation. Future researches into the INCA controller suggest using it for drag minimization [39] or FTC [40].

With the focus of maximizing the efficiency of the DEP aircraft, it is interesting to use the freedom in control allocation for minimal power consumption of the propellers for which a method is suggested in [41]. Here, the inner rotational and outer translational INDI control loops are synthesized using control allocation. The controller then solves the rotational and translational problem in one step, optimizing the control inputs for minimal power consumption. This allocation philosophy together with the INCA framework will, form the basis for the control allocation in this thesis.

1-3 Research questions

The previous section discussed the results found in literature for the nonlinear controller and control allocation aspect. It was concluded that an INDI based controller for both translational and rotational control will be used. Combining this with control allocation defined as mixed optimization with QP gives the INCA controller. This controller will be used to explore the full potential of the DEP aircraft, focusing on maximizing tracking performance and minimizing power consumption. From this, the following research question was defined.
How can an INCA controller be designed to exploit the extra control authorities of the DEP aircraft and utilize these to its full potential in terms of tracking performance and efficiency?

By answering this research question, a solution to the more general problem formulated in Section 1-1 will be found. The research question is divided in sub-questions, where each of these will be answered in the different subsequent chapters of this thesis.

- ***How can the translational and rotational control loops of the baseline INDI be developed for the DEP aircraft and then synthesized, so that simultaneous control of the velocity, altitude and attitude is achieved?***
  This research question is twofold, where firstly a model of the DEP aircraft including PAI effects needs to be developed, so that the conventional INDI controller can be tested on this model. Secondly, as the differential thrust and PAI effects affect both the translation and rotation of the aircraft, an INDI based controller is required which can control both these aspects. Synthesizing these loops allows finding all required control inputs in one step. This controller will form the baseline for the control allocation strategies developed in this thesis.

- ***How can the differential thrust and PAI effects of the DEP aircraft be incorporated in an INCA controller and how does exploiting full control effectiveness knowledge improve tracking performance?***

Augmenting on the proposed synthesized INDI controller, a control allocation method will need to be devised for which the INCA concept is explored. To show the full potential of the DEP aircraft with INCA, the differential thrust and PAI need to be converted to their respective control effectiveness. It is hypothesized that by including these effects in the controller knowledge, tracking performance is improved. To analyze this, the performance will need to be compared against the baseline controller. Furthermore, an uncertainty analysis will be performed to verify whether the proposed control method is robust against modeling errors, especially considering the uncertainty in PAI control capability. Finally, robustness against both propeller failure and external disturbances will be tested.

- ***How can the freedom in terms of extra control authorities be exploited to optimize for minimal power consumption of the DEP aircraft and how can this be incorporated into the INCA controller objective functions?***
  As one of the main goals in the development of the DEP aircraft is minimizing energy consumption, the control allocation will focus on efficiency. Potentially, using an objective function that describes the consumed power by the propellers, the INCA controller can be used to optimize for minimal power. The synthesized INDI controller, discussed in the first sub-question, will form the basis for this control allocation method where control inputs are calculated to control both translation and rotation while minimizing power. To test the performance of this control allocation, the power consumption will be checked against the baseline controller. Also, modeling uncertainties will be introduced to analyze the robustness of power optimization against modeling errors.

By answering these sub-questions, this thesis aims to answer the main research question. The sub-questions suggest the development of different control allocation techniques combined with an INDI controller for reference tracking of altitude, velocity and attitude commands. It is hypothesized that the developed controller improves tracking performance and power consumption of the DEP aircraft. To analyze the possible increase in performance in terms of tracking and efficiency, a baseline controller is required to compare against. This controller will be based on the controller discussed at the end of Section 1-2-1 where two control loops are designed for translation and rotational control respectively.

1-4 Thesis contributions

Following the research objectives proposed in the previous section, the main goal of this thesis is to develop a novel INCA controller that uses all control authorities of the DEP aircraft. This controller should provide robust performance over the complete operating range of the aircraft and increase the efficiency. To test the performance of the proposed INCA controller, a simulation framework was set up in SIMULINK where the controller was tested for different reference signals. Following the development of the novel INCA controller and the results obtained in simulation, the following thesis contributions can be formulated.

- ***Design of a control method which can actively use the differential thrust and PAI effects of the DEP aircraft over a large part of the flight envelope.***
  In this thesis, a first-order method is proposed which can model the PAI using analytical

relations. Also, the effect of differential thrust is modeled and for both these control authorities, the control effectiveness is determined. Incorporating this effectiveness into the INCA formulation, results in a nonlinear control allocation scheme that can be used over the complete operating range of the aircraft. This work is the first to include the full control authority of the control surfaces, differential thrust and PAI effects, thereby showing the full potential of the DEP aircraft. Also, as the INCA controller is robust to modeling errors and can easily be adapted, it forms an effective framework for including new analysis methods for PAI effects.

- ***Extension of the INCA controller with a translational control module and synthesizing the translational and rotational control loops in the control allocation.***
  Previous work on the INCA controller only used attitude control in the control allocation with simple PID outer loops to control the altitude and velocity. This thesis extends on this work by adding translational control in the control allocation scheme. This allows finding the optimal control inputs for both the translational and rotational reference commands. Synthesizing the controllers, the control input can be determined in one step using control allocation. Stability and robustness of the proposed method is verified by performing a sampling time analysis.

- ***Reformulation of the INCA secondary objective function so that the freedom in control inputs is exploited for minimal power consumption.***
  The INCA controller allows finding the optimal control inputs for different secondary objectives. In this work, a method is proposed to find the optimal control inputs for minimal power consumption. For this, a propeller model is added to the simulation which estimated the consumed power. Combining this with the synthesized translational and rotational INCA controller, allows to find the minimal power control input distribution. Using this method, the efficiency of the DEP aircraft can be increased.

- ***Design of a Model predictive control (MPC) controller augmenting the INCA controller to deal with the actuator dynamics incrementally.***
  The INCA controller allows adding position and rate constraints on the control inputs so that feasible control input commands are computed. A major drawback of the method is that when the rate constraints are combined with actuator dynamics, the controller becomes over-conservative. Therefore, this thesis proposes an MPC controller which ensures that the actuators follow the incremental control commands given by the INCA controller, taking into account the control input constraints. Although this method relies on assumptions regarding direct state measurements, which makes it harder to implement, a significant improvement of tracking performance and efficiency can be achieved when implementing this MPC controller.

1-5 Outline of the thesis

Following the research questions defined in Section 1-3, the remainder of this thesis is structured as follows. Chapter 2 introduces the general aircraft's EoM and methods for modeling the propeller and PAI effects. This model is used for the development of the simulation in which all controllers are tested. Chapter 3 discusses the INDI control method, deriving it from NDI and stating the relevant assumptions and limitations of this method. The translational and rotational control loops will be introduced and synthesized so that they can be used for control allocation. As synthesizing these loops violates part of the INDI assumptions, the INDI control law will be redefined and stability will be analyzed using a sampling time analysis. Chapter 4 introduces the INCA controller in more detail and derives the control effectiveness for all control authorities of the DEP aircraft. Optimizing for minimal power consumption of the propellers will then be introduced in the INCA framework and the MPC controller is discussed to compensate for the actuator dynamics incrementally. In Chapter 5, the performance of the proposed controllers is verified using the simulation framework set up in SIMULINK. These controllers will be tested for tracking performance, power consumption and robustness to modeling uncertainties, external disturbances and propeller failure. Finally, in Chapter 6 this thesis will be concluded by answering the research questions proposed in Section 1-3 and giving suggestions for future work following up on the research contributions of this thesis.

Chapter 2

Modeling of a scaled Distributed electric propulsion (DEP) aircraft

In this chapter, the model for the DEP aircraft will be introduced. It will first introduce the general Equations of motion (EoM) for aircraft, specifying the relevant reference frames and transformations between them. After this, the external forces and moments on the DEP aircraft will be identified. The control inputs of the DEP aircraft and their constraints and dynamics will be discussed, after which a method for propeller and PAI effects modeling will be introduced. A method for making the forces and moment non-dimensional using control and stability derivatives will be given which forms the aerodynamic and control model for the DEP aircraft. Furthermore, the approach of scaled flight testing will be discussed, showing how results from the SFD translate to the real-scale aircraft. Finally, a linear analysis of the DEP model around its trim conditions will be performed, so that stability and controllability around these operating points can be analyzed.

2-1 Frames and Equations of motion (EoM) for general aircraft

In this section the EoM for general aircraft will be derived. This model will form the basis to which the differential thrust and PAI effects will be added at a later stage. To derive the EoM first the different reference frames will be introduced and a method for transformation between these frames will be given.

2-1-1 Reference frames

The derivation of the EoM is based on Newton's second law which requires an **inertial frame of reference** F_{I}. In [42], a right-handed coordinate system with its center at the center of mass of the Earth for F_{I} is defined. The z-axis Z_{I} points towards the North along the spin axis of the Earth, the x-axis X_{I} is directed through the equator at the location where the ecliptic and equator cross and the y-axis Y_{I} completes the right-handed coordinate system perpendicular to X_I and Z_I. The **vehicle-carried normal Earth reference frame** F_E is placed at the aircraft's center of gravity GG. The x-axis X_E points towards the north and the z-axis Z_E-axis points towards the center of the Earth, where a perfectly spherical earth is assumed. The y-axis Y_E completes the reference frame following right-hand rule conventions. The orientation of the aircraft is expressed in the F_E frame with ϕ the roll angle around X_E, θ the pitch angle around Y_E and ψ the yaw angle around Z_E. Both the F_I and F_E frame a shown in Figure 2-1a.

The next frame considered is the **body-fixed reference frame** F_b, which also has its origin at G but rotates with the aircraft's attitude. In this frame, the x-axis X_b point forwards, the z-axis Z_b downwards and the y-axis Y_b to the right following the right-hand convention. The linear and angular velocity of this frame with respect to the center of gravity, are given as $\boldsymbol{V}_\mathrm{G}^\mathrm{b} = \begin{bmatrix} u & w & v \end{bmatrix}^\mathrm{T}$ and $\boldsymbol{\Omega}_\mathrm{G}^\mathrm{b} = \begin{bmatrix} p & q & r \end{bmatrix}^T$. Furthermore, the **aerodynamic reference frame** F_a is considered. This frame is defined by rotating the F_b frame by the angle of attack α and angle of sideslip β so that the x-axis X_a is parallel to the undisturbed velocity vector. Figure 2-1b shows how F_b and F_a relate to each other. Finally, the **velocity frame** F_V is defined by rotating the F_a frame by the roll angle ϕ.

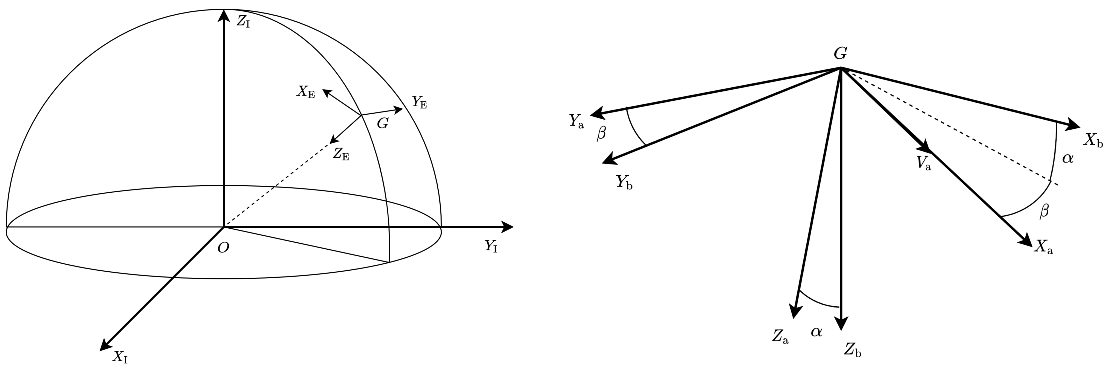

(a) Inertial F_I and vehicle carried Earth center F_E reference frame.

(b) Body F_b and aerodynamic F_a reference frame.

Figure 2-1: Overview of the different frames used for aircraft modeling, here 0 is the origin of the inertial frame and G the center of gravity of the aircraft.

2-1-2 Transformation between reference frames

With the different reference frames described, a method for transformation between these reference frames is required. Transformation is accomplished with a matrix $\mathbf{T}$ using Euler angles. The transformation is described by three successive rotations, each around another axis. For the standard sequence of rotations $\phi_z \rightarrow \phi_y \rightarrow \phi_x$ the transformation matrix is defined as

$$\mathbf{T} = \begin{bmatrix} 1 & 0 & 0 \\ 0 & \cos\phi_x & \sin\phi_x \\ 0 & -\sin\phi_x & \cos\phi_x \end{bmatrix} \begin{bmatrix} \cos\phi_y & 0 & -\sin\phi_y \\ 0 & 1 & 0 \\ \sin\phi_y & 0 & \cos\phi_y \end{bmatrix} \begin{bmatrix} \cos\phi_z & \sin\phi_z & 0 \\ -\sin\phi_z & \cos\phi_z & 0 \\ 0 & 0 & 1 \end{bmatrix}, \tag{2-1}$$

where it is important to note that a singularity exist at $\phi_y = \pm 90\,\mathrm{deg}$ [42]. Note that this method is only valid for reference frames that are not moving or rotating with respect to each other.

2-1-3 Equations of motion (EoM)

This section will follow the method of deriving the equations of motions based on [42] and [43]. A few simplifications are made throughout the derivation of the EoM which will be highlighted throughout this section. The full list of assumptions is given in Appendix A-2. The EoM for an aircraft are derived from Newton's second law of physics. This states that the summation of all external forces and moments acting on a body is equal to the time rate of change of momentum on that body. This statement is only valid measuring from an inertial point of reference, so the F_{I} frame is used. However, the most convenient frame to express the EoM for aircraft is the F_{b} frame. This is because if F_{I} frame is used and the aircraft rotates, the mass moment of inertia matrix $\mathbf{I}$ will vary over time [43]. Expressing the EoM in the F_{b} frame gives a constant $\mathbf{I}$ matrix, as this frame rotates with the attitude. Therefore, a transformation between the inertial F_{I} frame and moving and rotating F_{b} frame is required.

A method for the transformation between these two types of frames is given in [42], where three vectors are defined. First, a vector $\boldsymbol{R}$ from the origin O of the fixed frame to the origin G of the moving and rotating frame is constructed. Then a vector $\boldsymbol{r}$ between point P and the origin G of a moving and rotating reference frame, to which this point P is fixed, is defined. Finally, the vector $\boldsymbol{R}_{\mathrm{P}}$ from the origin O in a fixed reference frame to point P is constructed. These vectors are illustrated below.

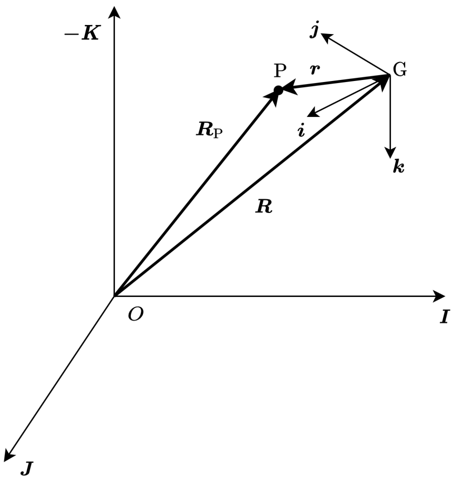

Figure 2-2: Illustration of a moving and rotating reference frame with origin P with respect to an inertial frame with the origin O.

The time derivative of the vector $\boldsymbol{R}_{\mathrm{P}}$ with respect to the inertial reference frame F_{I} is defined as

$$\left.\frac{d\boldsymbol{R}_{\mathrm{P}}}{dt}\right|_{\mathrm{I}}^{\mathrm{I}} = \left.\frac{d\boldsymbol{R}}{dt}\right|_{\mathrm{I}}^{\mathrm{I}} + \left.\frac{d\boldsymbol{r}}{dt}\right|_{\mathrm{b}}^{\mathrm{I}} + \boldsymbol{\Omega}_{\mathrm{bI}}^{\mathrm{I}} \times \boldsymbol{r}^{\mathrm{I}}. \tag{2-2}$$

The subscript after | defines in which reference frame the derivative is taken and the superscript in which frame it is expressed. For the rotational velocity vector $\boldsymbol{\Omega}$, the subscript defines the relative angular velocity of one reference frame to another. The superscript again denotes in which reference frame $\boldsymbol{\Omega}$ and $\boldsymbol{r}$ are expressed. Eq. (2-2) thus calculates the time derivative of vector $\boldsymbol{R}_{\mathrm{P}}$ with respect to and expressed in F_{I}, by summing the time derivative of $\boldsymbol{R}$ with respect to F_{I}, the time derivative of vector $\boldsymbol{r}$ with respect to F_{b} and the cross product between the relative angular velocity of F_{b} with respect to F_{I} times the vector $\boldsymbol{r}$. Eq. (2-2) serves as an example and can be applied to any two reference frames as long as they are expressed in the same frame.

One of the important assumptions in [42] is that the earth is flat and non-rotating. As a consequence the orientation of the F_{E} frame with respect to the F_{I} frame is constant. Going from F_{I}, in which Newton's second law is defined, to F_{b} is thus the same as going from F_{E} to F_{b}. The time derivative of the velocity vector $\boldsymbol{V}$ with respect to the F_{E} frame expressed in the F_{b} frame can be calculated using Eq. (2-2). As F_{b} only rotates and not moves with respect to F_{E}, the first term in this equation disappears which gives

$$\left.\frac{d\boldsymbol{V}^{\mathrm{b}}}{dt}\right|_{\mathrm{E}}^{\mathrm{b}} = \left.\frac{d\boldsymbol{V}}{dt}\right|_{\mathrm{b}}^{\mathrm{b}} + \boldsymbol{\Omega}_{\mathrm{bE}}^{\mathrm{b}} \times \boldsymbol{V}^{\mathrm{b}}. \tag{2-3}$$

Assuming there is no wind so that the kinematic velocity in F_b or F_E is equal to the aerodynamic velocity in F_a Eq. (2-3) is reduced to

$$\begin{aligned} \left.\frac{d\boldsymbol{V}^{\mathrm{b}}}{dt}\right|_{\mathrm{E}}^{\mathrm{b}} &= \begin{bmatrix} \dot{u} \\ \dot{v} \\ \dot{w} \end{bmatrix} + \begin{bmatrix} p \\ q \\ r \end{bmatrix} \times \begin{bmatrix} u \\ v \\ w \end{bmatrix}, \\ &= \begin{bmatrix} \dot{u} + qw - rv \\ \dot{v} + ru - pw \\ \dot{w} + pv - qu \end{bmatrix}. \end{aligned} \tag{2-4}$$

Here u, v and w are the linear velocities in the F_{b} x-, y-, z-axis respectively. Furthermore, p, q and r represent the roll, pitch and yaw rate in F_{b} respectively. Multiplying with the aircraft's mass m gives the forces X, Y and Z in each direction of F_{b} so that

$$m \begin{bmatrix} \dot{u} + qw - rv \\ \dot{v} + ru - pw \\ \dot{w} + pv - qu \end{bmatrix} = \begin{bmatrix} X \\ Y \\ Z \end{bmatrix} = \boldsymbol{\mathcal{F}}_{\mathrm{b}}^{\mathrm{ext}}, \tag{2-5}$$

where the external forces applied to the aircraft are gathered in the vector $\boldsymbol{\mathcal{F}}_b^{ext}$.

The same method is used to derive the EoM for the rotations. The derivative of the moment of impulse $\boldsymbol{H}$ with respect to the body frame is again calculated with Eq. (2-2). Discarding the first term and substituting for $\boldsymbol{H}^{\mathrm{b}} = \mathbf{I}\boldsymbol{\Omega}_{\mathrm{bE}}^{\mathrm{b}}$ gives

$$\begin{aligned} \left.\frac{d\mathbf{I}\boldsymbol{\Omega}_{\mathrm{bE}}^{\mathrm{b}}}{dt}\right|_{\mathrm{E}}^{\mathrm{b}} &= \left.\frac{d\mathbf{I}\boldsymbol{\Omega}_{\mathrm{bE}}^{\mathrm{b}}}{dt}\right|_{\mathrm{b}}^{\mathrm{b}} + \boldsymbol{\Omega}_{\mathrm{bE}}^{\mathrm{b}} \times \mathbf{I}\boldsymbol{\Omega}_{\mathrm{bE}}^{\mathrm{b}}, \\ &= \mathbf{I}\dot{\boldsymbol{\Omega}}_{\mathrm{bE}}^{\mathrm{b}} + \boldsymbol{\Omega}_{\mathrm{bE}}^{\mathrm{b}} \times \mathbf{I}\boldsymbol{\Omega}_{\mathrm{bE}}^{\mathrm{b}}. \end{aligned} \tag{2-6}$$

In this equation $\mathbf{I}$ is the mass moment of inertia matrix. This matrix can be simplified when it is assumed that XZ is a symmetry plane, which is the case for almost all aircraft including DEP, so that

$$\mathbf{I} = \begin{bmatrix} I_{xx} & -I_{xy} & -I_{xz} \\ -I_{xy} & I_{yy} & -I_{yz} \\ -I_{xz} & -I_{yz} & I_{zz} \end{bmatrix} = \begin{bmatrix} I_{xx} & 0 & -I_{xz} \\ 0 & I_{yy} & 0 \\ -I_{xz} & 0 & I_{zz} \end{bmatrix}. \tag{2-7}$$

Substituting gives the EoM for the rotational motion of the aircraft defined as

$$\begin{bmatrix} I_{xx}\dot{p} - (I_{yy} - I_{zz})\,qr - I_{xz}(pq + \dot{r}) \\ I_{yy}\dot{q} + (I_{xx} - I_{zz})\,pr + I_{xz}\,(p^2 - r^2) \\ I_{zz}\dot{r} - (I_{xz} - I_{yy})\,pq + I_{xz}(qr - \dot{p}) \end{bmatrix} = \begin{bmatrix} l \\ m \\ n \end{bmatrix} = \boldsymbol{\mathcal{M}}_{\mathrm{b}}^{\mathrm{ext}}. \tag{2-8}$$

Here l, m and n are the moments around the aircraft's body $x-$, $y-$ and $z-$axis respectively. The external moments applied to the aircraft are gathered in vector $\boldsymbol{\mathcal{M}}_{\mathrm{b}}^{\mathrm{ext}}$.

2-1-4 External forces and moments

Having defined the EoM for both the translational Eq. (2-5) and rotational direction Eq. (2-8), the external forces $\boldsymbol{\mathcal{F}}_{\mathrm{b}}^{\mathrm{ext}}$ and moments $\boldsymbol{\mathcal{M}}_{\mathrm{b}}^{\mathrm{ext}}$ need to be identified. Following the approach of [44], the external forces and moments can be categorized as follows. It is assumed that the external effects are made up of aerodynamic (a), gravitational (g), control (c), propulsion (p) and atmospheric disturbances (d) effects, which for the external forces and moments gives

$$\boldsymbol{\mathcal{F}}_{\mathrm{b}}^{\mathrm{ext}} = \boldsymbol{\mathcal{F}}_{\mathrm{a}} + \boldsymbol{\mathcal{F}}_{\mathrm{g}} + \boldsymbol{\mathcal{F}}_{\mathrm{c}} + \boldsymbol{\mathcal{F}}_{\mathrm{p}} + \boldsymbol{\mathcal{F}}_{\mathrm{d}}, \tag{2-9a}$$

$$\boldsymbol{\mathcal{M}}_{\mathrm{b}}^{\mathrm{ext}} = \boldsymbol{\mathcal{M}}_{\mathrm{a}} + \boldsymbol{\mathcal{M}}_{\mathrm{g}} + \boldsymbol{\mathcal{M}}_{\mathrm{c}} + \boldsymbol{\mathcal{M}}_{\mathrm{p}} + \boldsymbol{\mathcal{M}}_{\mathrm{d}}. \tag{2-9b}$$

The PAI effects are captured in the control contribution, as these effects are used actively for control. The atmospheric disturbances $\boldsymbol{\mathcal{F}}_{\mathrm{d}}$ and $\boldsymbol{\mathcal{M}}_{\mathrm{d}}$ are modeled using the Von Kármán turbulence model provided by the MIL-F-8785C military specification [45] for which the implementation is given in Appendix A-6.

As F_{b} is fixed to the aircraft's center of gravity, the gravitational effects do not cause any moments. It does contribute to the external forces which are decomposed in the F_{b} frame as

$$\boldsymbol{\mathcal{F}}_{\mathrm{g}} = \begin{bmatrix} -mg\sin\theta \\ mg\sin\phi\cos\theta \\ mg\cos\phi\cos\theta \end{bmatrix}, \tag{2-10a}$$

$$\boldsymbol{\mathcal{M}}_{\mathrm{g}} = 0. \tag{2-10b}$$

Here g is the gravitational acceleration, which is assumed to be a constant 9.81 m/s^2. As the remainder of the external forces and moment are defined specifically for the DEP aircraft, these will be discussed in the next section.

2-2 Control inputs, constraints and dynamics

In traditional aircraft control, aerodynamic surfaces deflect to control the moment around the aircraft. These surfaces include:

- aileron δ_{a} for roll control around the x-axis,
- elevator δ_{e} for pitch control around the y-axis,
- rudder δ_{r} for yaw control around the z-axis.

The propeller thrust T_p is traditionally used to control the aircraft's velocity [25]. As for the DEP aircraft the propeller thrust is used actively for control, this gives new opportunities which include:

- differential thrust for yaw control around the z-axis,
- PAI effects local lift increase for roll control around the x-axis,
- PAI effects total lift increase for altitude control.

These effects are summarized in Figure 2-3. In this figure, the blue arrows represent the control surface effects, the red the differential thrust effects and the orange the PAI effects. Note that T_p is replaced with n_p so that the rotational velocity of the propeller is controlled.

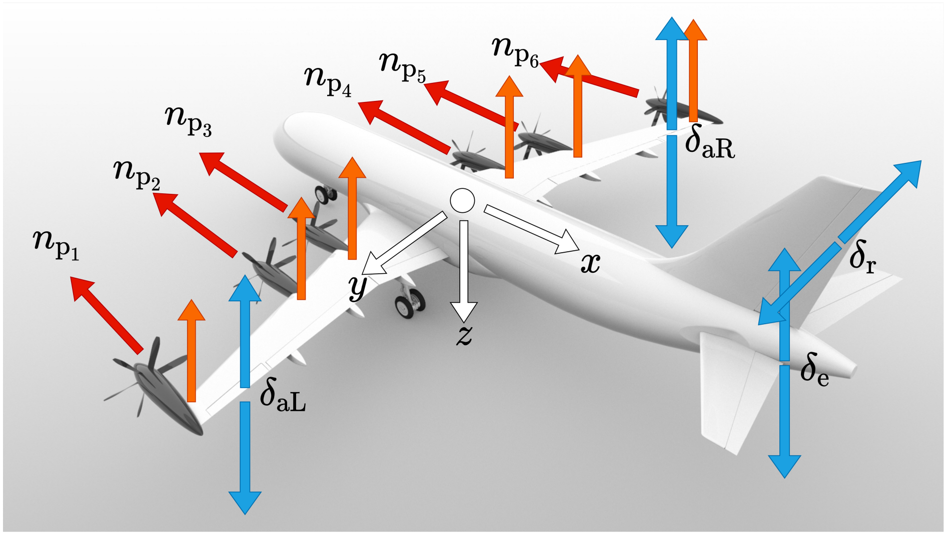

Figure 2-3: Overview of the control input effects on the DEP aircraft, where the blue arrows represent the control surface deflections, the red the differential thrust and the orange the PAI effects in the F_b frame. (
acsDEP-SFD render ©Orange Aerospace 2021)

As all six propeller are thus used separately, this gives the following control input vector

$$\boldsymbol{u} = \begin{bmatrix} \delta_\mathrm{aL} & \delta_\mathrm{aR} & \delta_\mathrm{e} & \delta_\mathrm{r} & n_\mathrm{p1} & n_\mathrm{p2} & n_\mathrm{p3} & n_\mathrm{p4} & n_\mathrm{p5} & n_\mathrm{p6} \end{bmatrix}^\mathrm{T}, \tag{2-11}$$

where the left δ_aL and right δ_aR aileron are controlled separately. The control surface deflections $\boldsymbol{\delta}$ are subject to position and rate constraints which are defined as

$$\boldsymbol{\delta}_\mathrm{min} \leq \boldsymbol{\delta} \leq \boldsymbol{\delta}_\mathrm{max}, \tag{2-12a}$$

$$|\dot{\boldsymbol{\delta}}| \leq \dot{\boldsymbol{\delta}}_\mathrm{max}. \tag{2-12b}$$

For the propeller rotational velocity n_p is also limited by the constraints

$$\boldsymbol{n}_{\mathrm{p}_\mathrm{min}} \leq \boldsymbol{n}_\mathrm{p} \leq \boldsymbol{n}_{\mathrm{p}_\mathrm{max}}, \tag{2-13a}$$

$$|\dot{\boldsymbol{n}}_\mathrm{p}| \leq \dot{\boldsymbol{n}}_{\mathrm{p}_\mathrm{max}}, \tag{2-13b}$$

which represents rotational velocity and acceleration constraints respectively. The constraint values for both $\boldsymbol{\delta}$ and $\boldsymbol{n}_\mathrm{p}$.

All control inputs are also subject to actuator dynamics. This means that the control inputs do not instantaneously go to their commanded value. These actuator dynamics are modeled using a second-order transfer function $A(s)$ defined as

$$A(s) = \frac{\omega_\mathrm{a}^2}{s^2 + \zeta_\mathrm{a}\omega_\mathrm{a} s + \omega_\mathrm{a}^2}, \tag{2-14}$$

where ω_aa is the natural frequency and ζ_aa the damping coefficient of the actuator. The constraints and actuator dynamics values for each actuator are given in Table A-5 and Table A-6.

2-3 Modeling of DEP

In this section, the different models which are specific for the DEP aircraft will be derived. For this, first a look will be taken into the modeling of the propellers regarding the thrust they produce and power they consume. After this, the PAI effects will be identified and methods proposed to model these effects. Finally, a method for making the aerodynamic and control effects non-dimensional will be given. Using this method, the complete model of the DEP aircraft can be described so that it can be used for controller design.

2-3-1 Propeller modeling

The propulsive forces $\boldsymbol{\mathcal{F}}_\mathrm{p}$ and moments $\boldsymbol{\mathcal{M}}_\mathrm{p}$ are produced by the six electric propellers. Rather than controlling the thrust of the propellers, which is traditionally done for aircraft control [25], in this thesis the rotational velocity $\boldsymbol{n}_\mathrm{p}$ of the propellers is controlled. With the rotational velocity, the power consumed by the propellers can be estimated. This will be used later to optimize the control inputs for minimal power consumption as will be discussed in Section 4-2-3.

The thrust and power produced by the propeller can be estimated using the thrust C_T and power C_P coefficient [46]. For the thrust, this gives the following relation

$$T = C_\mathrm{T}\rho n_\mathrm{p}^2 D_\mathrm{p}^4, \tag{2-15}$$

where ρ is the air density an D_p the propeller diameter. The thrust coefficient is dependent on

$$C_T = C_T(\beta_{0.75}, J, M_0, Re). \tag{2-16}$$

Here, $\beta_{0.75}$ is the 0.75 chord, J the advance ratio, M_0 the mach number and R_e the Reynolds number respectively. For the DEP aircraft the pitch is fixed at $\beta_{0.75} = 45°$. The advance ratio J is defined as

$$J = \frac{V_\infty}{n_\mathrm{p} D_\mathrm{p}}, \tag{2-17}$$

where V_∞ is the true airspeed. The power propeller power P_p is defined as

$$P_\mathrm{p} = C_P \rho n_\mathrm{p}^3 D_\mathrm{p}^5, \tag{2-18}$$

where the power coefficient depends on the same parameters as the thrust coefficient so that

$$C_P = C_P(\beta_{0.75}, J, M_0, Re). \tag{2-19}$$

As the DEP aircraft flies at a low Mach number, effects related to M_0 are neglected. Also, effects of a changing Reynolds number are not taken into account and as the pitch is fixed C_T only depends on J. This relationship was confirmed from experimental data which is given in Appendix A-3-1. The next section will discuss how this prop interacts with the airframe.

2-3-2 Propulsion airframe interaction (PAI) effects

As discussed before, modeling the PAI effects is key to use the full potential in terms of control of the DEP aircraft. Modeling these effects is hard, as they are nonlinear and depend on the operating conditions of both the aircraft and propeller. In [47] different methods are suggested to analyze these effects for the tractor configuration. In this configuration, the propellers are placed in front of the wing, as is done for the DEP aircraft. For this configuration, two major effects can be identified which include the wing effect on the propeller and the propeller effect on the wing. As the second effect plays the most significant role in terms of control, changing the force $\boldsymbol{\mathcal{F}}_\mathrm{c}$ and moment vector $\boldsymbol{\mathcal{M}}_\mathrm{c}$, this is the only effect that will be considered in the remainder of this thesis.

As stated in [47], the propeller has a large influence on the airflow passing the wing which is called the slipstream. This slipstream consists of an axial and swirl component which influences the lift and drag distribution over the wing. The axial component locally increases the dynamic pressure q, which gives an increase in local lift and drag. The dynamic pressure is defined as

$$q = \frac{1}{2}\rho V_\infty^2. \tag{2-20}$$

The swirl component changes the local angle of attack α where the up-going blade increases α, and the down-going blade decreases α.

Furthermore, the wingtip mounted propellers also interact with the wingtip vortex which is directed outboards up. When the propeller rotates against the direction of the wingtip vortex, thus inboards up, the swirl velocity cancels out the tangential velocity of the wingtip vortex [48]. This effect reduces the induced drag which leads to more efficient flight. A method for modeling the general and wingtip propellers PAI effects is given in the two subsequent sections.

General interaction effects

To model the PAI effects, the method of [49] is used. This method only gives an estimate of the effects, but allows to finding relations that can be used in the controller. For simplicity, it discards the swirl velocity component and only considers the increase in axial velocity, which is assumed to be uniform. For the full list of assumptions, the reader is referred to Appendix A-3-2. The relations defined here will form the framework in which the capabilities of actively controlling the PAI is tested. The parameters for the proposed method are defined in Figure 2-4.

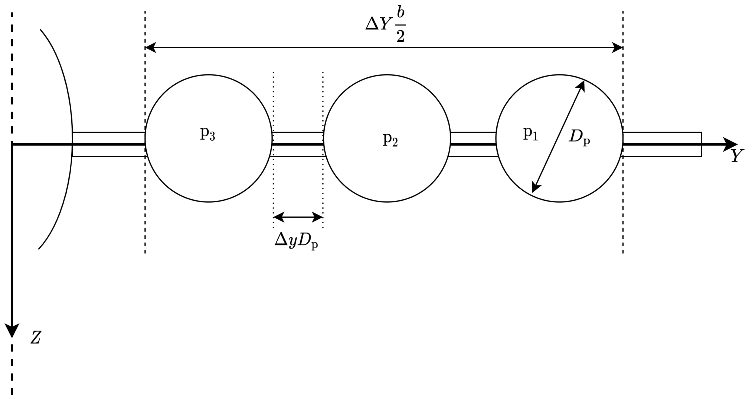

Figure 2-4: Wing and propeller parameters for PAI effects analysis definition.

For each propeller thrust T_p, the axial induction factor at the propeller disk a_p is calculated using actuator disk theory, which gives

$$a_\mathrm{p} = \frac{V_\mathrm{p} - V_\infty}{V_\infty} = \frac{1}{2}\left(\sqrt{1 + \frac{8T_\mathrm{p}}{\pi \rho V_\infty^2 D_\mathrm{p}^2}} - 1\right), \tag{2-21}$$

where V_p is the slipstream velocity at the propeller disk. The slipstream velocity on the wing is higher than the one leaving the propeller disk because of contraction. This contraction ratio is calculated as

$$\frac{R_\mathrm{w}}{R_\mathrm{p}} = \sqrt{\frac{1 + a_\mathrm{p}}{1 + a_\mathrm{p}\left(1 + (x_\mathrm{p}/R_\mathrm{p})/\sqrt{(x_\mathrm{p}/R_\mathrm{p})^2 + 1}\right)}}, \tag{2-22}$$

where $x_\mathrm{p}/R_\mathrm{p}$ gives the ratio of the placement of the propeller with respect to the leading edge in the x-direction divided by the radius of the propeller. From this ratio, following conservation of mass for incompressible flow, the axial induction factor at the wing leading edge a_w equals

$$a_\mathrm{w} = \frac{a_\mathrm{p} + 1}{(R_\mathrm{w}/R_\mathrm{p})^2} - 1. \tag{2-23}$$

Using this factor the sectional wing lift coefficient C_l increase can be calculated as

$$\Delta C_l = 2\pi\left[(\sin(\alpha) - a_\mathrm{w}\beta_\mathrm{corr}\sin(\alpha_\mathrm{p} - \alpha))\sqrt{(a_\mathrm{w}\beta_\mathrm{corr})^2 + 2a_\mathrm{w}\beta_\mathrm{corr}\cos\alpha_\mathrm{p} + 1} - \sin(\alpha)\right], \tag{2-24}$$

where α_p is the angle of attack of the propeller and β_corr the finite-slipstream correction factor. Note that in this formulation, C_l is the sectional lift-coefficient and not the roll coefficient. Determining β_corr is crucial, as the lift increase will otherwise be significantly overestimated. This is especially true for small ratios of slipstream radius and chord, which is the case for DEP. To calculate β_corr, a surrogate model developed with a two-dimensional CFD analysis for a NACA 0012 airfoil with an actuator disk in front is used. This model is defined in Appendix A-3-3 by Eq. (A-8) and Eq. (A-9) [50].

The wing lift-coefficient C_L increase can then be calculated with the sectional increase C_l as

$$\Delta C_L = \Delta c_l \cdot \Delta Y, \tag{2-25}$$

where ΔY is the spanwise interval the propellers occupy with respect to the wingspan b.

The increase in drag consists of two components

$$\Delta C_D = \Delta C_{D_0} + \Delta C_{D_\mathrm{i}}, \tag{2-26}$$

where the first component represents the increase in skin friction drag due to increased dynamic pressure and the second the increase in induced drag. The first factor is computed using

$$\Delta C_{D_0} = \Delta Y a_w^2 c_\mathrm{f}, \tag{2-27}$$

where c_f is the sectional skin friction coefficient for which a value of 0.009 is used [49]. Note that this method neglects the increase in wetted area due to installment of the propellers. The lift-induced drag increases due to an increase in C_L^2 and a change in the Oswald factor e. Assuming a parabolic drag polar, the second factor can be estimated as

$$\Delta C_{D_i} = \frac{\Delta C_L^2 + 2C_{L,\text{ airframe}}\,\Delta C_L}{\pi ARe}, \tag{2-28}$$

where AR is the aspect ratio defined as $AR = b\bar{c}$ and e the spanwise efficiency factor.

In [49], it is assumed that there is no change in span efficiency. For this thesis, the change in e is modeled, as this represents the increase in efficiency because of canceling out tip vortices. This effect is described in the next section.

Tip propeller interaction

Another aerodynamic effect of DEP is the counteracting from the tip propellers of the tip vortices. In [51], it was shown through wind tunnel testing, this leads to a reduction in induced drag for the inboard-up rotating propeller. This is due to wingtip-vortex attenuation and swirl recovery. It was also shown that this aerodynamic benefit can be captured by the increase of the span-efficiency parameter e. As discussed in the previous section, the drag coefficient is made up of two components

$$\begin{aligned} C_D &= C_{D_0} + C_{D_i} \\ C_D &= C_{D_0} + \frac{C_L^2}{\pi ARe}, \end{aligned} \tag{2-29}$$

where the first is the zero-lift drag and the second the lift-induced drag. As one can see, an increase in e will lead to a decrease in C_{D_i} and thus more efficient flight.

From wind tunnel testing, [51] found a relation between the thrust-coefficient C_T and the spanwise efficiency factor e. For a velocity of $V_\infty = 40m/s$ it was identified that e increases with 40% approximately at the optimum value of C_T. Further increasing C_T results in a reduction of e. The values for this research can be found in the left column of Table 2-1. As the range of C_T values is smaller in this research than for the DEP aircraft, the values for e were scaled. This was required as directly using the values will lead to overestimation of e, which will give unrealistic high values of drag reduction. The scaled values for the DEP aircraft are given in the right column of Table 2-1. Note the decrease in e is specific for the operating conditions which makes it difficult to translate this relation to the DEP aircraft. It

Table 2-1: Relationship between C_T and e from wind tunnel test data scaled to the DEP aircraft.

	Sinnige et al. [51]		DEP	
	C_T	e	C_T	e
min	0	0.8	0	0.8
optimum	0.123	1.12 (+40%)	0.2669	1.12 (+40%)
max	0.168	0.68 (-15%)	0.3645	1.12 (+40%)

was, therefore, assumed for the DEP aircraft that e does not decrease after the optimal C_T value. Rather, the e value is limited to the maximum, as shown in the right column of the table below.

This method simplifies the tip propeller interaction significantly. Firstly, it uses a limited number of data points with one operating condition to find a relationship which is assumed to be linear. Secondly, the data points are scaled to the DEP operating conditions. As no wind tunnel testing has been performed for the DEP aircraft, it is not known how these conditions relate and whether this scaling gives reliable results. Still, as the main goal of this thesis is to show that these effects can be used actively for control, not to model them as accurately as possible, it is assumed that this method suffices. If wind tunnel data of DEP is acquired at a later stage, this can be used to model these effects more accurately.

Assuming a linear relation based on Table 2-1 gives

$$\begin{aligned} e(C_\mathrm{T}) &= 0.8 + 1.1991 C_\mathrm{T},\ C_\mathrm{T} \leq 0.2669 \\ e(C_\mathrm{T}) &= 1.12,\ C_\mathrm{T} > 0.2669. \end{aligned} \tag{2-30}$$

The drag coefficient including the tip propeller effect C_{D_tip}, can then be found with

$$C_{D_\mathrm{tip}} = C_D + 0.5\left(\frac{C_L^2}{\pi A R e_\mathrm{L}} - \frac{C_L^2}{\pi A R e_0}\right) + 0.5\left(\frac{C_L^2}{\pi A R e_\mathrm{R}} - \frac{C_L^2}{\pi A R e_0}\right), \tag{2-31}$$

where $e_0 = 0.8$ is the span-efficiency factor without propeller effects.

2-3-3 Aileron tip propeller interaction

Another interaction effect regarding the tip propellers, is the coupling between these propellers and the ailerons. As the ailerons are placed behind the tip propellers, they are influenced by their slipstream. For simplicity, is is assumed that the ailerons are fully immersed in this slipstream and that this slipstream is uniform over the span of the aileron. These assumptions were also used for the PAI derived previously. The roll moment produced by the aileron, taking into account the slipstream, is defined as

$$l_{\delta_\mathrm{a}} = \frac{1}{2} C_{l_{\delta_\mathrm{a}}} \rho V_\mathrm{a}^2 S b \delta_\mathrm{a}, \tag{2-32}$$

where V_a is the velocity of the slipstream at the aileron. This is higher than V, as $V_\mathrm{j} > V_\mathrm{a} > V_\infty$ if the propellers produce thrust. Note that the notation l_{δ_a} is used to indicate the rolling moment produced by δ_a exclusively. To calculate V_a, the method introduced for the general interaction effects is used. Firstly, the slipstream contraction ratio at the aileron is calculated as

$$\frac{R_{\mathrm{a}}}{R_{\mathrm{p}}} = \sqrt{\frac{1+a_{\mathrm{p}}}{1+a_{\mathrm{p}}\left(1+\left(x_{\mathrm{a}}/R_{\mathrm{p}}\right)/\sqrt{\left(x_{\mathrm{a}}/R_{\mathrm{p}}\right)^2+ll1}\right)}}, \tag{2-33}$$

where $x_{\mathrm{a}}/R_{\mathrm{p}}$ is the axial position of the propeller with respect to the aileron divided by the propeller radius. It is assumed that the aileron is a distance mean aerodynamic chord $\bar{c}$ behind the wing leading edge. This assumption gives $x_{\mathrm{a}}/R_{\mathrm{p}} = 3.3279$. The axial induction factor a_{a} at the aileron is then calculated as

$$a_{\mathrm{a}} = \frac{a_{\mathrm{P}}+1}{\left(R_{\mathrm{a}}/R_{\mathrm{P}}\right)^2} - 1, \tag{2-34}$$

so that

$$V_{\mathrm{a}} = \beta_{\mathrm{corr}} a_{\mathrm{a}} V_\infty + V_\infty, \tag{2-35}$$

where β_{corr} is again determined using the surrogate model of Appendix A-3-3. Finally, note that the drag produced by the ailerons also increases, because of the increase in slipstream velocity at the aileron. The drag of the aileron can be defined as

$$D_{\delta_{\mathrm{a}}} = \frac{1}{2} C_{D_{\delta_{\mathrm{a}}^2}} \rho V_{\mathrm{a}}^2 S \delta_{\mathrm{a}}^2, \tag{2-36}$$

which also increases as $V_{\mathrm{a}} > V_\infty$.

2-3-4 Aerodynamic and control effects

The remainder of the external forces and moments depend on the aerodynamics (a) of the airframe and the control inputs (c). A convenient method to express the effects for both the airframe and control effectors is by making them non-dimensional. As explained in [52], this is done by dividing by the dynamic pressure q defined in Eq. (2-20), the wing surface area S, the wing mean geometric chord $\bar{c}$ and the wingspan b. The non-dimensional force and moment coefficients are defined in the F_{b} frame as

$$C_X = \frac{X}{qS},\ C_Y = \frac{Y}{qS},\ C_Z = \frac{Z}{qS} \tag{2-37a}$$

$$C_l = \frac{L}{qSb},\ C_m = \frac{M}{qS\bar{c}},\ C_n = \frac{N}{qSb}. \tag{2-37b}$$

Relevant force coefficients in the F_a frame are

$$C_L = \frac{L}{qS},\ C_D = \frac{D}{qS}, \tag{2-38}$$

where C_L is the lift coefficient and C_D the drag coefficient. These replace C_X and C_Z in Eq. (2-37). As the aerodynamic coefficients for the SFD are expressed in the F_{a} frame, the focus of the remainder of this section will be on modeling in this frame.

Assuming a full-scale conventional airplane in quasi-steady flow, so that the flowfield adjusts instantaneously to changes, at a low-Mach number the dependence of the non-dimensional coefficients on the states and control inputs is given as [53]

$$C_i = C_i\left(\hat{V}, \alpha, \beta, \hat{p}, \hat{q}, \hat{r}, \hat{\dot{\alpha}}, \hat{\dot{\beta}}, \boldsymbol{u}\right), \tag{2-39}$$

where

$$\hat{V} = \frac{V}{V_0},\ \hat{p} = \frac{pb}{2V},\ \hat{q} = \frac{q\bar{c}}{2V},\ \hat{r} = \frac{rb}{2V},\ \hat{\dot{\alpha}} = \frac{\dot{\alpha}\bar{c}}{2V},\ \hat{\dot{\beta}} = \frac{\dot{\beta}b}{2V}, \tag{2-40}$$

are the non-dimensional state-variables for $i = D, Y, L, l, m, n$. The equations for the different non-dimensional coefficients defined in Eq. (2-39) are non-linear in their parameters which makes it difficult to model or identify them. A method to simplify this, is using the small-disturbance theory as suggested in [43]. Here it is assumed that the analyzed motion of the airplane is a small deviation from the steady flight condition. For this, a first-order Taylor expansion as described below is used.

First Order Taylor Expansion [17]
Given a general nonlinear and non-autonomous system $\dot{\boldsymbol{x}} = \boldsymbol{f}(\boldsymbol{x}, \boldsymbol{u})$, where $\boldsymbol{x}$ is the state and $\boldsymbol{u}$ the input vector. This system is assumed to be continuously differentiable. The first order Taylor expansion around the equilibrium point ($\boldsymbol{x} = \boldsymbol{x}_0, \boldsymbol{u} = \boldsymbol{u}_0$) is defined as

$$\dot{\boldsymbol{x}} = \boldsymbol{f}(\boldsymbol{x}_0, \boldsymbol{u}_0) + \left.\frac{\partial \boldsymbol{f}}{\partial \boldsymbol{x}}\right|_{\boldsymbol{x}=\boldsymbol{x}_0, \boldsymbol{u}=\boldsymbol{u}_0} (\boldsymbol{x} - \boldsymbol{x}_0) + \left.\frac{\partial \boldsymbol{f}}{\partial \boldsymbol{u}}\right|_{\boldsymbol{x}=\boldsymbol{x}_0, \boldsymbol{u}=\boldsymbol{u}_0} (\boldsymbol{u} - \boldsymbol{u}_o) + \boldsymbol{f}_{\text{h.o.t}}(\boldsymbol{x}, \boldsymbol{u}). \tag{2-41}$$

Here $\boldsymbol{f}_{\text{h.o.t.}}$ are the higher order terms which are not included in a first-order Taylor expansion. If the equilibrium is $\boldsymbol{f}(\boldsymbol{x}_0, \boldsymbol{u}_0) = 0$ Eq. (2-41) can be further reduced to

$$\dot{\boldsymbol{x}} = \left.\frac{\partial \boldsymbol{f}}{\partial \boldsymbol{x}}\right|_{\boldsymbol{x}=0, \boldsymbol{u}=0} \boldsymbol{x} + \left.\frac{\partial \boldsymbol{f}}{\partial \boldsymbol{u}}\right|_{\boldsymbol{x}=0, \boldsymbol{u}=0} \boldsymbol{u} + \boldsymbol{f}_{\text{h.o.t}}(\boldsymbol{x}, \boldsymbol{u}). \tag{2-42}$$

The longitudinal and lateral coefficients are decoupled [53] so that the longitudinal coefficients are given as

$$C_D = C_{D_0} + C_{D_V}\hat{V} + C_{D_\alpha}\alpha + C_{D_\beta}\beta + C_{D_{\dot{\alpha}}}\hat{\dot{\alpha}} + C_{D_q}\hat{q} + \boldsymbol{C}_{D_{\boldsymbol{u}}}\boldsymbol{u}, \tag{2-43a}$$

$$C_L = C_{L_0} + C_{L_V}\hat{V} + C_{L_\alpha}\alpha + C_{L_\beta}\beta + C_{L_{\dot{\alpha}}}\hat{\dot{\alpha}} + C_{L_q}\hat{q} + \boldsymbol{C}_{L_{\boldsymbol{u}}}\boldsymbol{u}, \tag{2-43b}$$

$$C_m = C_{m_0} + C_{m_V}\hat{V} + C_{m_\alpha}\alpha + C_{m_\beta}\beta + C_{m_{\dot{\alpha}}}\hat{\dot{\alpha}} + C_{m_q}\hat{q} + \boldsymbol{C}_{m_{\boldsymbol{u}}}\boldsymbol{u}, \tag{2-43c}$$

and the lateral coefficients as

$$C_Y = C_{Y_0} + C_{Y_\alpha}\alpha + C_{Y_\beta}\beta + C_{Y_{\dot{\beta}}}\hat{\dot{\beta}} + C_{Y_p}\hat{p} + C_{Y_r}\hat{r} + \boldsymbol{C}_{Y_{\boldsymbol{u}}}\boldsymbol{u}, \tag{2-44a}$$

$$C_l = C_{l_0} + C_{l_\alpha}\alpha + C_{l_\beta}\beta + C_{l_{\dot{\beta}}}\hat{\dot{\beta}} + C_{l_p}\hat{p} + C_{l_r}\hat{r} + \boldsymbol{C}_{l_{\boldsymbol{u}}}\boldsymbol{u}, \tag{2-44b}$$

$$C_n = C_{n_0} + C_{n_\alpha}\alpha + C_{n_\beta}\beta + C_{n_{\dot{\beta}}}\hat{\dot{\beta}} + C_{n_p}\hat{p} + C_{n_r}\hat{r} + \boldsymbol{C}_{n_{\boldsymbol{u}}}\boldsymbol{u}. \tag{2-44c}$$

Here, the vector $\boldsymbol{u}$ contains all control inputs which were identified in Section 2-2. The above equations are defined using a first-order Taylor expansion Eq. (2-41) which means that higher-order terms are discarded. Note that these derivatives are defined around the operating point $(\boldsymbol{x}_0, \boldsymbol{u}_0)$, so that these can change for different operating conditions. The different derivatives can be found by differentiating the respective coefficient with the relevant parameter. So for example

$$C_{D_\alpha} = \left.\frac{\partial C_D}{\partial \alpha}\right|_{\boldsymbol{x}_0, \boldsymbol{u}_0},\ C_{D_u} = \left.\frac{\partial C_D}{\partial u}\right|_{\boldsymbol{x}_0, \boldsymbol{u}_0}. \tag{2-45}$$

The partial derivatives with respect to the states $(V, \alpha, \dot{\alpha}, \beta, \dot{\beta}, p, q, r)$ are called the stability derivatives. The partial derivatives with respect to the control input $\boldsymbol{u}$ are called the control derivatives. Note that $\boldsymbol{u}$ is a vector, which means that there are multiple control derivatives.

The relations defined in Eq. (2-43) and Eq. (2-44) assume a linear relationship between the stability or control derivative and its parameter. For large amplitudes, rapid deviations from the reference flight conditions or non-linear relations, this can cause a model mismatch. To capture these effects, nonlinear terms need to be added for which different methods are suggested in [53]. The first is introducing higher-order terms in Eq. (2-43) and Eq. (2-44). For example, C_L can also be made dependent on α^2 and the coupling term $\alpha\beta$ by introducing the stability derivatives

$$C_{L_{\alpha^2}} = \left.\frac{\partial^2 C_L}{\partial \alpha^2}\right|_{\boldsymbol{x}_0,\boldsymbol{u}_0}, \; C_{L_{\alpha\beta}} = \left.\frac{\partial^2 C_L}{\partial \alpha \beta}\right|_{\boldsymbol{x}_0,\boldsymbol{u}_0}. \tag{2-46}$$

Another method suggested in [53], is to make the aerodynamic coefficients depend on α and β. For example, the lift coefficient C_L can change over the operating range. This effect can be captured with a nonlinear function $C_L(\alpha,\beta)$. This is an example and the model can be simplified or expanded by ex- or including more nonlinear terms. Using this method, the stability and control derivatives can be defined over the complete operating range of the aircraft.

Note that these equations describe the aerodynamic model in the most general form. For the SFD, the most relevant effects were identified using wind tunnel testing. The coefficients of this aerodynamic model are given in Appendix A-4. The coefficients include linear, quadratic and nonlinear terms, which were identified using the method described in this section.

2-4 Scaled flight testing

As discussed in Chapter 1, using an SFD forms the ideal test platform to develop radically new aircraft concepts of which DEP is one of the most promising technologies. This section discusses the theory behind scaled flight testing and how the SFD was scaled down from the Airbus A320. For the SFD project, all dimensions are scaled with the same factor defined as $n = 1/8.5$. Note that there is an important difference between geometric and dynamic scaling. Rather than scaling the exact dimensions, dynamic scaling aims at developing a model with the same external forces and kinematic responses as the full-scale model. A dynamic scale model is thus a geometric scale model that is designed so that the scale model has comparable flow properties and flight characteristics as the full-scale aircraft. This scale model does not behave the same as the full-scale model, but according to predefined relations which can be used to correlate the results to the full-scale aircraft. To distinguish a dynamically scaled model from a geometric one, the following similitude requirement are defined where l is the reference length [54]

Relative density factor $\frac{m}{\rho l^3}$, ensures that both aircraft fly at the same lift coefficient in level flight.

Relative mass moment of inertia $\frac{I}{\rho l^5}$, ensures that the inertial properties of both aircraft are according to scale.

Froude number $\frac{V^2}{gl}$, gives the ratio between the inertial and gravitational forces.

Mach number $\frac{V}{c}$ gives the ratio between the velocity and speed of sound c.

Reynolds number $\frac{\rho V l}{\mu}$, gives the ratio between inertial and viscous forces where μ is the absolute viscosity.

Ideally one meets all these requirements, but in practice this cannot be achieved. Specifically, meeting the last three requirements results in too large scale factors, so that the benefits in terms of risk and cost for scaled flight testing become too small. For the SFD project, the highest priority is designing a scaled model with the same dynamic and flight physical behavior [3]. The Froude number assures that for the same control inputs, the scaled and full-scale aircraft follow the same flight path and reach the same altitudes [55]. These motions are in a proportional time-scale and can thus be used to compare the dynamics of both aircraft. Therefore, the Froude number is used in the design of the SFD together with the relative density and mass moment of inertia factor. Note that the SFD thus flies at a different Mach and Reynolds number. Using the Froude scaled model the following relations for the motion of the aircraft can be defined [54].

Table 2-2: Scaling factor of a Froude scaled model for kinematic parameters.

Parameter	Scale factor
Linear displacement	n
Linear velocity	$\sqrt{n}$
Linear acceleration	1
Angular displacement	1
Angular rate	$1/\sqrt{n}$
Angular acceleration	$1/n$
Time	$\sqrt{n}$

Based on the definitions defined above and the scale factor $n = 1./8.5$ the design and performance parameters of the SFD can be defined. The main parameters for this are given in Table A-4 in Appendix A-4.

2-5 Linear analysis

The first step in controller design for aircraft is finding the trim conditions. In these conditions, the aircraft is in steady flight which means the forces and moments around the aircraft are all in equilibrium. The state vector for the DEP aircraft is defined as

$$\boldsymbol{x} = \begin{bmatrix} x & y & z & u & v & w & \phi & \theta & \psi & p & q & r \end{bmatrix}^{\mathrm{T}}. \tag{2-47}$$

The first three states describe the position of the aircraft in the F_{E} frame, the next three the velocity in the F_{b} frame, the next three the attitude in the F_{E} frame and the final three the angular velocity in the F_b frame. Note that the aircraft can be described completely using 8 states as will be shown later when discussing the eigenmodes. Still, using these 12 states they all have a physical meaning which makes them more intuitive to work with.

The input and output vector for trimming are defined as

$$\boldsymbol{u} = \begin{bmatrix} \delta_\mathrm{s} & n_\mathrm{p} \end{bmatrix}^\mathrm{T}, \tag{2-48a}$$

$$\boldsymbol{y} = \begin{bmatrix} \alpha & V & h \end{bmatrix}^\mathrm{T}, \tag{2-48b}$$

where in trimming all propellers rotate with the same velocity n_p and δ_s is the deflection of the horizontal stabilizer. The trim condition of the aircraft depends both on the altitude h and the velocity V. The DEP aircraft was trimmed for a range of velocities between 30 and 60 m/s in steps of 5 m/s and a range of altitudes between 100 and 1100 m with steps of 200 m, which gives a total of 42 trim points.

To find the trim conditions, $\dot{\boldsymbol{x}}$ is set equal to zero except for the time derivative of the position in x-direction. This $\dot{x}$ should have a constant value which is set equal to V. Furthermore, z should be equal to $-h$ so that the aircraft keeps the same prescribed altitude. Using the MATLAB function `findop` [56], the trim conditions of the DEP aircraft were determined. For $V = 35, 45, 55$ m/s and $h = 300$ m, the following values were found.

Table 2-3: Trim values of the DEP aircraft for $V = 35, 45, 60$ m/s and $h = 300$ m.

	$V = 35$ m/s, $h = 300$ m	$V = 45$ m/s, $h = 300$ m	$V = 55$ m/s, $h = 300$ m
δ_s	$-2.73°$	$-1.61°$	$-0.80°$
n_p	51.0 rev/s	58.6 rev/s	69.4 rev/s
α	$9.84°$	$5.74°$	$3.44°$

Using the `MATLAB` function `linearize` [57], the linear state space describing the linear dynamics around the trimming points was found. Using this state space the eigenmodes of the aircraft were determined. Again, for $V = 35, 45, 55$ m/s and $h = 300$ m, the following values were found.

Table 2-4: Trim values of the DEP aircraft for $V = 35, 45, 60$ m/s and $h = 300$ m.

Eigenmode	$V = 35$ m/s, $h = 300$ m	$V = 45$ m/s, $h = 300$ m	$V = 55$ m/s, $h = 300$ m
Short period	$-1.523 \pm 2.264i$	$-1.9989 \pm 3.0988i$	$-2.4324 \pm 3.7993i$
Phugoid	$-0.007 \pm 0.3060i$	$-0.0115 \pm 0.2492i$	$-0.0140 \pm 0.2067i$
Dutch roll	$-0.7309 \pm 3.0466i$	$-0.8710 \pm 3.8116i$	$-1.0151 \pm 4.6350i$
Roll damping	-3.2260	-4.3891	-5.5343
Spiral mode	-0.0169	-0.0105	-0.0100

As all these eigenmodes have negative eigenvalues, the DEP aircraft is stable. Note, that stability was checked for the complete set of 42 trim points. Therefore, when an external disturbance is applied, the aircraft will return to a steady equilibrium. In terms of disturbance rejection, a controller can make sure that this equilibrium is reached faster, especially considering the slow phugoid and spiral modes. Furthermore, a controller is required for tracking reference signals.

Before designing a control method, controllability of the DEP aircraft was analyzed where

$$\boldsymbol{u} = \begin{bmatrix} \delta_{\mathrm{a}} & \delta_{\mathrm{e}} & \delta_{\mathrm{r}} & T_{\mathrm{p}} \end{bmatrix}^{\mathrm{T}} \tag{2-49a}$$

$$\boldsymbol{y} = \begin{bmatrix} V & h & p & q & r \end{bmatrix}^{\mathrm{T}}, \tag{2-49b}$$

and the state vector $\boldsymbol{x}$ defined as in Eq. (2-47). Note that n_{P} was replaced by T_{p} to simplify the analysis. Still, the results of this analysis hold as only the propeller model discussed in Section 2-3-1 needs to be implemented to find n_{p} for the required T_{p}. The linear state space for the Multiple input multiple output (MIMO) system is then defined as

$$\begin{aligned} \dot{\boldsymbol{x}} &= \mathbf{A}\boldsymbol{x} + \mathbf{B}\boldsymbol{u}, \\ \boldsymbol{y} &= \mathbf{C}\boldsymbol{x} + \mathbf{D}\boldsymbol{u}, \end{aligned} \tag{2-50}$$

where $\mathbf{A} \in \mathbb{R}^{n\times n}$, $\mathbf{B} \in \mathbb{R}^{n\times p}$, $\mathbf{C} \in \mathbb{R}^{m\times n}$ with n the number of states, p the number of inputs and m the number of outputs. Also, $\mathbf{D} = 0$ as there is no direct feed-through of the inputs signals to the output. The state-space matrices are $\mathbf{A}, \mathbf{B}, \mathbf{C}$ are given in Appendix A-7 for $V = 45\ m/s$ and $h = 300\ m$. Controllability can then be analyzed by determining the rank of the controllability matrix $\mathcal{C}$ defined as

$$\mathcal{C} = \begin{bmatrix} \mathbf{B} & \mathbf{AB} & \mathbf{A}^2\mathbf{B} & \dots & \mathbf{A}^{n-1}\mathbf{B} \end{bmatrix}. \tag{2-51}$$

It was derived that $\mathrm{rank}(\mathcal{C}) = 12$, so that controllability of all states $\boldsymbol{x}$ with control input $\boldsymbol{u}$ was confirmed. This means that a controller can be designed using the method proposed in the Chapter 3. Finally, note that in Eq. (2-49a) not all control authorities of the DEP aircraft are used, as the propellers are not controlled separately. This increases the number of control inputs as each propeller can be controlled individually. Therefore, the conclusion regarding controllability still holds. Considering individual control of the propellers, control allocation is required which will be discussed in Chapter 4.

2-6 Conclusions

In this chapter, the model and EoM for the DEP aircraft were derived. Starting from the EoM for general aircraft, defining the relevant reference frames, the additional forces and moment for the DEP aircraft were identified. These include differential thrust and PAI effects. To model these effects, first a method for determining the thrust and power of the propellers was introduced. After this, the different PAI effects were identified and a method was proposed to determine their values. As modeling of these effects is difficult, it was decided to use a relative straightforward analytical model. This model allows capturing the most important effects, which can then be implemented in the controller design discussed in the next chapters. If new data becomes available in the future, through for example CFD or wind tunnel testing, more accurate models can be added to the model and controllers. Next to that, the method of non-dimensionalizing the stability and control derivatives was proposed, which forms the framework for the aerodynamic and control model used in the controllers. Furthermore, the method of scaled flight testing was given, discussing how the SFD was scaled from the full-scale Airbus A320. Finally, a linear analysis was performed around the nonlinear DEP model. In this analysis, stability and controllability around the different operating points was concluded.

Chapter 3

Nonlinear aircraft control

This chapter will describe the nonlinear control method used to control the DEP aircraft. It will first introduce the general nonlinear control problem, after which different control methods will be proposed. Based on the Nonlinear dynamics inversion (NDI), method the control problem will be solved incrementally which gives Incremental nonlinear dynamic inversion (INDI). This method is robust to both modeling errors and external disturbances. The NDI and INDI methods will be combined, forming a controller with different inner and outer loops for both translational and rotational control of the DEP aircraft. This controller will then be reformulated, so that the control problem can be solved in one step, without the use of outer control loops. Stability and robustness of this controller will be proven, so that it shapes the framework of the controller design for the remainder of this thesis.

3-1 General control problem

A general nonlinear time-invariant system is described by

$$\dot{\boldsymbol{x}} = \boldsymbol{f}(\boldsymbol{x}, \boldsymbol{u}), \tag{3-1a}$$

$$\boldsymbol{y} = \boldsymbol{h}(\boldsymbol{x}), \tag{3-1b}$$

where $\boldsymbol{x} \in \mathbb{R}^n$ is the state, $\boldsymbol{u} \in \mathbb{R}^p$ the input and $\boldsymbol{y} \in \mathbb{R}^m$ the output vector. Both $\boldsymbol{f}$ and $\boldsymbol{h}$ are smooth vector fields. This means these functions have continuous partial derivatives of any required order [17]. The system considered is thus Multiple input multiple output (MIMO). The goal of the controller design is to find an input $\boldsymbol{u}$, so that the output $\boldsymbol{y}$ tracks the reference output $\boldsymbol{y}_{\text{ref}}$.

Different methods were discussed in Section 1-2-1, to design a controller for reference tracking. To control the aircraft over the complete operating range, a nonlinear controller is required. Furthermore, the controller should be robust against modeling errors and external disturbances especially considering that the PAI effects are hard to model. It was concluded that Incremental nonlinear dynamic inversion (INDI) [23] is the most suitable controller regarding these requirements. As this controller feeds back sensor measurements, it relies less on the aircraft's model. This makes the controller inherently robust to modeling errors and external disturbances, where the latter are captured in the sensor measurements.

The INDI controller was derived from the Nonlinear dynamics inversion (NDI) controller which is a nonlinear controller able to control the aircraft over the complete operating range. The next section will give the derivation of this NDI controller from which the INDI controller will then be formulated.

3-2 Nonlinear dynamics inversion (NDI)

This nonlinear control method is based on the more general feedback linearization method developed in [17]. Feedback linearization cancels the nonlinear dynamics, so that the closed-loop dynamics are in linear form. In this form, simple linear control techniques can be used to control the system. Feedback linearization can be directly applied to a nonlinear system which is in the companion a controllability canonical form.

In general systems are not in this form, so that [17] proposes two alternatives. The first method finds an algebraic transformation $\boldsymbol{z} = \boldsymbol{z}(\boldsymbol{x})$, which puts the dynamics into controllability normal form. This is referred to as input-state linearization. As the reference values also need to be expressed in the new states, this method is complex for tracking. The second method is based on partial linearization of the system dynamics, called input-output linearization. This method aims at finding a direct linear relationship between the system output $\boldsymbol{y}$ and the control input $\boldsymbol{u}$ so that it is more suitable for tracking reference signals. As this is the objective of the control problem defined at the beginning of this chapter, this section will further elaborate on this method.

The main idea of input-output feedback linearization is to differentiate the output ρ times, until an explicit relation between the input and output is found. Here, ρ represents the relative degree of the system. For any controllable system of order n, $\rho \leq n$. If $\rho < n$, part of the system dynamics are unobservable in the input-output linearization. This part is called the internal dynamics, as it cannot be seen from the external input-output relation. For the controller design to work, the internal dynamics should be stable. If the outputs and inputs are carefully selected, there are no internal dynamics, as a direct relation between the inputs and derivative of the output is found. For the derivation of NDI, it is useful to introduce the concept of the Gradient and Jacobian and Lie derivative.

Gradient and Jacobian [17]

Given a smooth scalar function $h(\boldsymbol{x}) : \mathbb{R}^n \to \mathbb{R}$, where $\boldsymbol{x}$ represents the state of the system, the gradient $\nabla \boldsymbol{h}$ is given as

$$\nabla \boldsymbol{h} = \frac{\partial h}{\partial \boldsymbol{x}}. \tag{3-2}$$

The gradient is a row-vector filled with the elements $(\nabla \boldsymbol{h})_j = \partial h / \partial \boldsymbol{x}_j$. For a vector field $\boldsymbol{f} : \mathbb{R}^n \to \mathbb{R}^n$ the Jacobian of $\boldsymbol{f}$ is

$$\nabla \mathbf{f} = \frac{\partial \boldsymbol{f}}{\partial \boldsymbol{x}}. \tag{3-3}$$

The Jacobian is represented by an $n \times n$ matrix filled with elements $(\nabla \mathbf{f})_{ij} = \partial \boldsymbol{f}_i / \partial \boldsymbol{x}_j$

Lie Derivative [17]
Given the same $\boldsymbol{f}$ and h as defined above, the Lie derivative of h with respect to $\boldsymbol{f}$, $L_{\boldsymbol{f}}h$, is a scalar function defined as

$$L_{\boldsymbol{f}}h = \nabla \boldsymbol{h}\boldsymbol{f}. \tag{3-4}$$

The Lie derivative is thus the directional derivative of h along the direction of vector $\boldsymbol{f}$. The Lie derivative can be defined recursively with repeated derivatives.

$$L^0_{\boldsymbol{f}}h = h, \tag{3-5a}$$
$$L_{\boldsymbol{f}}h = \nabla \boldsymbol{h}\boldsymbol{f}, \tag{3-5b}$$
$$L^i_{\boldsymbol{f}}h = L_{\boldsymbol{f}}\left(L^{i-1}_{\boldsymbol{f}}h\right) = \nabla\left(L^{i-1}_{\boldsymbol{f}}h\right)\boldsymbol{f} \text{ for i = 1,2,...} \tag{3-5c}$$

When another vector field $\boldsymbol{g}$ is introduced the Lie derivative is defined as

$$L_{\boldsymbol{g}}L_{\boldsymbol{f}}h = \nabla\left(L_{\boldsymbol{f}}h\right)\boldsymbol{g}. \tag{3-6}$$

For the derivation of NDI, the general nonlinear time-invariant MIMO system defined in Eq. (3-1) is rewritten to

$$\dot{\boldsymbol{x}} = \boldsymbol{f}(\boldsymbol{x}) + \mathbf{g}(\boldsymbol{x})\boldsymbol{u} \tag{3-7a}$$
$$\boldsymbol{y} = \boldsymbol{h}(\boldsymbol{x}), \tag{3-7b}$$

where $\mathbf{g} \in \mathbb{R}^{n\times m}$ is a matrix of which the columns $\boldsymbol{g}_i$ are smooth vector fields. It is thus assumed that the number of inputs is equal to the number of outputs, so that $p = m$. This assumption holds throughout the remainder of this chapter. In Chapter 4 the full set of control inputs of the DEP, as discussed in Section 2-2, will be used so that $p > m$ for which control allocation techniques are required. In the form of Eq. (3-7), the dynamics are nonlinear in the states $\boldsymbol{x}$ but linear in the inputs $\boldsymbol{u}$. This simplifies the derivation of NDI but as shown in [17], by means of a variable substitution, a general nonlinear system can always be expressed in the form of Eq. (3-7). Representing this system as a sum of scalar entries gives

$$\dot{\boldsymbol{x}} = \boldsymbol{f}(\boldsymbol{x}) + \sum_{j=1}^{m} \boldsymbol{g}_j(\boldsymbol{x})u_j, \tag{3-8a}$$
$$\boldsymbol{y} = \left[h_1(\boldsymbol{x}), h_2(\boldsymbol{x}), ..., h_m(\boldsymbol{x})\right]^{\mathrm{T}}, \tag{3-8b}$$

where u_j and $h_i(\boldsymbol{x})$ are the scalar j-th input and i-th output respectively, and the vector $\boldsymbol{g}_j(\boldsymbol{x}) \in \mathbb{R}^n$ gives the dynamics for the j-th input. To find a relation between the output and input, the output y_i needs to be differentiated until one of the inputs u_i appears. For the i-th output, differentiating k times, this gives

$$\begin{aligned}
\dot{y}_i &= \nabla h_i \frac{\partial \boldsymbol{x}}{\partial t} = \nabla h_i \left(\boldsymbol{f}(\boldsymbol{x}) + \sum_{j=1}^{m} \boldsymbol{g}_j(\boldsymbol{x}) u_j \right) = L_{\boldsymbol{f}} h_i(\boldsymbol{x}) + \sum_{j=1}^{m} L_{\boldsymbol{g}_j} h_i(\boldsymbol{x}) u_j, \\
\ddot{y}_i &= L_{\boldsymbol{f}}^2 h_i(\boldsymbol{x}) + \sum_{j=1}^{m} L_{\boldsymbol{g}_j} L_{\boldsymbol{f}} h_i(\boldsymbol{x}) u_j, \\
&\vdots \\
y_i^{(k)} &= L_{\boldsymbol{f}}^k h_i(\boldsymbol{x}) + \sum_{j=1}^{m} L_{\boldsymbol{g}_j} L_{\boldsymbol{f}}^{k-1} h_i(\boldsymbol{x}) u_j.
\end{aligned} \tag{3-9}$$

Differentiating is performed as long as

$$L_{\boldsymbol{g}_j} L_{\boldsymbol{f}}^{k-1} h_i(\boldsymbol{x}) = 0, \forall j = 1, ..., m. \tag{3-10}$$

If $L_{\boldsymbol{g}_j} L_{\boldsymbol{f}}^{k-1} h_i(\boldsymbol{x}) \neq 0$ for at least one j, differentiating for the output channel y_i is completed. This means that a direct relation between the k-th derivative of y_i and one of the control inputs u_j is found. The relative degree ρ_i for y_i equals k_i, the number of differentiations required to find this relation. The vector relative degree is defined as $\boldsymbol{\rho} = \begin{bmatrix} \rho_1 & \rho_2 & \dots & \rho_m \end{bmatrix}^{\mathrm{T}}$, so that the total relative degree

$$\rho = ||\boldsymbol{\rho}||_1 = \sum_{i=1}^{m} \rho_i \leq n, \tag{3-11}$$

is thus smaller or equal than the number of states n. If $\rho = n$, there are no internal dynamics which can destabilize the system. Applying this method for all outputs y_i, the total output dynamics of the system can be defined as

$$\underbrace{\begin{bmatrix} y_1^{(\rho_1)} \\ y_2^{(\rho_2)} \\ \vdots \\ y_m^{(\rho_m)} \end{bmatrix}}_{\boldsymbol{y}^{(\boldsymbol{\rho})}} = \underbrace{\begin{bmatrix} L_{\boldsymbol{f}}^{(\rho_1)} h_1(\boldsymbol{x}) \\ L_{\boldsymbol{f}}^{(\rho_2)} h_2(\boldsymbol{x}) \\ \vdots \\ L_{\boldsymbol{f}}^{(\rho_m)} h_m(\boldsymbol{x}) \end{bmatrix}}_{\boldsymbol{a}(\boldsymbol{x})} + \underbrace{\begin{bmatrix} L_{\boldsymbol{g}_1} L_{\boldsymbol{f}}^{\rho_1 - 1} h_1(\boldsymbol{x}) & L_{\boldsymbol{g}_2} L_{\boldsymbol{f}}^{\rho_1 - 1} h_1(\boldsymbol{x}) & \dots & L_{\boldsymbol{g}_m} L_{\boldsymbol{f}}^{\rho_1 - 1} h_1(\boldsymbol{x}) \\ L_{\boldsymbol{g}_1} L_{\boldsymbol{f}}^{\rho_1 - 1} h_2(\boldsymbol{x}) & L_{\boldsymbol{g}_2} L_{\boldsymbol{f}}^{\rho_1 - 1} h_2(\boldsymbol{x}) & \dots & L_{\boldsymbol{g}_m} L_{\boldsymbol{f}}^{\rho_1 - 1} h_2(\boldsymbol{x}) \\ \vdots & \vdots & \ddots & \vdots \\ L_{\boldsymbol{g}_1} L_{\boldsymbol{f}}^{\rho_m - 1} h_m(\boldsymbol{x}) & L_{\boldsymbol{g}_2} L_{\boldsymbol{f}}^{\rho_m - 1} h_m(\boldsymbol{x}) & \dots & L_{\boldsymbol{g}_m} L_{\boldsymbol{f}}^{\rho_m - 1} h_m(\boldsymbol{x}) \end{bmatrix}}_{\mathcal{B}(\boldsymbol{x})} \boldsymbol{u}. \tag{3-12}$$

It is assumed that the partial relative degrees ρ_i are all well defined, which means that the derivatives in $\mathcal{B}(\boldsymbol{x})$, for $\boldsymbol{x}$ in the region of interest, can be calculated [16]. This thus means that $\mathcal{B}$ is invertible for this complete region, as $\mathcal{B}$ is square for the square system defined in Eq. (3-7). Nonlinearities are now canceled by using the control input

$$\boldsymbol{u} = \mathcal{B}^{-1}(\boldsymbol{x})(\boldsymbol{\nu} - \boldsymbol{a}(\boldsymbol{x})) = \mathcal{B}(\boldsymbol{x})^{-1} \begin{bmatrix} \nu_1 - L_{\boldsymbol{f}}^{\rho_1} h_1(\boldsymbol{x}) \\ \vdots \\ \nu_m - L_{\boldsymbol{f}}^{\rho_m} h_m(\boldsymbol{x}) \end{bmatrix}, \tag{3-13}$$

where $\boldsymbol{\nu} = \boldsymbol{y}^{\boldsymbol{\rho}}$ equals the virtual control input which can be defined with any linear controller. This virtual control input can then be used to steer the output $\boldsymbol{y}$ to a desired output $\boldsymbol{y}_{\text{ref}}$ using $\boldsymbol{\nu} = \boldsymbol{y}_{\text{ref}}^{\boldsymbol{\rho}}$. As ν_k only affects the output y_k, u is a decoupling control law with $\mathcal{B}(\boldsymbol{x})$ the decoupling matrix. The system has relative degree $\boldsymbol{\rho} = \begin{bmatrix} \rho_1 & \rho_2 & \dots & \rho_m \end{bmatrix}^{\mathrm{T}}$ and the total relative degree of the system is $\rho = \rho_1 + ... + \rho_m$.

The main advantage of using NDI compared to more traditional methods as gain scheduling, is that it enables controlling the aircraft over the complete flight envelope with one linear controller. This avoids the need for the design of multiple controllers, each around a different operating point. Important to realize is that the NDI method has limitations. The full state vector $\boldsymbol{x}$ needs to be known and the relative degree $\boldsymbol{\rho}$ of the system needs to be defined. Furthermore, as this method depends completely on the model of the system, robustness against modeling errors and external disturbances is not guaranteed. For these reasons, the next section extends on the NDI method to design a more robust controller.

3-3 Incremental nonlinear dynamic inversion (INDI)

To make the NDI controller more robust, it is reformulated in the incremental form, which gives Incremental nonlinear dynamic inversion (INDI). For this method, the control inputs $\boldsymbol{u}$ are computed incrementally using feedback of sensor measurements. As these sensor measurements replace part of the model equations and the sensors also measure the external disturbances, this makes the controller more robust.

The INDI control law is derived in its most general form following the method proposed by [58] which starts from the general nonlinear system given in Eq. (3-1). A constraint of INDI is that there is a direct relation between the input and the derivative of the output [23]. Referring back to NDI this thus means that

$$L_{\boldsymbol{g}_j} h_k(\boldsymbol{x}) u_j \neq 0, \, \forall k = 1, ...m, \tag{3-14}$$

for at least one input u_j. The nonlinear system given in Eq. (3-1) can be linearized using the first-order Taylor expansion defined in Eq. (2-41) which gives

$$\dot{\boldsymbol{x}} \approx \boldsymbol{f}(\boldsymbol{x}_0, \boldsymbol{u}_0) + \frac{\partial \boldsymbol{f}(\boldsymbol{x}, \boldsymbol{u})}{\partial \boldsymbol{x}} (\boldsymbol{x} - \boldsymbol{x}_0) \bigg|_{\boldsymbol{x}=\boldsymbol{x}_0, \boldsymbol{u}=\boldsymbol{u}_0} + \frac{\partial \boldsymbol{f}(\boldsymbol{x}, \boldsymbol{u})}{\partial \boldsymbol{u}} \bigg|_{\boldsymbol{x}=\boldsymbol{x}_0, \boldsymbol{u}=\boldsymbol{u}_0} (\boldsymbol{u} - \boldsymbol{u}_0) + \text{h.o.t.} \tag{3-15}$$

To simplify the notation define $\mathbf{F}(\boldsymbol{x}_0, \boldsymbol{u}_0) = \frac{\partial \boldsymbol{f}(\boldsymbol{x}, \boldsymbol{u})}{\partial \boldsymbol{x}} (\boldsymbol{x} - \boldsymbol{x}_0) \Big|_{\boldsymbol{x}=\boldsymbol{x}_0, \boldsymbol{u}=\boldsymbol{u}_0}$, $\mathbf{G}(\boldsymbol{x}_0, \boldsymbol{u}_0) = \frac{\partial \boldsymbol{f}(\boldsymbol{x}, \boldsymbol{u})}{\partial \boldsymbol{u}} \Big|_{\boldsymbol{x}=\boldsymbol{x}_0, \boldsymbol{u}=\boldsymbol{u}_0}$, $\Delta \boldsymbol{x} = \boldsymbol{x} - \boldsymbol{x}_0$ and $\Delta \boldsymbol{u} = \boldsymbol{u} - \boldsymbol{u}_0$. Also note that $\boldsymbol{f}(\boldsymbol{x}_0, \boldsymbol{u}_0) = \dot{\boldsymbol{x}}_0$, the derivative of the states at the current time. Discarding higher order terms simplifies the equation above to

$$\dot{\boldsymbol{x}} \approx \dot{\boldsymbol{x}}_0 + \mathbf{F}(\boldsymbol{x}_0, \boldsymbol{u}_0) \Delta \boldsymbol{x} + \mathbf{G}(\boldsymbol{x}_0, \boldsymbol{u}_0) \Delta \boldsymbol{u}. \tag{3-16}$$

This equation can be further simplified using the time-scale separation principle. This assumption states that for a given time increment, the change of the states $\Delta \boldsymbol{x}$ is much smaller than the change of the control input $\Delta \boldsymbol{u}$. This means that $\mathbf{F}(\boldsymbol{x}_0, \boldsymbol{u}_0) \Delta \boldsymbol{x} \ll \mathbf{G}(\boldsymbol{x}_0, \boldsymbol{u}_0) \Delta \boldsymbol{u}$, which is valid for aircraft attitude control for small time increments [23]. Implementing the time-scale separation principle, further simplifies Eq. (3-16) to

$$\dot{\boldsymbol{x}} \approx \dot{\boldsymbol{x}}_0 + \mathbf{G}(\boldsymbol{x}_0, \boldsymbol{u}_0) \Delta \boldsymbol{u}. \tag{3-17}$$

Assuming direct full state measurement meaning $\boldsymbol{y} = \boldsymbol{x}$ gives a direct relation between the derivative of the output $\dot{\boldsymbol{y}}$ and the control input increment $\Delta \boldsymbol{u}$. Setting the virtual control input equal to $\boldsymbol{\nu} = \dot{\boldsymbol{y}} = \dot{\boldsymbol{x}}$ and solving Eq. (3-17) using NDI, the control input increment is calculated as

$$\Delta \boldsymbol{u} = \mathbf{G}^{-1}(\boldsymbol{x}_0, \boldsymbol{u}_0)(\boldsymbol{\nu} - \dot{\boldsymbol{x}}_0), \tag{3-18}$$

where the virtual control input $\boldsymbol{\nu}$ is calculated using a linear controller so that $\boldsymbol{y}_{\text{ref}}$ is tracked, as for NDI. The total control input is then simply calculated using

$$\boldsymbol{u} = \boldsymbol{u}_0 + \Delta \boldsymbol{u}, \tag{3-19}$$

where the incremental step $\Delta \boldsymbol{u}$ is added to the current control input $\boldsymbol{u}_0$.

Comparing Eq. (3-18) with Eq. (3-13), one can see that part of the model dynamics $\boldsymbol{a}(\boldsymbol{x})$ is replaced by $\dot{\boldsymbol{x}}_0$. These current state derivatives can be provided by sensor measurements, making the INDI control law less dependent on the aircraft's model. Also, any modeling errors in the control effectiveness matrix $/MG$ will be immediately measured by the sensors when Δu is applied. As these measurements are fed back in the control law, and the control inputs Furthermore, as the sensors measure external disturbances applied to the aircraft, these are also captured in the control law. This makes the INDI method more robust to modeling errors and disturbances, as compared to NDI.

3-4 NDI and INDI control laws for the DEP aircraft

In the traditional INDI and NDI implementation, the angular rates $[p \quad q \quad r]^{\text{T}}$, attitude $[\phi \quad \theta \quad \psi]^{\text{T}}$ or aerodynamic angles $[\phi \quad \alpha \quad \beta]^{\text{T}}$ of the aircraft are controlled [23]. As for the DEP aircraft, the aim is to design a controller which actively uses the propellers while optimizing for minimal power, also translational control needs to be added. In this case, not only the moments, but also the forces around the aircraft are controlled. The implementation of this controller is based on [25], where an outer translational and inner rotational control loop is used. For this thesis, there are two major differences in terms of implementation, as compared with this research. First of all, in the original implementation, the reference outputs are defined as aircraft's positions in the F_{E} frame. In this thesis, the reference values are defined as

$$\boldsymbol{y}_{\text{ref}} = \begin{bmatrix} h_{\text{ref}} \\ V_{\text{ref}} \\ \phi_{\text{ref}} \\ \beta_{\text{ref}} \end{bmatrix}, \tag{3-20}$$

so that the reference altitude h, velocity V, roll angle ϕ and sideslip angle β are tracked. By default, $\beta_{\text{ref}} = 0$ so that the angle of sideslip is minimized, which gives coordinated turns and leads to most efficient flight. Furthermore, in the baseline controller, the aerodynamic forces are defined in the F_{b} frame whereas for the DEP aircraft these are defined in the F_{a} frame. This means that part of the translational equations are rewritten for easier adaptation of the DEP aerodynamic model.

Following the same method as in [25] relations that only involve kinematics will be controlled using the NDI method described in Section 3-2 as they do not contain modeling errors. For the dynamic relations, the INDI method described in Section 3-3 will be so that these control loops more robust against modeling uncertainties. Before deriving the different control loops, define the following state variables

$$\boldsymbol{x}_0 = \begin{bmatrix} x & y & z \end{bmatrix}^{\mathrm{T}}, \tag{3-21a}$$

$$\boldsymbol{x}_1 = \begin{bmatrix} V & \chi & \gamma \end{bmatrix}^{\mathrm{T}}, \bar{\boldsymbol{x}}_1 = \begin{bmatrix} V & \gamma \end{bmatrix}^{\mathrm{T}}, \tag{3-21b}$$

$$\boldsymbol{x}_2 = \begin{bmatrix} \phi & \alpha & \beta \end{bmatrix}^{\mathrm{T}}, \bar{\boldsymbol{x}}_2 = \begin{bmatrix} \phi & \beta \end{bmatrix}^{\mathrm{T}}, \tag{3-21c}$$

$$\boldsymbol{x}_3 = \begin{bmatrix} p & q & r \end{bmatrix}^{\mathrm{T}}, \tag{3-21d}$$

and the following control variables

$$\boldsymbol{u}_1 = \begin{bmatrix} \alpha_{\mathrm{des}} & T \end{bmatrix}^{\mathrm{T}}, \tag{3-22a}$$

$$\boldsymbol{u}_3 = \begin{bmatrix} \delta_{\mathrm{a}} & \delta_{\mathrm{e}} & \delta_{\mathrm{r}} \end{bmatrix}^{\mathrm{T}}. \tag{3-22b}$$

In Eq. (3-21c), χ is the kinematic azimuth angle and γ the flight path angle. The first describes the position of the aircraft in the xy plane and the latter the position in the z-axis of F_{E}. Also note that $\boldsymbol{u}_3$ only includes the control surfaces deflections. Differential thrust and the PAI effects for active control will be added in Chapter 4.

The structure of the control is shown in Figure 3-1, where control of $\boldsymbol{x}_0$ and $\boldsymbol{x}_1$ is thus in the translational block and control of $\boldsymbol{x}_2$ and $\boldsymbol{x}_3$ in the rotational block. Note that there are two kinematic relations, $\boldsymbol{x}_0 \to \boldsymbol{x}_1$ and $\boldsymbol{x}_2 \to \boldsymbol{x}_3$ which are thus controlled using the NDI method (controller 1 and 3). The dynamic relations, $\boldsymbol{x}_1 \to \boldsymbol{u}_1$ and $\boldsymbol{x}_3 \to \boldsymbol{u}_3$, are controlled using INDI (controller 2 and 4) to improve robustness. Separating these control loops is based on the time-scale separation principle, which states that slower outer loops and faster inner loops can be controlled individually. It is thus assumed that each subsequent loop is faster than the preceding loop. Note that two different subscripts are defined, where the subscript ref is used for reference commands which the aircraft is to follow and the subscript des gives the desired commands generated by the controller. The first NDI and INDI controller block, forms the translational control loop which will be discussed in Section 3-4-1. The second block is for rotational control, which will be discussed in Section 3-4-2, after which an overview of the total control loop is given in Section 3-4-3.

3-4-1 Translational control loop

Altitude h control

The first step of this control loop involves calculating the desired flight path angle γ_{des}, using the NDI method as this only involves kinematic relations (controller 1 Figure 3-1). The relation between $\boldsymbol{x}_0$ Eq. (3-21a) and $\boldsymbol{x}_1$ Eq. (3-21b) is defined as

$$\dot{\boldsymbol{x}}_0 = \begin{bmatrix} V\cos\chi\cos\gamma \\ V\sin\chi\cos\gamma \\ -V\sin\gamma \end{bmatrix}. \tag{3-23}$$

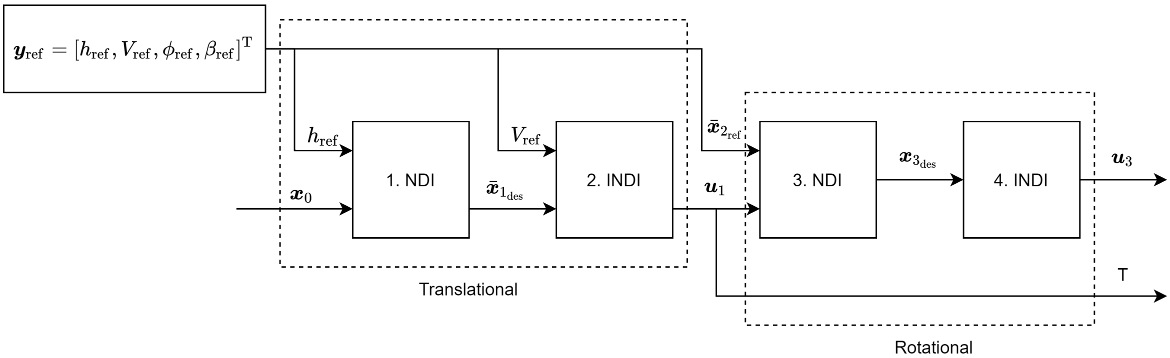

Figure 3-1: Four control loops for $\boldsymbol{y}_{\text{ref}}$ where NDI is used for the kinematic and INDI for the dynamic relations. The loops are separated based on the time-scale separation principle.

Using the last row of Eq. (3-23) and setting the virtual control input ν_z equal to $\dot{z}$ then gives

$$\gamma_{\text{des}} = -\arcsin\left(\frac{\nu_z}{V_{\text{ref}}}\right), \tag{3-24}$$

where ν_z is calculated using a proportional gain on the error signal of z as

$$\nu_z = K_{\text{h}}(-h_{\text{ref}} - z). \tag{3-25}$$

Flight path angle γ and velocity V control

The next translational control loop controls $\bar{\boldsymbol{x}}_1$ Eq. (3-21b), where the values V_{ref} and γ_{des} are used as reference values and $\boldsymbol{u}_1$ Eq. (3-22a) as the input to control these references. As this involves dynamic relations, the INDI method will be used (controller 2 Figure 3-1). The dynamics for $\boldsymbol{x}_1$ are defined as

$$\dot{\boldsymbol{x}}_1 = \begin{bmatrix} \frac{1}{m} & 0 & 0 \\ 0 & \frac{1}{mV\cos\gamma} & 0 \\ 0 & 0 & -\frac{1}{mv} \end{bmatrix} \left(\mathbf{T}_{\text{Va}} \begin{bmatrix} X_{\text{a}} \\ Y_{\text{a}} \\ Z_{\text{a}} \end{bmatrix} + \mathbf{T}_{\text{VE}} \begin{bmatrix} 0 \\ 0 \\ mg \end{bmatrix} \right), \tag{3-26}$$

where the vector $[X_{\text{a}}, Y_{\text{a}}, Z_{\text{a}}]^{\text{T}}$ contains the aerodynamic and propulsive forces in the F_a frame and $\mathbf{T}_{\text{Va}}$ and $\mathbf{T}_{\text{VE}}$ are defined in Eq. (A-1) and Eq. (A-2) respectively. Substituting these rotation matrices gives

$$\dot{\boldsymbol{x}}_1 = \begin{bmatrix} \frac{1}{m} & 0 & 0 \\ 0 & \frac{1}{mV\cos\gamma} & 0 \\ 0 & 0 & -\frac{1}{mV} \end{bmatrix} \left(\begin{bmatrix} X_{\text{a}} \\ \cos\phi Y_{\text{a}} - \sin\phi Z_{\text{a}} \\ \sin\phi Y_{\text{a}} + \cos\phi Z_{\text{a}} \end{bmatrix} + \begin{bmatrix} -mg\sin\gamma \\ 0 \\ mg\cos\gamma \end{bmatrix} \right). \tag{3-27}$$

To the determine the required $\boldsymbol{u}_1$, the forces X_{a} and Z_{a} need to be written in the affine-in-control form using non-dimensional force coefficients as explained in Section 2-3-4. As defined before $\boldsymbol{u}_1 = \begin{bmatrix} \alpha_{\text{des}} & T \end{bmatrix}^{\text{T}}$ which thus gives

$$\begin{aligned} X_{\text{a}} &= qSC_{X_{\text{a}}} = qs\left(C_{X_{\text{a}_0}} - C_{D_\alpha}\alpha + C_{X_{\text{a}_T}}T\right), \\ Z_{\text{a}} &= qSC_{Z_{\text{a}}} = qs\left(C_{Z_{\text{a}_0}} - C_{L_\alpha}\alpha + C_{Z_{\text{a}_T}}T\right). \end{aligned} \tag{3-28}$$

As χ will not be controlled, instead the roll angle ϕ_{ref} is specified in $\boldsymbol{y}_{\text{ref}}$ Eq. (3-20), only the first and third row of Eq. (3-27) will be considered where $\bar{\boldsymbol{x}}_1 = [V, \gamma]^{\text{T}}$ Eq. (3-21b). Also, assuming small β, which is minimized by the controller, the control derivatives for the thrust can be expressed in the F_{a} frame as

$$\begin{aligned} C_{X_{\text{a}_T}} &= C_{X_T} \cos\alpha, \\ C_{Z_{\text{a}_T}} &= -C_{X_T} \sin\alpha, \end{aligned} \tag{3-29}$$

where $C_{X_{\text{T}}}$ is in the F_{b} frame. It it thus assumed that the propellers only provide thrust in F_{b} x-direction. In the affine-in-control form the dynamics of $\bar{\boldsymbol{x}}_1$ are defined as

$$\dot{\bar{\boldsymbol{x}}}_1 = \bar{\boldsymbol{f}}_1(\boldsymbol{x}_1, \boldsymbol{x}_2) + \bar{\mathbf{G}}_1 \boldsymbol{u}_1, \tag{3-30}$$

where $\boldsymbol{x}_2$ contains the aerodynamic angles Eq. (3-21c) and $\boldsymbol{u}_1$ the desired agle of attack α_{des} and thrust T Eq. (3-22a). Putting Eq. (3-27) in affine-in control form then gives

$$\bar{\boldsymbol{f}}_1(\boldsymbol{x}_1, \boldsymbol{x}_2) = \begin{bmatrix} -g\sin\gamma + \frac{qS}{m} C_{X_{\text{a}_0}} \\ -\frac{Y_{\text{a}}\sin\phi}{mV} - \frac{g\cos\gamma}{V} - \frac{qS}{mV} C_{Z_{\text{a}_0}} \cos\phi \end{bmatrix}, \tag{3-31}$$

and

$$\bar{\mathbf{G}}_1 = \frac{qS}{mV} \begin{bmatrix} -VC_{D_\alpha}\alpha & VC_{X_T}\cos\alpha \\ C_{L_\alpha}\cos\phi & C_{X_T}\sin\alpha\cos\phi \end{bmatrix}. \tag{3-32}$$

As stated before, the relation in Eq. (3-30) is a dynamic relation, so that INDI is used to control $\dot{\bar{\boldsymbol{x}}}_1$. Using a first-order Taylor expansion and the time-scale separation principle, as explained in Section 3-3, Eq. (3-30) can be defined in incremental form as

$$\begin{aligned} \dot{\bar{\boldsymbol{x}}}_1 &= \dot{\bar{\boldsymbol{x}}}_{1,0} + \bar{\mathbf{G}}_1 \Delta\boldsymbol{u}_1 \\ \dot{\bar{\boldsymbol{x}}}_{1,0} &= \bar{\boldsymbol{f}}_1\left(\bar{\boldsymbol{x}}_{1,0}, \bar{\boldsymbol{x}}_{2,0}\right) + \bar{\mathbf{G}}_1 \boldsymbol{u}_{1,0}. \end{aligned} \tag{3-33}$$

Setting the virtual control input $\boldsymbol{\nu}_{\bar{x}_1}$ equal to $\dot{\bar{\boldsymbol{x}}}_1$, the incremental $\Delta\boldsymbol{u}_1$ and total control input $\boldsymbol{u}_1$ can be calculated as

$$\begin{aligned} \Delta\boldsymbol{u}_1 &= \bar{\mathbf{G}}_1^{-1}\left(\boldsymbol{\nu}_{\bar{x}_1} - \dot{\bar{\boldsymbol{x}}}_{1,0}\right) \\ \boldsymbol{u}_1 &= \boldsymbol{u}_{1,0} + \Delta\boldsymbol{u}_1, \end{aligned} \tag{3-34}$$

The virtual control input $\boldsymbol{\nu}_{\bar{x}_1}$ is determined using a proportional gain $\mathbf{K}_{\bar{x}_1}$ on the error signal so that

$$\boldsymbol{\nu}_{\bar{x}_1} = \mathbf{K}_{\bar{x}_1}\left(\begin{bmatrix} V_{\text{ref}} \\ \gamma_{\text{des}} \end{bmatrix} - \begin{bmatrix} V \\ \gamma \end{bmatrix}\right). \tag{3-35}$$

Finally, it is important to note is that $\boldsymbol{u}_{1,0} = \begin{bmatrix} \alpha_0 & T_0 \end{bmatrix}^{\text{T}}$, where α_0 is the current actual angle of attack measured by a sensor and thus not the previous desired value ($\alpha_0 \neq \alpha_{\text{des}_0}$). This is because, the desired angle of attack commands α_{des} cannot be reached instantaneously. The NDI controller defined in Eq. (3-24) and INDI controller defined Eq. (3-34), together form the translational block shown in Figure 3-1. The next section will discuss the rotational block in Figure 3-1.

3-4-2 Rotational control loop

Aerodynamic angles ϕ, α and β control

Now that the desired angle of attack α_{des} has been determined, the reference vector $\boldsymbol{x}_{2_{\text{des}}} = [\phi_{\text{ref}}, \alpha_{\text{des}}, \beta_{\text{ref}}]^{\text{T}}$ is used to calculate the reference angular rates $\boldsymbol{x}_{3_{\text{des}}} = \boldsymbol{\omega}_{\text{des}} = \begin{bmatrix} p_{\text{des}} & q_{\text{des}} & r_{\text{des}} \end{bmatrix}^{\text{T}}$. This is the first block of the rotational control loop in Figure 3-2 (controller 3). The desired roll angle ϕ_{ref} and sideslip angle $\beta_{\text{ref}} = 0$ are specified by the reference values in Eq. (3-20) and α_{des} follows from the translational control law defined in Eq. (3-34). As the relations going from $\boldsymbol{x}_2$ to $\boldsymbol{x}_3$ only involves kinematics, an NDI controller will be designed. Firstly, for the roll angle ϕ the kinematics are defined as

$$\dot{\phi} = \underbrace{\begin{bmatrix} 1 & \sin\phi\tan\theta & \cos\phi\tan\theta \end{bmatrix}}_{a_\phi(\boldsymbol{x})} \begin{bmatrix} p \\ q \\ r \end{bmatrix}. \tag{3-36}$$

Secondly, the angle of attack α is calculated as

$$\alpha = \arcsin\frac{w}{V}, \tag{3-37}$$

so that the time-derivative is

$$\dot{\alpha} = \frac{u\dot{w} - w\dot{u}}{u^2 + w^2}. \tag{3-38}$$

The accelerations in the body frame F_{b} are found by rewriting Eq. (2-5) in Section 2-1-3, so that

$$\begin{aligned} \dot{u} &= A_x - g\sin\theta + rv - qw, \\ \dot{v} &= A_y + g\sin\phi\cos\theta - ru + pw, \\ \dot{w} &= A_z + g\cos\theta\cos\phi + qu - pv, \end{aligned} \tag{3-39}$$

where A_x, A_y and A_z are the accelerations caused by external forces exerted on the aircraft in the F_{b} frame. Substituting for $\dot{u}$ and $\dot{w}$ gives

$$\dot{\alpha} = \underbrace{\left(\frac{1}{u^2+w^2}\right)\left(u\left(A_z + g\cos\theta\cos\phi\right) - w\left(A_x - g\sin\theta\right)\right)}_{b_\alpha(\boldsymbol{x})} + \underbrace{\begin{bmatrix} \frac{-uv}{u^2+w^2} & 1 & \frac{-vw}{u^2+w^2} \end{bmatrix}}_{a_\alpha(\boldsymbol{x})} \begin{bmatrix} p \\ q \\ r \end{bmatrix} \tag{3-40}$$

The sideslip angle is defined as

$$\beta = \sin^{-1}\frac{u}{V}, \tag{3-41}$$

so that the time-derivative is equal to

$$\dot{\beta} = \frac{\dot{v}V - v\dot{V}}{V\sqrt{u^2+w^2}} = \frac{\dot{v}}{\sqrt{u^2+w^2}} - \frac{v(u\dot{u} + v\dot{v} + w\dot{w})}{(u^2+v^2+w^2)\sqrt{u^2+w^2}}. \tag{3-42}$$

Substituting $\dot{u}$, $\dot{v}$ and $\dot{w}$ from Eq. (3-39) gives

$$\dot{\beta} = \underbrace{\left(\frac{1}{\sqrt{u^2+w^2}}\right)(F_x + F_y + F_z)}_{b_\beta(\boldsymbol{x})} + \underbrace{\begin{bmatrix} \frac{w}{\sqrt{u^2+w^2}} & 0 & \frac{-u}{\sqrt{u^2+w^2}} \end{bmatrix}}_{a_\beta(\boldsymbol{x})} \begin{bmatrix} p \\ q \\ r \end{bmatrix}, \tag{3-43}$$

with

$$\begin{aligned} F_x &= -\frac{uv}{V^2}(A_x - g\sin\theta), \\ F_y &= \left(1 - \frac{v^2}{V^2}\right)(A_y + g\sin\phi\cos\theta), \\ F_z &= -\frac{vw}{V^2}(A_z + g\cos\phi\cos\theta). \end{aligned} \tag{3-44}$$

The above equations can be combined into

$$\begin{bmatrix} \dot{\phi} \\ \dot{\alpha} \\ \dot{\beta} \end{bmatrix} = \begin{bmatrix} 0 \\ b_\alpha(\boldsymbol{x}) \\ b_\beta(\boldsymbol{x}) \end{bmatrix} + \begin{bmatrix} a_\phi(\boldsymbol{x}) \\ a_\alpha(\boldsymbol{x}) \\ a_\beta(\boldsymbol{x}) \end{bmatrix} \begin{bmatrix} p \\ q \\ r \end{bmatrix}, \tag{3-45}$$

where the row vectors for $a(\boldsymbol{x})$ and $b(\boldsymbol{x})$ are given in Eq. (3-36), Eq. (3-40) and Eq. (3-43). As stated before, the relations in Eq. (3-45) are purely kinematic, so that the NDI can be applied which gives

$$\boldsymbol{x}_{3_{\text{des}}} = \begin{bmatrix} p_{\text{des}} \\ q_{\text{des}} \\ r_{\text{des}} \end{bmatrix} = \begin{bmatrix} a_\phi(\boldsymbol{x}) \\ a_\alpha(\boldsymbol{x}) \\ a_\beta(\boldsymbol{x}) \end{bmatrix}^{-1} \left(\begin{bmatrix} \nu_\phi(\boldsymbol{x}) \\ \nu_\alpha(\boldsymbol{x}) \\ \nu_\beta(\boldsymbol{x}) \end{bmatrix} - \begin{bmatrix} 0 \\ b_\alpha(\boldsymbol{x}) \\ b_\beta(\boldsymbol{x}) \end{bmatrix} \right). \tag{3-46}$$

The virtual control input vector $\boldsymbol{\nu}_{\boldsymbol{x}_3} = \begin{bmatrix} \nu_\phi & \nu_\alpha & \nu_\beta \end{bmatrix}^{\text{T}}$ is determined using a proportional gain $\mathbf{K}_{\boldsymbol{x}_3}$ on the error signal so that

$$\boldsymbol{\nu}_{\boldsymbol{x}_3} = \mathbf{K}_{\boldsymbol{x}_3} \left(\begin{bmatrix} \phi_{\text{ref}} \\ \alpha_{\text{des}} \\ \beta_{\text{ref}} \end{bmatrix} - \begin{bmatrix} \phi \\ \alpha \\ \beta \end{bmatrix} \right). \tag{3-47}$$

Angular rates p, q and r control

The second controller of the rotational control block in Figure 3-1, involves calculating the required control surface deflections $\boldsymbol{u}_3$ Eq. (3-22b) from the desired angular rate $\boldsymbol{x}_{3_{\text{des}}}$ Eq. (3-21d). As these relations involve dynamics, the INDI method is used to increase robustness (controller 4 Figure 3-1). The dynamics of $\boldsymbol{x}_3$ are defined in the EoM of Eq. (2-6) in Section 2-1-3. For ease of notation, replace $\boldsymbol{\Omega}^b_{bE}$ with $\boldsymbol{\omega}$ which gives

$$\begin{aligned} \mathbf{I}\dot{\boldsymbol{\omega}} + \boldsymbol{\omega} \times \mathbf{I}\boldsymbol{\omega} &= \boldsymbol{\mathcal{M}}, \\ \mathbf{I}\dot{\boldsymbol{\omega}} + \boldsymbol{\omega} \times \mathbf{I}\boldsymbol{\omega} &= \boldsymbol{\mathcal{M}}_{\text{a}} + \boldsymbol{\mathcal{M}}_{\text{c}}, \end{aligned} \tag{3-48}$$

where $\mathbf{I}$ is given by Eq. (2-7), $\boldsymbol{\mathcal{M}}_a$ are the moments generated by the aerodynamics of the airframe and $\boldsymbol{\mathcal{M}}_c$ are the moments generated by the control inputs. Note that for the DEP aircraft, these moments do not only include the ones produced by the control surfaces as for traditional aircraft control (e.g. [23], [25]) but also the differential thrust and PAI effects as stated in Section 2-2. As stated at the beginning of this section, for now only rotational control by the control surface deflections is assumed, to give a unique solution to the control problem.

Solving Eq. (3-48) for $\dot{\boldsymbol{\omega}}$ and setting $\boldsymbol{x}_3 = \boldsymbol{\omega}$ gives

$$\begin{aligned}\dot{\boldsymbol{\omega}} &= \mathbf{I}^{-1}\left(\boldsymbol{\mathcal{M}}_a + \boldsymbol{\mathcal{M}}_c - \boldsymbol{\omega} \times \mathbf{I}\boldsymbol{\omega}\right)\\ \dot{\boldsymbol{x}}_3 &= \mathbf{I}^{-1}\left(\boldsymbol{\mathcal{M}}_a + \boldsymbol{\mathcal{M}}_c - \boldsymbol{x}_3 \times \mathbf{I}\boldsymbol{x}_3\right).\end{aligned} \tag{3-49}$$

For more compact notation, define the state dependent part as

$$\boldsymbol{f}_3(\boldsymbol{x}) = \mathbf{I}^{-1}\left(\boldsymbol{\mathcal{M}}_a - \boldsymbol{x}_3 \times \mathbf{I}\boldsymbol{x}_3\right), \tag{3-50}$$

so that

$$\dot{\boldsymbol{x}}_3 = \boldsymbol{f}_3(\boldsymbol{x}) + \mathbf{I}^{-1}\boldsymbol{\mathcal{M}}_\mathrm{c}. \tag{3-51}$$

Using a first-order Taylor expansion and the time-scale separation principle, as explained in Section 3-3, Eq. (3-51) can be defined as

$$\begin{aligned}\dot{\boldsymbol{x}}_3 &= \dot{\boldsymbol{x}}_{3,0} + \mathbf{G}_3\Delta\boldsymbol{u}_3,\\ \dot{\boldsymbol{x}}_{3,0} &= \boldsymbol{f}_3(\boldsymbol{x}_0) + \mathbf{G}_3\boldsymbol{u}_{3,0}.\end{aligned} \tag{3-52}$$

By setting $\boldsymbol{\nu}_{\boldsymbol{x}_3} = \dot{\boldsymbol{y}}_3 = \dot{\boldsymbol{x}}_3$ the required incremental control input can be calculated as

$$\begin{aligned}\Delta\boldsymbol{u}_3 &= \mathbf{G}_3^{-1}\left(\boldsymbol{\nu}_{\boldsymbol{x}_3} - \dot{\boldsymbol{x}}_{3,0}\right)\\ \boldsymbol{u}_3 &= \boldsymbol{u}_{3,0} + \Delta\boldsymbol{u}_3.\end{aligned} \tag{3-53}$$

Using only the control surfaces, $\mathbf{G}_3$ is defined using the control derivatives of the control surfaces, as explained in Section 2-3-4, so that

$$\mathbf{G}_3 = \mathbf{I}^{-1}qS\begin{bmatrix} bC_{l_{\delta\mathrm{a}}} & 0 & bC_{l_{\delta\mathrm{r}}}\\ 0 & C_{m_{\delta\mathrm{e}}} & 0\\ bC_{n_{\delta\mathrm{a}}} & 0 & bC_{n_{\delta\mathrm{r}}}\end{bmatrix}. \tag{3-54}$$

The NDI controller defined in Eq. (3-46) and Incremental nonlinear dynamic inversion (INDI) controller defined in Eq. (3-53) together form the rotational control loop shown in Fig. 3-1. With the control laws for translation and rotation determined the next section will give an overview of the total control loop.

3-4-3 Total control loop

In the two preceding sections, controllers for following the reference values defined in Eq. (3-20) were determined. In total, this involves four control loops where the first and third are controlled using NDI. The second and fourth are controlled with INDI to provide robustness against modeling errors and external disturbances, as shown in Figure 3-1. It was assumed that the total propeller thrust T only provides a force in the F_b x-axis. Furthermore, it was assumed that the moments around the aircraft are only controlled by the control surfaces $\boldsymbol{\delta}$. This gives the control vector $\boldsymbol{u} = \begin{bmatrix} T & \delta_\mathrm{a} & \delta_\mathrm{e} & \delta_\mathrm{r}\end{bmatrix}^\mathrm{T}$. Note that this control input vector is thus different from the one defined in Section 2-2 where the ailerons and propellers are all controlled separately. This means that the PAI effects and differential thrust of the propellers are not taken into account. This controller thus does not use the full potential of the DEP aircraft, but rather forms the baseline controller to which the more extensive controllers, which will be discussed in Chapter 4, will be compared. An overview of the control loops is given below.

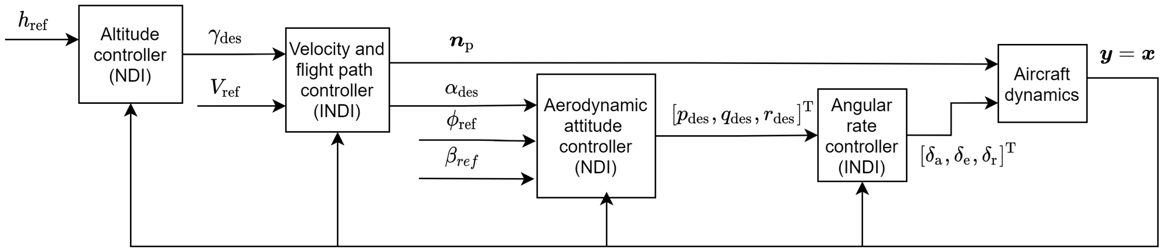

Figure 3-2: The total controller showing the four different loops, two NDI and two INDI controllers, to follow the aircraft's reference values $\boldsymbol{y}_{\mathrm{ref}}$.

Also, remember that the separation of the four different control loops relies on the time-scale separation principle, where variables in the inner loop are assumed to reach their commanded value instantaneously in the slower outer loop. In [59], exponential stability for the commanded values of the outer loop is proven as long as the inner loop gains are sufficiently large. These high gains result in a high inner loop frequency and thus to faster responses satisfying the condition for the time-scale separation principle. From simulation results, it should be found whether the gains are correctly tuned so that the time-scale separation principle holds. Finally, actuator and sensor dynamics were not taken into account in the derivation above. Their effects and methods to deal with them will be discussed in the next section.

3-5 Implementation of the INDI control law

An important assumption in the INDI controller derivation, is that all states are known and that these are measured with ideal sensors containing no bias or noise [23]. This is especially important for feeding back the acceleration signals $\dot{\boldsymbol{x}}_1$ and $\dot{\boldsymbol{x}}_3$. These cannot be provided by a standard Inertial measurement unit (IMU) so that these measurements, in reality, are not ideal. A filtering technique will be introduced in Section 3-5-1 so that noisy state measurements can be used to calculate derivatives. Also, actuator dynamics were not taken into account, so that it was assumed that the values of $\boldsymbol{u}_1$ and $\boldsymbol{u}_3$ are reached instantaneously. In reality, all actuators have dynamics, and a method to deal with this will be discussed in Section 3-5-2.

3-5-1 Sensor measurements filtering

As stated previously, the state derivative measurements $\dot{\boldsymbol{x}}_1$ and $\dot{\boldsymbol{x}}_3$ cannot be provided by standard sensors. A solution to this can be to take derivatives of the states and use these in the INDI control law. Still, as sensors measurements are subject to measurement noise, differentiation of these noisy state measurements amplifies noise. It is, therefore, suggested to use a second-order filter to filter out this noise in [60]. These filters introduce delays in the sensors' measurements. To synchronize the signals in the control loop, the same filter is applied to the actuator measurements. The second-order filter $F(s)$ is defined as

$$F(s) = \frac{\omega_{\mathrm{f}}^2}{s^2 + \zeta_{\mathrm{f}}\omega_{\mathrm{f}}s + \omega_{\mathrm{f}}^2} \tag{3-55}$$

, where ω_f is the natural frequency and ζ_f the damping coefficient of the filter.

In [61], this method was implemented for a passenger aircraft. Therefore, the values in this research were used as a guideline for the DEP aircraft. The damping ratio was set equal to $\zeta_\mathrm{f} = 1$. The value of the natural frequency of the filter ω_f was determined so that high frequency noise is attenuated, but the dynamics are still captured. As the DEP is an SFD, the dynamics are faster than for a full scale passenger aircraft, so that the natural frequency was set equal to $\omega_\mathrm{f} = 30\ rad/s$. For implementation in the INDI controller, $F(s)$ is discretized to $F(z)$ using the Tustin transformation with $f_\mathrm{s} = 100$ Hz.

3-5-2 Pseudo control hedging (PCH)

The idea of PCH is to hedge the control signal with the difference between the commanded and achieved control input. Because of this difference, the applied forces or moments on the aircraft are different. The PCH formulation compensates for this, by subtracting the difference from the control commands. This difference is defined as an estimated amount $\boldsymbol{\nu}_h$. Using this method saturation of the actuators, while trying to keep tracking the reference values, is prevented. This pseudo-control hedge is computed as

$$\boldsymbol{\nu}_\mathrm{h}(\boldsymbol{x}) = \boldsymbol{\nu}_\mathrm{c}(\boldsymbol{x}) - \hat{\boldsymbol{\nu}}(\boldsymbol{x}), \tag{3-56}$$

where $\boldsymbol{\nu}_\mathrm{c}(x)$ is the commanded virtual control input and $\hat{\boldsymbol{\nu}}(\boldsymbol{x})$ the estimated achieved control input which is based on the measured actuator states. For the proposed translation and rotational INDI control loops defined in Section 3-4, $\boldsymbol{\nu} = \dot{\boldsymbol{y}} = \dot{\boldsymbol{x}} = \boldsymbol{f}(\boldsymbol{x}, \boldsymbol{u})$, so that the actual virtual control input can be estimated with $\hat{\boldsymbol{\nu}}(\boldsymbol{x}) = \boldsymbol{f}(\boldsymbol{x}_0, \boldsymbol{u}_0)$. To implement hedging, a first order reference model is designed. Implementing this reference model gives

$$\boldsymbol{\nu}_\mathrm{rm} = \mathbf{K}_\mathrm{rm}(\boldsymbol{y}_\mathrm{ref} - \boldsymbol{x}_\mathrm{rm}), \tag{3-57}$$

where $\mathbf{K}_\mathrm{rm}$ is a diagonal matrix containing the reference model gains, $\boldsymbol{x}_\mathrm{c}$ is the commanded and $\boldsymbol{x}_\mathrm{rm}$ the reference model state vector. The signal sent to the control system is $\boldsymbol{x}_\mathrm{rm}$, which is given by

$$\boldsymbol{x}_\mathrm{rm} = \frac{1}{s}(\boldsymbol{\nu}_\mathrm{rm} - \boldsymbol{\nu}_\mathrm{h}). \tag{3-58}$$

When there is no saturation $\boldsymbol{\nu}_\mathrm{h} = 0$, as there is no difference between the commanded and actual $\boldsymbol{\nu}$. For this situation, the reference model acts as low-pass filter with bandwidth K_{rm_i} for the i-th state of $\boldsymbol{x}_\mathrm{c}$. When there is saturation, $\boldsymbol{\nu}_\mathrm{h}$ will give the difference between the commanded and achieved virtual control input as defined in Eq. (3-56). The PCH for incremental control is defined by substituting Eq. (3-17) in Eq. (3-56) which gives

$$\begin{aligned}\boldsymbol{\nu}_\mathrm{h} &= [\dot{\boldsymbol{x}}_0 + \mathbf{G}(\boldsymbol{x}_0, \boldsymbol{u}_0)(\boldsymbol{u}_\mathrm{c} - \boldsymbol{u}_0)] - [\dot{\boldsymbol{x}}_0 + \mathbf{G}(\boldsymbol{x}_0, \boldsymbol{u}_0)(\boldsymbol{u} - \boldsymbol{u}_0)] \\ &= \mathbf{G}(\boldsymbol{x}_0, \boldsymbol{u}_0)(\boldsymbol{u}_\mathrm{c} - \boldsymbol{u}).\end{aligned} \tag{3-59}$$

The general INDI control loop for the reference $\boldsymbol{y}_\mathrm{ref}$, states $\boldsymbol{x}$, control inputs $\boldsymbol{u}$, outputs $\boldsymbol{y}$ and control effectiveness matrix $\mathbf{G}$ is shown in the right block of Figure 3-3. Note how the discrete filter $F(z)$ is implemented both on the sensor and actuator measurements to synchronize these signals. The block $D(z)$ represents the discrete time derivative. The PCH loop is shown in the left block. Note how the virtual control input computed by the reference model $\boldsymbol{\nu}_\mathrm{rm}$,

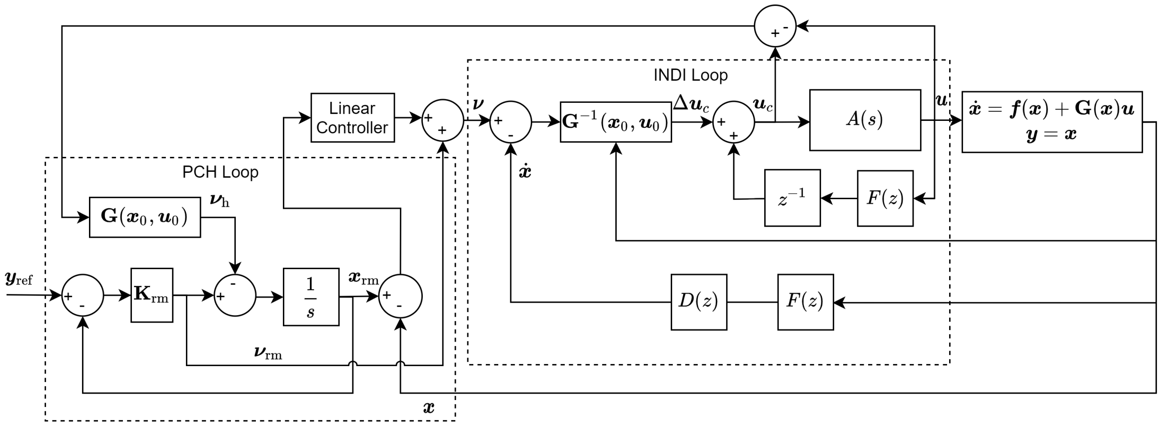

Figure 3-3: General INDI control loop with PCH and filtering of the states and control inputs.

is used as a feedforward term. This term is used as $\dot{\boldsymbol{y}}_{\mathrm{ref}}$ in the INDI controller to improve tracking performance [62].

Implementing the PCH method for the INDI loop controlling $\bar{\boldsymbol{x}}_1$ in Eq. (3-33) gives

$$\boldsymbol{\nu}_{\mathrm{h}_{\boldsymbol{x}_1}} = \mathbf{G}_1(\boldsymbol{x}_0, \boldsymbol{u}_0)\left(\boldsymbol{u}_{1_c} - \boldsymbol{u}_1\right), \tag{3-60}$$

and for the INDI control loop controlling $\boldsymbol{x}_3$ in Eq. (3-52)

$$\boldsymbol{\nu}_{\mathrm{h}_{\boldsymbol{x}_3}} = \mathbf{G}_3(\boldsymbol{x}_0, \boldsymbol{u}_0)\left(\boldsymbol{u}_{3_c} - \boldsymbol{u}_3\right). \tag{3-61}$$

3-6 Reformulated INDI without time-scale separation

For the INDI controller defined in the above sections two separate loops were designed for controlling $\bar{\boldsymbol{x}}_1$ an $\boldsymbol{x}_3$ with the control inputs $\boldsymbol{u}_1$ Eq. (3-22a) and $\boldsymbol{u}_3$ Eq. (3-22b). For controlling the DEP aircraft, the propeller thrust T_{p} influences both the translation and rotation of the aircraft. For translation, an increase in propeller thrust will increase the velocity V and the lift created by the PAI effects ΔC_L. The second effect in turn increases the flight path angle γ which thus leads to an increase in altitude. For rotation, an increase in propeller thrust T_{p} creates both a yawing moment n caused by differential thrust and a rolling moment l caused by a local increase in ΔC_L.

As the propeller rotational velocity T_{p} thus influences both the translation and rotation, merging the two control loops should result in better performance of the controller with respect to tracking the reference variables in Eq. (3-20). Merging the two control loops is also required for energy optimal control allocation as will be discussed in Section 4-2-3. As a first step in this section the two INDI control loops defined in Section 3-4-1 and Section 3-4-2, controlling $\bar{\boldsymbol{x}}_1$ and $\boldsymbol{x}_3$ will be merged. Here the thrust of the propellers is thus not controlled separately but rather the total thrust T is used. This means that the differential thrust and PAI effects are not included yet. Rather, this analysis forms the basis for the merging of the control loops which will then be used in Chapter 4 to unlock the full potential of the DEP aircraft. The state vector for merging the control loops is defined as

$$\boldsymbol{x} = \begin{bmatrix} \bar{\boldsymbol{x}}_1 & \boldsymbol{x}_3 \end{bmatrix}^{\mathrm{T}} = \begin{bmatrix} V & \gamma & p & q & r \end{bmatrix}^{\mathrm{T}}, \tag{3-62}$$

and control input vector as

$$\boldsymbol{u} = \begin{bmatrix} \boldsymbol{u}_1 & \boldsymbol{u}_3 \end{bmatrix}^{\mathrm{T}} = \begin{bmatrix} \alpha_{\mathrm{des}} & T & \delta_{\mathrm{a}} & \delta_{\mathrm{e}} & \delta_{\mathrm{r}} \end{bmatrix}^{\mathrm{T}}. \tag{3-63}$$

Full-state measurement is assumed so that $\boldsymbol{y} = \boldsymbol{x}$, where $\boldsymbol{y}$ contains the states which are to be controlled. The EoM are then defined as

$$\begin{aligned} \dot{\boldsymbol{x}} &= \boldsymbol{f}(\boldsymbol{x}) + \mathbf{G}(\boldsymbol{x})\boldsymbol{u} \\ \boldsymbol{y} &= \boldsymbol{h}(\boldsymbol{x}) \end{aligned} \tag{3-64}$$

with $\boldsymbol{f} \in \mathbb{R}^n$, $\mathbf{G} \in \mathbb{R}^{n\times p}$ and $\boldsymbol{h} \in \mathbb{R}^m$. As the control input vector $\boldsymbol{u}$ is given by Eq. (3-63), $p = m = 5$, so that

$$\boldsymbol{f}(\boldsymbol{x}) = \begin{bmatrix} \bar{\boldsymbol{f}}_1(\boldsymbol{x}) \\ \boldsymbol{f}_3(\boldsymbol{x}) \end{bmatrix}, \tag{3-65a}$$

$$\mathbf{G}(\boldsymbol{x}) = \left[\begin{array}{cc|c} \multicolumn{2}{c|}{\bar{\mathbf{G}}_1} & 0 \\ \hline 0 & 0 & \\ I_{yy}^{-1} q S \bar{c} C_{m_\alpha} & 0 & \mathbf{G}_3 \\ 0 & 0 & \end{array}\right]. \tag{3-65b}$$

Looking at the bottom left of $\mathbf{G}$, control input α_{des} has a significant effect on the state q which is captured with C_{m_α}. The state q is not influenced by T, and the other angular rates p and r are not influenced by either α_{des} or T. The control surface deflections $\boldsymbol{\delta}$ are assumed to have a negligible effect on V and γ which is why the upper right part of $\mathbf{G}$ is set equal to zero. Taking into account the drag of the control surface deflection will be done in Chapter 4. For now, these effects are modeled as external disturbances. Finally, note that γ for this controller is defined in the instantaneous center of rotation of the DEP aircraft [63]. This is to prevent non-minimum phase behavior between the elevator deflection δ_{e} and γ. An overview of the control loop for the synthesized INDI controller is shown in Figure 3-4.

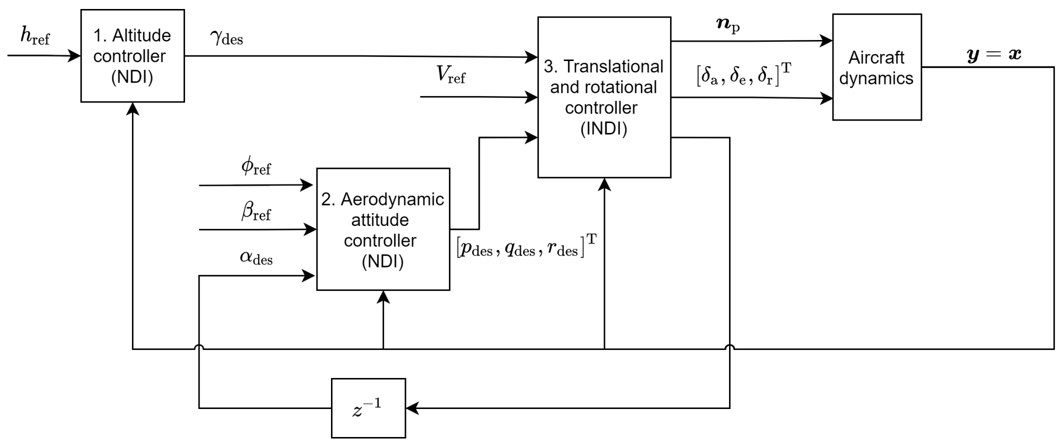

Figure 3-4: Synthesized INDI control for $\bar{\boldsymbol{x}}_1 and \boldsymbol{x}_3$ with two NDI loops for the altitude and aerodynamic attitude

Controller 1 in this figure, represents the control law defined in Eq. (3-24). Controller 2 the one defined in Eq. (3-46). Controller 3 then merges the INDI control laws of Eq. (3-34) and

Eq. (3-53). This control law is defined using the general INDI formulation of (3-18) given as

$$\Delta \boldsymbol{u} = \mathbf{G}^{-1}(\boldsymbol{x}_0, \boldsymbol{u}_0)(\boldsymbol{\nu} - \dot{\boldsymbol{x}}_0). \tag{3-66}$$

Here, $\mathbf{G}(\boldsymbol{x})$ is defined in Eq. (3-65b) and $\dot{\boldsymbol{x}}_0 = \begin{bmatrix} \dot{V}_0 & \dot{\gamma}_0 & \dot{p}_0 & \dot{q}_0 & \dot{r}_0 \end{bmatrix}^{\mathrm{T}}$. The virtual control input $\boldsymbol{\nu}$ is defined as

$$\boldsymbol{\nu} = \mathrm{diag}\left(\begin{bmatrix} \mathbf{K}_{\bar{x}_1} & \mathbf{K}_{\boldsymbol{x}_3} \end{bmatrix}\right)(\boldsymbol{x}_{\mathrm{des}} - \boldsymbol{x}), \tag{3-67}$$

where $\boldsymbol{x}$ is given in Eq. (3-62).

It is important to note that merging the two INDI control loops violates the time-scale separation principle $\Delta \boldsymbol{x} \ll \Delta \boldsymbol{u}$. This is especially true when looking at the pitch rate q and control input α_{des}. Note that when α is increased, this increases the pitch angle θ if the flight path angle γ is not decreased as $\theta = \alpha + \gamma$. From Eq. (A-4) in Appendix A-1, it can be seen that

$$\dot{\theta} = \cos\phi q - \sin\phi r, \tag{3-68}$$

which means that q is directly related to the derivative of θ. A change in α will thus lead to an even larger change in q, so that $\Delta q \not\ll \Delta\alpha_{\mathrm{des}}$, where $q \in \boldsymbol{x}$ and $\alpha_{\mathrm{des}} \in \boldsymbol{u}$. The next section will, therefore, reformulate the INDI control law without the time-scale separation principle.

3-6-1 Stability proof without time-scale separation

In [15], the INDI control law is reformulated without using the time-scale separation principle for a general system with arbitrary relative degree $\boldsymbol{\rho}$. This general system is defined as

$$\boldsymbol{y}^{\boldsymbol{\rho}} = \boldsymbol{a}(\boldsymbol{x}) + \mathcal{B}(\boldsymbol{x})\boldsymbol{u}, \tag{3-69}$$

where $\boldsymbol{y}^{\boldsymbol{\rho}}$, $\boldsymbol{a}(\boldsymbol{x})$ and $\mathcal{B}(\boldsymbol{x})$ are defined in Eq. (3-12). The method of [15] will be applied to the combined INDI control law defined in Eq. (3-66) to prove stable performance. Full-state measurement was assumed so that $\boldsymbol{y} = \boldsymbol{x}$ which means $\dot{\boldsymbol{y}} = \dot{\boldsymbol{x}}$. Also, it was assumed that $\mathcal{B}(\boldsymbol{x})$ is full-rank so that all states can be controlled, else there would be an under-determined problem for $p = m$. This means that there is a direct relation between $\dot{y}_i$ and $\boldsymbol{u}$ for each output channel so that $\rho_1 = \rho_2 = ... = \rho_5 = 1$ and $||\boldsymbol{\rho}||_1 = 5 = n$. The system is thus full-state feedback linearizable so that there are no unobservable internal dynamics. The reformulated INDI control law is given in Appendix B-1 and the reader is referred to this section for the complete derivation. Summarizing, the closed loop INDI control law without time-scale separation is given by

$$\begin{aligned} \dot{\boldsymbol{x}} &= \boldsymbol{\nu} + \boldsymbol{\delta}(\boldsymbol{x}, \Delta t) \\ \boldsymbol{y} &= \boldsymbol{x}, \end{aligned} \tag{3-70}$$

where the perturbation term $\boldsymbol{\delta}$ is defined as

$$\boldsymbol{\delta}(\boldsymbol{x}, \Delta t) = \left.\frac{\partial\left(\boldsymbol{a}(\boldsymbol{x}) + \mathcal{B}(\boldsymbol{x})\boldsymbol{u}\right)}{\partial \boldsymbol{x}}\right|_0 \Delta \boldsymbol{x} + \mathcal{O}^2. \tag{3-71}$$

This perturbation term thus captures changes with respect to the state $\boldsymbol{x}$ and higher-order terms which were discarded in the conventional INDI derivation in Section 3-3. It is shown in Appendix B-1 that there exists a bound on $\boldsymbol{\delta}(\boldsymbol{x}, \Delta t)$, defined as $\bar{\delta}$ and that this bound can be decreased by increasing the sampling frequency for a stable virtual control input $\boldsymbol{\nu}$. This statement is formalized in Theorem 1 in Appendix B-1. Therefore, by increasing the sampling frequency the influence of the perturbation term $\boldsymbol{\delta}(\boldsymbol{x}, \Delta t)$ is reduced so that $\dot{\boldsymbol{y}} \approx \boldsymbol{\nu}$. This means that stability can be concluded if the sampling frequency is high enough.

3-6-2 Robustness analysis

Next to a stability analysis, it is important to analyze the robustness regarding uncertainties. Three main sources of uncertainty can be identified, which include external disturbances, modeling uncertainties and singular perturbations. The last factor increases the order of the system which for the DEP can mainly be found in the form of actuator dynamics and sensors filters as the higher-order elastic dynamics play a relatively small role. These dynamics and filters introduce lags for which the INDI controller should compensate. A method to synchronize the signals, taking into account sensor filters, was discussed in Section 3-5-1. In Section 4-4, a method will be proposed to compensate for the actuator dynamics, so that performance with respect to this aspect is increased.

For the modeling uncertainties, it is shown in [15] that the norm of the perturbation term $\boldsymbol{\delta}$, which also captures the modeling errors, is again reduced by reducing the sampling frequency. It will be analyzed in Section 5-4 how these errors affect the tracking performance.

The external disturbances can be prescribed using the Von Kármán turbulence model [45] for which the implementation method is given in Appendix A-6. As is shown in Appendix B-1, for an external disturbance $\boldsymbol{d}$ with bound $\bar{d}$, there exists a bound on the state $\boldsymbol{x}$ which is a class $\mathcal{K}$ function of $\bar{\delta}$ and $\bar{d}$. This statement if formalized in Theorem 2. The ultimate bound is defined as $\boldsymbol{\mathcal{T}}$ and depends on the following aspects.

1. The system dynamics where $||\boldsymbol{\delta}(x, \Delta t)||_2 \leq \bar{\delta}$ is reduced by increasing the sampling frequency. For rigid aircraft control this is normally set at $f_s = 100\text{Hz}$.

2. The disturbance intensity $\bar{d}$ where larger disturbances lead to larger ultimate bounds $\boldsymbol{\mathcal{T}}$.

3. The gains for $\mathbf{K}$ where larger gains lead to smaller ultimate bounds $\boldsymbol{\mathcal{T}}$. Still one has to take into account that the increase in $\mathbf{K}$ is constrained by the actuators and that noise is amplified through $\mathbf{K}$.

4. The sampling frequency where both $\bar{\delta}$ and $\bar{d}$ are reduced by increasing the sampling frequency. Also, in incremental form $\boldsymbol{d} = \boldsymbol{d}_0 + \Delta\boldsymbol{d}$, where the main part of the disturbance $\boldsymbol{d}_0$ is included by measurement of $\dot{\boldsymbol{x}}_0$. This means that only $\Delta\boldsymbol{d}$ perturbs $\boldsymbol{x}$ when an INDI controller compensates for $\dot{\boldsymbol{x}}_0$. This influence is again reduced by increasing the sampling frequency.

The performance of the proposed INDI controller needs to be determined in simulation, so that the bound $\boldsymbol{\mathcal{T}}$ can be determined. The external disturbance is prescribed using the Von Kármán model and the sampling frequency f_s is changed so that acceptable bounds can be found. As the turbulence mainly influences the states q and z, the maximum bounds $|e_q|_\infty$ and $|e_{Vz}|_\infty$ are determined for $\boldsymbol{\mathcal{T}}$. The gains $\mathbf{K}$ used in this simulation are the low set of proportional gains given in Table B-1 in Appendix B-2. The high set of proportional gains is not used, as increasing the gains results in lower bounds as long as the actuators can provide the required control input. In this analysis, the ultimate bound needs to be determined, where the high proportional gains will give a lower bound.

For the simulation, the sampling time Δt of the controller is increased from $0.005s$ to $0.06s$ with steps of $0.001s$. Note that the simulation sampling time, which is not the same as the controller sampling time, was kept at a constant value of 2000Hz which should be enough to simulate the continuous dynamics [15]. To show the influence of increasing external disturbances the wind speed at an altitude of $6m$ in the Von Kármán model was changed from $2.5m/s$ to $10m/s$. This increases the bound $\bar{d}$ which should therefore increase the bound . The results for the analysis for the bounds on e_q and e_{V_z} are given in Figure 3-5a en Figure 3-5b respectively.

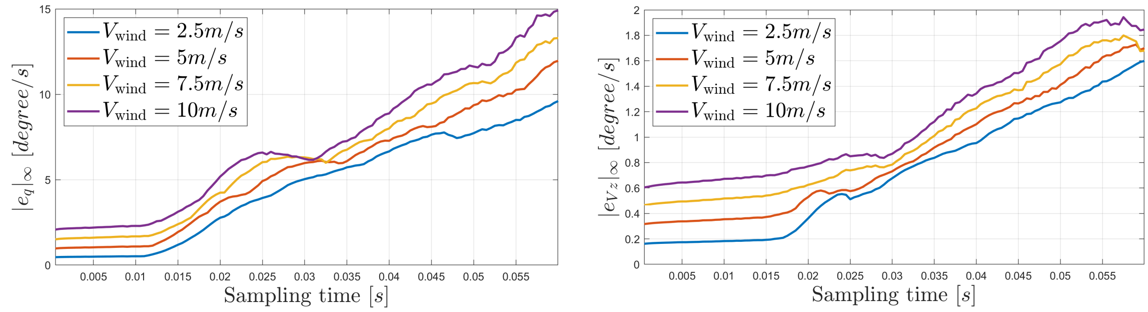

(a) Maximum bound on the pitch rate e_q.

(b) Maximum bound on the vertical velocity e_{V_z}.

Figure 3-5: Maximum bounds of e_q and e_{V_z} for different controller sampling times and turbulence fields of different magnitude.

From the above plots it can be concluded that an acceptable bound on both e_q and e_{V_z} can be set for the given sampling frequency of $f_s = 100$ Hz. Further decreasing the sampling time has no significant effect on the performance while computational load increases. Increasing the sampling time leads to larger ultimate bounds from which it can be concluded that the performance deteriorates. Also, note that for larger external disturbances, the ultimate bounds increase, which confirms the theory discussed above. The error plots e_q and e_{Vz} for the different turbulence fields with sampling time $f_s = 100$ Hz are shown in Figure 3-6a and Figure 3-6b respectively. Here it is again confirmed that by increasing the external disturbances, the error on the state increases.

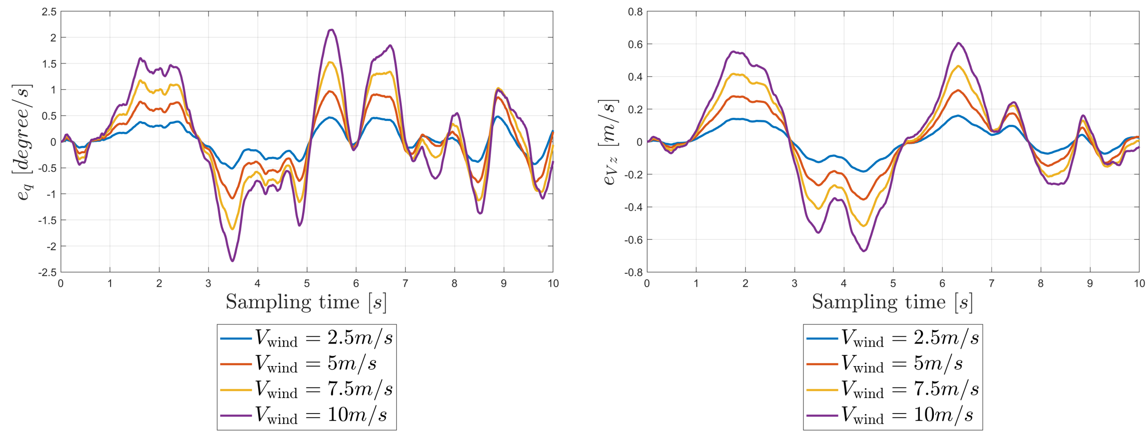

(a) Error on the pitch rate q.

(b) Error on the vertical velocity V_z.

Figure 3-6: Errors of e_q and e_{V_z} for the DEP flying through turbulence fields of different magnitudes.

Adequate performance of the merged INDI controller can be concluded for $f_s = 100$Hz. Sampling at this rate both $\bar{\delta}$ and $\bar{d}$, the bounds on the perturbation term and external disturbances, are sufficiently small, so that stability and robustness are achieved. This controller, therefore, forms the basis of the control allocation discussed in the next chapter.

3-7 Conclusions

In this chapter, the nonlinear controller for the DEP aircraft was derived. As discussed in Section 1-2-1, the INDI controller seems the most suitable. This controller allows controlling the nonlinear dynamics of the DEP aircraft over the complete flight envelope while being robust to external disturbances and modeling uncertainties. As for the DEP aircraft the propellers are actively controlled, rotational control was added to the traditional NDI and INDI implementation. This allows for controlling the altitude, velocity, roll angle and sideslip angle by specifying their respective reference values. The control law was designed with an outer loop for translational and an inner loop for rotational control. These control loops were merged to allow for solving the control problem in one step. This is required to optimize the control allocation for efficiency, as will be shown in Section 4-2-3. It was realized that this formulation violates the time-scale separation principle, which is why the control law was reformulated without this assumption. Stability and robustness were analyzed for different sampling frequencies, from which it was concluded that the controller has adequate performance for $f_s = 100$ Hz. It can, therefore, be concluded that this controller forms the framework for the control allocation methods derived in the next chapter.

Chapter 4

Control allocation

This chapter describes the control allocation method designed for the DEP aircraft, so that all control authorities can be used. Firstly, the general control allocation problem will be introduced and methods will be proposed to solve this. The allocation problem will then be redefined incrementally, so that nonlinearities and effector interactions, which are present for the DEP aircraft, can be taken into account in real-time allocation. This method will be formulated for translational and rotational control. Also, a look will be taken into how the control freedom can be used to optimize for efficiency. To do so, the different control effectiveness factors for the DEP aircraft will be derived and the power consumption of the propellers will be analyzed. Finally, a method will be introduced to compensate for the actuator dynamics which results in better control allocation performance both for tracking and efficiency.

4-1 General allocation problem

Throughout Chapter 3 it was assumed that for the general nonlinear EoM defined in Eq. (3-1), the number of outputs m equals the number of inputs p. This was required to calculate the inverse of the control effectiveness matrix $\mathbf{G}$ for the INDI controller. In reality, for the DEP aircraft, $p > m$ as the aircraft is over-actuated. This leads to a control allocation problem, where there is freedom in the choice of the control input $\boldsymbol{u}$ to satisfy the required reference $\boldsymbol{y}_{\text{ref}}$. To layout the control allocation problem, consider the EoM for aircraft in the following form

$$\begin{aligned} \dot{\boldsymbol{x}} &= \boldsymbol{f}(\boldsymbol{x}) + \mathbf{g}(\boldsymbol{x})\boldsymbol{\tau}, \\ \boldsymbol{y} &= \boldsymbol{h}(\boldsymbol{x}), \end{aligned} \tag{4-1}$$

where $\boldsymbol{x} \in \mathbb{R}^n$ is the state vector, $\boldsymbol{\tau} \in \mathbb{R}^m$ the control moment and force vector, $\boldsymbol{y}$ the output vector and $\boldsymbol{f}(\boldsymbol{x}) \in \mathbb{R}^n$, $\boldsymbol{h}(\boldsymbol{x}) \in \mathbb{R}^m$ and $\mathbf{g}(\boldsymbol{x}) \in \mathbb{R}^{n \times m}$ smooth vector functions. Note that $\boldsymbol{\tau}$ is thus not the control input, but rather contains the relevant forces and moments created by these control inputs. These control forces and moments are defined by a nonlinear mapping $\boldsymbol{\Phi}$ of the states $\boldsymbol{x}$ and the control input vector $\boldsymbol{u} \in \mathbb{R}^p$ as

$$\boldsymbol{\tau} = \boldsymbol{\Phi}(\boldsymbol{x}, \boldsymbol{u}). \tag{4-2}$$

The control inputs often have position and rate constraints defined as

$$\boldsymbol{u}_{\min} \leq \boldsymbol{u} \leq \boldsymbol{u}_{\max}, \tag{4-3a}$$

$$|\dot{\boldsymbol{u}}| \leq \dot{\boldsymbol{u}}_{\max}. \tag{4-3b}$$

For aircraft control the allocation algorithms run on Flight control system (FCS) in discrete-time which means that the control input is computed at each time step for the current state $\boldsymbol{x}_0$. This means that given the current state $\boldsymbol{x}_0$, $\boldsymbol{\Phi}(\boldsymbol{x}, \boldsymbol{u})$ becomes a nonlinear mapping $\boldsymbol{\Phi}(\boldsymbol{x}_0, \boldsymbol{u}) : \mathbb{R}^p \to \mathbb{R}^m$. As the allocation algorithms run on FCS, the constraints in Eq. (4-3) need to be transformed into discrete time. Here the position and rate constraint can be combined to form an upper $\overline{\boldsymbol{u}}$ and lower $\underline{\boldsymbol{u}}$ bound on $\boldsymbol{u}$. The limits are defined as

$$\overline{\boldsymbol{u}} = \min\left(\boldsymbol{u}_{\max}, \boldsymbol{u}_0 + \dot{\boldsymbol{u}}_{\max}\Delta t\right), \tag{4-4a}$$

$$\underline{\boldsymbol{u}} = \max\left(\boldsymbol{u}_{\min}, \boldsymbol{u}_0 - \dot{\boldsymbol{u}}_{\max}\Delta t\right). \tag{4-4b}$$

The control allocation problem is formulated as follows [38]. Given the current state $\boldsymbol{x}_0$, the control effector model $\boldsymbol{\tau} = \boldsymbol{\Phi}(\boldsymbol{x}_0, \boldsymbol{u})$ and the control force and moment command $\boldsymbol{\tau}_{\mathrm{c}}$, determine the control vector $\boldsymbol{u}$ for

$$\begin{aligned} &\boldsymbol{\Phi}(\boldsymbol{x}_0, \boldsymbol{u}) = \boldsymbol{\tau}_{\mathrm{c}}, \\ &\text{subject to } \underline{\boldsymbol{u}} \leq \boldsymbol{u} \leq \overline{\boldsymbol{u}}. \end{aligned} \tag{4-5}$$

As for the DEP aircraft $p > m$, the problem defined in Eq. (4-5) is ill-posed so that control allocation is required.

Different methods were discussed in Section 1-2-2 to solve the allocation problem. It was concluded that solving the optimization with nonlinear methods is computationally too expensive. If control input constraints need to be taken into account, solving the allocation problem using linear optimization gives the best performance. For this, a linear relationship is assumed, so that the control allocation problem is defined as

$$\begin{aligned} &\mathbf{B}(\boldsymbol{x}_0)\boldsymbol{u} = \boldsymbol{\tau}_{\mathrm{c}}, \\ &\text{subject to } \underline{\boldsymbol{u}} \leq \boldsymbol{u} \leq \overline{\boldsymbol{u}}, \end{aligned} \tag{4-6}$$

where $\mathbf{B}$ depends on the current state, so that the allocation problem is solved statically, updating $\mathbf{B}$ every time step [26]. Solving the allocation using linear optimization allows for online computation including control input constraints. Also, this method is not sensitive to the initial solution provided to the algorithm, which is a limitation of other allocation methods. Defining the minimization as a mixed optimization problem is most suitable, as it can be solved fastest and with better properties compared to other minimization problems [33]. This optimization problem is defined with the l_2 norm, as this tends to distribute the control effort over more effectors [34]. For the DEP aircraft specifically this means that all possible control authorities are used which is the goal of the allocation algorithm. The mixed optimization function with the l_2 norm is defined as

$$\begin{aligned} &\min_{\boldsymbol{u}} \mathbf{Q}\left|\left|\mathbf{B}\boldsymbol{u} - \boldsymbol{\tau}_{\mathrm{c}}\right|\right|_2^2 + \mathbf{W}\left|\left|\boldsymbol{u} - \boldsymbol{u}_{\mathrm{p}}\right|\right|_2^2, \\ &\text{subject to } \underline{\boldsymbol{u}} \leq \boldsymbol{u} \leq \overline{\boldsymbol{u}}. \end{aligned} \tag{4-7}$$

Here $\mathbf{Q}$ and $\mathbf{W}$ are positive definite weighting matrices used to prioritize the different objectives in the optimization. The secondary objective is introduced to find a unique solution to the optimization, by defining a control preference vector $\boldsymbol{u}_{\mathrm{p}}$. This vector sets the value for each control input preferred value and is often set equal to zero, so that the control activity is minimized. Generally, $\mathbf{Q} \gg \mathbf{W}$ to prioritize the allocation error over the secondary objective.

Different algorithms can be used to solve this QP problem including fixed point, interior-points and active set methods. [34]. In this research, it was concluded that the active set method converges in a finite number of steps to the optimum and is computationally efficient for a small and medium size control allocation problem, which is the size of the DEP control input vector. It has also proven to deliver accurate results in online flight control, which is why the active-set method proposed in [64] is used. Here, the mixed optimization problem is redefined using Weighted least squares (WLS) as

$$\begin{aligned} &\min_{\boldsymbol{u}} \left\| \begin{pmatrix} \mathbf{QB} \\ \mathbf{W} \end{pmatrix} \boldsymbol{u} - \begin{pmatrix} \mathbf{Q}\boldsymbol{\tau}_{\mathrm{c}} \\ \mathbf{W}\boldsymbol{u}_{\mathrm{p}} \end{pmatrix} \right\|_2^2, \\ &\text{subject to } \mathbf{C}\boldsymbol{u} \geq \boldsymbol{U}, \end{aligned} \tag{4-8}$$

where $\mathbf{C} = \begin{bmatrix} \mathbf{I} & -\mathbf{I} \end{bmatrix}^{\mathrm{T}}$ and $\boldsymbol{U} = \begin{bmatrix} \underline{\boldsymbol{u}} & \overline{\boldsymbol{u}} \end{bmatrix}^{\mathrm{T}}$. The active set algorithm solves this optimization problem by solving a sequence of equality constrained problems. For each step, a set of the inequality constraints is regarded as a equality constraint forming the working set $\boldsymbol{\mathcal{W}}$. The remaining inequality constraints are discarded and the working set at the optimum is then defined as the active set of the solution. The active set algorithm is given in Appendix B-5.

The method proposed in this section to solve the control allocation problem, assumes a linear relationship between the control inputs and the control force and moment vector as defined in Eq. (4-6). A limitation of this method is that control effector interaction cannot be taken into account. Also, as a linear relationship is assumed, nonlinear relations in the allocation problem cannot be implemented. Looking at the DEP aircraft, both these limitations are relevant. The two outer propellers affect the slipstream over the aileron and thus their control effectiveness. Also, as the PAI effects are nonlinear, assuming a linear relationship will not give satisfactory results. The next section aims to overcome these limitations by introducing a new control allocation method, further developing the approach discussed in this section.

4-2 Incremental nonlinear control allocation (INCA)

In [38], a new method is proposed for solving the control allocation problem defined in Eq. (4-5). For this method, the control allocation is solved incrementally, following the same philosophy as in Section 3-3. Solving the allocation problem incrementally allows taking into account control effector interactions and nonlinearities. This problem can be solved as a linear mixed optimization problem using QP, as defined in Eq. (4-7). The next section will introduce the INCA method in general, after which it will be implemented for the synthesized translation and rotational INDI controller which was derived in Section 3-6.

4-2-1 General INCA

For derivation of the INCA controller, consider again Eq. (4-1), where the control force and moment vector is divided into $\boldsymbol{\tau} = \boldsymbol{\tau}_\mathrm{a} + \boldsymbol{\tau}_\mathrm{c}$. Here, the first factor represent the forces and moment created by the airframe and the second the ones create by the control effectors. In general, the forces and moments created by these effectors can be calculated using the nonlinear mapping

$$\boldsymbol{\tau}_\mathrm{c} = \boldsymbol{\Phi}(\boldsymbol{x}, \boldsymbol{u}), \tag{4-9}$$

where $\boldsymbol{\Phi} : \mathbb{R}^n \times \mathbb{R}^p \to \mathbb{R}^n$. The system dynamics of Eq. (4-1) can then be rewritten as

$$\begin{aligned} \dot{\boldsymbol{x}} &= [\boldsymbol{f}(\boldsymbol{x}) + \mathbf{g}(\boldsymbol{x})\boldsymbol{\tau}_\mathrm{a}] + \mathbf{g}(\boldsymbol{x})\boldsymbol{\Phi}(\boldsymbol{x}, \boldsymbol{u}) \\ &= \boldsymbol{F}(\boldsymbol{x}) + \mathbf{g}(\boldsymbol{x})\boldsymbol{\Phi}(\boldsymbol{x}, \boldsymbol{u}), \end{aligned} \tag{4-10}$$

where the state-dependent part $\boldsymbol{F}(\boldsymbol{x})$ thus also includes the moments produced by $\boldsymbol{\tau}_a$. As for the INDI method, the system dynamics can be locally linearized using the Taylor expansion around the current state $\boldsymbol{x}_0$ and the current actuator position $\boldsymbol{u}_0$ with Eq. (2-41). Using $\dot{\boldsymbol{x}}_0 = \boldsymbol{F}(\boldsymbol{x})$, the current dynamics are replaced with sensor measurements. Discarding changes with respect to $\boldsymbol{x}$ for sufficient high sampling frequency, as discussed in Section 3-6, Eq. (4-10) in incremental form becomes

$$\dot{\boldsymbol{x}} = \dot{\boldsymbol{x}}_0 + \mathbf{g}(\boldsymbol{x}_0)\frac{\partial \boldsymbol{\Phi}(\boldsymbol{x}_0, \boldsymbol{u}_0)}{\partial \boldsymbol{u}}\Delta\boldsymbol{u}. \tag{4-11}$$

Defining the virtual control input $\boldsymbol{\nu} = \dot{\boldsymbol{y}} = \dot{\boldsymbol{x}}$, where it is assumed that all states can be measured, INDI can be applied to calculate $\Delta\boldsymbol{u}$ as

$$\Delta\boldsymbol{u} = \left[\frac{\partial \boldsymbol{\Phi}(\boldsymbol{x}_0, \boldsymbol{u}_o)}{\partial \boldsymbol{u}}\right]^{-1} \mathbf{g}(\boldsymbol{x}_0)^{-1}\left(\boldsymbol{\nu} - \dot{\boldsymbol{x}}_0\right). \tag{4-12}$$

Here, $\frac{\partial \boldsymbol{\Phi}(\boldsymbol{x}_0, \boldsymbol{u}_o)}{\partial \boldsymbol{u}} = \nabla_{\boldsymbol{u}}\boldsymbol{\Phi}(\boldsymbol{x}_0, \boldsymbol{u}_0) \in \mathbb{R}^{m\times p}$ to simplify notation using the Jacobian ∇ as defined in Eq. (3-3). Also define the incremental control force and moment vector $\Delta\boldsymbol{\tau}_\mathrm{c} \in \mathbb{R}^m$ as

$$\Delta\boldsymbol{\tau}_\mathrm{c} = \mathbf{g}(\boldsymbol{x}_0)^{-1}\left(\boldsymbol{\nu} - \dot{\boldsymbol{x}}_0\right). \tag{4-13}$$

It is important to note that Eq. (4-11) establishes an affine relationship between the virtual control input $\boldsymbol{\nu} = \dot{\boldsymbol{x}}$ and increments of the control effectors $\Delta\boldsymbol{u}$. Nonlinearities and interactions between the control effectors are defined in the Jacobian matrix $\nabla_{\boldsymbol{u}}\boldsymbol{\Phi}(\boldsymbol{x}_0, \boldsymbol{u}_0)$. This Jacobian matrix is updated at every time step with the current state and actuator position. As for INDI, the total control input is calculated with $\boldsymbol{u} = \boldsymbol{u}_0 + \Delta\boldsymbol{u}$.

As stated before, for over-actuated aircraft, $p > m$ so that the Jacobian in Eq. (4-12) cannot be inverted directly. Therefore, the control allocation problem is defined with the same structure as Eq. (4-5), only now incrementally. Given the current state $\boldsymbol{x}_0$, the current actuator input $\boldsymbol{u}_0$, state derivatives $\dot{\boldsymbol{x}}_0$ and the control force and moment vector $\boldsymbol{\tau}_\mathrm{c}$, determine the incremental control input $\Delta\boldsymbol{u}$ so that

$$\begin{aligned} &\nabla_{\boldsymbol{u}}\boldsymbol{\Phi}(\boldsymbol{x}_0, \boldsymbol{u}_0)\Delta\boldsymbol{u} = \Delta\boldsymbol{\tau}_\mathrm{c}, \\ &\text{subject to } \underline{\Delta\boldsymbol{u}} \leq \Delta\boldsymbol{u} \leq \overline{\Delta\boldsymbol{u}}. \end{aligned} \tag{4-14}$$

Here $\underline{\Delta \boldsymbol{u}}$ and $\overline{\Delta \boldsymbol{u}}$ are the upper and lower bounds of the local increments of the actuators. These are defined by the local position and rate constraints. The constraints of Eq. (4-4) thus need to be transformed in incremental form. In discrete time, the rate limits can be converted into position limits in incremental form defined as

$$\begin{aligned} \Delta \boldsymbol{u}^{\mathrm{r}}_{\max} &= \dot{\boldsymbol{u}}_{\max} \Delta t, \\ \Delta \boldsymbol{u}^{\mathrm{r}}_{\min} &= -\dot{\boldsymbol{u}}_{\max} \Delta t. \end{aligned} \tag{4-15}$$

In similar fashion, the position constraints can be written in incremental form as

$$\begin{aligned} \Delta \boldsymbol{u}^{\mathrm{p}}_{\max} &= \boldsymbol{u}_{\max} - \boldsymbol{u}_0, \\ \Delta \boldsymbol{u}^{\mathrm{p}}_{\min} &= \boldsymbol{u}_{\min} - \boldsymbol{u}_0. \end{aligned} \tag{4-16}$$

The local upper and lower bound of the increment of control input is determined by the most restrictive bound on the local rate and position limits defined by Eq. (4-15) and Eq. (4-16). This gives the incremental constraints defined as

$$\begin{aligned} \overline{\Delta \boldsymbol{u}} &= \min\left(\dot{\boldsymbol{u}}_{\max} \Delta t, \boldsymbol{u}_{\max} - \boldsymbol{u}_0\right), \\ \underline{\Delta \boldsymbol{u}} &= \max\left(-\dot{\boldsymbol{u}}_{\max} \Delta t, \boldsymbol{u}_{\min} - \boldsymbol{u}_0\right). \end{aligned} \tag{4-17}$$

The incremental control allocation problem defined in Eq. (4-14) is linear in the optimization variable $\Delta \boldsymbol{u}$. Therefore, the mixed optimization defined as a QP problem can be used, which optimizing for the incremental control input $\Delta \boldsymbol{u}$ gives

$$\begin{aligned} &\min_{\Delta \boldsymbol{u}} ||\mathbf{Q}\left(\nabla_{\boldsymbol{u}} \boldsymbol{\Phi}(\boldsymbol{x}_0, \boldsymbol{u}_0) \Delta \boldsymbol{u} - \Delta \boldsymbol{\tau}_c\right)||_2^2 + ||\mathbf{W}(\Delta \boldsymbol{u} - \Delta \boldsymbol{u}_{\mathrm{p}})||_2^2 \\ &\text{subject to } \underline{\Delta \boldsymbol{u}} \leq \Delta \boldsymbol{u} \leq \overline{\Delta \boldsymbol{u}}, \end{aligned} \tag{4-18}$$

where the constraints are defined with Eq. (4-17) and $\mathbf{Q}$ and $\mathbf{W}$ are again weighting matrices where $\mathbf{Q} \gg \mathbf{R}$ to prioritize the allocation error over the secondary objective. Note that the control preference vector $\Delta \boldsymbol{u}$ is now also defined incrementally. This incremental preference has to be calculated at every time step, driving the actuators to their preferred position, with

$$\Delta \boldsymbol{u}_{\mathrm{p}} = \min\left(|\boldsymbol{u}_{\mathrm{p}} - \boldsymbol{u}_0|, \dot{\boldsymbol{u}}_{\max} \Delta t\right) \cdot \operatorname{sign}(\boldsymbol{u}_{\mathrm{p}} - \boldsymbol{u}_0). \tag{4-19}$$

By defining this INCA optimization function as a WLS in the same way as for Eq. (4-8), the INCA optimization can also be solved efficiently online using the active set algorithm. As the INCA controller allows to take into account nonlinearities and effector interactions, which are important factors in the design of the controller for the DEP aircraft, this method will be used for control allocation. It will be further developed in the subsequent sections.

4-2-2 INCA for rotational and translational control

As discussed in Section 3-6, the control allocation method is used to synthesize the translational and rotational loop. Implementation of this controller in the INCA framework will be discussed in this section. The incremental EoM for combined translational and rotational control are defined as

$$\begin{aligned} \dot{\boldsymbol{x}} &= \dot{\boldsymbol{x}}_0 + \mathbf{g}(\boldsymbol{x}_0) \Delta \boldsymbol{\tau}, \\ \dot{\boldsymbol{x}} &= \dot{\boldsymbol{x}}_0 + \mathbf{g}(\boldsymbol{x}_0) \nabla_{\boldsymbol{u}} \boldsymbol{\Phi}(\boldsymbol{x}_0, \boldsymbol{u}_0) \Delta \boldsymbol{u}, \\ \boldsymbol{y} &= \boldsymbol{x}, \end{aligned} \tag{4-20}$$

where

$$\Delta\boldsymbol{\tau} = \begin{bmatrix} \Delta\dot{V} & \Delta\dot{\gamma} & \Delta l & \Delta m & \Delta n \end{bmatrix}^{\mathrm{T}}, \tag{4-21}$$

and

$$\mathbf{g}(\boldsymbol{x}) = \begin{bmatrix} 1 & 0 & 0 \\ 0 & 1 & 0 \\ 0 & 0 & \mathbf{I}^{-1} \end{bmatrix}. \tag{4-22}$$

The control effectiveness matrix for translational and rotational control is defined as

$$\nabla_{\boldsymbol{u}}\boldsymbol{\Phi}(\boldsymbol{x}_0, \boldsymbol{u}_0) = \begin{bmatrix} \frac{\partial \dot{V}}{\partial u_1}\Big|_{x_0,u_0} & \frac{\partial \dot{V}}{\partial u_2}\Big|_{x_0,u_0} & \cdots & \frac{\partial \dot{V}}{\partial u_{11}}\Big|_{x_0,u_0} \\ \frac{\partial \dot{\gamma}}{\partial u_1}\Big|_{x_0,u_0} & \frac{\partial \dot{\gamma}}{\partial u_2}\Big|_{x_0,u_0} & \cdots & \frac{\partial \dot{\gamma}}{\partial u_{11}}\Big|_{x_0,u_0} \\ \frac{\partial l}{\partial u_1}\Big|_{x_0,u_0} & \frac{\partial l}{\partial u_2}\Big|_{x_0,u_0} & \cdots & \frac{\partial l}{\partial u_{11}}\Big|_{x_0,u_0} \\ \frac{\partial m}{\partial u_1}\Big|_{x_0,u_0} & \frac{\partial m}{\partial u_2}\Big|_{x_0,u_0} & \cdots & \frac{\partial m}{\partial u_{11}}\Big|_{x_0,u_0} \\ \frac{\partial n}{\partial u_1}\Big|_{x_0,u_0} & \frac{\partial n}{\partial u_2}\Big|_{x_0,u_0} & \cdots & \frac{\partial n}{\partial u_{11}}\Big|_{x_0,u_0} \end{bmatrix}, \tag{4-23}$$

for the control input vector

$$\boldsymbol{u} = \begin{bmatrix} \alpha_{\mathrm{des}} & n_{\mathrm{p1}} & n_{\mathrm{p2}} & n_{\mathrm{p3}} & n_{\mathrm{p4}} & n_{\mathrm{p5}} & n_{\mathrm{p6}} & \delta_{\mathrm{aL}} & \delta_{\mathrm{aR}} & \delta_{\mathrm{e}} & \delta_{\mathrm{r}} \end{bmatrix}^{\mathrm{T}} \in \mathbb{R}^{11}. \tag{4-24}$$

In this form, the control allocation problem can be solved online using QP with Eq. (4-18). The control preferce vector is defined as

$$\boldsymbol{u}_{\mathrm{p}} = \begin{bmatrix} \alpha_{\mathrm{trim}} & n_{\mathrm{Ptrim}} & n_{\mathrm{Ptrim}} & n_{\mathrm{Ptrim}} & n_{\mathrm{Ptrim}} & n_{\mathrm{Ptrim}} & n_{\mathrm{Ptrim}} & 0 & 0 & 0 & 0 \end{bmatrix}^{\mathrm{T}} \in \mathbb{R}^{11}. \tag{4-25}$$

As discussed in Section 3-4, the forces and moment produced by the control inputs are expressed in control derivatives. Using non-dimensional scaling, as introduced in Section 2-3-4, the partial derivatives in Eq. (4-23), for one of the control inputs u of Eq. (4-24), are defined as

$$\frac{\partial \dot{V}}{\partial u} = \frac{qS}{m}\frac{\partial C_X}{\partial u} = -\frac{qS}{m}\frac{\partial C_D}{\partial u}, \tag{4-26a}$$

$$\frac{\partial \dot{\gamma}}{\partial u} = -\frac{qS}{mV}\frac{C_Z}{\partial u} = \frac{qS}{mV}\frac{C_L}{\partial u}\cos(\phi), \tag{4-26b}$$

$$\frac{\partial l}{\partial u} = qSb\frac{\partial C_l}{\partial u}, \tag{4-26c}$$

$$\frac{\partial m}{\partial u} = qS\bar{c}\frac{\partial C_m}{\partial u}, \tag{4-26d}$$

$$\frac{\partial n}{\partial u} = qSb\frac{\partial C_n}{\partial u}, \tag{4-26e}$$

where C_X and C_Z are defined in the F_{V} frame, C_D and C_L in the F_{a} frame and C_l, C_m and C_n in the F_{b} frame. As the control derivatives affecting $\dot{V}$ and $\dot{\gamma}$ are defined in the F_{V} and F_{a} frame, the transformation $\mathbf{T}_{\mathrm{Va}}$ is already applied to Eq. (4-26a) and Eq. (4-26b) where only the second of these two equations needs to be rotated by ϕ. An overview of these frames was given in Section 2-1-1 and the transformation $\mathbf{T}_{\mathrm{Va}}$ in Appendix A-1.

The derivatives with respect to $\alpha, \delta_{\mathrm{aL}}, \delta_{\mathrm{aR}}, \delta_{\mathrm{e}}, \delta_{\mathrm{r}}$ were taken from wind tunnel data of the SFD and are given in Appendix A-4. The derivatives with respect to $n_{\mathrm{p1}}, ..., n_{\mathrm{p6}}$ describe the differential thrust and PAI effects discussed in Section 2-3 which are unique for the DEP aircraft. Finding these partial derivatives will be discussed in Section 4-3.

4-2-3 INCA for optimizing with respect to propeller power

One of the objectives for the DEP control allocation is to increase efficiency. A look will be taken in this section how the secondary objective of the INCA method can be used for that. To find the optimal control allocation with respect to power, the partial derivative $\frac{P_\mathrm{p}}{m_\mathrm{p}}$ needs to be determined. To do so, the model for propeller power introduced in Section 2-3-1 is used so that

$$\begin{aligned}\frac{\partial P_\mathrm{p}}{\partial n_\mathrm{p}} &= \frac{\partial C_\mathrm{p}(J)\rho n_\mathrm{p}^3 D_\mathrm{p}^5}{\partial n_\mathrm{p}},\\ &= \frac{\partial C_\mathrm{p}(J)}{\partial n_\mathrm{p}}\rho n_\mathrm{p}^3 D_\mathrm{p}^5 + C_\mathrm{p}(J)3\rho n_\mathrm{p}^2 D_\mathrm{p}^5,\end{aligned} \tag{4-27}$$

where

$$\begin{aligned}\frac{\partial C_\mathrm{p}(J)}{\partial n_\mathrm{p}} &= \frac{\partial C_\mathrm{p}(J)}{\partial J}\frac{\partial J}{\partial n_\mathrm{p}},\\ &= \frac{\partial C_\mathrm{p}(J)}{\partial J}\frac{-V_\infty}{D_\mathrm{p} n_\mathrm{p}^2}.\end{aligned} \tag{4-28}$$

Substituting then gives

$$\frac{\partial P_\mathrm{p}}{\partial n_\mathrm{p}}(V_\infty, \rho, n_\mathrm{p}) = -\frac{\partial C_\mathrm{p}(J)}{\partial J} V_\infty \rho n_\mathrm{p} D_\mathrm{p}^4 + 3C_\mathrm{p}(J) n_\mathrm{p}^2 D_\mathrm{p}^5, \tag{4-29}$$

so that this derivative depends on V_∞, ρ and n_p whereas D_p remains constant. The values of $C_\mathrm{p}(J)$ and $\frac{\partial C_\mathrm{p}(J)}{\partial J}$ are determined using the experimental data given in Appendix A-3-1. A fifth-order polynomial was fit through this data, so that the partial derivative with respect to J can be calculated efficiently.

Defining the power effectiveness matrix $\nabla_{\boldsymbol{u}}\boldsymbol{\Omega}(\boldsymbol{x}_0, \boldsymbol{u}_0) \in \mathbb{R}^{6\times 11}$ as

$$\nabla_{\boldsymbol{u}}\boldsymbol{\Omega}(\boldsymbol{x}_0, \boldsymbol{u}_0) = \begin{bmatrix} 0 & \dots & 0 & \frac{\partial P_\mathrm{p1}}{\partial n_\mathrm{p1}} & 0 & 0 & 0 & 0 & 0 \\ 0 & \dots & 0 & 0 & \frac{\partial P_\mathrm{p2}}{\partial n_\mathrm{p2}} & 0 & 0 & 0 & 0 \\ 0 & \dots & 0 & 0 & 0 & \frac{\partial P_\mathrm{p3}}{\partial n_\mathrm{p3}} & 0 & 0 & 0 \\ 0 & \dots & 0 & 0 & 0 & 0 & \frac{\partial P_\mathrm{p4}}{\partial n_\mathrm{p4}} & 0 & 0 \\ 0 & \dots & 0 & 0 & 0 & 0 & 0 & \frac{\partial P_\mathrm{p5}}{\partial n_\mathrm{p5}} & 0 \\ 0 & \dots & 0 & 0 & 0 & 0 & 0 & 0 & \frac{\partial P_\mathrm{p6}}{\partial n_\mathrm{p6}} \end{bmatrix}, \tag{4-30}$$

the secondary objective in the INCA formulation with control preference vector $\boldsymbol{u}_\mathrm{p}$ given in Eq. (4-18) can be replaced. The new optimization problem including propeller power, implemented in the INCA framework becomes

$$\min_{\Delta \boldsymbol{u}} ||\mathbf{Q}\left(\nabla_{\boldsymbol{u}}\boldsymbol{\Phi}(\boldsymbol{x}_0, \boldsymbol{u}_0)\Delta\boldsymbol{u} - \Delta\boldsymbol{\tau}_c\right)||_2^2 + ||\mathbf{W}\left(\nabla_{\boldsymbol{u}}\boldsymbol{\Omega}(\boldsymbol{x}_0, \boldsymbol{u}_0)\Delta\boldsymbol{u} + \boldsymbol{P}_0\right)||_2^2, \tag{4-31}$$

where $\boldsymbol{P}_0$ is the current power consumed by the propellers. Solving the control allocation problem with this optimization will give the optimal control distribution for minimal propeller power. Increasing the angle of attack α or the control deflections $\boldsymbol{\delta}$ will increase the drag. This means that extra thrust is required to satisfy $\Delta\boldsymbol{\tau}_\mathrm{c}$ for $\Delta\dot{V}$ in particular. Furthermore, using the propellers both to control yaw using differential thrust or roll using the PAI effects will also increase power as n_p for that specific propeller is increased. Using the above formulation thus will give the optimal trade-off between using the control surfaces $\boldsymbol{\delta}$ and propeller differential thrust and PAI effects by changing the propeller rotational velocity $\boldsymbol{n}_\mathrm{p}$, regarding propeller power.

4-2-4 INCA for Fault tolerant control (FTC)

As was discussed in Chapter 1, the introduction of extra propellers for DEP, can make the aircraft more robust against actuator faults. This is of particular interest when one of the propellers fails. The other propellers should be able to compensate for this and stabilize the aircraft. If one of the actuators fails, its control effectiveness becomes zero so that the corresponding column in the control effectiveness matrix $\nabla_{\boldsymbol{u}}\Phi(\boldsymbol{x}_0, \boldsymbol{u}_0) = 0$. The required control forces and moments should then be distributed over the remaining actuators to satisfy $\boldsymbol{y}_\mathrm{ref}$. Note that the control effectiveness matrix should remain full rank to remain fully controllable.

In [38] it was suggested to use INCA for FTC and this concept was further developed in [40]. For this method, the weights $\mathbf{W}$ of the INCA optimization defined in Eq. (4-18) are changed. In this thesis, the same method will be used. A fault will be introduced on one of the propellers and its corresponding weight W will be increased by a factor of 100. Also, $\Delta\boldsymbol{u}_\mathrm{p}$ will be set equal to zero, so that the control input is not changed anymore. By feeding back sensors measurements, the INCA controller should be able to find a new control allocation, satisfying the reference signals. As fault detection is not the goal of this thesis it was assumed that the fault can be detected using an Fault detection and isolation (FDI) algorithm. A delay between the fault and detection is assumed, which is defined as t_detect, so that there is time for the to be designed algorithm to detect the fault.

4-3 DEP control authorities in INCA controller

As described in Section 2-3, two effects regarding control of DEP aircraft can be identified: differential thrust and PAI effects. In this thesis, it is assumed that the thrust of the propellers is directed in the F_b x-direction, so that differential thrust only creates a moment n around the F_b z-axis. The PAI effects locally affect the lift force L, which primarily creates a moment l around the F_b x-axis. A secondary effect of this increase in lift, is that the local drag force D is increased which also primarily creates a moment around the F_b z-axis. Note that both the lift and drag force also create a moment around the F_b z-axis and x-axis respectively, by decomposing these forces from the F_a frame into the F_b frame for $\alpha \neq 0 \vee \beta \neq 0$. Although these contributions are relatively small, for completeness these effects are also modeled. This will also result in better optimization for power, as more effects are included in the controller. Note that the control effectiveness for the general propeller p is derived where $p \in p_1, p_2, ...p_6$ for all six propellers.

4-3-1 Differential thrust

Firstly, the partial derivative $\frac{\partial T_{\mathrm{p}}}{\partial n_{\mathrm{p}}}$ needs to be determined. Using the propeller model discussed in Section 2-3-1 this partial derivative can be defined as

$$\begin{aligned} \frac{\partial T_{\mathrm{p}}}{\partial n_{\mathrm{p}}} &= \frac{\partial C_{\mathrm{T}}(J)\rho D_{\mathrm{p}}^4 n_{\mathrm{p}}^2}{\partial n_{\mathrm{p}}}, \\ &= \frac{\partial C_{\mathrm{T}}(J)}{\partial n_{\mathrm{p}}}\rho D_{\mathrm{p}}^4 n_{\mathrm{p}}^2 + C_{\mathrm{T}}(J) 2\rho D_{\mathrm{p}}^4 n_{\mathrm{p}}, \end{aligned} \tag{4-32}$$

where

$$\begin{aligned} \frac{C_{\mathrm{T}}(J)}{\partial n_{\mathrm{p}}} &= \frac{\partial C_{\mathrm{T}}(J)}{\partial J}\frac{\partial J}{\partial n_{\mathrm{p}}}, \\ &= \frac{\partial C_{\mathrm{T}}(J)}{\partial J}\frac{-V_\infty}{D_{\mathrm{p}} n_{\mathrm{p}}^2}. \end{aligned} \tag{4-33}$$

Substituting then gives

$$\frac{\partial T_{\mathrm{p}}}{\partial n_{\mathrm{p}}}(V_\infty, \rho, n_{\mathrm{p}}) = -\frac{\partial C_{\mathrm{T}}(J)}{\partial J} V_\infty \rho D_{\mathrm{p}}^3 + C_{\mathrm{T}}(J) 2\rho D_{\mathrm{p}}^4 n_{\mathrm{p}}, \tag{4-34}$$

so that this derivative changes with the parameters V_∞, ρ and n_{p} whereas D_{p} remains constant. The values for $C_{\mathrm{T}}(J)$ and $\frac{\partial C_{\mathrm{T}}(J)}{\partial J}$ were determined using the experimental data of the propeller. A sixth-order polynomial was fit through this data so that the partial derivative $\frac{\partial C_{\mathrm{T}}(J)}{\partial J}$ can be efficiently calculated. The data and polynomial fit are shown in Appendix A-3-1. Dividing by qS gives the non-dimensional coefficient $\frac{\partial C_{T_{\mathrm{p}}}}{\partial n_{\mathrm{p}}}$. These are rotated to the F_{V} frame in which V and γ are defined using $\mathbf{T}_{\mathrm{Va}}$ Eq. (A-1) and $\mathbf{T}_{\mathrm{ab}}$ Eq. (A-5) to give

$$\begin{aligned} \frac{\partial C_X}{\partial n_{\mathrm{p}}}(V_\infty, \rho, n_{\mathrm{p}}, \alpha)_{\mathrm{thrust}} &= \cos(\alpha)\frac{\partial C_{T_{\mathrm{p}}}}{\partial n_{\mathrm{p}}} \\ \frac{\partial C_Z}{\partial n_{\mathrm{p}}}(V_\infty, \rho, n_{\mathrm{p}}, \alpha, \phi)_{\mathrm{thrust}} &= -\sin(\alpha)\cos(\phi)\frac{\partial C_{T_{\mathrm{p}}}}{\partial n_{\mathrm{p}}} \end{aligned} \tag{4-35}$$

Defining the distance of each propeller in the F_{b} y-direction from the Center of gravity (CG) as y_{p}, the differential thrust effect can be defined as

$$\frac{\partial C_n}{\partial n_{\mathrm{p}}}(V_\infty, \rho, n_{\mathrm{p}})_{\mathrm{thrust}} = -\frac{y_{\mathrm{p}}}{b}\frac{\partial C_{T_{\mathrm{p}}}}{\partial n_{\mathrm{p}}}, \tag{4-36}$$

where y_{p} is constant for each propeller.

4-3-2 PAI effects

General interaction effects

An analytical model for the PAI effects was given in Section 2-3-2. As was discussed, these effect create a local increase in lift ΔC_L and in drag ΔC_D, which are a function of the propeller thrust T_{p}. This section will, therefore, derive the different partial derivatives with respect to

T_p, after which the chain-rule will be applied to find the derivative with respect to n_p. As defined in Section 2-3-2 the local increase in lift an drag can be calculated with

$$\Delta C_L = 2\pi\left[(\sin(\alpha) - a_\mathrm{w}\beta_\mathrm{corr}\sin(\alpha_\mathrm{p}-\alpha))\sqrt{(a_\mathrm{w}\beta_\mathrm{corr})^2 + 2a_\mathrm{w}\beta\cos\alpha_\mathrm{p} + 1} - \sin(\alpha)\right]\Delta Y, \tag{4-37}$$

$$\begin{aligned}\Delta C_D &= \Delta C_{D_0} + \Delta C_{D_i},\\ &= \Delta Y a_\mathrm{w}^2 c_\mathrm{f} + \frac{\Delta C_L^2 + 2C_{L_\mathrm{ac}}\Delta C_L}{\pi A e}.\end{aligned} \tag{4-38}$$

Using the chain rule, the partial derivative with respect to T_p are defined as

$$\frac{\partial \Delta C_L}{\partial T_\mathrm{p}} = \frac{\partial \Delta C_L}{\partial a_\mathrm{w}}\frac{\partial a_\mathrm{w}}{\partial T_\mathrm{p}} + \underbrace{\frac{\partial C_L}{\partial \beta}\frac{\partial \beta_\mathrm{corr}}{\partial T_\mathrm{p}}}_{\approx 0} \tag{4-39a}$$

$$\frac{\partial \Delta C_D}{\partial T_\mathrm{p}} = \frac{\partial C_{D_0}}{\partial a_\mathrm{w}}\frac{\partial a_\mathrm{w}}{\partial T_\mathrm{p}} + \frac{\partial C_{D_i}}{\partial \Delta C_L}\frac{\partial \Delta C_L}{\partial T_\mathrm{p}}. \tag{4-39b}$$

Computing the change of β_corr with respect to T_p is complicated, as β_corr is determined using a surrogate model based on experimental data. Still, from simulation it was found that changes of β_corr with respect to the propeller thrust T_p are negligibly small. Therefore, $\frac{\partial \beta_\mathrm{corr}}{\partial T_\mathrm{p}} \ll \frac{\partial a_\mathrm{w}}{\partial T_\mathrm{p}}$ so that the second component of Eq. (4-39a) is assumed to be zero. The partial derivatives are then defined as

$$\begin{aligned}\frac{\partial \Delta C_L}{\partial a_\mathrm{w}} &= \pi\beta_\mathrm{corr}\Delta Y\frac{\sin(\alpha+\alpha_\mathrm{p}) + 3\sin(\alpha-\alpha_\mathrm{p}) + 3a_\mathrm{w}\beta_\mathrm{corr}\sin(\alpha-2\alpha_\mathrm{p})}{\sqrt{{a_\mathrm{w}}^2\beta_\mathrm{corr}^2 + 2\cos(\alpha_\mathrm{p})a_\mathrm{w}\beta_\mathrm{corr} + 1}}\\ &+ \frac{4{a_\mathrm{w}}^2\beta^2\sin(\alpha-\alpha_\mathrm{p}) + 5a_\mathrm{w}\beta_\mathrm{corr}\sin(\alpha)}{\sqrt{{a_\mathrm{w}}^2\beta_\mathrm{corr}^2 + 2\cos(\alpha_\mathrm{p})a_\mathrm{w}\beta_\mathrm{corr} + 1}}\end{aligned}, \tag{4-40a}$$

$$\frac{\partial a_\mathrm{w}}{\partial T_\mathrm{p}} = \frac{2\left(\frac{x_\mathrm{p}/R_\mathrm{p}}{\sqrt{x_\mathrm{p}/{R_\mathrm{p}}^2+1}} + 1\right)}{{D_\mathrm{p}}^2 V_\infty^2\rho\pi\sqrt{\frac{8T_\mathrm{p}}{{D_\mathrm{p}}^2{V_\infty}^2\rho\pi}+1}}, \tag{4-40b}$$

$$\frac{\partial C_{D_0}}{\partial a_\mathrm{w}} = 2a_\mathrm{w}c_\mathrm{f}\Delta Y, \tag{4-40c}$$

$$\frac{\partial C_{D_i}}{\partial \Delta C_L} = \frac{2C_{L_\mathrm{ac}} + 2\Delta C_L}{Ae\pi}, \tag{4-40d}$$

and the partial derivative with respect to n_p is then found using

$$\frac{\partial \Delta C_L}{\partial n_\mathrm{p}} = \frac{\partial \Delta C_L}{\partial n_\mathrm{p}}\frac{\partial T_\mathrm{p}}{\partial n_\mathrm{p}}, \tag{4-41a}$$

$$\frac{\partial \Delta C_D}{\partial n_\mathrm{p}} = \frac{\partial \Delta C_D}{\partial n_\mathrm{p}}\frac{\partial T_\mathrm{p}}{\partial n_\mathrm{p}}. \tag{4-41b}$$

Rotating the local increase of lift and drag caused by the PAI effects then gives

$$\frac{\partial C_X}{\partial n_\mathrm{p}}(V_\infty, \rho, n_\mathrm{p}, \alpha, C_{L_\mathrm{ac}}, \beta_\mathrm{corr})_\mathrm{PAI} = -\frac{\partial \Delta C_D}{\partial n_\mathrm{p}} \tag{4-42a}$$

$$\frac{\partial C_Z}{\partial n_\mathrm{p}}(V_\infty, \rho, n_\mathrm{p}, \alpha, \beta_\mathrm{corr})_\mathrm{PAI} = -\cos(\mu)\frac{\partial \Delta C_{L_\mathrm{ac}}}{\partial n_\mathrm{p}} \tag{4-42b}$$

The local increase and lift ΔC_L and drag ΔC_D, also cause a moment around the x- and z-axis of the F_b frame. Rotating $\frac{\partial \Delta C_L}{\partial n_\text{p}}$ and $\frac{\partial \Delta C_L}{\partial n_\text{p}}$ to the F_b frame using $\mathbf{T}_\text{ba}$ Eq. (A-5) and multiplying with the distance from the CG then gives

$$\frac{\partial C_l}{n_\text{p}}(V_\infty, \rho, n_\text{p}, \alpha, \beta, C_{L_\text{ac}}, \beta_\text{corr})_\text{PAI} = \frac{y_\text{p}}{b}\left(-\frac{\partial \Delta C_L}{n_\text{p}}\cos(\alpha) - \frac{\partial \Delta C_D}{n_\text{p}}\sin(\alpha)\cos(\beta)\right) \quad \text{(4-43a)}$$

$$\frac{\partial C_n}{n_\text{p}}(V_\infty, \rho, n_\text{p}, \alpha, \beta, C_{L_\text{ac}}, \beta_\text{corr})_\text{PAI} = -\frac{y_\text{p}}{b}\left(\frac{\partial \Delta C_L}{n_\text{p}}\sin(\alpha) - \frac{\partial \Delta C_D}{n_\text{p}}\cos(\alpha)\cos(\beta)\right). \quad \text{(4-43b)}$$

Tip propeller wingtip vortex interaction

Another aspect to consider regarding the PAI effects, is the interaction of both outer propellers with the wing tip vortices as explained in Section 2-3-2. As can be seen in Eq. (2-31), the change in C_D for both the left and right tip is defined as

$$\Delta C_{D_\text{tipL}} = 0.5\frac{CL^2}{\pi A R e_L}, \quad \text{(4-44a)}$$

$$\Delta C_{D_\text{tipR}} = 0.5\frac{CL^2}{\pi A R e_R}. \quad \text{(4-44b)}$$

As for the previous derivations, the partial derivative with respect to n_p will need to be found. The derivative describing the tip interaction effect for the left wing tip and propeller (p_1) will be derived here. Note that the same method can be applied for the right wing tip and propeller (p_6). By applying the chain-rule, the partial derivative can be defined as

$$\frac{\partial \Delta C_{D_\text{tipL}}}{\partial n_{\text{p}_1}} = \frac{\partial \Delta C_{D_\text{tipL}}}{\partial e_\text{L}}\frac{\partial e_\text{L}}{\partial C_{T_\text{p1}}}\frac{\partial C_{T_\text{p1}}}{\partial n_\text{p1}}. \quad \text{(4-45)}$$

These partial derivatives are defined as

$$\frac{\partial \Delta C_{D_\text{tipL}}}{\partial e_\text{L}} = -0.5\frac{C_{L_\text{ac}}^2}{\pi A R e_L^2}, \quad \text{(4-46a)}$$

$$\frac{\partial e_\text{L}}{\partial C_{T_\text{p1}}} = 1.1991, \quad \text{(4-46b)}$$

$$\frac{\partial C_{T_\text{p1}}}{\partial n_\text{p1}} = -\frac{\partial C_{T_\text{p1}}(J)}{\partial J}\frac{V_\infty}{D_\text{p} n_\text{p}^2}, \quad \text{(4-46c)}$$

so that

$$\frac{\partial C_D}{\partial n_\text{p1}}(V_\infty, \rho, n_\text{p1}, e_\text{L}, C_{L_\text{ac}})_\text{PAITip} = \frac{\partial \Delta C_{D_\text{tipL}}}{\partial n_{\text{p}_1}}, \quad \text{(4-47a)}$$

$$\frac{\partial C_D}{\partial n_\text{p6}}(V_\infty, \rho, n_\text{p6}, e_\text{R}, C_{L_\text{ac}})_\text{PAITip} = \frac{\partial \Delta C_{D_\text{tipR}}}{\partial n_\text{p6}}. \quad \text{(4-47b)}$$

Note that if $C_{T_\text{p}} > 0.2669$, $\frac{\partial \Delta C_{D_\text{tip}}}{\partial n_\text{p}} = 0$ for that respective propeller, as otherwise the e values will get unrealistically high. This follows the definition of the tip vortex interaction effects given in Section 2-3-2.

Aileron tip propellers interaction

The final PAI effect to consider is the interaction between the outer propellers and the left and right aileron respectively. As discussed in Section 2-3-2, the tip propellers increase the slipstream velocity over the aileron, which increases their effectiveness as

$$l_{\delta_{\mathrm{a}}} = \frac{1}{2} C_{l_{\delta_{\mathrm{a}}}} \rho V_{\mathrm{a}}^2 S b \delta_{\mathrm{a}}, \tag{4-48}$$

where $V_{\mathrm{a}} > V_\infty$. The partial derivative with respect to n_{p} needs to be established to find the control effectiveness. As the formulas for the slipstream V_{a} are defined using T_{p}, first the partial derivative with respect to T_{p} is determined using

$$\frac{\partial l_{\delta_{\mathrm{a}}}}{\partial T_{\mathrm{p}}} = \frac{\partial l(\delta_{\mathrm{a}})}{\partial a_{\mathrm{a}}} \frac{\partial a_{\mathrm{a}}}{\partial T_{\mathrm{p}}} + \underbrace{\frac{\partial l(\delta_{\mathrm{a}})}{\partial \beta} \frac{\partial \beta_{\mathrm{corr}}}{\partial T_{\mathrm{p}}}}_{\approx 0}, \tag{4-49}$$

where the assumption $\frac{\partial \beta_{\mathrm{Corr}}}{T_{\mathrm{p}}} \ll \frac{\partial a_{\mathrm{a}}}{T_{\mathrm{p}}}$ is again applied. The partial derivatives are defined as

$$\frac{\partial l_{\delta_{\mathrm{a}}}}{\partial a_{\mathrm{a}}} = C_{l_{\delta_{\mathrm{a}}}} S {V_\infty}^2 b \beta_{\mathrm{corr}} \delta_{\mathrm{a}} \rho \left(a_{\mathrm{a}} \beta_{\mathrm{corr}} + 1 \right), \tag{4-50a}$$

$$\frac{\partial a_{\mathrm{a}}}{\partial T_{\mathrm{p}}} = \frac{2 \left(\frac{x_{\mathrm{a}}/R_{\mathrm{p}}}{\sqrt{x_{\mathrm{a}}/{R_{\mathrm{p}}}^2 + 1}} + 1 \right)}{{D_{\mathrm{p}}}^2 V_\infty^2 \rho \pi \sqrt{\frac{8 T_{\mathrm{p}}}{{D_{\mathrm{p}}}^2 {V_\infty}^2 \rho \pi} + 1}}. \tag{4-50b}$$

The control effectiveness with respect to n_{p} for the left and right aileron is then given as

$$\frac{\partial C_l}{\partial n_{\mathrm{p1}}} (V_\infty, \rho, n_{\mathrm{p1}}, \delta_{\mathrm{aL}}, \beta_{\mathrm{corr}})_{\mathrm{PAI}\delta_{\mathrm{aL}}} = \frac{1}{qSb} \frac{\partial l_{\delta_{\mathrm{aL}}}}{\partial T_{\mathrm{p1}}} \frac{T_{\mathrm{p1}}}{n_{\mathrm{p1}}}, \tag{4-51a}$$

$$\frac{\partial C_l}{\partial n_{\mathrm{p6}}} (V_\infty, \rho, n_{\mathrm{p6}}, \delta_{\mathrm{aR}}, \beta_{\mathrm{corr}})_{\mathrm{PAI}\delta_{\mathrm{aR}}} = \frac{1}{qSb} \frac{\partial l_{\delta_{\mathrm{aR}}}}{\partial T_{\mathrm{p6}}} \frac{T_{\mathrm{p6}}}{n_{\mathrm{p6}}}. \tag{4-51b}$$

As stated in Section 2-3-2, the increase in slipstream velocity also results in an increase in drag as

$$D_{\delta_{\mathrm{a}}} = \frac{1}{2} C_{D_{\delta_{\mathrm{a}}^2}} \rho V_{\mathrm{a}}^2 S \delta_{\mathrm{a}}^2, \tag{4-52}$$

where $V_{\mathrm{a}} > V_\infty$. Determining the partial derivative of this increase with respect to T_{p} gives

$$\frac{\partial D(\delta_{\mathrm{a}})}{\partial T_{\mathrm{p}}} = \frac{\partial D(\delta_{\mathrm{a}})}{\partial a_{\mathrm{a}}} \frac{\partial a_{\mathrm{a}}}{\partial T_{\mathrm{p}}} + \underbrace{\frac{\partial D(\delta_{\mathrm{a}})}{\partial \beta_{\mathrm{corr}}} \frac{\partial \beta_{\mathrm{corr}}}{\partial T_{\mathrm{p}}}}_{\approx 0}, \tag{4-53}$$

applying the same assumption that changes in β_{corr} are negligibly small. The partial derivative $\frac{\partial a_{\mathrm{a}}}{\partial T_{\mathrm{p}}}$ is given by Eq. (4-50b) and

$$\frac{\partial D_{\delta_{\mathrm{a}}}}{\partial a_{\mathrm{a}}} = C_{D_{{\delta_{\mathrm{a}}}^2}} S {V_\infty}^2 \beta_{\mathrm{corr}} {\delta_{\mathrm{a}}}^2 \rho \left(a_{\mathrm{a}} \beta_{\mathrm{corr}} + 1 \right). \tag{4-54}$$

The incremental increase in drag with respect to n_p for the left and right aileron is then given by

$$\frac{\partial C_D}{\partial n_{\mathrm{p1}}}(V_\infty, \rho, n_{\mathrm{p1}}, \delta_{\mathrm{aL}}, \beta_{\mathrm{corr}})_{\mathrm{PAI}\delta_{\mathrm{aL}}} = \frac{1}{qs}\frac{\partial D_{\delta_{\mathrm{aL}}}}{\partial T_{\mathrm{p1}}}\frac{T_{\mathrm{p1}}}{n_{\mathrm{p1}}}, \tag{4-55a}$$

$$\frac{\partial C_D}{\partial n_{\mathrm{p6}}}(V_\infty, \rho, n_{\mathrm{p6}}, \delta_{\mathrm{aR}}, \beta_{\mathrm{corr}})_{\mathrm{PAI}\delta_{\mathrm{aR}}} = \frac{1}{qs}\frac{\partial D_{\delta_{\mathrm{aR}}}}{\partial T_{\mathrm{p6}}}\frac{T_{\mathrm{p6}}}{n_{\mathrm{p6}}}. \tag{4-55b}$$

4-3-3 Control effectiveness

This section will summarize the control effectiveness of all control inputs in $\boldsymbol{u}$ defined in Eq. (4-24) for the control and moment vector $\Delta\boldsymbol{\tau}$ defined in Eq. (4-21). The effectiveness of all these control inputs, forms the control effectiveness matrix $\nabla_{\boldsymbol{u}}\boldsymbol{\Phi}(\boldsymbol{x}_0, \boldsymbol{u}_0)$ given in Eq. (4-23). This can be summarized as follows

$$\begin{aligned}\Delta\dot{V} = \frac{qS}{m}\Bigg(&-\frac{\partial C_D}{\partial\alpha}(\alpha)\Delta\alpha + \sum_{i=1}^{6}\frac{\partial C_X}{\partial n_{\mathrm{p_i}}}(V_\infty, \rho, n_{\mathrm{p_i}}, \alpha)_{\mathrm{thrust}}\Delta n_{\mathrm{p_i}} + \sum_{i=1}^{6}\frac{\partial C_X}{\partial n_{\mathrm{p_i}}}(V_\infty, \rho, n_{\mathrm{p_i}}, \alpha, C_{L_{\mathrm{ac}}}, \beta_{\mathrm{corr}})_{\mathrm{PAI}}\Delta n_{\mathrm{p_i}}\\ &-\frac{\partial C_D}{\partial n_{\mathrm{p1}}}(V_\infty, \rho, n_{\mathrm{p1}}, e_{\mathrm{L}}, C_{L_{\mathrm{ac}}})_{\mathrm{PAITip}}\Delta n_{\mathrm{p1}} - \frac{\partial C_D}{\partial n_{\mathrm{p6}}}(V_\infty, \rho, n_{\mathrm{p6}}, e_{\mathrm{R}}, C_{L_{\mathrm{ac}}})_{\mathrm{PAITip}}\Delta n_{\mathrm{p6}}\\ &-\frac{\partial C_D}{\partial n_{\mathrm{p1}}}(V_\infty, \rho, n_{\mathrm{p1}}, \delta_{\mathrm{aL}}, \beta_{\mathrm{corr}})_{\mathrm{PAI}\delta_{\mathrm{aL}}}\Delta n_{\mathrm{p1}} - \frac{\partial C_D}{\partial n_{\mathrm{p6}}}(V_\infty, \rho, n_{\mathrm{p6}}, \delta_{\mathrm{aR}}, \beta_{\mathrm{corr}})_{\mathrm{PAI}\delta_{\mathrm{aR}}}\Delta n_{\mathrm{p6}}\\ &-\frac{\partial C_D}{\partial\delta_{\mathrm{e}}}(\delta_{\mathrm{e}}, \alpha)\Delta\delta_{\mathrm{e}} - \frac{\partial C_D}{\partial\delta_{\mathrm{r}}}(\delta_{\mathrm{r}})\Delta\delta_{\mathrm{r}}\Bigg) - \frac{q_{\delta_{\mathrm{aL}}}S}{m}\frac{\partial C_D}{\partial\delta_{\mathrm{aL}}}(\delta_{\mathrm{aL}})\Delta\delta_{\mathrm{aL}} - \frac{q_{\delta_{\mathrm{aR}}}S}{m}\frac{\partial C_D}{\partial\delta_{\mathrm{aR}}}(\delta_{\mathrm{aR}})\Delta\delta_{\mathrm{aR}}\end{aligned}, \tag{4-56a}$$

$$\begin{aligned}\Delta\dot{\gamma} = \frac{qS}{mV}\Bigg(&\frac{\partial C_L}{\partial\alpha}(\alpha, \beta)\cos(\mu)\Delta\alpha - \sum_{i=1}^{6}\frac{\partial C_Z}{\partial n_{\mathrm{p_i}}}(V_\infty, \rho, n_{\mathrm{p_i}}, \alpha, \mu)_{\mathrm{thrust}}\Delta n_{\mathrm{p_i}}\\ &-\sum_{i=1}^{6}\frac{\partial C_Z}{\partial n_{\mathrm{p_i}}}(V_\infty, \rho, n_{\mathrm{p_i}}, \alpha, \beta_{\mathrm{corr}})_{\mathrm{PAI}}\Delta n_{\mathrm{p_i}} + \frac{\partial C_L}{\partial\delta_{\mathrm{e}}}\Delta\delta_{\mathrm{e}}\Bigg)\end{aligned}, \tag{4-56b}$$

$$\begin{aligned}\Delta l = qSb\Bigg(&\sum_{i=1}^{6}\frac{\partial C_l}{n_{\mathrm{p_i}}}(V_\infty, \rho, n_{\mathrm{p_i}}, \alpha, \beta, C_{L_{\mathrm{ac}}}, \beta_{\mathrm{corr}})_{\mathrm{PAI}}\Delta n_{\mathrm{p_i}} + \frac{\partial C_l}{\partial n_{\mathrm{p1}}}(V_\infty, \rho, n_{\mathrm{p1}}, \delta_{\mathrm{aL}}, \beta_{\mathrm{corr}})_{\mathrm{PAI}\delta_{\mathrm{aL}}}\Delta n_{\mathrm{p1}}\\ &+\frac{\partial C_l}{\partial n_{\mathrm{p6}}}(V_\infty, \rho, n_{\mathrm{p6}}, \delta_{\mathrm{aR}}, \beta_{\mathrm{corr}})_{\mathrm{PAI}\delta_{\mathrm{aR}}}\Delta n_{\mathrm{p6}} + \frac{\partial C_l}{\partial\delta_{\mathrm{r}}}\Delta\delta_{\mathrm{r}}\Bigg) + q_{\delta_{\mathrm{aL}}}Sb\frac{\partial C_l}{\partial\delta_{\mathrm{aL}}}\Delta\delta_{\mathrm{aL}} + q_{\delta_{\mathrm{aR}}}Sb\frac{\partial C_l}{\partial\delta_{\mathrm{aR}}}\Delta\delta_{\mathrm{aR}}\end{aligned}, \tag{4-56c}$$

$$\Delta m = qS\bar{c}\left(\frac{\partial C_m}{\partial\alpha}(\alpha, \beta)\Delta\alpha + \frac{\partial C_m}{\partial\delta_{\mathrm{e}}}\Delta\delta_{\mathrm{e}} + \frac{\partial C_m}{\partial\delta_{\mathrm{r}}}(\delta_{\mathrm{r}})\Delta\delta_{\mathrm{r}}\right), \tag{4-56d}$$

$$\begin{aligned}\Delta n = qSb\Bigg(&\sum_{i=1}^{6}\frac{\partial C_n}{\partial n_{\mathrm{p_i}}}(V_\infty, \rho, n_{\mathrm{p_i}})_{\mathrm{thrust}}\Delta n_{\mathrm{p_i}} + \sum_{i=1}^{6}\frac{\partial C_n}{n_{\mathrm{p_i}}}(V_\infty, \rho, n_{\mathrm{p_i}}, \alpha, \beta, C_{L_{\mathrm{ac}}}, \beta_{\mathrm{corr}})_{\mathrm{PAI}}\Delta n_{\mathrm{p_i}}\\ &+\frac{\partial C_n}{\delta_{\mathrm{r}}}\Delta\delta_{\mathrm{r}}\Bigg) + q_{\delta_{\mathrm{aL}}}Sb\frac{\partial C_n}{\partial\delta_{\mathrm{aL}}}\Delta\delta_{\mathrm{aL}} + q_{\delta_{\mathrm{aR}}}Sb\frac{\partial C_n}{\partial\delta_{\mathrm{aR}}}\Delta\delta_{\mathrm{aR}}\end{aligned}. \tag{4-56e}$$

In these equations $q_{\delta_{\mathrm{aL}}}$ and $q_{\delta_{\mathrm{aR}}}$ represent the dynamic pressure at the left and right aileron respectively. Note that this is higher than q because of the slipstream velocity increase behind the wing tip propellers. Furthermore, all control derivatives with functions parameters are nonlinear, which can be taken into account as the control effectiveness is defined incrementally.

4-4 Model predictive control (MPC) for actuator dynamics

A limitation of the INCA method is that the combination of rate constraints with actuator dynamics leads to an over-conservative controller. The rate constraints set a bound on the maximum $\Delta \boldsymbol{u}$ computed by the INCA controller. When the actuator dynamics are combined with the INCA controller, a problem presents itself. As the actuator dynamics damp out the commanded control input $\boldsymbol{u}_\mathrm{c}$, the commanded incremental control input $\Delta \boldsymbol{u}_\mathrm{c}$ is not equal to the actual $\Delta \boldsymbol{u}_\mathrm{a}$. As a consequence, $\Delta \boldsymbol{u}_\mathrm{a} < \Delta \boldsymbol{u}_\mathrm{c}$ which makes the controller over-conservative. This effect is illustrated in Figure 4-1a, where the commanded and actual $\Delta\delta_{\mathrm{aL}}$ for a sequence of reference inputs on the roll angle ϕ of $0°$, $35°$, $-35°, 0°$ is given.

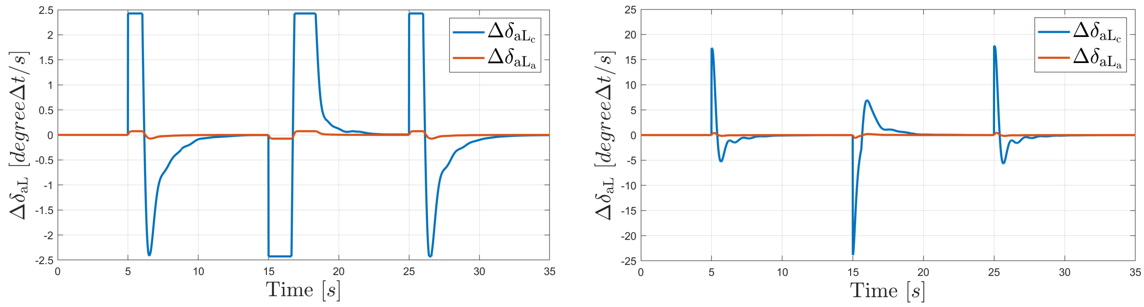

(a) δ_{aL} with rate constraints.

(b) δ_{aL} without rate constraints.

Figure 4-1: Incremental commanded and actual δ_{aL}, where for removing the rate constraint δ_{aL} becomes significantly higher.

As one can see in Figure 4-1a, the actual $\Delta \boldsymbol{u}_\mathrm{a}$ is much lower than the commanded $\Delta \boldsymbol{u}_\mathrm{c}$. This is caused by the actuator dynamics that are between these two signals. Looking at the DEP aircraft, this mismatch has two consequences. Firstly, the full potential of the DEP aircraft is not used as the achieved control inputs $\boldsymbol{u}_\mathrm{a}$ are lower. Secondly, as the achieved and commanded $\Delta \boldsymbol{u}$ differ that much, the power optimization will also have a decrease in performance. The INCA controller assumes that the commanded $\Delta \boldsymbol{u}_\mathrm{c}$ is achieved, so that the control allocation is optimized for efficiency. Still, if the actual allocation differs from the one commanded due to the actuator dynamics, the actual increase in efficiency will be less.

A common solution for this problem is removing the rate constraints. This makes the controller less conservative, as $\Delta \boldsymbol{u}_\mathrm{c}$ will increase so that $\Delta \boldsymbol{u}_\mathrm{a}$ also increases. An analysis in simulation is then required to see whether the actuators do not saturate for their maximum rate. For removing the constraints, the commanded and actual $\Delta\delta_{\mathrm{aL}}$ is shown in Figure 4-1b. As one can see, by removing the rate constraint, $\Delta\delta_{\mathrm{aL_c}}$ can be increased significantly. Thereby, $\Delta\delta_{\mathrm{aL_a}}$ is increased so the δ_{aL} deflection is larger. Note that the actuator dynamics are still in the simulation, so that the achieved control inputs are feasible. Still, there is a large mismatch between the commanded and achieved $\Delta \boldsymbol{u}$, which is also present for the other control inputs. This mismatch means that the achieved control distribution is different from the one determined by the INCA controller, which has two consequences. Firstly, when the gains of the controller are further increased, producing faster response times, the allocation error causes deterioration in terms of tracking performance. Secondly, as stated before, the power optimization still decreases in performance because of the mismatch in allocation. The hypotheses stated in Chapter 1 in terms of increase in tracking performance and efficiency, will thus only be partly fulfilled and the complete potential of the DEP aircraft is thus clearly not used.

This thesis, therefore, proposes a method to compensate for the actuator dynamics, so that the commanded control input $\Delta \boldsymbol{u}_{\mathrm{c}}$ equals the achieved $\Delta \boldsymbol{u}_{\mathrm{a}}$. For this, an MPC controller is used which is based on the method in [36]. In this research, the actuator dynamics are also compensated using MPC. This controller is redefined, so that it can compensate for incremental control inputs, using $\Delta \boldsymbol{u}_{\mathrm{c}}$ determined by the INCA controller as the reference. The concept of MPC is introduced in the Section 4-4-1 and implementation of this controller to the INCA framework in Section 4-4-2.

4-4-1 General formulation MPC controller

The method of MPC is based on optimal control methods as Linear-quadratic regulator (LQR), where the control input $\boldsymbol{u}$ is calculated using an optimization function. The main advantage of MPC is that state-, input- and output constraints can be incorporated. Using these constraints to compensate for the actuator dynamics, actuator saturation can be prevented. Also non-linear dynamics can be taken into account, because of the finite horizon used in the optimization problem [65]. The system controlled with MPC is generally modeled as a discrete state-space, which in the most general form is defined as

$$\boldsymbol{x}(k+1) = \boldsymbol{f}\left(\boldsymbol{x}(k), \boldsymbol{u}(k), \boldsymbol{w}(k), k\right), \tag{4-57a}$$

$$\boldsymbol{y}(k) = \boldsymbol{h}\left(\boldsymbol{x}(k), \boldsymbol{u}(k), \boldsymbol{v}(k), k\right), \tag{4-57b}$$

where $\boldsymbol{x} \in \mathbb{R}^n$ is the state vector, $\boldsymbol{u} \in \mathbb{R}^p$ the input vector, $\boldsymbol{y} \in \mathbb{R}^m$ the output vector, $\boldsymbol{w} \in \mathbb{R}^n$ the process noise vector and $\boldsymbol{v} \in \mathbb{R}^m$ the measurement noise vector.

The control law for MPC is obtained by minimizing an optimization problem for the control input $\boldsymbol{u}$. The generic formal definition of this control law is given in Appendix B-4 [66]. It is usually expressed in a quadratic form where for reference tracking the error between the reference signal and predicted output signal is minimized as

$$J(N_{\mathrm{p}}, N_{\mathrm{c}}, k) = \sum_{j=1}^{N_{\mathrm{p}}} \left|\mathbf{Q}(\hat{\boldsymbol{y}}(k+j|t) - \boldsymbol{r}(k+j))\right|^2 + \sum_{j=1}^{N_{\mathrm{u}}} \left|\mathbf{R}(\boldsymbol{u}(k+j) - \boldsymbol{u}_{\mathrm{nom}}(k+j))\right|^2, \tag{4-58}$$

where $\mathbf{Q}$ and $\mathbf{R}$ are weighting matrices putting more emphasis on either the tracking of the reference or the control activity. N_{p} is the prediction horizon and N_{c} the control horizon. These values give the number of intervals over which MPC controller evaluates its tracking error and over which it changes the control input respectively. Implementing with finite N, where $N_{\mathrm{u}} \leq N_{\mathrm{p}}$, gives a receding horizon, where a new $\boldsymbol{u}$ is calculated and implemented at each time step. Using this approach, possible mismatches between the predicted and real output due to modeling errors and external disturbances can be compensated for [67]. The nominal control input is defined as $\boldsymbol{u}_{\mathrm{nom}}$. If the control inputs are not to be penalized, $\mathbf{R}$ can be set equal to zero, so that only the error with respect to the reference trajectory is minimized. In the implementation of the MPC controller, discussed in the next section, the objective function defined in Eq. (4-58) is used for a Single-input single-output (SISO) system. This means that the matrices and vectors in this objective function become scalars. Also, $R = 0$, as the MPC controller will only optimize for the reference values.

An important aspect to consider is that for optimization of the objective function, the MPC controller needs to know all states of the system. As all actuators are modeled as a second-order system, these states are the control input u and control input rate $\dot{u}$. In this thesis, it is assumed that only the control input can be measured, so that $y = u$. As stated in Eq. (4-57), this measurement is subject to both process noise $\boldsymbol{w}$ and measurement noise v. Therefore, a state-estimator is required, for which for example an asymptotic observer can be used. Note, that this observer does not take into account process and measurement noise. A more applicable method is therefore the Kalman filter (KF). This is a recursive filter that gives an unbiased minimum variance estimate of a linear dynamic system [68]. For this filter, it is assumed that the process and measurement noise are modeled as a Gaussian distribution. Another assumption is that the filter is a first-order Markov process. For such a process, it is stated that the conditional probability density function of the current state, given the previous state, only depends on this previous state on not on earlier state measurements [69]. The filter is defined in two steps: the time-update and measurement-update step. In the first step, the current state is predicted, based on the state estimate of the previous time step. In the measurement update-step, this estimate is combined with the current measurement to improve this state estimate. Weighting matrices are defined to characterize the process and measurement noise, thereby giving more relative importance to either the time-update or measurement-update step.

The KF can be extended to the Extended Kalman filter (EKF) for nonlinear systems, where the system is linearized locally in each time step [70]. The Iterated extended Kalman filter (IEKF) develops this algorithm by iterating on the linearization to give an improved estimate of the state [71]. As discussed in the next section, for this thesis it is assumed that the actuator dynamics can be modeled as an LTI system so that the standard KF, with a stationary Kalman gain, can be used [68]. The innovation predictor model to estimate the states for an LTI SISO system is then given as [72]

$$\hat{\boldsymbol{x}}(k+1) = \mathbf{A}\hat{\boldsymbol{x}}(k) + \boldsymbol{B}u(k) + \mathbf{K}\left(y(k) - \boldsymbol{C}\hat{\boldsymbol{x}}(k)\right), \tag{4-59a}$$

$$\hat{y}(k) = \boldsymbol{C}\hat{\boldsymbol{x}}(k), \tag{4-59b}$$

which is asymptotically stable if the Kalman gain $\mathbf{K}$ is computed from the positive-definite solution of the Discrete-time algebraic Riccati equation (DARE). Derivation of the stationary solution for the LTI system Kalman filter problem is given in Appendix B-3.

The combination of MPC with the KF gives a promising framework for compensation of actuator dynamics. As constraints can be incorporated, actuator saturation can be prevented which would lead to deterioration of the control performance. Also, as the MPC and KF methods can be extended to work with nonlinear dynamics, the approach can be applied to nonlinear actuator dynamics for future research. Finally, as the KF takes into account both process and measurement noise, this makes the compensation method more robust. The implementation of the compensation method for the DEP aircraft is discussed in the next section.

4-4-2 Incremental actuator dynamics compensation using MPC

For implementation of MPC for incremental control inputs, the transfer function from $\Delta \boldsymbol{u}_{\mathrm{a}}$ to $\boldsymbol{u}_{\mathrm{a}}$ needs to be found. This is shown in the box with the dashed line in Figure 4-2. For the generic transfer actuator dynamics transfer function $A(s)$, the closed loop transfer function is defined as

$$\frac{u_{\mathrm{a}}(s)}{\Delta u_{\mathrm{a}}(s)} = H_{\mathrm{ac}}(s) = \frac{A(s)}{1 - A(s)}, \tag{4-60}$$

where the actuator dynamics for all control inputs u are modeled as second order systems. By canceling out pole-zero pairs, the transfer function $H_{\mathrm{ac}}(s)$ remains a second order system. To implement this in the MPC controller, the system was discretized using Zero-order hold (ZOH) and transformed into a state space representation. For the generic actuator ac, this gives the following discrete state space.

$$\begin{bmatrix} x_1(k+1) \\ x_2(k+1) \end{bmatrix} = A_{\mathrm{ac}} \begin{bmatrix} x_1(k) \\ x_2(k) \end{bmatrix} + B_{\mathrm{ac}} \Delta u_{\mathrm{a}}, \tag{4-61a}$$

$$u_{\mathrm{a}} = C_{ac} \begin{bmatrix} x_1(k) \\ x_2(k) \end{bmatrix}. \tag{4-61b}$$

The reference signal send to the MPC controller is $\boldsymbol{u}_{\mathrm{c}} = \boldsymbol{u}_{\mathrm{a}} + \Delta \boldsymbol{u}_{\mathrm{c}}$, which is the sum of the current actual control input and the incremental control input command of the INCA controller respectively. The MPC controller then aims to minimize the error between $\boldsymbol{u}_{\mathrm{c}}$ and $\boldsymbol{u}_{\mathrm{a}}$, so that the commanded control inputs by the INCA controller are actually achieved. As stated in the previous section, MPC depends on two parameters regarding the time horizons, namely the prediction horizon N_{p} and control horizon N_{c}. The control horizon was set to $N_{\mathrm{u}} = 1$, as the desired reference should be reached as fast as possible. The prediction horizon was to $N_{\mathrm{p}} = 3$, which results in a fast response with feasible $\Delta \boldsymbol{u}_{\mathrm{a}}$ and minimal computational effort. The full MPC control loop is shown in Fig. 4-2. The triangle gain block in this figure represent extension of the signals over the prediction horizon N_{p} into matrices. In these matrices, each row represents a control input and each column the value of this control input at t up to and including $t + N_{\mathrm{p}}\Delta t$. These matrices for $N_{\mathrm{p}} = 3$ are thus defined as

$$\Delta \mathbf{u}_{\mathrm{c}} = \begin{bmatrix} \Delta \boldsymbol{u}_{\mathrm{c}} & 2\Delta \boldsymbol{u}_{\mathrm{c}} & 3\Delta \boldsymbol{u}_{\mathrm{c}} \end{bmatrix}, \tag{4-62a}$$

$$\mathbf{u}_{\mathrm{c}} = \begin{bmatrix} \boldsymbol{u}_{\mathrm{c}} & \boldsymbol{u}_{\mathrm{c}} & \boldsymbol{u}_{\mathrm{c}} \end{bmatrix}, \tag{4-62b}$$

where the incremental control input $\Delta \boldsymbol{u}_{\mathrm{c}}$ is thus added over the control horizon N_{P}.

For the tuning weights, as the value of $\Delta \boldsymbol{u}_{\mathrm{a}}$ should not be penalized, the weight on the control inputs was set equal to $\mathbf{R} = 0$. Leaving the weight $\mathbf{Q} = 1$, the default value, gives satisfactory tracking performance. In the MPC control loop Figure 4-2, a Kalman filter is placed so that the states $\boldsymbol{u}$ and $\dot{\boldsymbol{u}}$ can be estimated while being subject to process and measurement noise, as discussed in the previous section. It was assumed that $\boldsymbol{w}(k)$ and $\boldsymbol{v}(k)$ are uncorrelated zero-mean white noise with variance one. Constraints were implemented on the output of the MPC controller $\boldsymbol{y} = \boldsymbol{u}_{\mathrm{a}}$, so that

$$\underline{\boldsymbol{u}} \leq \boldsymbol{u}_{\mathrm{a}} \leq \overline{\boldsymbol{u}}. \tag{4-63}$$

This formulation ensures that the control inputs will not saturate. The constraints were softened so that a feasible solution is found, even if the actuators are subject to disturbances.

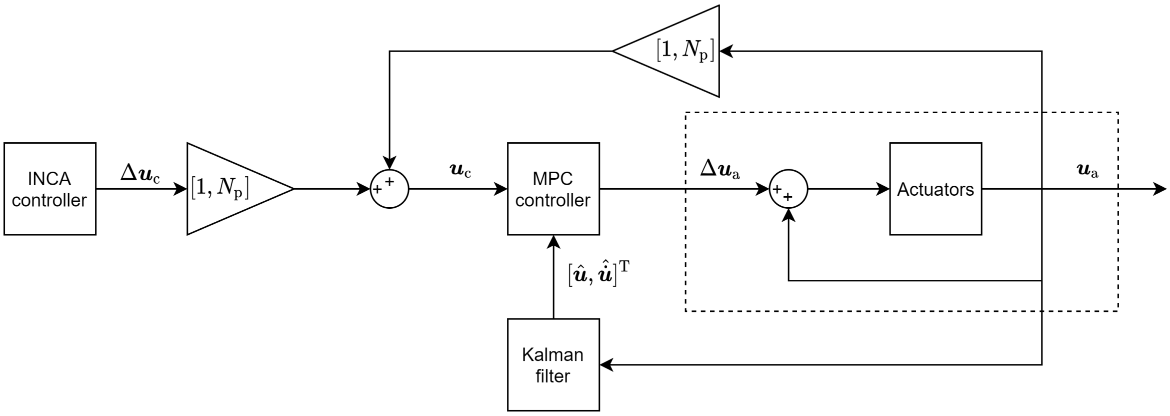

Figure 4-2: Controller structure for of MPC for actuator dynamics compensation. The closed loop transfer function of the actuator is given in the dashed line block.

Note, that these disturbances were not modeled in the simulation but will be present in reality. The MPC controller was implemented using the `mpc` function in MATLAB. For full documentation of this function, the reader is referred to [73].

For the same reference signal on ϕ as introduced at the beginning of this section, the commanded and actual incremental control input of the left aileron $\Delta\delta_{\mathrm{aL}}$ is shown in Figure 4-3 together with the roll angle ϕ. Note that the MPC controller is now implemented, so that the commanded and actual control input are very similar. When comparing Figure 4-3a with Figure 4-1a, one can see that the commanded values are the same, but these are now achieved. The commanded deflections are much shorter, as the achieved deflection is now larger and can thus be shorter while achieving the required roll moment. This means that the incremental control inputs calculated by the INCA controller are now actually achieved, which was the objective of the MPC controller design.

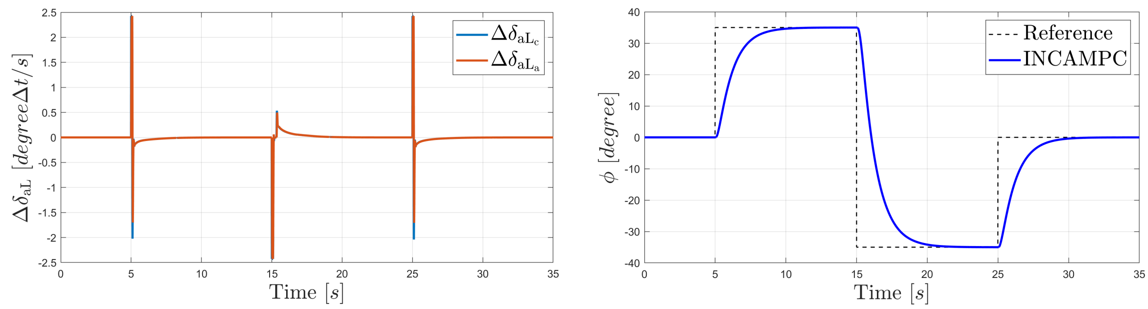

(a) Incremental commanded and actual δ_{aL}.

(b) Roll angle ϕ with the reference signal.

Figure 4-3: The incremental aileron deflection and roll angle with MPC controller to compensate for the actuator dynamics.

The effect of this solution regarding tracking performance and power optimization will be shown in Chapter 5. Note that an important limitation of the proposed method is that it is sensitive to delays of state measurements, so that the filtering techniques proposed in Section 3-5-1 cannot be implemented. For the MPC method, it is assumed that the state derivative vector $\dot{\boldsymbol{y}} = \begin{bmatrix} \dot{V} & \dot{\gamma} & \dot{p} & \dot{q} & \dot{r} \end{bmatrix}^T$ can be measured directly. Improvement of the performance of INDI with direct angular accelerometer feedback was shown in [74]. It is realized that this assumption makes the implementation of this method more difficult. Still, it was decided that this method forms the framework for the research of increasing controller potential for DEP. Possible future improvements can make the proposed method better suited for implementation.

4-5 Conclusions

This chapter derived the INCA controller for the DEP aircraft. Starting from the general allocation problem, it was shown that this most efficiently can be solved using a linear mixed optimization QP problem, where actuator constraints can be taken into account. As this method cannot take into account nonlinearities and effector interactions, which are present for the DEP aircraft, the control allocation problem was redefined incrementally. This gives the INCA controller, which can solve the allocation problem including nonlinearities and effector interactions online defined as an efficient QP problem. The INCA controller was then formulated so that it can control both translation and rotation and the secondary objective was reformulated to represent the power consumption of the propellers. This allows using the INCA controller to optimize for efficiency. Also, a method was proposed for FTC in combination with INCA. This should make the controller more robust for propeller failure. The control effectiveness of the differential thrust and PAI effects was found with partial derivatives, so that these effects can be used actively for control. Finally, an MPC controller was designed which allows compensating for the actuator dynamics while satisfying actuator constraints. Implementing this compensation method should result in better tracking and efficiency for which the results will be shown in the next chapter.

Chapter 5

Simulation results

This chapter shows the results for the different controllers designed in the preceding chapters. These controllers are compared against the baseline INDI controller with outer loop translational and inner loop rotational control. Firstly, this chapter introduces the simulation framework, specifying the different controllers, the reference trajectory, a method for introducing modeling uncertainty and the performance metrics used to quantify controller performance. After this, the INCA controller including differential thrust and PAI effects will be compared against the baseline INDI controller in terms of tracking both for a low and high set of gains. Furthermore, the performance of the INCA controller concerning minimizing power consumption is evaluated. Modeling errors will be introduced to analyze the robustness of the controller in terms of tracking and power optimization. Next to that, robustness with respect to propeller failure and external disturbances will be analyzed. Finally, this chapter will conclude with final remarks regarding the performance of the different controllers.

5-1 Simulation setup

As described in Chapter 2, the simulations were run in the MATLAB and SIMULINK framework. In SIMULINK, the DEP SFD model including the EoM and aerodynamic and control model was implemented. This simulation was then used to analyze the performance of different controllers for the reference trajectory. The subsequent subsections discuss how this simulation framework was set up and what methods were used to quantify the performance of the controllers.

5-1-1 Types of controllers

Different controllers were realized in the simulation environment to test their performance. A summary of these controllers is given in the table below.

Table 5-1: Types of controllers used in the simulation.

Controller	Gains		Secondary objective	
	Low	High	Control preference $\boldsymbol{u}_\mathrm{p}$	Propeller power $\boldsymbol{P}_\mathrm{p}$
1. INDI low	x		n.a.	
2. INDI high		x	n.a.	
3. INCA low	x		x	
4. INCA high		x	x	
5. INCA MPC high		x	x	
6. INCA power	x			x
7. INCA power MPC	x			x

The baseline INDI controllers (1,2) refer to the controller developed in Section 3-4, where an inner loop for rotational and outer loop for translational control is used. The INCA controllers of (3,4,5) refer to the controller developed in Section 4-2-2 with control preference vector $\boldsymbol{u}_\mathrm{p}$ as secondary objective. The INCA Power controllers (6,7) refer to the controller developed in Section 4-2-3 where the secondary objective is changed to the propeller power $\boldsymbol{P}_\mathrm{p}$. For the controllers including MPC (5,7), the method discussed in Section 4-4 is added to increase performance either for tracking (5) or power optimization (7). For the INCA controllers without MPC (3,4 and 7), the rate constraints are not included as the controller will otherwise be over-conservative. Note that only the low gains are used for power optimization as optimizing for power is not valuable when controlling the DEP aircraft at the limits of its control authority. The low and high set of gains used for the different controllers are given in Table B-1 in Appendix B. These gains are the proportional gains discussed in Section 3-4 for the different control loops.

5-1-2 Reference trajectory

In almost all simulations the same reference trajectory is used, so that they can be compared. This reference trajectory is specified with the following vector

$$\boldsymbol{y}_\mathrm{ref} = \begin{bmatrix} h_\mathrm{ref} & V_\mathrm{ref} & \phi_\mathrm{ref} & \beta_\mathrm{ref} \end{bmatrix}^\mathrm{T}. \tag{5-1}$$

For this vector, the $\boldsymbol{y}_\mathrm{ref}$ vector was set equal to $h_\mathrm{ref} = 300\ m$ for the altitude, $V_\mathrm{ref} = 45\ m/s$ for the velocity, $\phi_\mathrm{ref} = 0°, 35°, -35°, 0°$ for the roll angle and $\beta_\mathrm{ref} = 0°$ for the sideslip angle. Note that the reference on the roll angle is thus a square wave signal, so that the roll angle changes throughout the simulation. Using this reference signal allows showing how the DEP aircraft uses the control surfaces, differential thrust and PAI effects to control the attitude of the aircraft while maintaining constant velocity, altitude and minimizing the sideslip angle. The roll angle was determined for a rate 1-turn, scaled to the SFD with the scale factor n as determined in Table 2-2. A rate 1-turn is specified as a turn of 180° in 60 s which by scaling for the SFD gives a turn in approximately 20.6 s, so that for a coordinated turn at $V = 45\ m/s$ a roll angle of approximately 35° is required.

For one simulation, to show controller performance for changing operating conditions, also h_ref and V_ref will be changed. In this simulation, a reference step of 300 m on h and 45 m/s on V will be applied starting from $h_\mathrm{init} = 100\ m$ and $V_\mathrm{init} = 40\ m/s$. This gives a climbing and accelerating reference trajectory. After these values are reached, h_{ref} is increased to 500 m and V_{ref} to 55 m/s with $\phi_{\text{ref}} = 35°$. This gives a climbing and accelerating spiral motion. Using this reference, a larger space of the flight envelope is reached, showing the capabilities of using a nonlinear controller.

5-1-3 Modeling uncertainty

As discussed several times throughout this thesis, robustness for modeling errors is important, especially considering the PAI effects. Therefore, different modeling errors of different quantities will be introduced to analyze robustness for tracking performance, allocation error and optimization for efficiency.

Uncertainty can be introduced both by scaling and introducing an offset so that

$$\nabla_{\boldsymbol{u}} \hat{\boldsymbol{\Phi}}(\boldsymbol{x}_0, \boldsymbol{u}_0) = k_{\text{offset}} \nabla_{\boldsymbol{u}} \boldsymbol{\Phi}_{\max} + k_{\text{scale}} \nabla_{\boldsymbol{u}} \boldsymbol{\Phi}(\boldsymbol{x}_0, \boldsymbol{u}_0), \tag{5-2}$$

where $\nabla_{\boldsymbol{u}} \boldsymbol{\Phi}_{\max}$ contains the maximum values of the relevant control effectiveness factors over the reference trajectory specified in Section 5-1-2. The factors k_{offset} and k_{scale} represent the scaling factors introduced, which will be varied so that performance against different levels of uncertainty can be checked. Note that Eq. (5-2) is a general formula, and only specific parts of the control effectiveness matrix will be changed.

5-1-4 Performance metrics

To quantitatively analyze the performance of the different controllers, different metrics were defined. These performance parameters include:

- Tracking error $\boldsymbol{\epsilon}_{\text{track}} = \boldsymbol{y}_{\text{ref}} - \boldsymbol{y}$
- Allocation error $\boldsymbol{\epsilon}_{\text{alloc}} = \boldsymbol{\tau}_{\text{c}} - \boldsymbol{\tau}$
- Power consumption $P, E = \int P dt$

The tracking error will be quantified for all controlled states, which were defined as

$$\bar{\boldsymbol{x}}_1 = \begin{bmatrix} V & \gamma \end{bmatrix}^{\text{T}}, \tag{5-3a}$$

$$\boldsymbol{x}_2 = \begin{bmatrix} \phi & \alpha & \beta \end{bmatrix}^{\text{T}}, \tag{5-3b}$$

$$\boldsymbol{x}_3 = \begin{bmatrix} p & q & r \end{bmatrix}^{\text{T}}. \tag{5-3c}$$

The allocation error will be defined for the controlled moments around the aircraft, where

$$\boldsymbol{\tau}_{\text{c}} = \begin{bmatrix} l & m & m \end{bmatrix}^{\text{T}}. \tag{5-4}$$

To quantify these errors, the Root-mean-square error (RMSE) is used, which is defined as

$$y_{\text{RMSE}} = \sqrt{\frac{1}{N} \sum_{k=1}^{N} (y_k - y_{k,\text{ref}})^2}. \tag{5-5}$$

The power consumption is defined as the total W consumed by the propellers. This can be defined as $P = |\boldsymbol{P}_\mathrm{p}|_1$ or $P = |\boldsymbol{P}_\mathrm{p}|_2$, using the one- or two-norm respectively. This can be integrated to give the total energy consumed in J for a defined reference trajectory.

Furthermore, for a reference step input of $\phi_\mathrm{ref} = 35°$ on the roll angle, the following characteristics will be analyzed.

- Rise time, defined as the times it takes to go from 5% to 95% of the response.
- Overshoot, defined as the percentage the peak of the response gets higher than the reference.

In finding the gains, as given in Table B-1, there is a trade-off between these values. Increasing the gains gives a faster response time and thus less rise time. Still, if the gains are increased too much, the response will overshoot compared to its reference value. Generally, for tuning the highest set of gains without overshoot was found.

Finally, a look was taken into the bode magnitude plot of the DEP aircraft with either the INDI or INCA controller for $\phi_\mathrm{ref} \rightarrow \phi$. This allows quantifying how the aircraft will follow reference signals on ϕ_ref in the frequency domain. Note that as the system is nonlinear, the Bode magnitude plot does not only depend on the frequency but also on the amplitude of the reference signal. As stated in [75], it is difficult to find the frequency response function for nonlinear systems analytically, but it can be found from simulation. Therefore, the amplification gain will be checked in simulation for different frequencies, thereby forming the Bode magnitude plot. Note that the system should be uniformly convergent, which means that for a bounded input, the states are bounded with a unique steady-state solution. It was, therefore, checked in simulation whether the states stay bounded for the range of frequencies of ϕ_ref when implementing this method.

5-2 INCA with control preference vector

The first set of simulations that was run, analyzed the performance of the INCA controller with the control preference vector $\boldsymbol{u}_\mathrm{p}$. The performance of this controller was tested against the baseline controller, looking at the tracking performance for the reference signal. The next subsection discusses these results for the low set of proportional gains and the subsection thereafter for the high set of proportional gains.

5-2-1 Low proportional gains

As a first analysis, the performance of the INCA controller with $\boldsymbol{u}_\mathrm{p}$ was evaluated against the performance of the baseline INDI controller with the low set of proportional gains. These are thus controller 3 and 1 in Table 5-1 respectively. The purpose of this simulation was to show how the differential thrust and PAI effect can be used by the INCA controller, achieving at least similar tracking performance compared to the baseline INDI controller.

The gains of this INDI controller were tuned, so that the rise time and overshoot are minimized. The gains for the INCA controller were then tuned so that similar performance with

Table 5-2: Rise time and overshoot for controllers with low gains.

Controller	INDI low (1)	INCA low (3)
Rise time $[s]$	2.4618	2.3530
Overshoot $[\%]$	0.5610	0.4093

respect to rise time and overshoot was achieved. The values for these criteria are given in the table below, where it can be seen that they are very similar.

The responses of the reference values are given in Figure 5-1 and Figure 5-2. As can be seen in Figure 5-1a, the reference trajectory for ϕ is followed with minimal overshoot for both controllers. Also, the sideslip angle β is kept close to zero, as can be seen in Figure 5-1b. Interesting to note is that the altitude is more closely followed by the INCA than the INDI controller, as can be seen in Figure 5-2a. This is a result of the merged translational and rotational control loop, as discussed in Section 3-6. As these are controlled simultaneously, this leads to better performance in translational control, particularly considering the altitude. This effect can also be seen in the subsequent sections, when comparing an INCA controller with the baseline INDI.

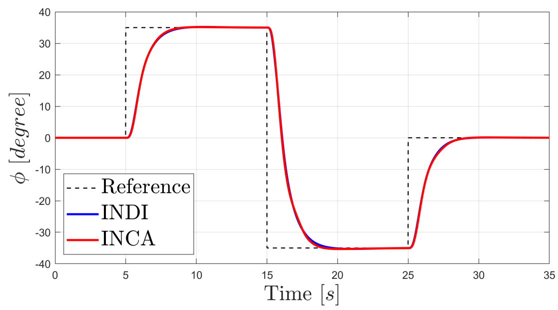

(a) Roll angle ϕ response, with the reference signal.

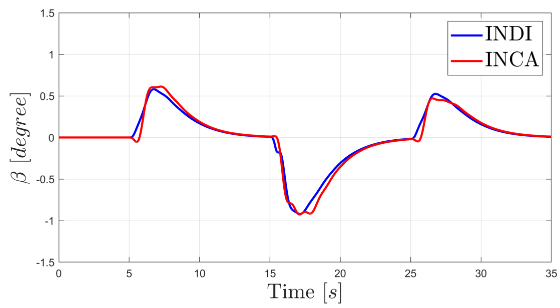

(b) Sideslip angle β response, where $\beta_{\text{ref}} = 0°$.

Figure 5-1: Time responses of the roll and sideslip angle for the INDI (1) and INCA (3) controller with low gains.

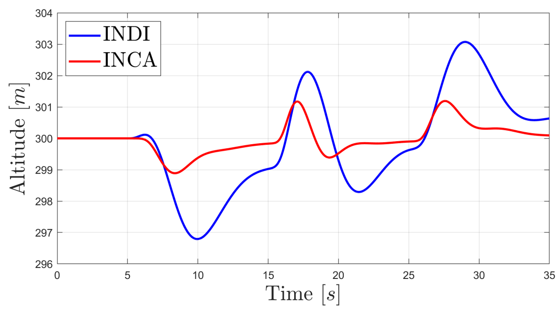

(a) Altitude h response, where $h_{\text{ref}} = 300\ m$.

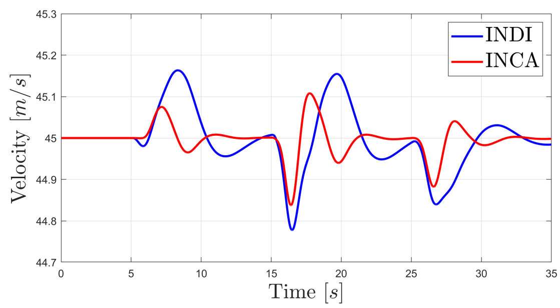

(b) Velocity V response, where $V_{\text{ref}} = 45\ m/s$.

Figure 5-2: Time responses of the altitude and velocity for the INDI (1) and INCA controller (3) with low proportional gains.

The simulation results were quantified using the RMSE values for the different controlled states. These values are given in the table below.

Table 5-3: Tracking performance $\boldsymbol{x}_1$.

RMSE($\epsilon_{\text{track}}(\boldsymbol{x}_1)$)		
Controller	INDI	INCA
V $[m/s]$	0.086	0.046
h $[m]$	1.690	0.530

Table 5-4: Tracking performance $\boldsymbol{x}_2$.

RMSE($\epsilon_{\text{track}}(\boldsymbol{x}_2)$)		
Controller	INDI	INCA
ϕ [°]	13.40	13.41
α [°]	0.808	0.630
β [°]	0.318	0.334
Total	7.750	7.751

Table 5-5: Tracking performance $\boldsymbol{x}_3$.

RMSE($\epsilon_{\text{track}}(\boldsymbol{x}_3)$)		
Controller	INDI	INCA
p [°$/s$]	0.142	0.134
q [°$/s$]	0.125	0.788
r [°$/s$]	0.006	0.009
Total	0.109	0.462

Here it is confirmed again that performance is comparable, where two results stand out. Firstly, the RMSE value for h in Table 5-3 is significantly lower for the INCA controller than for the INDI controller, confirming that tracking performance is improved. Note that the tracking error for q in Table 5-5 is increased when using the INCA controller. This is probably caused by the fact that closer tracking of the altitude, results in larger reference values for α and thus for q. Re-tuning the gain of the INCA controller (3) for q, can result in an improvement of the tracking error. Still, as tracking performance of the altitude is already improved, compared to the baseline INDI controller (1), it was decided to not go into further detail for this.

Finally, it is interesting to look into the difference concerning the control inputs for the INDI and INCA controller. The relevant control surface deflections for controlling the required roll and yaw moment for the reference trajectory, are the aileron and rudder deflection. These are shown in Figure 5-3. For the aileron deflection δ_{a}, it is interesting to see that the deflection is much smaller for the INCA controller in Figure 5-3a. Also, the rudder deflection is in an opposing direction when comparing the INDI and INCA controller. These results can both be explained by the rational velocity of the propellers $\boldsymbol{n}_{\text{p}}$ in Fig. 5-4. Firstly, by using the PAI effects actively, roll control is provided by the propellers. As the DEP aircraft roll to the right in the beginning of the simulation, the left propeller produce more thrust. When rolling to the left, the right side of the propellers produce more thrust. This means that the ailerons need to provide less rolling moment, hence their smaller deflection. Secondly, an increase of $\boldsymbol{n}_{\text{p}}$ on one side of the aircraft creates a yaw moment, for which the rudder needs to compensate. This explains the opposing rudder deflection δ_{r} in Figure 5-3b. Note that this control allocation is not necessarily efficient, as the control inputs are providing opposite yaw moments to compensate for each other. Optimizing for power, as discussed in Section 4-2-3 can provide a solution to this and the results of this method will be shown in Section 5-3.

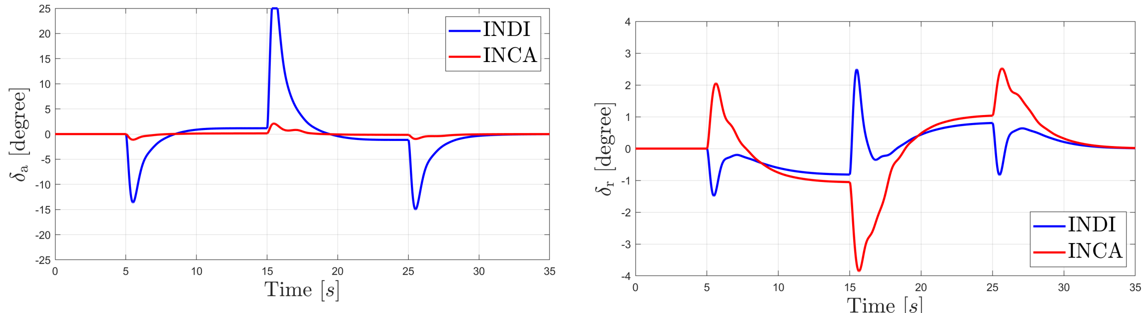

(a) Aileron deflection δ_a, where for the INCA only the right aileron is shown.

(b) Rudder deflection δ_r.

Figure 5-3: Control surface deflections of the INDI (1) and INCA (3) controller with low proportional gains.

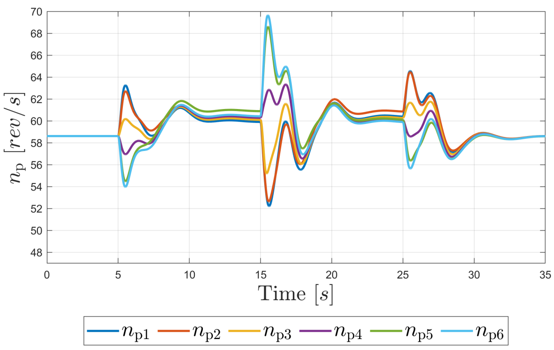

Figure 5-4: Rotational velocity of the individual propellers n_p for the INCA (3) controller with low gains.

It can be concluded that the INCA controller (3), derived in Section 4-2-2 provides a framework in which the differential thrust and PAI effects are used to actively control the moments around the aircraft. Furthermore, the reference altitude and velocity are followed, where a significant improvement of tracking performance for altitude is shown when compared to the baseline INDI controller (1). The next section will extend on this method by increasing the gains, thereby possibly improving tracking performance for ϕ_{ref}.

5-2-2 High proportional gains

In this section, the high set of proportional gains, as specified in Table B-1, will be used. As was hypothesized in Chapter 1, by including the differential thrust and PAI effects, the DEP aircraft should have more control authority. If the controller is designed correctly, this should lead to better tracking performance in terms of faster rise times with minimal overshoot. As discussed in Section 4-4, a limitation of the INCA controller is that the combination of rate constraints and actuator dynamics results in an over-conservative controller. Therefore, the full potential of the DEP cannot be demonstrated with the standard INCA controller. A solution to this problem is adding an MPC controller in the control loop which compensates for the actuator dynamics. This controller assures that the achieved incremental control input $\Delta \boldsymbol{u}_a$ equals the one commanded by the INCA controller $\Delta \boldsymbol{u}_c$.

In the simulations, the performance of the INDI (2), INCA (4) and INCA with MPC controller (5), as defined in Table 5-1 will be analyzed with the high set of proportional gains as defined in Table B-1. The gains were tuned so that the rise time of the INCA MPC controller was reduced with minimal overshoot. It was then reviewed whether the response of the INDI controller was still stable for the same rise time. Note that the gains for the INCA MPC controller can be further increased, leading to even faster rise times. Still, as the performance needs to be compared against the INDI controller it was decided not to further increase the gains. Next to that, looking at handling qualities of the DEP, faster response times will not be realistic and make the DEP difficult to handle. Note that regarding this aspect, the response times for the high proportional gains are already quite fast. This is with the goal of showing the full potential of the INCA MPC (5) controller. When implementing this controller it should be investigated whether the handling qualities are still satisfactory with such fast responses. Also, further increasing the gains makes the controller more sensitive to measurement noise, which can have significant effects when implementing the controller in the future.

The rise times and overshoot values for the three controllers are given in Table 5-6. As can be seen, the gains of the controller are tuned as such that the rise times are almost similar. Looking at the overshoot, one can see that as expected the INDI controller has a significant amount as it cannot provide the control authority that is required for such a fast response. For the INCA controller without MPC (4), the overshoot is reduced but still present. For completeness, the time responses of this controller are shown in Figure C-1, up to and including Figure C-3b in Appendix C.

Table 5-6: Rise time and overshot for controllers with high gains

Controller	INDI high (2)	INCA high (4)	INCA MPC high (5)
Rise time [s]	0.7074	0.7165	0.7028
Overshoot [%]	12.27	5.500	0.1625

The overshoot for the INCA controller (4) can be explained by the fact that for removing the rate constraints, the actuators can saturate. If this occurs, the commanded incremental control inputs will deviate by a significant amount from the achieved incremental control input. Therefore, allocation errors are developed which causes a deterioration in performance as can be seen for the given overshoot. Note that these errors become larger when increasing the gains, so that it did not play a significant role in the previous section. When the MPC controller (5) is included, the rate constraints can be added to the INCA controller again, so that the allocation error becomes insignificant. This results in much better tracking performance where the same rise time is achieved without overshoot, as can be seen in Table 5-6.

The responses of the reference values for the INDI (2) and INCA MPC (5) controllers are shown in Figure 5-5 and Figure 5-6. As can be seen in Figure 5-5a, the response to ϕ_{ref} is faster, which results in the smaller rise time. The INDI controller (2) shows much overshoot and thus the performance is not satisfactory. By combining INCA with MPC (5), the full potential of the DEP is used, showing fast rise times with minimal overshoot in Figure 5-5a. Note that in Figure 5-5b, performance is significantly improved concerning the sideslip angle β for the INCA with MPC (5) controller. This can be explained by the fact that the INDI controller (2) cannot satisfy the roll response, but still tries to follow it as close as possible.

While doing so, the angle of sideslip is controlled less, as the INDI controller (2) does not have enough control authority for both. This results in higher angles of sideslip and thus less efficient flight. In Figure 5-6a and Figure 5-6b, it can again be seen that using the INCA controller, the reference variables for the altitude and velocity are more closely tracked.

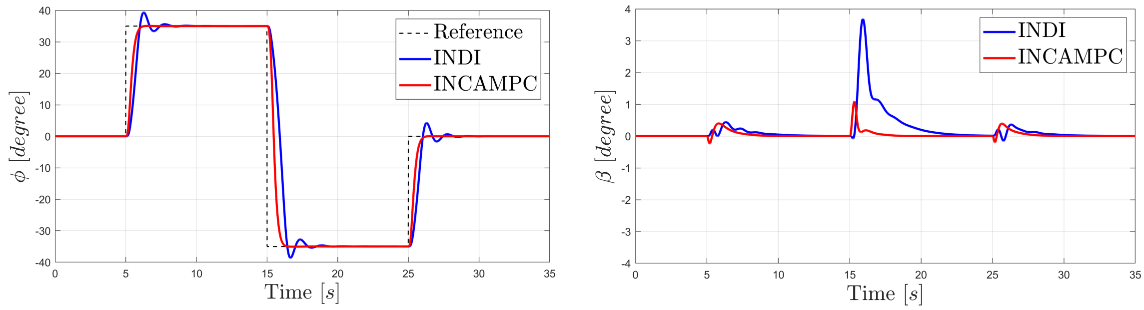

(a) Roll angle ϕ response with the reference signal. **(b)** Sideslip β response, where $\beta_{\text{ref}} = 0°$

Figure 5-5: Time responses of the roll and sideslip angle for the INDI (2) and INCA MPC (5) controller with high gains.

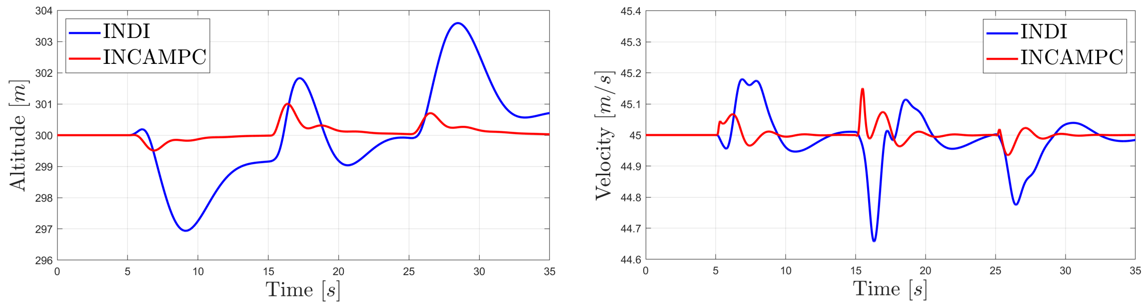

(a) Altitude h response, where $h_{\text{ref}} = 300\ m$ **(b)** Velocity V response, where $V_{\text{ref}} = 45\ m/s$

Figure 5-6: Time responses of the altitude and velocity for the INDI and INCA MPC (5) controller with high gains.

These simulation results were again quantified using the RMSE values for the controlled states. These values are given in the tables below for the INDI high (2) and INCA MPC high (5) controller.

Table 5-7: Tracking performance $\boldsymbol{x}_1$

RMSE($\epsilon_{\text{track}}(\boldsymbol{x}_1)$)		
Controller	INDI	INCA
V $[m/s]$	0.094	0.021
h $[m]$	1.644	0.239

Table 5-8: Tracking performance $\boldsymbol{x}_2$

RMSE($\epsilon_{\text{track}}(\boldsymbol{x}_2)$)		
Controller	INDI	INCA
ϕ [°]	11.48	8.576
α [°]	0.994	0.528
β [°]	0.512	0.122
Total	6.660	4.961

Table 5-9: Tracking performance $\boldsymbol{x}_3$

RMSE($\epsilon_{\text{track}}(\boldsymbol{x}_3)$)		
Controller	INDI	INCA
p [°/s]	0.282	0.151
q [°/s]	0.173	0.028
r [°/s]	0.036	0.017
Total	0.192	0.089

The observations of the time response for the reference values are confirmed by these numbers. Looking at the RMSE values, all are lower for the INCA controller indicating better tracking performance. The RMSE value for the roll angle ϕ in Table 5-8 is reduced significantly, indicating that performance with respect to ϕ_{ref} is increased. Note that when comparing to Table 5-4, the RMSE value for ϕ of the INDI controller is lower with higher proportional gains. This is because the rise time is faster, resulting in smaller errors, although the overshoot is significantly increased. As overshoot should be minimized, satisfactory performance of the INDI controller with high gains (2) cannot be concluded, even though the RMSE value for ϕ is smaller. Finally, in Table 5-9, note that for the INCA controller with MPC (5) the RMSE value of the pitch rate q is reduced when compared to Table 5-5. This indicates that by adding the actuator rate constraints and compensating for actuator dynamics, the pitch rate is controlled more accurately.

The performance of the INDI (1) with low proportional gains and INCA MPC (5) controller with high proportional gains can also be compared in the frequency domain. This analysis shows, how by increasing the gains, response times are increased. For this, the method introduced in Section 5-1-4 is used so that the Bode magnitude plot for a nonlinear system can be determined. From simulation, it was found that for the relation $\phi_{\text{ref}} \rightarrow \phi$, the amplification gain is amplitude independent. This is because, the INDI and INCA controller cancels out the nonlinear dynamics. Therefore, the Bode magnitude plot shown in Figure 5-7 can be generated, for the general amplitude of ϕ_{ref}. Note that ϕ_{ref} should stay within the physical limits of the DEP aircraft.

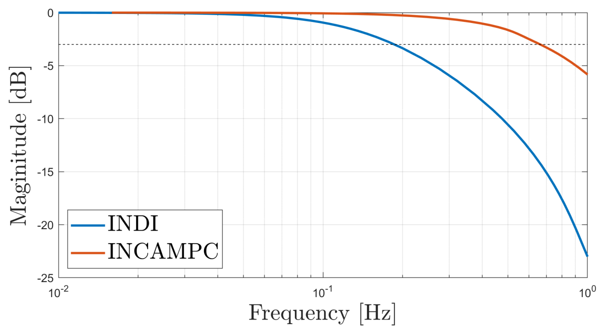

Figure 5-7: Bode magnitude plot of the INDI (1) and INCA MPC (5) controller for $\phi_{\text{ref}} \rightarrow \phi$.

As can be seen in Figure 5-7, the bandwidth for the INCA MPC (5) controller is significantly increased as compared to the INDI controller with low gains (1). Defining the bandwidth as the frequency at which the Bode magnitude plot drops below -3dB, the bandwidths are 0.663 Hz and 0.186 Hz respectively. These values confirm that by using the full potential of the DEP aircraft, including the differential thrust and PAI effects, tracking performance can be significantly increased.

To see how this performance is increased, a look is taken into the relevant control inputs providing the required roll and yaw moment. As shown in Figure 5-8a, for both the INDI (2) and INCA MPC (5), the aileron deflection δ_{a} reaches its limit of 25°. For the INDI controller these saturation levels are attained for a longer period. Here the controller tries, but is not able, to achieve the required roll moments. For the INCA MPC (5) controller, part of this rolling moment is produced by the PAI effects, as is shown by the rotational velocity of the propellers $\boldsymbol{n}_{\text{p}}$ in Figure 5-9. Here, $\boldsymbol{n}_{\text{p}}$ is increased at one side of the aircraft, thereby creating a roll moment caused by the PAI effects and a yaw moment caused by the differential thrust. As part of the roll moment is taken up by the PAI effects, the ailerons do not saturate, which results in better tracking performance. For the INDI controller, the rudder deflection δ_r is used for roll control, thereby deteriorating performance with respect to β, as was shown in Figure 5-5b. For the INCA MPC controller, δ_r together with the differential thrust shown in Figure 5-9, minimizes the sideslip angle β.

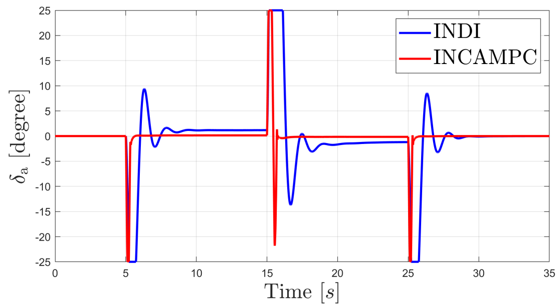

(a) Aileron deflection δ_a, where for INCA only the right aileron is shown.

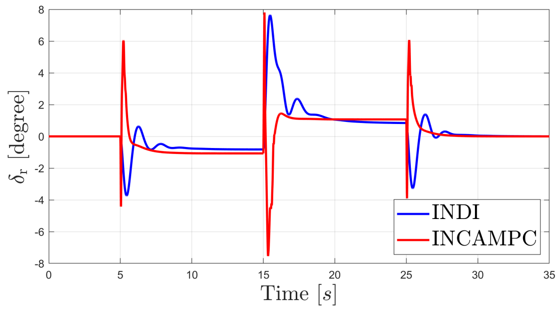

(b) Rudder deflection δ_r.

Figure 5-8: Control surface deflection of the INDI (2) and INCA MPC (5) controller with high gains.

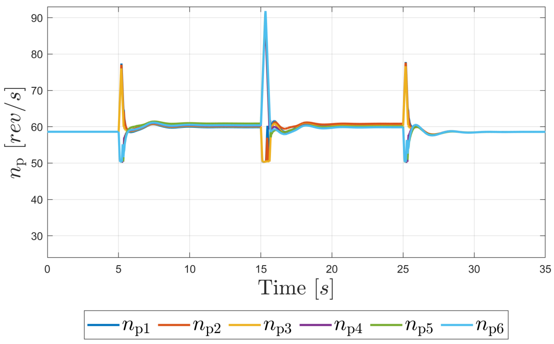

Figure 5-9: Rotational velocity of the individual propellers n_p for the INCA MPC controller (5) with high gains.

Finally, to confirm that by using the differential thrust and PAI effects actively, the control authority is increased, the roll moment and yaw moment are plotted in Figure 5-10a and Figure 5-10b respectively. As one can the roll moment is significantly increased, showing the benefit of using the PAI effects actively. Also, the yaw moment is increased, because of differential thrust so that the sideslip angle β can be kept closer to zero.

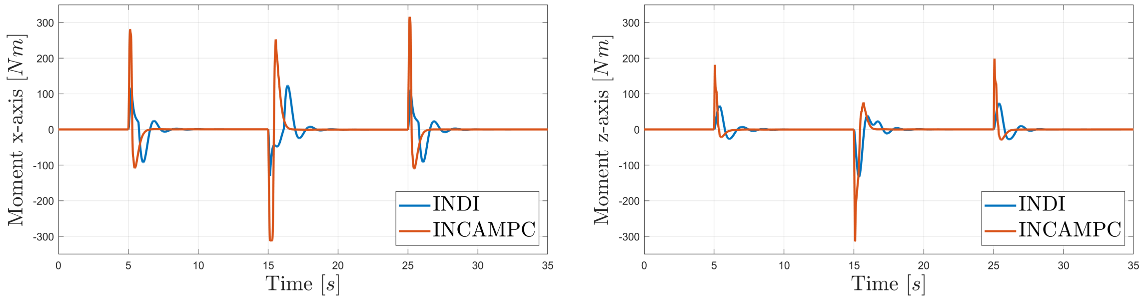

(a) Moment l around the x-axis

(b) Moment n around the z-axis

Figure 5-10: Moments around the aircraft's x and z-axis for the INDI (2) and INCA MPC (5) controller with high gains.

To conclude, it was shown in this section how for increasing gains the full potential of the DEP aircraft is used. By combing the control authority of the control surfaces, differential thrust and PAI effects, the tracking performance for reference variables was significantly increased. This was analyzed using the amount of overshoot, the RMSE value, the bandwidth and the produced moments. The INCA controller needs to be augmented with an MPC controller to compensate for the actuator dynamics, thereby showing the full performance gain. The next section will show the results of another potential performance increase in terms of efficiency for the propeller power.

5-3 INCA for power optimization

As stated before in Chapter 1, the potential increase in performance for the DEP aircraft is not only in terms of tracking, but also for possible efficiency increase. Therefore, in Section 4-2-3, the secondary objective of the INCA controller was reformulated, so that it represents the power consumed by the propellers. The results for these controllers will be shown in this section, which refers to controllers 6 and 7 in Table 5-1. Note that only the low proportional gains are used in the power optimization as optimizing for power will not have significant results when the DEP is operated at the limit of its control authority. For the high proportional gains, all control inputs are required whereas for the low gains a trade-off needs to be made, and this extra freedom can be used for power optimization. As discussed in Section 4-4, combining INCA with MPC to compensate for the actuator dynamics, potentially leads to a further increase of the efficiency. This is because, without compensation for the actuator dynamics, the achieved incremental control input does not equal the commanded value by the INCA controller. This means that the optimal control allocation for efficiency is not achieved, so that the increase in efficiency is less. The difference in INCA for power optimization with and without MPC, controller 7 and 6 in Table 5-1 respectively, will therefore also be compared in this section.

During simulation, it was found that by increasing the controller frequency, the performance of the controller was significantly increased. For the standard simulation frequency of $f_s = 100$ Hz, the control inputs show small high-frequency oscillations. This indicates that too large incremental control inputs are applied for the power optimization regarding $\frac{\partial \boldsymbol{P}_\mathrm{p}}{\partial \boldsymbol{n}_\mathrm{p}}$. Increasing f_s resulted in fewer oscillations but also an increase in computation time. Therefore, it was decided that the controller frequency was increased to $f_s = 200$ Hz, showing a good trade-off between computation time and controller performance.

As the same low set of proportional gains is used as in Section 5-2-1, the same response with respect to the reference values was found for INCA power optimization controllers (6 and 7). These responses were shown in Figure 5-1 and Figure 5-2 for the INCA controller and will, therefore, not be repeated in this section. The RMSE values for the different state variables using the INCA power with MPC (7) controller are shown in Table 5-10. As one can see, the values are very similar to the ones presented in Table 5-3 up to and including Table 5-5. Performance is increased by a small amount as the MPC controller now compensates for the actuator dynamics, as opposed to the value from Section 5-2-1 where no MPC controller is used.

			RMSE(ϵ_{track})				
V $[m/s]$	h $[m]$	ϕ [°]	α [°]	β [°]	p [°/s]	q [°/s]	r [°/s]
0.013	0.171	12.44	0.313	0.262	0.0579	0.007	0.006
Total			7.188			0.033	

Table 5-10: Tracking performance of INCA MPC (7) controller with power optimization.

As the control allocation method is different, now optimizing for minimal power, the control inputs change. The relevant control inputs for INCA power optimization with MPC (7) are shown in Fig. 5-11 and Fig. 5-12. Comparing the values for the aileron deflection with Figure 5-3a, one can see that this deflection is significantly increased. This indicates that it is more efficient to use the ailerons for roll control as opposed to mainly using the PAI effects. Looking at the difference in aileron deflection, because of interaction with the tip propellers, one can see in Figure 5-11a that this difference is small. Still around $t = 15$ s, when the largest roll moment is required, $\delta_{\text{aL}} = -15.50°$ and $\delta_{\text{aR}} = 15.88°$. This difference is small, but indicates that there is at least a small benefit in controlling the ailerons separately. The PAI effects are still used, as can be seen in Figure 5-12, but less when comparing these values with Figure 5-4. Rudder deflection in Figure 5-11b has comparable amplitudes compared to Figure 5-3b, only for shorter periods, which thus reduces the drag produced by the rudder. Also, the direction is the same as for the INDI controller after the fast initial deflection. This shows that the power optimization prevents complementary control inputs that lead to higher power consumption. Also, looking at Figure 5-12, it is interesting to see the difference in $\boldsymbol{n}_{\text{p}}$ at the first 5 seconds of the simulation, when the aircraft is still in cruise conditions. This occurs because the INCA power MPC (7) controller uses the knowledge that rotating the outer propellers reduces drag, which thus increases efficiency. Rotating these propellers even faster will give a higher power consumption which is thus not beneficial.

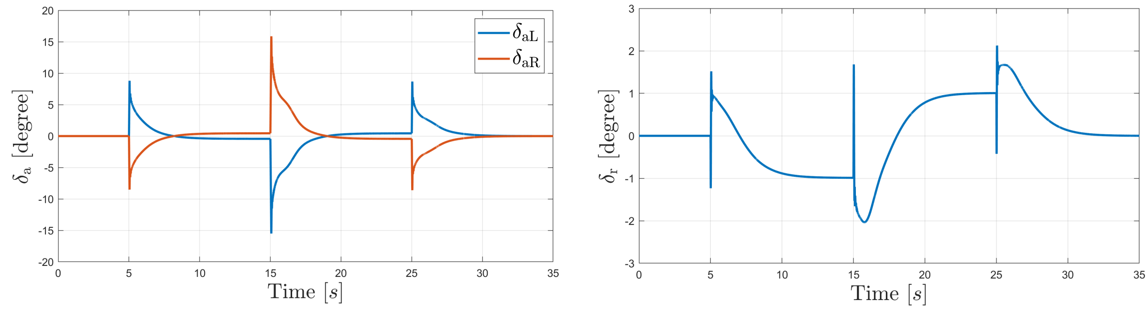

(a) Aileron deflection δ_{aL} and δ_{aR}.

(b) Rudder deflection δ_{r}.

Figure 5-11: Control surface deflection for INCA power MPC (7)

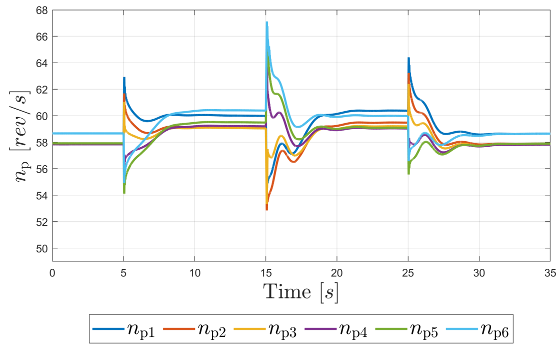

Figure 5-12: Rotational velocities of the individual propellers n_{p} for the INCA power MPC controller (7)

To compare the control inputs at different operating conditions, these are shown for a reference velocity of $V_{\mathrm{ref}} = 60\ m/s$ in Figure C-5 and Figure C-6. Note that this is a relative high velocity for the DEP aircraft, but this allows to show a significant difference in allocation. Here it can be seen, that for higher velocities smaller control surface deflections are required. In contrast, the rotational velocity of the propellers needs to be increased to achieve the same thrust. It, therefore, becomes more efficient to use the $\boldsymbol{\delta}$ instead of $\boldsymbol{n}_{\mathrm{p}}$ for controlling the DEP aircraft. These results show that the INCA controller can be used at different operating points, optimizing the allocation for these different conditions.

The same results were plotted for the INCA power controller (6) without MPC in Figure C-8 and Figure C-9. Comparing these with Figure 5-11 and Figure 5-12, one can see that the control inputs have smaller amplitudes but longer time spans for δ_{a}, δ_{r} and $\boldsymbol{n}_{\mathrm{p}}$. This is because, without MPC controller the required control inputs are reached slower, resulting in smaller control inputs which are applied for a longer time. In Figure C-9, the same effects of rotating the outer propellers faster to reduce drag can be seen as in Figure 5-12.

The total power consumed by the propellers is defined as $|\boldsymbol{P}_{\mathrm{p}}|_1$, summing all individual powers of each propeller. The result for the INCA power MPC controller (7) and for the baseline INDI controller (1) are shown in Figure 5-13. A few interesting remarks can be made from these figures. Firstly, the power consumption at the start of the simulation is significantly lower, as the INCA controller uses the knowledge that rotating the outer propellers faster leads to a decrease in drag and thus power consumption. Also, the peak value for the total power is significantly lower for the INCA controller as compared to the INDI. Finally, between ten and fifteen seconds and twenty to twenty-five seconds, the total power remains close to constant for the INCA controller in Figure 5-13. This indicates that the optimization finds a control allocation where the power is minimized for a roll angle of $\phi = \pm 35°$. In contrast for the INDI controller, the power keeps oscillating as can be seen in Figure 5-13. Note that the power values of the INDI controller also drops below the value of the INCA MPC controller. This is because, at these moments the reference values h_{ref} and V_{ref} are not satisfied for the INDI controller. This gives less power consumption but also larger tracking errors, which is not satisfactory. Looking at Figure C-10 for INCA without MPC (6), one can see that the peak is also higher and that less steady power levels, and thus control allocation, is achieved.

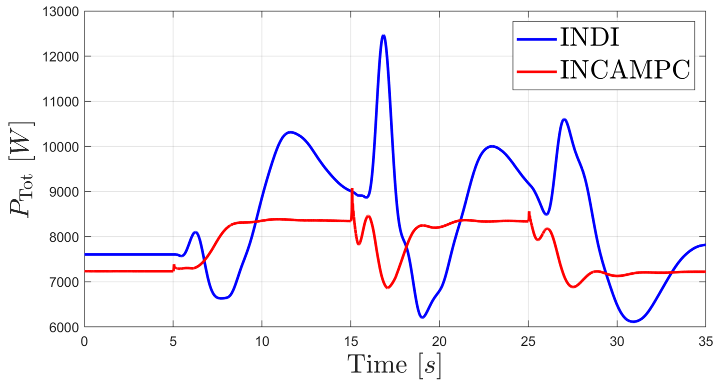

Figure 5-13: Total propeller power, defined as $|\boldsymbol{P}_{\text{p}}|_1$, for the INCA power MPC controller (7) and INDI controller (1).

The results were quantified and presented in Table 5-11. As the INCA power controller designed in 4-2-3 minimizes the two-norm of $\boldsymbol{P}_{\text{p}}$, these results are also given. Both the one-norm and two-norm of this vector were integrated over time to give the total energy in MJ. Also, the maximum total power of the propellers is given in this table.

	INDI (1)	INCA power (6)	INCA power MPC (7)
$\int \lvert\boldsymbol{P}_{\text{p}}\rvert_1 dt$ [MJ]	0.29082	0.27319	0.27133
$\int \lvert\boldsymbol{P}_{\text{p}}\rvert_2 dt$ [MJ]	0.11873	0.11197	0.11118
$\max(\lvert\boldsymbol{P}_{\text{p}}\rvert_1)$ [W]	12466	9738	9077

Table 5-11: Integrated one- and two-norm of the propeller powers and their maximum values for the INDI, INCA and INCA MPC controller.

Comparing the total power consumed between the INDI (1) and INCA power MPC (7) controller gives a significant decrease of 6.7% for the one-norm and 6.4% for the two-norm. Comparing these values with the INCA power (6) controller, without MPC, a decrease of 6.0% on the one-norm and 5.7% on the two-norm was found. As was already seen in the plots discussed above, the peak value of the power consumption of the propellers is significantly reduced.

It can, therefore, be concluded that by optimizing for propeller power $\boldsymbol{P}_{\text{p}}$ in the INCA controller, the efficiency of the aircraft can be substantially increased. By introducing the MPC methods, the efficiency is increased even further although not by a large amount. This is caused by the fact that a large amount of the efficiency increase is obtained with the wing tip propellers. Although the INCA power (6) controller (without MPC) does not reach the commanded as fast as with MPC, it asymptotically drives the control inputs to the correct values. This thus results in the most significant part of the efficiency increase. Still, note that by introducing MPC the efficiency is further increased which thus shows that it is beneficial to implement this method not only to improve tracking but also for less power consumption.

5-4 Modeling uncertainty

Another important aspect of the controller design for the DEP aircraft is robustness to modeling errors. As discussed in Chapter 1, these modeling errors can mainly be found in the PAI effects which are hard to model. This thesis assumed an analytical model, subject to numerous assumptions. Therefore, it is interesting to analyze how the controller deals with these kinds of uncertainties. Furthermore, it is interesting to see how the power optimization is influenced by modeling errors. From this, it can be analyzed whether efficiency increases are possible even though the DEP model is not known accurately. The next two subsections analyze these effects first for tracking and then for power optimization.

5-4-1 Influence on tracking

To analyze the robustness of the controller against modeling uncertainties for tracking, the INCA low gains (3) controller is used. This is the nominal controller for which analyzing modeling errors makes the most sense. The high set of proportional gains can only be used if the model is known sufficiently accurate, as this controller operates at the boundary of the capabilities of the DEP aircraft. Furthermore, it was found in simulation that the MPC controller corrects very rapid for any modeling errors, which can lead to oscillations in the responses.

In terms of tracking, the control effectiveness of the control surfaces, the differential thrust and PAI effects with respect to the moments around the aircraft have the largest influence. Therefore, the first analysis changes the control effectiveness of the differential thrust PAI effects

$$\frac{\partial C_l}{n_{\mathrm{p_i}}}(V_\infty, \rho, n_{\mathrm{p_i}}, \alpha, \beta, C_{L_{\mathrm{ac}}}, \beta_{\mathrm{corr}}) \text{ for } i = 1, 2, , , 6, \tag{5-6a}$$

$$\frac{\partial C_n}{n_{\mathrm{p_i}}}(V_\infty, \rho, n_{\mathrm{p_i}}, \alpha, \beta, C_{L_{\mathrm{ac}}}, \beta_{\mathrm{corr}}) \text{ for } i = 1, 2, , , 6, \tag{5-6b}$$

to show the effect of their modeling uncertainty. As these are both nonlinear functions, depending on multiple variables, both an offset and scaling factor is used to introduce uncertainty with the method introduced in Section 5-1-3. The scaling factor was changed from 0.4 to 3.5 and the offset factor from -0.25 to 2.5. Note that by further decreasing either of these factors, the control effectiveness changes sign for which the response becomes unstable. Still, it can be assumed that the direction of the effects is known, as a higher $\boldsymbol{n}_{\mathrm{p}}$ will increase the local lift and thus roll moment and the yaw moment. Switching the signs of these effects physically does not make sense.

For the set of offset and scales, the results were checked for the RMSE value of the tracking error of $\boldsymbol{x}_2$ and the allocation error of $\boldsymbol{\tau}_{\mathrm{c}}$. Note that the $\boldsymbol{\tau}$ vector in this case only contains the moments and not the $\dot{V}$ and $\dot{\gamma}$. The results for the tracking and allocation error are shown in Figure 5-14a and Figure 5-14b respectively. The nominal values are for $k_{\text{offset}} = 0$ and $k_{\text{scale}} = 1$, which is shown by the plus sign in these figures. It can be seen that both for the tracking and allocation error, reducing the scale and offset factor leads to better performance. This effect was already recognized in [29] and can be explained as follows. By decreasing either the scale factor or offset, the control effectiveness is underestimated, thus leading to larger control inputs. This effectively increases the proportional gain of the control loop, which increases tracking performance and decreases the allocation error. There is a limit to this, as the actuators will saturate or the control effectiveness changes sign. Increasing both these factors leads to deterioration in performance, which can be seen going to the top right corner of both Figure 5-14a and Figure 5-14b. Increasing of these factors leads to overestimation of the control effectiveness, so that the $\boldsymbol{n}_{\text{p}}$ control input becomes lower. Note that the offset and scale factor can be increased by much but for an offset factor of two and a scale factor of three, the allocation error is almost doubled. From simulation, it was found that for increasing the values further, the reference values keep oscillating so that performance is not satisfied anymore. Still, it can be concluded from these plots that the PAI effects are allowed to have large modeling errors. Performance is only affected when they are over-estimated by a large value or when the sign switches.

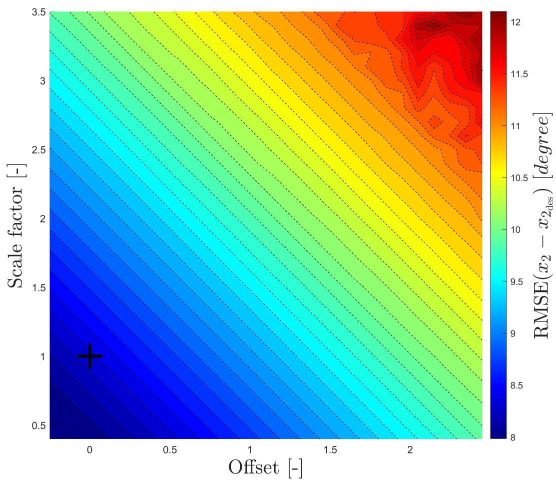

(a) Tracking error of $\boldsymbol{x}_2$ expressed in $degree$.

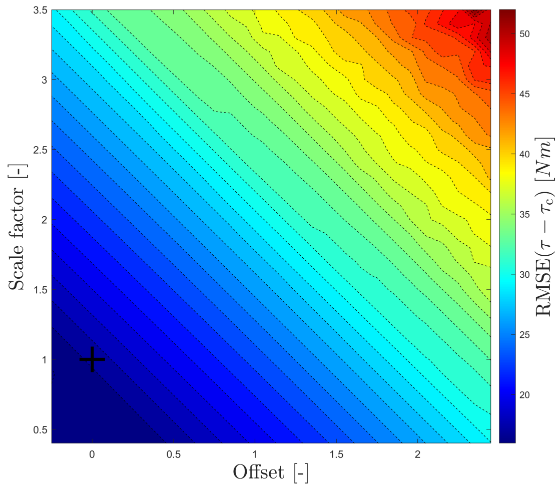

(b) Allocation error of $\boldsymbol{\tau}$ expressed in Nm.

Figure 5-14: Tracking and allocation error plotted with respect to the offset and scale factors for the PAI effects.

The second set of control effectiveness that was changed, were the control derivatives of the control surfaces. These also produce the required moments around the aircraft, together with the differential thrust and PAI effects. Changing the effectiveness of the control surfaces thus has a large influence on the tracking and allocation error. Note that as these values were determined in wind tunnel testing, they should be more accurately known, as compared to the PAI effects. Still, analyzing these methods forms an important insight into how sensitive the INCA controller is. The values that were changed include

$$C_{l_{\delta_\mathrm{a}}} = \frac{\partial C_l}{\partial \delta_\mathrm{a}}, \tag{5-7a}$$

$$C_{m_{\delta_\mathrm{e}}} = \frac{\partial C_m}{\partial \delta_\mathrm{e}}, \tag{5-7b}$$

$$C_{n_{\delta_\mathrm{r}}} = \frac{\partial C_n}{\partial \delta_\mathrm{r}}, \tag{5-7c}$$

which are all constant values as shown in Appendix A-4. Therefore, only a scaling factor K_scale is applied to these values. This scaling factor was changed from 0.05 to 3.5.

The results for this analysis are shown in Figure 5-15a and Figure 5-15b. It can be seen that both for the tracking and allocation error, optimal values are obtained around the real control effectiveness values for $k_\mathrm{scale} = 1$. Increasing k_scale up to 2.5 results in less tracking and allocation performance. If the scale factor is increased even further, performance of the controller cannot be guaranteed anymore, as reference values start oscillating. Decreasing the scale factors, also gives less performance where a sudden increase in allocation error can be found around 0.2. This is caused by excessive use of the control surfaces, as their control effectiveness is underestimated, leading to much worse allocation errors. Overall, it can be concluded that modeling errors for the control surfaces play a considerable role. Still, the scale factors should be significantly high or low to deteriorate performance, so that robustness against modeling errors of the control surfaces can be concluded. Also, remember that these values are known up to a higher degree of certainty as compared to the PAI effects, because of wind tunnel testing of the SFD.

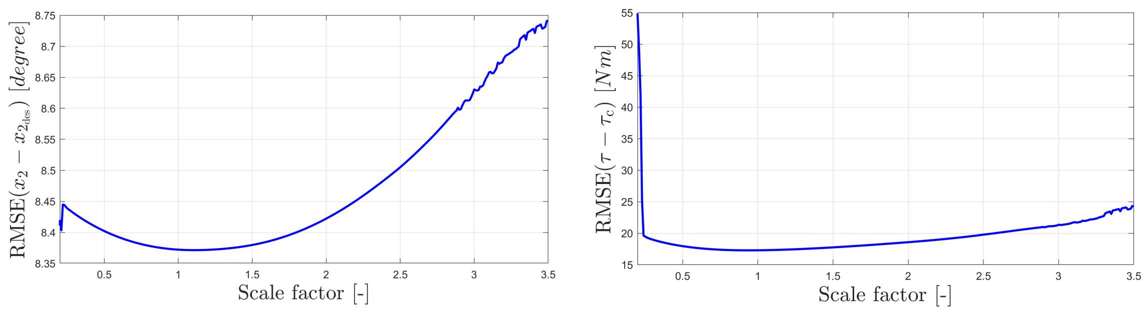

(a) Tracking error of $\boldsymbol{x}_2$ expressed in $degree$.

(b) Allocation error of $\boldsymbol{\tau}$ expressed in Nm.

Figure 5-15: Tracking and allocation error with respect to the scale factor for the control surfaces.

5-4-2 Influence on power optimization

Next to modeling robustness for tracking, it is interesting to analyze how modeling errors affect the power optimization. Two variables were considered for this

$$\frac{\partial P_{\mathrm{p_i}}}{n_{\mathrm{p_i}}}(V_\infty, \rho, n_\mathrm{p}) \text{ for } i = 1, 2, ...6, \tag{5-8a}$$

$$\frac{\partial C_D}{\partial n_{\mathrm{p_i}}}(V_\infty, \rho, n_{\mathrm{p_i}}, e_{\mathrm{L/R}}, C_{L_\mathrm{ac}})_\mathrm{PAITip} \text{ for } i = 1, 6, \tag{5-8b}$$

which represent the increase in power and decrease in drag for an increase in propeller rotational velocity. Increasing or decreasing the first factor results in taking too small or large incremental steps of $\boldsymbol{n}_\mathrm{p}$ with respect to the power optimization. For the second factor, the drag reduction with respect to the tip propeller is another PAI effects that is uncertain. It is thus of great value to check how a different partial derivative affects the power optimization. As both these variables are nonlinear functions, depending on multiple parameters, uncertainty will be introduced with a scaling and offset factor as described in Section 5-1-3.

Firstly the power increase factor in Eq. (5-8a) will be analyzed, where the k_offset was changed from -0.8 to 0.8 and the k_scale from 0.2 to 1.5. Note that by decreasing both of these factors, $\frac{\partial \boldsymbol{P}_\mathrm{p}}{\partial \boldsymbol{n}_\mathrm{p}}$ will switch sign. This will result in the controller making the propeller rotate faster for less power, which does not make sense physically. The total energy consumed and maximum total power of the propellers are given in Figure 5-16a and Figure 5-16b respectively. Note that in a large range around the real value, where $k_\mathrm{offset} = 0$ and $k_\mathrm{scale} = 1$, both the total energy and maximum power do not change. This can be explained as follows. In the INCA formulation with power optimization of Eq. (4-31), the current power of the propellers $\boldsymbol{P}_0$ is fed back into the optimization problem. If the factor $\frac{\partial \boldsymbol{P}_\mathrm{p}}{\partial \boldsymbol{n}_\mathrm{p}}$, is over-estimated, smaller steps of $\boldsymbol{n}_\mathrm{p}$ will be taken, but the allocation will still asymptotically drive the propellers to the value where $\boldsymbol{P}_0$ is minimum. If the same factor is under-estimated, going to the bottom left corner of Figure 5-16a and Figure 5-16b, the allocation algorithm will take larger steps of $\boldsymbol{n}_\mathrm{p}$. As can be seen, when the under-estimation becomes too large, this leads to overshoot of the optimal solution, which results in oscillating control inputs and thus higher power consumption. As stated before, even further decreasing the scale and offset factors results in sign switching for which the power consumption is excessively increased.

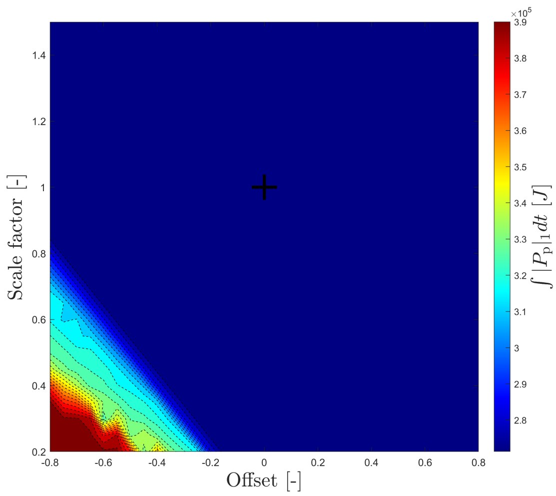

(a) Total energy consumed in J.

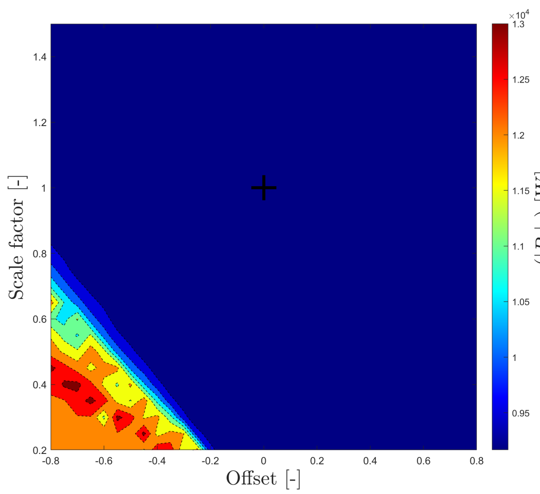

(b) Maximum total power in W.

Figure 5-16: Total energy consumed and maximum total propeller power of $\boldsymbol{P}_\mathrm{p}$ plotted with respect to the offset and scale factors for the propeller power increase effectiveness.

The second analysis for modeling uncertainty robustness with power optimization, is the decrease in drag caused by the tip propellers. This factor is defined as $\frac{\partial C_D}{\boldsymbol{n}_\mathrm{p}}$ given in Eq. (5-8b) for propeller one and six. In Section 2-3-2, it was argued that by increasing the tip-propeller rotational velocity, the drag of the aircraft is decreased. Still, modeling this effect is difficult and researches state different levels of drag reduction. Therefore, this factor was changed over a large number of values where k_offset was changed from -2 to 2 and k_scale also from -2 to 2. The results for this analysis for the total energy consumed and maximum total power, are given in Figure 5-17a and Figure 5-17b. Over-estimating the effect does not have a large influence, as can be seen in the top-right of both figures. As explained for the previous effect, this leads to smaller changes in $\boldsymbol{n}_\mathrm{p}$, but as $\boldsymbol{P}_0$ is fed back, the propellers are asymptotically driven to their optimal values. Under-estimating, the bottom-left corner of Figure 5-17a and Figure 5-17b, gives higher total energy and maximum power values. As a significant amount of the efficiency increase is achieved with the tip-propellers, using these propellers less results in higher power consumption. For $k_\mathrm{offest} \approx -1.5$ and $k_\mathrm{gain} \approx -1$, the effect in Eq. (5-8b) will switch sign, so that the inner propellers are now used more. This explains the sudden increase in both total energy and maximum total power. For the INDI (1) controller the total energy was approximately 2.9×10^5 J and the maximum power 12466 W. For the total energy, this is in the far bottom left corner of Figure 5-17a and for the maximum power this is outside the plot of Figure 5-17b. This means that even with significant under-estimation, the INCA controller performance is substantially improved compared to the INDI controller.

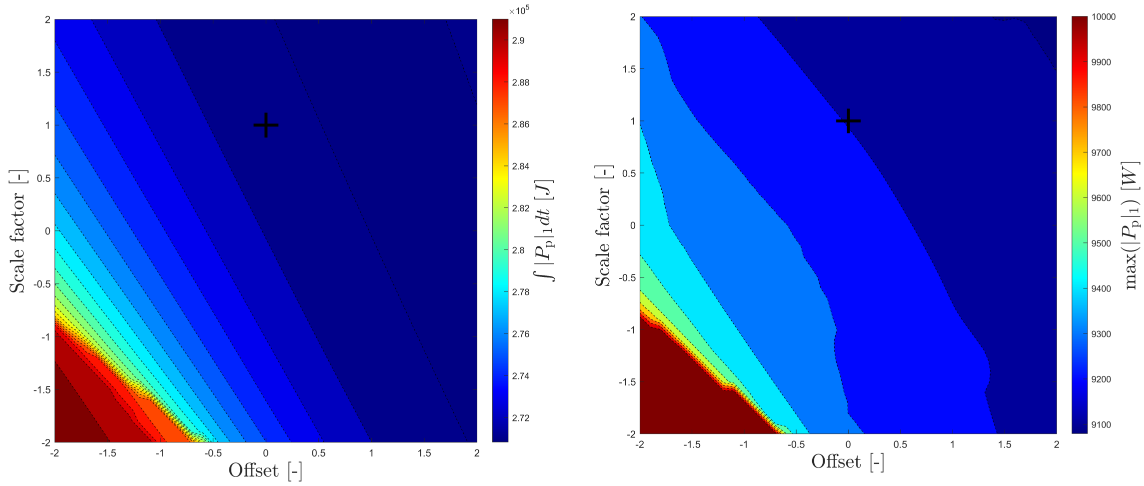

(a) Total energy consumed in J.

(b) Maximum total power in W.

Figure 5-17: Total energy consumed and maximum total propeller power of $\boldsymbol{P}_\mathrm{p}$ plotted with respect to the offset and scale factors for change in drag caused by the tip-propellers.

Overall, it can be concluded that for both $\frac{\partial \boldsymbol{P}_\mathrm{p}}{\boldsymbol{n}_\mathrm{p}}$ and $\frac{\partial C_D}{\boldsymbol{n}_\mathrm{p}}$, over-estimation of the effects does not have a large influence on the efficiency. As $\boldsymbol{P}_0$ is fed back in the allocation problem, the propellers will be asymptotically driven to their optimal values for minimal power consumption. Note that for this method to work, it is thus important that real-time measurements of the propeller power are acquired. Under-estimation does have a significant influence, but only if the values are decreased considerably. For $\frac{\partial \boldsymbol{P}_\mathrm{p}}{\boldsymbol{n}_\mathrm{p}}$, this leads to oscillations in $\boldsymbol{n}_\mathrm{p}$ as too large steps are taken. Decreasing the values even further, the factor changes sign which physically does not make sense. For $\frac{\partial C_D}{\boldsymbol{n}_\mathrm{p}}$, this effect can change sign for certain operating conditions as this aerodynamic effect is highly uncertain. Decreasing this factor increases power consumption and when the sign switches, the power consumption is increased excessively.

5-5 Control over a larger part of the flight envelope

As stated in Chapter 1, a nonlinear controller was defined, so that the DEP aircraft can be controlled over the complete flight envelope. The proposed INDI and INCA controllers are nonlinear, where the INCA controller should thus be able to find a control allocation over a large part of the flight envelope, minimizing the propeller power. To analyze this, the second reference trajectory in Section 5-1-2 was implemented. For this, the DEP aircraft starts at a velocity of 40 m/s and altitude of 100 m. The velocity and altitude is then increased, after which a reference on the roll angle ϕ is applied. This results in a spiral motion, where the aircraft at the end of the trajectory is at an altitude of 500 m and velocity of 55 m/s. The position and velocity are shown in Figure 5-18, where the described climb and spiral with velocity increase can be seen.

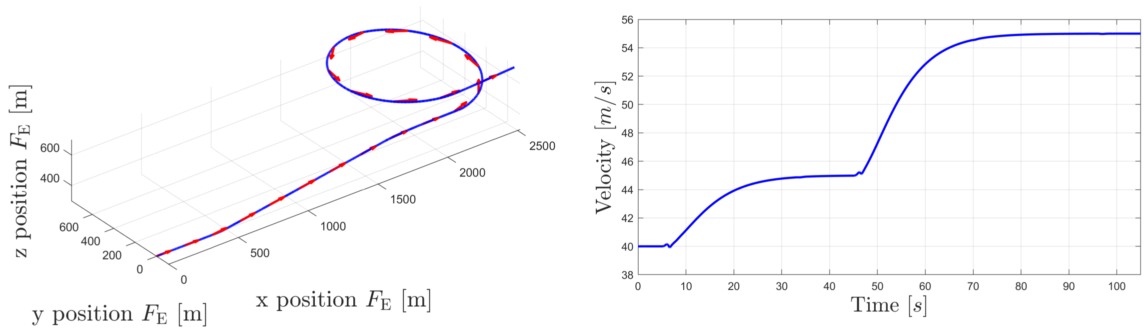

(a) Position in the F_{E} frame.

(b) Velocity response for changing V_{ref}.

Figure 5-18: Time responses of the position and velocity for the INCA power MPC (7) controller.

The control surfaces deflection δ_{a}, δ_{r} and δ_{e} are given in Figure 5-19 and Figure 5-20a. Note that δ_{e} in this case is also plotted, as the altitude changes for which elevator deflections are required. The rotational velocity of the propellers is shown in Figure 5-20b. Looking at these figures, one can again see that a combination of control surfaces deflection, differential thrust and PAI effects is used to control the attitude of the aircraft. Also, a combination of lift generated by the airframe and by the PAI effects is used, to correctly follow the reference altitude. Finally, the propellers provide the required thrust for the reference velocity. This trajectory thus shows that the nonlinear INCA controller can indeed be used over a larger part of the flight envelope. It finds the optimal control allocation regarding propeller power for changing operating conditions, showing the full benefit of using a nonlinear controller.

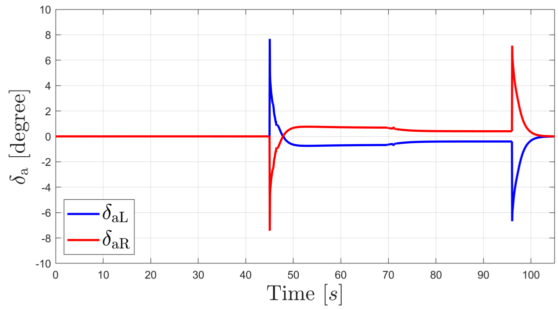

(a) Aileron deflection δ_{aL} and δ_{aR}.

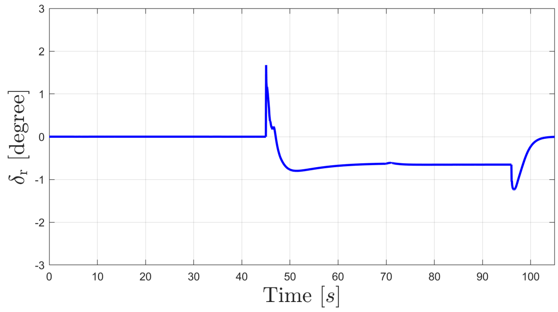

(b) Rudder deflection δ_r.

Figure 5-19: Control surface deflection of INCA power MPC (7) for accelerating and climbing trajectory

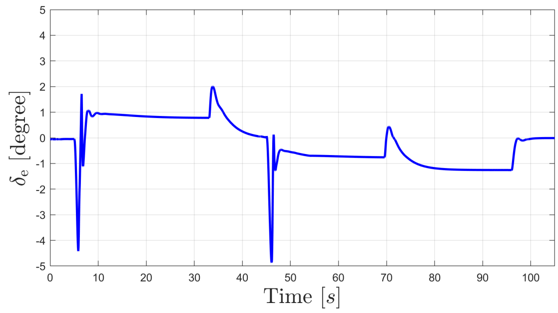

(a) Elevator deflection δ_e.

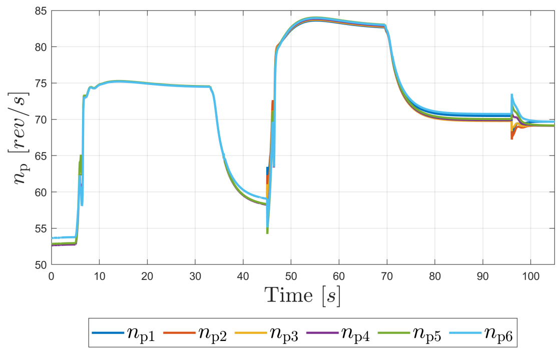

(b) Rotational velocities of the individual propellers n_p of INCA power MPC (7) for accelerating and climbing trajectory

The same reference trajectory was applied to the INDI (1) controller with low proportional gains to compare the efficiency. The total power, defined as $|P_p|_1$, is plotted in Figure 5-21 for both this controller and the INCA power MPC (7) controller. Note that the power for the INDI controller is oscillating intensively because of oscillating $\boldsymbol{n}_p$. An efficiency increase around 6% was again found. Note that comparing the power values is difficult, as the INDI control does not perform well. Looking at Figure 5-21, one can still see that when P_{Tot} reaches a steady value, the INCA controller clearly outperforms the INDI controller. It is hypothesized that the deterioration in controller performance of the INDI (1) controller can have two reasons. Firstly, the INDI controller might not be well tuned, so that changing velocity or altitude references result in oscillations. Secondly, the PAI effects are not included in the INDI controller but modeled as disturbances. For changing h_{ref} or V_{ref}, these artificial disturbances can become larger, leading to oscillating control inputs. Still, from Figure 5-21, it can be concluded that the power for the INCA power MPC (7) controller is less and that this controller is able to find a stable control distribution for the changing reference variables.

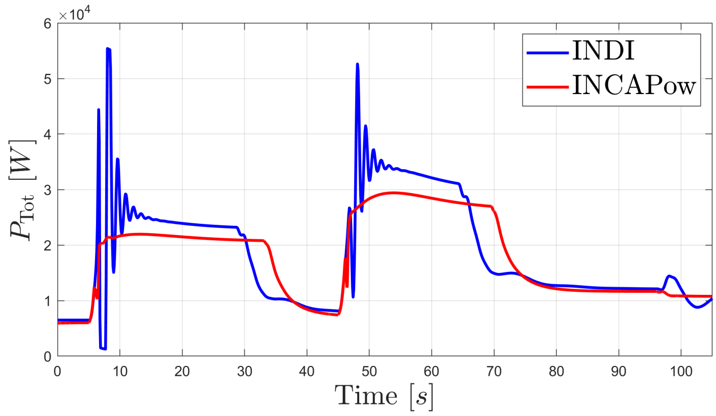

Figure 5-21: Total propeller power, defined as $|\boldsymbol{P}_{\text{p}}|_1$, for the INCA power MPC controller (7) for accelerating and climbing trajectory

5-6 FTC using INCA for tip propeller failure

Another important aspect of the DEP is the robustness against actuator faults, especially considering the propellers. As there are six propellers in total for the DEP aircraft, it should inherently be robust when one of the propellers fails. As discussed in Section 4-2-4, the INCA controller can be used for FTC by increasing the weight W and setting the incremental control preference $\Delta u_{\text{p}} = 0$ of the faulty control input.

To analyze the performance of this FTC method, a fault is introduced on the left propeller (p_1). The tip propellers provide most roll and yaw moment, as their distance from the CG is largest, failure of one of these propellers is most interesting. Failure is modeled so that the propeller after five seconds does not provide any thrust anymore, so that $T_{\text{p}_1} = n_{\text{p}_1} = 0$. Note that in reality, a stationary propeller will produce drag, but this effect is not modeled in this simulation. Drag values for the propeller are not known, and as the focus of this analysis is on FTC for actuator failure, it was decided not to include this effect. It is expected that if this effect is included at a later stage, it can be compensated for. The INCA controller will see it as an external disturbance which is captured by the sensor measurements but performance should be checked in simulation. The fault in propeller one is introduced at five seconds and it is assumed that the fault is detected after six seconds. This thus means that $t_{\text{detect}} = 1\ s$, where as discussed before in Section 4-2-4, it is assumed that the fault can be detected by an FDI algorithm. Furthermore, the INCA controller with low proportional gains (3) is used. It is assumed that when a fault is detected the controller will go to the low gains as the main goal is to keep tracking the reference signals and not power optimization or fast rise times.

The same reference signal with square wave on ϕ_{ref} of $\pm 35°$ is used. The responses of the reference variables are plotted in Figure 5-22 and Figure 5-23. Note that the fault is introduced after five seconds, which can be seen in these plots. In particular for Figure 5-22a and Figure 5-22b, one can see a sudden decrease in ϕ and increase in β. As the fault is detected after six seconds, the controller compensates for this so that all references values, including V_{ref} and h_{ref} are tracked again.

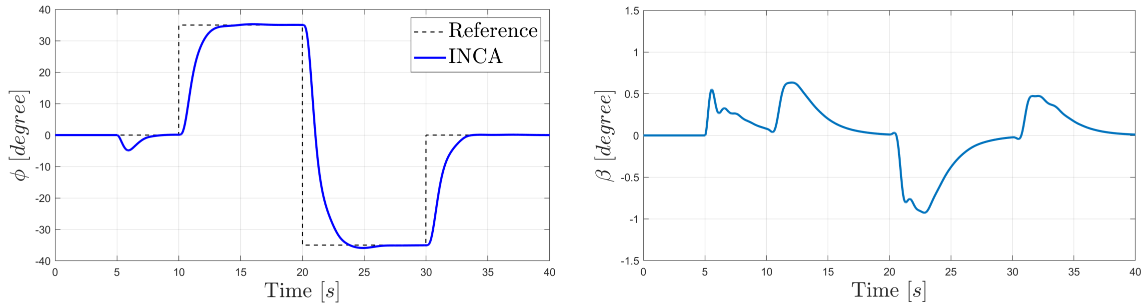

(a) Roll angle ϕ response, with the reference signal.

(b) Sideslip angle β response, where $\beta_{\mathrm{ref}} = 0°$.

Figure 5-22: Time responses of the roll and sideslip angle for INCA (3) controller with low gains and actuator fault

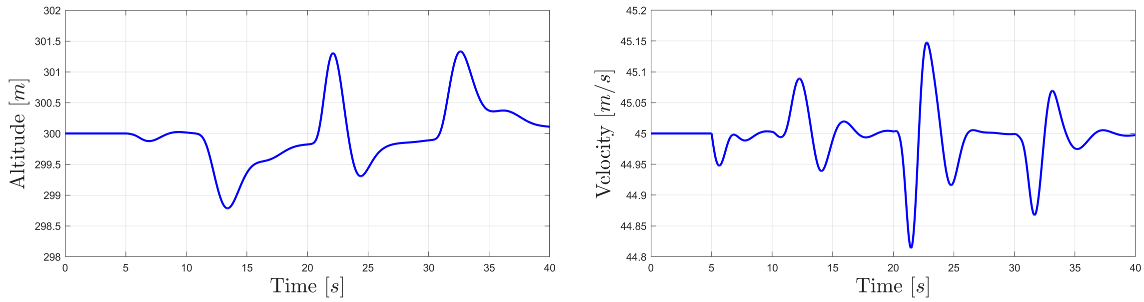

(a) Altitude h response, where $h_{\mathrm{ref}} = 300\ m$.

(b) Velocity V response, where $V_{\mathrm{ref}} = 45\ m/s$.

Figure 5-23: Time responses of the altitude and velocity for INCA controller (3) with low gains and actuator fault.

In Figure 5-24 and Figure 5-25, the relevant control surface deflections and the rotational velocity of the propellers is plotted. It is interesting to see how the INCA controller compensates for the propeller failure. As can be seen in Figure 5-25, after five seconds propeller one does not provide any thrust. To compensate for this, the other propellers produce more thrust so that the velocity V_{ref} is still followed. Due to the PAI effects and differential thrust , this causes a moment l and n around the x- and z-axis respectively. The INCA (3) controller compensates for this, by deflecting the ailerons and rudder, as can be seen in Figure 5-24.

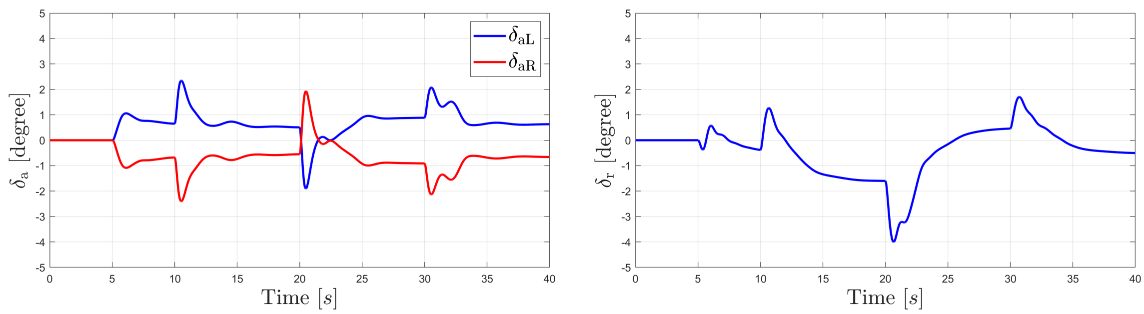

(a) Aileron deflection δ_{aL} and δ_{aR}.

(b) Rudder deflection δ_{r}.

Figure 5-24: Control surface deflection for INCA (3) controller with low gains and actuator fault.

It can, therefore, be concluded that the INCA (3) controller provides FTC for failure of

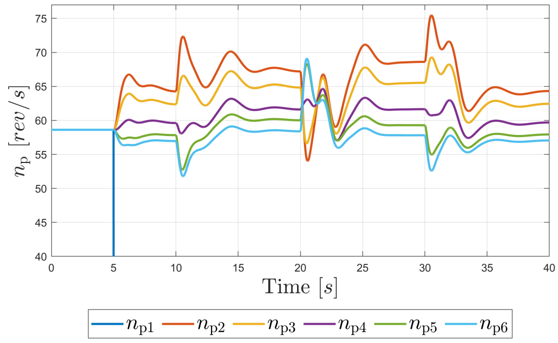

Figure 5-25: Rotational velocities of the individual propellers n_{p} for the INCA low gains (3) with actuator fault

the propeller. This is under the assumption that an FDI algorithm detects the fault with $t_{\mathrm{detect}} = 1\ s$. The controller compensates for this fault using the remaining control effectors, so that all reference variables in $\boldsymbol{y}_{\mathrm{ref}}$ can still be followed. For future research it will be of interest how the fault can be detected using an FDI algorithm, whether the assumed t_{detect} suffices and how the controller can switch to INCA with low proportional gains (3) in the case a failure is detected.

5-7 INCA for external disturbances

As a final analysis, performance of the INCA controller for external disturbances is investigated. To do so, the same turbulence field as in Section 3-6-2 is used, with wind velocity at 6 m altitude of 10 m/s. This is the highest wind velocity, resulting in the most intense turbulence levels. As stated in this section, robustness to external disturbances is increased when increasing the gains, as long as the actuators do not saturate. Therefore, the INCA (3) controller with low proportional gains will be investigated in this section. The maximum bound on the states should be larger than for the INCA MPC (4) controller with high gains. The method for implementation of the turbulence is given in Appendix A-6.

The results for the reference variables are given in Figure 5-26 and Figure 5-27. Note that as the turbulence directly influences β, this signal becomes noisy. The turbulence also affects ϕ as can be seen in Figure 5-26a. The reference square wave is still tracked, but the aircraft oscillates around these values, while the controller tries to correct for the turbulence. Comparing Figure 5-27 with Figure 5-2, one can see that due to the turbulence both the altitude and velocity differ more from their respective reference values. Note that in this case the ground velocity is plotted, as this is the value to be controlled. For this it was assumed that there are no steady gusts, so that the turbulence wind values on average are zero. If there are gusts, this value should be a filtered velocity V_{filter}, which filters out the noisy turbulence but takes into accounts gusts. In previous simulations, this was equal to V_{∞} as there was no wind, but for turbulence this is not the case.

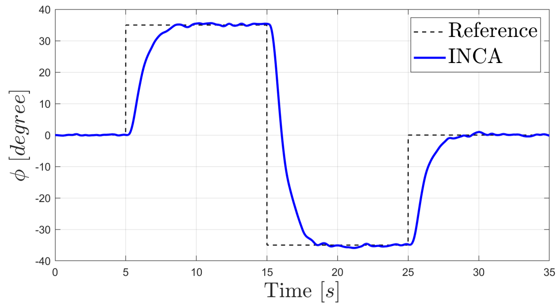

(a) Roll angle ϕ response, with the reference signal.

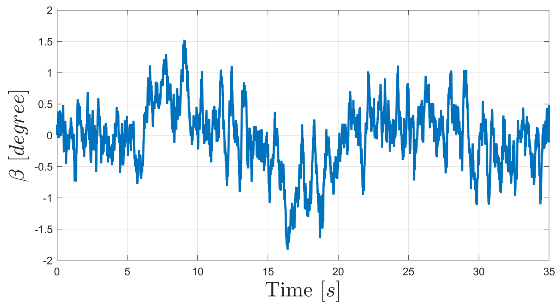

(b) Sideslip angle β response, where $\beta_{\mathrm{ref}} = 0°$.

Figure 5-26: Time responses of the roll and sideslip angle for INCA (3) controller with low gains in turbulence.

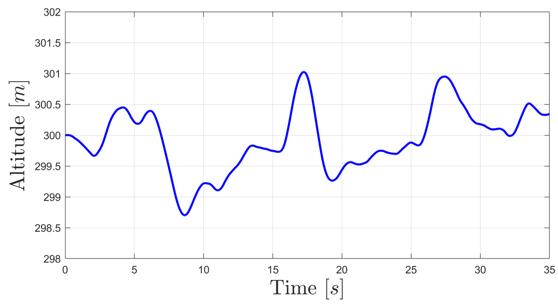

(a) Altitude h response, where $h_{\mathrm{ref}} = 300$ m.

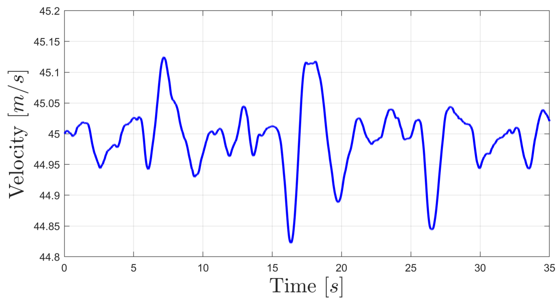

(b) Ground velocity V_{ground} response, where $V_{\mathrm{ref}} = 45$ m/s.

Figure 5-27: Time responses of the altitude and ground velocity for INCA controller (3) with low gains in turbulence.

The control surface deflections and rotational velocities of the propellers are shown in Figure 5-28 and Figure 5-29 respectively. As can be seen, the control surfaces δ_{a} and δ_{r} now show much more oscillations as they need to compensate for the turbulence. Here, δ_{a} is used to stabilize the aircraft in roll around ϕ_{ref}, and δ_{r} to stabilize the aircraft in yaw for β_{ref}. As the propellers control both the roll moment using the PAI effects, and yaw moment using the differential thrust, their thrust is used to actively stabilize the aircraft around both these axes.

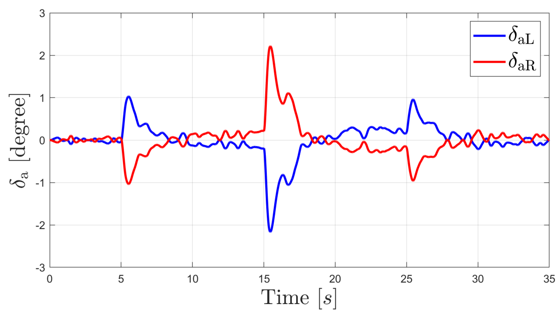

(a) Aileron deflection δ_{aL} and δ_{aR}.

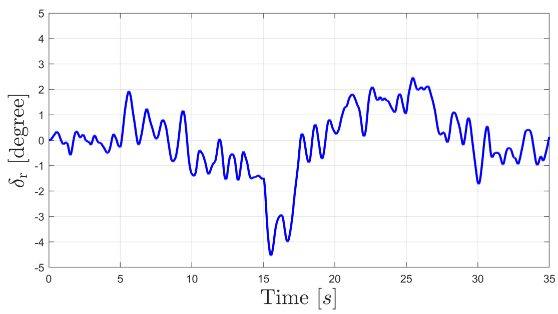

(b) Rudder deflection δ_{r}.

Figure 5-28: Control surface deflection for INCA (3) controller with low gains in turbulence.

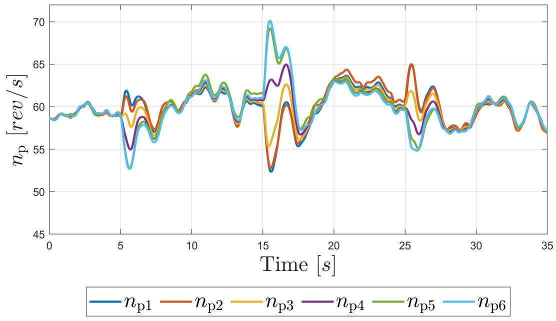

Figure 5-29: Rotational velocities of the individual propellers n_p for the INCA low gains (3) in turbulence

For completeness, the same analysis was done for the INCA MPC (5) controller with high proportional gains. The results for this are shown in Figure C-11 up to and including Figure C-14 in Appendix C. As one can see, by increasing the gains, the tracking of the reference values is improved. Also note, in Figure C-11a, that ϕ can now be tracked perfectly, without the turbulence affecting the roll angle. This is because, in the MPC controller, the actuator dynamics are canceled out. The influence of the disturbance can then be directly compensated as the state measurements, containing the influence of the disturbances, are fed back into the INCA controller. Looking at Figure C-13 and Figure C-14, one can see that the changes in control input are much higher as compared to Figure 5-28 and Figure 5-29 for the low gains controller. This is because the MPC controller immediately compensates for the noisy external disturbances, leading to noisy actuator inputs. It is of interest to investigate what the influence of this control design in combination with turbulence is on actuator wear.

5-8 Conclusions

In this chapter, the different controllers, defined in Table 5-1 were tested in simulation. The reference trajectory was specified as a square wave of 35° on the roll angle ϕ, while the remaining reference variables were kept at their constant trim value. Firstly, the INCA controller (3) was compared against the baseline INDI controller (1) with low proportional gains. Here it was shown, that the same performance can be achieved while using the differential thrust and PAI effects actively for control. Also, because the translational and rotational control loops are merged in the INCA controller, performance for altitude and velocity tracking is increased. The proportional gains were then increased, where it was shown that an MPC controller is required to compensate for the actuator dynamics. Comparing the INCA MPC controller (5) with the baseline INDI controller (2) with high proportional gains, it was shown that a significant performance increase can be achieved when the full potential of the DEP is used. The INCA MPC controller reduces the rise time and RMSE values for tracking while increasing the bandwidth.

Furthermore, the possible increase in propeller power efficiency was investigated. Here it was shown that the INCA power MPC controller (7) gives in an efficiency increase of 6.7% with respect to the baseline INDI controller (1). This value shows that by reformulating the INCA optimization for power consumption of the propellers, the efficiency of the DEP aircraft can be significantly increased. It was also shown how the control allocation changes with airspeed, demonstrating that the controller can be used at different operating points. Also, the introduction of modeling errors was analyzed, both for tracking performance and power optimization. For tracking, modeling errors on the differential thrust, PAI effects and control effectiveness of the control surfaces were introduced, where it was shown that performance only deteriorates when these factors are significantly over-estimated. Note that when these factors switch sign the controller becomes unstable. For power optimization, the incremental increase in power and decrease in drag for the rotational velocity of the propellers were analyzed. For both these factors, under-estimation leads to a decrease in efficiency. For the incremental decrease in drag, the effect can change sign, which results in an excessive increase in power consumption.

After this, the second reference trajectory was applied to the INCA power MPC controller (7). Here it was shown that this controller can find the optimal control distribution over a larger part of the flight envelope. This demonstrated the full advantage of using a nonlinear controller for different operating conditions. Finally, robustness for tip propeller failure and external disturbances was analyzed. Here it was shown that the INCA (3) controller with low proportional gains can compensate for the left propeller failing by stabilizing the aircraft. It is even still able to follow the reference square wave on ϕ, where it was assumed that detection of the fault is in one second. Finally, robustness against external disturbances was evaluated by flying the DEP aircraft through the same turbulence field as in Section 3-6-2. Here it was shown that the INCA (3) controller with low proportional gains can compensate for this, while satisfying the reference variables.

Chapter 6

Conclusion

In this last chapter, the thesis will be concluded by answering the research questions defined in Chapter 1 and giving an overall conclusion for this work. Finally, recommendations for future work, following up on this thesis, will be given in the last section.

6-1 Conclusion

The main goal of this thesis was to design a control allocation method that enables to use all control authorities of the DEP aircraft. It was hypothesized that by using all the control inputs to the full potential, tracking performance and efficiency can be increased. To that aim, it was investigated whether the differential thrust and PAI effects can be actively controlled with the INCA method, increasing efficiency by redefining the secondary objective of the allocation optimization function. The designed INCA controller should be adaptable, so that new aerodynamic information, especially for the uncertain PAI effects, can be easily added. Therefore, as discussed in Chapter 1, the main research question for this thesis was defined as follows.

How can an INCA controller be designed to exploit the extra control authorities of the DEP aircraft and utilize these to its full potential in terms of tracking performance and efficiency?

This research question was divided into three sub-questions which were answered throughout this thesis. An overview of these answers is given in this section and it will conclude with answering the main research question, which forms the general outcome of this thesis.

How can the translational and rotational control loops of the baseline INDI be developed for the DEP aircraft and then synthesized, so that simultaneous control of the velocity, altitude and attitude is achieved?
This research question contains two components. Firstly, there is the need to develop a simulation model in SIMULINK of the DEP aircraft describing all relevant control effects. This model was implemented starting from the general EoM for aircraft in Section 2-1. From

here, the differential thrust and PAI effects were implemented. Note that modeling of the PAI effects is difficult, as they introduce cross-coupled and nonlinear dynamics. Since this thesis focuses on the implementation of the PAI effects in the controller and not the actual modeling, the choice was made to use relatively straightforward analytical formulas describing these effects. This thesis therefore should be seen as the framework to which more accurate models describing the PAI can be added later. These analytical relations are given in Section 2-3, where also the model is given that defines the thrust and power of the propeller.

The second part of the sub-question involves the synthesis of the outer translation and inner rotational INDI control loop of the baseline controller defined in Section 3-4. Merging these two control loops allows for simultaneous control of the velocity, altitude and attitude. Still, as merging these control loops violates the time-scale separation principle, the INDI control law was reformulated without this assumption in Section 3-6. Here it was shown that for the synthesized INDI control law without internal dynamics, a bound can be set on the perturbation term affecting stability and robustness. This perturbation term becomes smaller when sampling at a higher frequency f_s. A sampling time analysis was therefore performed in Section 3-6 where the DEP aircraft was simulated flying through a Von Kármán turbulence field of different intensities. From this analysis, it was be concluded that when sampling at $f_s = 100$ Hz, the perturbation term stays within reasonable bounds. Stability and robustness of the synthesized INDI controller was, therefore, concluded for this sampling frequency.

How can the differential thrust and PAI effects of the DEP aircraft be incorporated in an INCA controller and how does exploiting full control effectiveness knowledge improve tracking performance?

Further development of the controller discussed in the previous sub-question leads to inclusion of the differential thrust and PAI effects in the control law. To do so, the INCA controller introduced in Section 4-2 is used. As a consequence, the control effectiveness for both of these effects needed to be determined. Using the analytical formulas defined in Section 2-3, the control effectiveness was determined using the method discussed in Section 4-3. Including these effects resulted in a controller having full knowledge of all control authorities.

The results for this controller were shown in Section 5-2, where for a low set of proportional gains it was shown that comparable performance with respect to the baseline INDI controller can be achieved, while using the differential thrust and PAI effects actively for attitude control. For a reference step of 35° on the roll angle ϕ, a rise time of approximately 2.4 seconds was achieved with negligible overshoot. As combining rate constraints with actuator dynamics leads to an over-conservative controller, the rate constraints were removed. For the low gains, the actuators do not saturate, so this did not affect the performance. Analysis of robustness against modeling errors was performed in Section 5-4-1. For both the PAI effects and the control surface deflection, overestimation of the effectiveness leads to deteriorated tracking performance of the attitude angles and larger errors concerning the allocated moments around the aircraft. Still note that performance is only severely degraded for significant overestimation of these effects. In contrast, underestimation of the PAI effects leads to better performance as long as the sign of the control effectiveness does not change. Small underestimation of the effectiveness of the control surfaces gives a small performance increase, but when this becomes too large, performance deterioration occurs. Overall, it was concluded that the method is robust to modeling errors, where satisfactory performance remains over a large range of effectiveness errors.

The INCA controller should have more control authority for both roll and yaw moments, so that increasing the proportional gains leads to faster response times. Nevertheless, for these higher gains, the actuators saturate, so that removing the rate constraints affects performance. Therefore, an MPC controller was proposed in Section 4-4 to compensate for the actuator dynamics incrementally, thereby allowing for the implementation of the rate constraints. Implementing the MPC controller allowed for higher proportional gains, where the rise time for a step input of 35° on the roll angle ϕ was decreased to 0.70 s with negligible overshoot. Looking at the frequency domain, the bandwidth of the system for $\phi_{\text{ref}} \rightarrow \phi$ was increased from 0.186 to 0.663 Hz. Note that for combining INCA with MPC, the controller relies on real-time measurements of state derivatives which makes implementation of this controller more difficult, especially considering filtered delayed states.

Finally, it was analyzed whether the INCA controller is robust against propeller faults and external disturbances. For the actuator fault, the left tip propeller's thrust was set to zero. Here it was shown that for a fault detection time of one second, the INCA controller can compensate and stabilize the DEP aircraft while tracking the reference variables. For the external disturbances, the DEP aircraft was flown through a disturbance field, where it was shown that the INCA controller can compensate for these disturbances. For this sub-question, it can therefore be concluded that the differential thrust and PAI effects can be used actively for control in the INCA framework. Augmenting this allocation method with an MPC controller to cancel out the actuator dynamics leads to a significant increase in performance, revealing the full potential of increased control authority using DEP. The INCA controller is robust against modeling errors, propeller failure and external disturbances.

How can the freedom in terms of extra control authorities be exploited to optimize for minimal power consumption of the DEP aircraft and how can this be incorporated into the INCA controller objective functions?

The final sub-question of this thesis explores the opportunity of using control allocation for improving the efficiency of the DEP aircraft. To do so, the secondary objective of the INCA controller is changed, so that it represents the power consumed by the propellers. Using the propeller model and implementing the drag produced by the control surfaces, the control allocation was optimized for minimal power consumption while following the reference signals, as explained in Section 4-2-3. Again, the MPC controller plays an important role in this optimization as the calculated optimal allocation will only be achieved if the commanded incremental control input equals the actual.

The results for this method are shown in Section 5-3. Comparing the power consumed by the propellers for the reference trajectory with the baseline INDI controller, an increase in efficiency of 6.7% was found. This indicates that actively using all control authorities provided by DEP, contributes to an efficiency increase. The performance of this controller concerning modeling uncertainties was evaluated in Section 5-4-2, showing that accurate propeller modeling is key to finding the optimal control allocation for efficiency. In particular, the wing-tip propeller drag reduction plays a significant role and under-estimating this value leads to higher power consumption. Finally, the power consumption for the INCA controller without MPC was analyzed, as this forms a more realistic platform to implement. Here it was shown that without compensation for the actuator dynamics, the efficiency increase is 6.0%. Without MPC the control effectors are still driven to their optimal values asymptotically, making this method a good alternative regarding implementation. For this sub-question, it can therefore be concluded that by using the INCA formulation, defining the secondary objective in terms of propeller power and including the drag effects of the control surfaces, the control allocation leads to an increase in efficiency. Also, a reference trajectory with changing velocity and altitude was introduced, to show performance of the controller over a larger part of the flight envelope. With this, the full advantage of a nonlinear controller was demonstrated, optimizing for propeller power for changing operating conditions.

Looking back at the research objective for this thesis defined in Chapter 1, it can be concluded that by designing an appropriate control allocation method for DEP, both the tracking performance and efficiency can be increased while showing robustness against modeling errors and external disturbances. The INCA controller framework forms a convenient method to design this controller, where the secondary objective is used to minimize the power consumption of the propellers. Augmenting this controller with an MPC controller to compensate for the actuator dynamics contributes to a significant increase in tracking performance. In terms of efficiency, introducing INCA gives a significant increase and augmenting with MPC further increases efficiency. Although this last increase is modest, it still results in more efficient flight. The INCA controller without MPC forms a good alternative in terms of implementation, as efficiency is still increased compared to the baseline INDI controller. Overall, this thesis concludes that by actively using all control authorities of the DEP aircraft, the full potential of this aircraft configuration is revealed so that this method supports the design of new aircraft with significantly less environmental impact.

6-2 Recommendations

Future research into the designed controller can support a further increase in tracking performance and efficiency. Furthermore, analyzing how this controller can be implemented and extending this method to other flying platforms are interesting research subjects. Therefore, the following recommendations, following up on this thesis, can be considered.

PAI effects model
The model considered in this thesis is relatively straightforward, describing the PAI effects with analytical formulas subject to a considerable list of assumptions. Although this thesis concluded that the proposed controller is robust against modeling errors, a more accurate model of the PAI effects will possibly result in better performance for tracking and efficiency. To achieve this, the following two methods can be considered.

- The PAI model can be improved by establishing a detailed CFD study of the SFD including the DEP system or wind tunnel testing. From the data gathered with either of these methods, relations describing the PAI effects can be found. Following the method presented in [38], the aerodynamic database can then be identified using a multivariate simplex B-spline. This allows for efficient computation of directional derivatives in the direction of the control input, so that the control effectiveness matrix can be updated every time step.

- Another method to improve the aerodynamic model is online system identification during flight testing. For this, the Two-step method (TSM) can be used where estimation of the state trajectory and aerodynamic parameters is divided [76]. If these parameters are updated online this leads to an adaptive controller, which directly uses the knowledge gained during system identification. An alternative would be to first analyze the obtained results during flight testing and implement them after careful testing in simulation.

Power optimization
The proposed power optimization method shows a significant decrease in power consumption of the propellers. Still, the power consumption of the DEP aircraft can be further decreased by considering the following two approaches.

- Using the INCA framework, both the first and second objective are optimized with respect to the l_2 norm. For power optimization, looking at the second objective, this means that the l_2 norm of the vector containing the power consumption of each propeller is optimized. To increase the efficiency, the l_1 norm of this vector can be optimized which represents the total power consumption of the propellers. In this thesis, a first attempt was made to implement the second objective with the l_1 norm, but the allocation algorithm did not converge for this, as complementary control inputs were activated. This resulted in large oscillations for these inputs. Further research into implementation of the l_1 norm for the second objective in the INCA controller can result in a further increase in efficiency.
- Another aspect to consider to decrease the power consumption of the DEP aircraft is the reference trajectory specified for the controller in the form of the reference altitude, velocity and attitude. As these have a large influence on the power consumed by the DEP aircraft, it is interesting to see how these can be optimized for efficiency. An example of this is to change the velocity based on an increase of reference altitude to achieve optimal climb velocity [77]. Optimizing these types of reference trajectories specifically for the DEP aircraft can give rise to a further increase in efficiency.

Implementation
The final step of the development of the INCA controller for the DEP-SFD, is implementation on the actual aircraft. Besides extensive testing, where a method should be developed to switch between the different controllers, the main challenge of implementation lays in the proposed MPC controller and design of an FDI algorithm for fault detection. Also, an interesting research opportunity is the implementation of the developed controller on other flying frameworks.

- The MPC controller designed to cancel out the actuator dynamics is subject to several assumptions. The most important limitation is that this method relies on real-time measurements of the state derivatives. By introducing filters, delays are presented in the control law, for which the MPC controller is very sensitive. This results in control inputs oscillating considerably, so that the reference is still tracked but the control inputs are far from their optimal values. Also, it has to be investigated how measurement noise and modeling errors regarding the actuator dynamics, affect the MPC controller's performance. This is a consequence of the MPC controller depending on measurements of the effector outputs and the assumption of linear actuator dynamic models. Furthermore, noisy external disturbances in the form of turbulence give noisy control inputs in combination with the MPC controller. For implementation, it should be investigated how significantly this influences actuator wear. Finally, nonlinear actuator dynamics can be modeled in the MPC controller by using a time-varying linear model, which should reduce the modeling errors and thus increase performance.

- As stated in Section 4-2-4, it was assumed that failure of the propellers can be detected within t_{detect}. In reality, this fault needs to be detected using an FDI algorithm. These can be either based on the innovation signal for the parameter estimation or on a model describing the aircraft [78]. An example of the first method is using TSM, introduced for online system identification, as a fault detection method. Here, the innovation signal of this method is used, which will jump to a high value when a fault occurs. For over-actuated aircraft, where the number of parameters is large, the proposed method might not have enough information to detect the fault. Model-based approaches in this case provide a better solution. An example of this is using the Kalman filter to estimate the states. If the estimated states diverge from the real states, a fault is detected. Note that these approaches rely on an accurate model of the DEP aircraft and it is to be investigated how for example modeling uncertainty in the PAI effects influences performance.

- As a final step, implementation of this INCA controller with power optimization regarding other flying platforms can be considered. Particularly, for over-actuated flying platforms using electric propellers, the controller can be relatively easily adapted. Transition vehicles presented in for example [41] or [79] can be interesting frameworks to apply the designed controller on. As these types of aircraft can use both the vertical propellers and lift of the wing to create the required vertical forces, the proposed INCA controller can find the optimal balance between these regarding efficiency. Also, other types of flying platforms can be considered, so that the proposed controller forms the basis of improving flight efficiency, thereby leading to more sustainable flight in the future.

Appendix A

DEP Model

A-1 Frame transformations

$$\mathbf{T}_{\mathrm{Va}} = \begin{bmatrix} 1 & 0 & 0 \\ 0 & \cos\phi & -\sin\phi \\ 0 & \sin\phi & \cos\phi \end{bmatrix} [25] \tag{A-1}$$

$$\mathbf{T}_{\mathrm{VE}} = \begin{bmatrix} \cos\chi\cos\gamma & \sin\chi\cos\gamma & -\sin\gamma \\ -\sin\chi & \cos\chi & 0 \\ \cos\chi\sin\gamma & \sin\chi\sin\gamma & \cos\gamma \end{bmatrix} [25] \tag{A-2}$$

$$\begin{bmatrix} p \\ q \\ r \end{bmatrix} = \begin{bmatrix} 1 & 0 & -\sin\theta \\ 0 & \cos\phi & \sin\phi\cos\theta \\ 0 & -\sin\phi & \cos\phi\cos\theta \end{bmatrix} \begin{bmatrix} \dot{\phi} \\ \dot{\theta} \\ \dot{\psi} \end{bmatrix} [42] \tag{A-3}$$

$$\begin{bmatrix} \dot{\phi} \\ \dot{\theta} \\ \dot{\psi} \end{bmatrix} = \begin{bmatrix} 1 & \sin\phi\tan\theta & \cos\phi\tan\theta \\ 0 & \cos\phi & -\sin\phi \\ 0 & \frac{\sin\phi}{\cos\theta} & \frac{\cos\phi}{\cos\theta} \end{bmatrix} \begin{bmatrix} p \\ q \\ r \end{bmatrix} [42] \tag{A-4}$$

$$\mathbf{T}_{\mathrm{ba}} = \begin{bmatrix} \cos\alpha\cos\beta & -\cos\alpha\sin\beta & -\sin\beta \\ \sin\beta & \cos\beta 0 & \\ \sin\alpha\cos\beta & -\sin\alpha\sin\beta & \cos\alpha \end{bmatrix} \tag{A-5}$$

A-2 EoM assumptions

To define the EoM, the following assumptions were made [42].

Spherical Earth : In reality the earth is an ellipsoid but will be modeled as a sphere.

Rigid body and constant mass : This assumptions is used to give a constant matrix of inertia and assumes there are no elastic modes and no fuel consumption

Non-rotating Earth : This assumption discards the influence of the coriolis and centripetal acceleration. These will only have an effect for large time-spans in the order of hours.

Flat Earth For relative short motion the curvature of the Earth has a negligible influence and Earth can thus be modeled as a flat surface.

Plane of symmetry : In the body fixed reference frame (F_B, which will be introduced later, this means that I_{xy} and I_{yz} are zero.

Conventional configuration : An aircraft with conventional configuration has one main wing, a horizontal and vertical tail, aileron, elevators and one rudder.

Zero wind velocity : This means that the undisturbed air is at rest relative to the earth so that the kinematic velocity is equal to the aerodynamic velocity.

A-3 PAI effects model

A-3-1 Propeller test data

The propeller test data from the XPROP for different advances ratios J is given in Figure A-1. In these figures the C_T and C_P values, with their polynomial fit are plotted. For C_T, this fit is as sixth-order polynomial defined as

$$\hat{C}_{\mathrm{T}}(J) = p_1 J^6 + p_2 J^5 + p_3 J^4 + p_4 J^3 + p_5 J^2 + p_6 J + p_7, \tag{A-6}$$

where the polynomial constants are defined as

Table A-1: Polynomial fit parameters C_T

p_1	0.0720
p_2	-0.7334
p_3	3.2110
p_4	-7.5925
p_5	9.7388
p_6	-6.2515
p_7	1.9049

For C_P, this fit is a fifth-order polynomial defined as

$$\hat{C}_{\mathrm{P}}(J) = p_1 J^5 + p_2 J^4 + p_3 J^3 + p_4 J^2 + p_5 J + p_6 J, \tag{A-7}$$

where the polynomial constants are defined as

Table A-2: Polynomial fit parameters C_P

p_1	0.3820
p_2	-2.7291
p_3	7.2036
p_4	-8.9120
p_5	5.1068
p_6	-0.3818

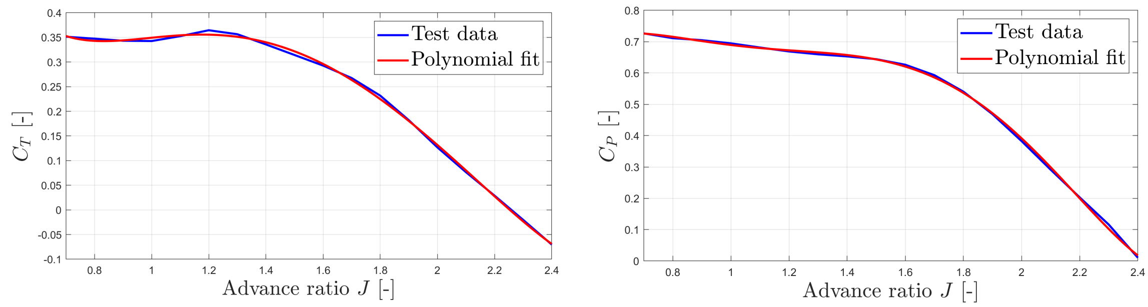

(a) Thrust coefficient C_T

(b) Power coefficient C_P

Figure A-1: The thrust and power coefficients C_T and C_P for different advance ratios J with their polynomial fit.

A-3-2 PAI model assumptions

The following assumptions apply to method for modeling the PAI effects [80].

- The velocity increase at the actuator disk is computed assuming uniform axial inflow
- Variations in lift due to swirl are neglected (actuator disk assumption)
- The airfoil is symmetric, and thus zero lift is produced at $\alpha = 0$.
- The effect of each propeller on the adjacent ones is neglected.
- The effect of the propellers on the wing is limited to the spanwise interval occupied by the disks $\Delta Y/b$
- Within this spanwise interval, the effect on the wing is considered uniform in spanwise direction. This assumption is more accurate if $\Delta y << 1$.
- The wing is supposed to be fully immersed in the slipstream, that is, half of the slipstream flows under the wing and half over the wing.

A-3-3 Slipstream correction factor

$$\begin{aligned}\beta &= K_0X + K_1X\left(\frac{R}{c}\right) + K_2X\left(\frac{R}{c}\right)^2 + K_3X\left(\frac{R}{c}\right)^3 + K_4X\left(\frac{R}{c}\right)^4 \\ &= \sum_{i=0}^{4} K_iX\left(\frac{R}{c}\right)^i,\end{aligned} \tag{A-8}$$

$$
\begin{aligned}
X &= \begin{bmatrix} 1 & u/c & (u/c)^2 & (u/c)\,(V_j/V_\infty) & (V_j/V_\infty) & (V_j/V_\infty)^2 \end{bmatrix}^T \\
K_0 &= \begin{bmatrix} 0.378269 & 0.748135 & -0.179906 & -0.056161 & -0.146746 & -0.015255 \end{bmatrix} \\
K_1 &= \begin{bmatrix} 3.071020 & -1.769885 & 0.436595 & 0.148643 & -0.989332 & 0.197910 \end{bmatrix} \\
K_2 &= \begin{bmatrix} -2.827730 & 2.054064 & -0.467410 & -0.277325 & 0.696981 & -0.008226 \end{bmatrix} \\
K_3 &= \begin{bmatrix} 0.997936 & -0.916118 & 0.199829 & 0.157810 & -0.143368 & -0.057385 \end{bmatrix} \\
K_4 &= \begin{bmatrix} -0.127846 & 0.135843 & -0.028919 & -0.026546 & 0.010470 & 0.012221 \end{bmatrix}.
\end{aligned}
\tag{A-9}
$$

A-4 Geometric and aerodynamic model

Table A-3: Aerodynamic model of the DEP aircraft

Coefficent		Dependency	Explanation
C_{i_a}	C_{i_a}	α	Airframe aerodynamics
	C_{i_a}	$\dot{\alpha}$	
	C_{i_a}	α, β	
C_{i_ω}	$\frac{pb}{2V} C_{i_p}$	-	Dynamic airframe aerodynamics
	$\frac{qc}{2V} C_{i_q}$	-	
	$\frac{rb}{2V} C_{i_r}$	-	
C_{i_δ}	$C_{i_{\delta_\mathrm{a}}}$	δ_a	Control surfaces
	$C_{i_{\delta_\mathrm{e}}}$	$\delta_\mathrm{e}, \alpha$	
	$C_{i_{\delta_\mathrm{r}}}$	δ_r	
	$C_{i_{\delta_\mathrm{s}}}$	-	
$C_{i_{n_p}}$	$C_{i_{n_\mathrm{p}}}$	$\alpha, \beta, \boldsymbol{n}_\mathrm{p}, V_\infty, \rho, C_{L_\mathrm{ac}}, \beta_\mathrm{corr}$	Differential thrust and PAI effects

Table A-4: Design and performance parameters full scale and SFD aircraft

Configuration parameter	Full scale	SFD
Span (m)	34	4
Wing aero (m^2)	122.4	1.694
Mean aerodynamic chord (m)	4.193	0.49
Reynolds number (-)	35.5×10^6	1.5×10^6
Climb mass (kg)	73800	130
Descent mass (kg)	59500	104
Flying altitude (m)	1067	300
Flying speed (m/s)	135	46

For the DEP aircraft, because of propeller and battery installation the mass was estimated at 146 kg. The mass moment of inertia matrix is given as

$$\mathbf{I} = \begin{bmatrix} 38.85 & -0.33 & 6.18 \\ -0.33 & 103.44 & -0.16 \\ 6.18 & -0.16 & 136.30 \end{bmatrix} \tag{A-10}$$

A-5 Control input constraints and actuator dynamics

Table A-5: Control inputs constraints

Limit	δ_{aL}	δ_{aR}	δ_{e}	δ_{r}	n_{p}
u_{min}	-25°	-25°	-15°	-30°	0 rev/s
u_{max}	25°	25°	30°	30°	100 rev/s
$\dot{u}_{\mathrm{max}}$	243°$/s$	243°$/s$	207°$/s$	207°$/s$	100 rev/s^2

Table A-6: Actuator dynamics

Second-order dynamics	δ_{aL}	δ_{aR}	δ_{e}	δ_{r}	n_{p}
ω_{n}	6.46	6.46	5.68	5.68	6
ζ	0.821	0.821	0.859	0.859	0.85

A-6 Turbulence implementation

To implement the turbulence the Von Kármán [45] turbulence model was used. This gives a wind velocity vector in the F_{b} frame defined as

$$\boldsymbol{V}_{\mathrm{wind}} = \begin{bmatrix} u_{\mathrm{wind}} & v_{\mathrm{wind}} & w_{\mathrm{wind}} \end{bmatrix}^{\mathrm{T}}. \tag{A-11}$$

The intensity of these values is based on the wind velocity at 6 m altitude. For a wind velocity of 10 m/s, the turbulence field is given in the Figure A-2.

The wind velocity is then added to the aircraft's velocity so that $\boldsymbol{V}_\infty = \boldsymbol{V} + \boldsymbol{V}_{\mathrm{wind}}$. Using the formulas in Section 3-4-2, which give a relation for α, $\dot{\alpha}$, β and $\dot{\beta}$, based on u, v, w which now included the wind velocity, the changes with respect to the angle of attack angle of sideslip and their rates were calculated. These changes, together with the change in $\boldsymbol{V}_\infty$ gives a change in forces and moments applied to the aircraft, which is the results of the turbulence field, where against the controllers were tested.

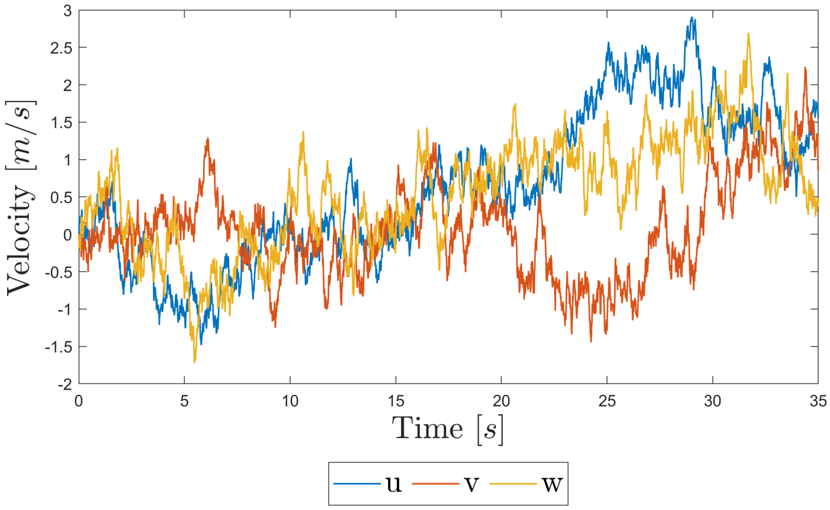

Figure A-2: Turbulence field velocities in the F_b frame for low altitude wind velocity equal to 10 m/s.

A-7 Linear state space

$$\mathbf{A} = \begin{bmatrix} 0 & 0 & 0 & 0.995 & 0 & 0.1 & 0 & 0 & 0 & 0 & 0 & 0 \\ 0 & 0 & 0 & 0 & 1 & 0 & -4.502 & 0 & 45 & 0 & 0 & 0 \\ 0 & 0 & 0 & -0.1 & 0 & 0.995 & 0 & -45 & 0 & 0 & 0 & 0 \\ 0 & 0 & 0 & -0.023 & 0 & 0.273 & 0 & -9.757 & 0 & 0 & -4.415 & 0 \\ 0 & 0 & 0 & 0 & 0.374 & 0 & 9.774 & 0 & 0 & 4.461 & 0 & -44.858 \\ 0 & 0 & 0 & -0.220 & 0 & -1.786 & 0 & -1.0 & 0 & 0 & 44.132 & 0 \\ 0 & 0 & 0 & 0 & 0 & 0 & 0 & 0 & 0 & 1.0 & 0 & 0.1 \\ 0 & 0 & 0 & 0 & 0 & 0 & 0 & 0 & 0 & 0 & 1.0 & 0 \\ 0 & 0 & 0 & 0 & 0 & 0 & 0 & 0 & 0 & 0 & 0 & 1.005 \\ 0 & 0 & 0 & 0 & -0.691 & -0.002 & 0.034 & 0 & 0 & -4.679 & -0.019 & 1.925 \\ 0 & 0 & 0 & 0.021 & -0.002 & -0.217 & 0 & 0 & 0 & -0.015 & -2.211 & 0.004 \\ 0 & 0 & 0 & 0 & 0.286 & 0 & -0.014 & 0 & 0 & 0.059 & -0.002 & -1.089 \end{bmatrix} \tag{A-12a}$$

$$\mathbf{B} = \begin{bmatrix} 0 & 0 & 0 & 0 \\ 0 & 0 & 0 & 0 \\ 0 & 0 & 0 & 0 \\ 0 & 0.407 & 0 & 0.043 \\ -0.138 & 0 & 3.071 & 0 \\ 0 & -4.26 & 0 & -0.043 \\ 0 & 0 & 0 & 0 \\ 0 & 0 & 0 & 0 \\ 0 & 0 & 0 & 0 \\ -10.805 & -0.117 & 6.525 & 0 \\ -0.034 & -13.789 & 0.006 & 0 \\ 0.3625 & -0.012 & 9.213 & 0 \end{bmatrix} \tag{A-12b}$$

$$\mathbf{C} = \begin{bmatrix} 0 & 0 & 0 & 0.995 & 0 & 0.1 & 0 & 0 & 0 & 0 & 0 & 0 \\ 0 & 0 & -1 & 0 & 0 & 0 & 0 & 0 & 0 & 0 & 0 & 0 \\ 0 & 0 & 0 & 0 & 0 & 0 & 0 & 0 & 0 & 1 & 0 & 0 \\ 0 & 0 & 0 & 0 & 0 & 0 & 0 & 0 & 0 & 0 & 1 & 0 \\ 0 & 0 & 0 & 0 & 0 & 0 & 0 & 0 & 0 & 0 & 0 & 1 \end{bmatrix} \tag{A-12c}$$

$$\mathbf{D} = 0 \tag{A-12d}$$

Appendix B

INCA controller

B-1 Derivation INDI without time-scale separation

In [15] the INDI is derived for a system with arbitrary relative degree $\boldsymbol{\rho}$ using the diffeomorphism $\boldsymbol{z} = \mathbf{T}(\boldsymbol{x}) = \begin{bmatrix} \mathbf{T}_1(\boldsymbol{x}) & \mathbf{T}_2(\boldsymbol{x}) \end{bmatrix}^{\mathrm{T}} = \begin{bmatrix} \boldsymbol{\eta} & \boldsymbol{\xi} \end{bmatrix}^{\mathrm{T}}$ where $\boldsymbol{\eta}$ are the internal dynamics and $\boldsymbol{\xi}$ the external dynamics respectively. As the system considered in Eq. (3-65) has no internal dynamics, $\boldsymbol{\eta} = 0$ and $\boldsymbol{\xi} = \boldsymbol{x}$. This simplifies the derivation for stability so that throughout the remainder of this section the notation of [15] is followed but without considering the internal dynamics. This gives

$$\begin{aligned} \dot{\boldsymbol{y}} &= \boldsymbol{a}(\boldsymbol{x}) + \mathcal{B}(\boldsymbol{x})\boldsymbol{u} \\ &= \boldsymbol{f}(\boldsymbol{x}) + \mathbf{G}(\boldsymbol{x})\boldsymbol{u}, \end{aligned} \tag{B-1}$$

where $\boldsymbol{f}(\boldsymbol{x})$ and $\mathbf{G}(\boldsymbol{x})$ are defined in Eq. (3-65). Taking the first-order Taylor expansion using Eq. (2-41) of $\dot{\boldsymbol{y}} = \boldsymbol{a}(\boldsymbol{x}) + \mathcal{B}(\boldsymbol{x})\boldsymbol{u}$ gives

$$\begin{aligned} \dot{\boldsymbol{y}} &= \dot{\boldsymbol{y}}_0 + \left.\frac{\partial\left(\boldsymbol{a}(\boldsymbol{x}) + \mathcal{B}(\boldsymbol{x})\boldsymbol{u}\right)}{\partial \boldsymbol{x}}\right|_0 \Delta\boldsymbol{x} + \left.\frac{\partial\left(\boldsymbol{a}(\boldsymbol{x}) + \mathcal{B}(\boldsymbol{x})\boldsymbol{u}\right)}{\partial \boldsymbol{u}}\right|_0 \Delta\boldsymbol{u} + \mathcal{O}(\Delta\boldsymbol{x}^2) + \mathcal{O}(\Delta\boldsymbol{u}^2) \\ \dot{\boldsymbol{y}} &= \dot{\boldsymbol{y}}_0 + \left.\frac{\partial\left(\boldsymbol{a}(\boldsymbol{x}) + \mathcal{B}(\boldsymbol{x})\boldsymbol{u}\right)}{\partial \boldsymbol{x}}\right|_0 \Delta\boldsymbol{x} + \mathcal{B}(\boldsymbol{x}_0)\Delta\boldsymbol{u} + \mathcal{O}(\Delta\boldsymbol{x}^2) \\ \dot{\boldsymbol{y}} &= \dot{\boldsymbol{y}}_0 + \mathcal{B}(\boldsymbol{x}_0)\Delta\boldsymbol{u} + \boldsymbol{\delta}(\boldsymbol{x}, \Delta t), \end{aligned} \tag{B-2}$$

The perturbation term $\boldsymbol{\delta}$ is thus given as

$$\boldsymbol{\delta}(\boldsymbol{x}, \Delta t) = \left.\frac{\partial\left(\boldsymbol{a}(\boldsymbol{x}) + \mathcal{B}(\boldsymbol{x})\boldsymbol{u}\right)}{\partial \boldsymbol{x}}\right|_0 \Delta\boldsymbol{x} + \mathcal{O}^2. \tag{B-3}$$

The incremental control input can then be designed as

$$\Delta\boldsymbol{u} = \mathcal{B}^{-1}(\boldsymbol{x}_0)\left(\boldsymbol{\nu} - \dot{\boldsymbol{y}}_0\right), \tag{B-4}$$

so that $\boldsymbol{u} = \Delta\boldsymbol{u} + \boldsymbol{u}_0$. The closed loop system for the INDI control law is then given as

$$\begin{aligned} \dot{\boldsymbol{x}} &= \boldsymbol{\nu} + \boldsymbol{\delta}(\boldsymbol{x}, \Delta t) \\ \boldsymbol{y} &= \boldsymbol{x}, \end{aligned} \tag{B-5}$$

whereas in the ideal case $\dot{\boldsymbol{y}}$ is completely controlled by the pseudo-control input $\boldsymbol{\nu}$ so that

$$\begin{aligned}\dot{\boldsymbol{x}} &= \boldsymbol{\nu}\\ \boldsymbol{y} &= \boldsymbol{x}.\end{aligned} \tag{B-6}$$

The $\boldsymbol{\delta}$ term is normally omitted in literature by stating that $\Delta\boldsymbol{x} << \Delta\boldsymbol{u}$ when the sampling frequency is high enough as was done in Section 3-3. As stated before this assumption does not hold for the combined EoM of Eq. (3-65).

For stability analysis the pseudocontrol input is designed as $\boldsymbol{\nu} = -\mathbf{K}\boldsymbol{x}$ so that $\dot{\boldsymbol{x}} = -\mathbf{K}\boldsymbol{x}$ is hurwitz. Including the perturbation term the closed loop system is then thus given as

$$\dot{\boldsymbol{x}} = -\mathbf{K}\boldsymbol{x} + \boldsymbol{\delta}(\boldsymbol{x}, \Delta t) \tag{B-7}$$

As the nominal system $\dot{\boldsymbol{x}} = -\mathbf{K}\boldsymbol{x}$ is Hurwitz, it is stable. Considering stability of the perturbed system the norm of the perturbation term is given as

$$||\boldsymbol{\delta}(\boldsymbol{x}, \Delta t)||_2 = \left|\left| \left.\frac{\partial\left(\boldsymbol{a}(\boldsymbol{x}) + \mathcal{B}(\boldsymbol{x})\boldsymbol{u}\right)}{\partial \boldsymbol{x}}\right|_0 \Delta\boldsymbol{x} + \mathcal{O}^2 \right|\right|_2 \tag{B-8}$$

Assuming that the partial derivatives of $\boldsymbol{a}(\boldsymbol{x})$ and $\mathcal{B}(\boldsymbol{x})$ with respect to $\boldsymbol{x}$ are bounded up to any order, because of continuity of $\boldsymbol{x}$

$$\lim_{\Delta t \to 0} ||\Delta\boldsymbol{x}||_2 = 0 \tag{B-9}$$

which means that the perturbation term satisfies

$$\lim_{\Delta t \to 0} ||\boldsymbol{\delta}(\boldsymbol{x}, \Delta t)||_2 = 0,\ \forall x \in \mathbb{R}^n \tag{B-10}$$

This equation indicates that $\forall\bar{\delta}$, $\exists\overline{\Delta t} \geq 0$, such that for all $0 < \Delta t \leq \overline{\Delta t}$, $\forall\boldsymbol{x} \in \mathbb{R}^n, \forall t \geq t_0$, $||\boldsymbol{\delta}(x, \Delta t)||_2 \leq \bar{\delta}$. This thus means that there exists a Δt that guarantees a bound on $\boldsymbol{\delta}(x, \Delta t)$ and this bound can be decreased by increasing the sampling frequency. The above statement can be formalized into [15]

Theorem 1. *If $||\boldsymbol{\delta}(x, \Delta t)||_2 \leq \bar{\delta}$ is satisfied for all, $\boldsymbol{x} \in \mathbb{R}^n$, then the state $\boldsymbol{x}$ is globally ultimately bounded by a class $\mathcal{K}$ function of $\bar{\delta}$,*

where the internal dynamics are not taken into account. A proof of this theorem including internal dynamics can be found in [15]. Note that the same analysis can be done for reference tracking using a feedforward term $\dot{\boldsymbol{r}}$ as this only shifts the equilibrium.

Considering an external disturbance $\boldsymbol{d}$ which is bounded so that

$$\bar{d} \triangleq \sup\left\{||\boldsymbol{d}(t), \boldsymbol{d} \in \mathbb{R}^n||\right\},\ \forall t \geq t_0 \tag{B-11}$$

and continuous which means $\lim_{\Delta t \to 0} ||\boldsymbol{d}||_2 = 0$ which means that for a given sampling frequency there exist a supremum of $||\Delta\boldsymbol{d}||_2$. Therefore,

$$\bar{d}(\Delta t) \triangleq \sup\left\{||\Delta\boldsymbol{d}(t), \Delta\boldsymbol{d} \in \mathbb{R}^n||\right\},\ \forall t \geq t_0, \tag{B-12}$$

which is reduced by increasing the sampling frequency. As the disturbance d is bounded this means that the state $\boldsymbol{x} \in \mathbb{R}^n$ is also bounded which can be formalized into [15]

Theorem 2. $||\boldsymbol{\delta}(x, \Delta t)||_2 \leq \bar{\delta}$ *is satisfied for all, $\boldsymbol{x} \in \mathbb{R}^n$, then the state $\boldsymbol{x}$ is ultimately bounded by a class $\mathcal{K}$ function of $\bar{\delta}$ and $\bar{d}$ which is defined as $\boldsymbol{\mathcal{T}}$,*

where the internal dynamics are not taken into account. A proof of this theorem including internal dynamics can be found in [15].

B-2 Gains and weighting matrices

Table B-1: Gains of the different controllers

Gains	INDI low (1)	INDI high (2)	INCA low (3,6,7)	INCA high (4)	INCA MPC high (5)
K_{h}	0.2	0.2	0.3	0.3	0.3
$\mathbf{K}_{\bar{\boldsymbol{x}}_1}$	$\mathrm{diag}\left([0.5, 0.5]\right)$	$\mathrm{diag}\left([0.5, 0.5]\right)$	$\mathrm{diag}\left([1, 1]\right)$	$\mathrm{diag}\left([1, 1]\right)$	$\mathrm{diag}\left([1, 1]\right)$
$\mathbf{K}_{\boldsymbol{x}_2}$	$\mathrm{diag}\left([0.8, 2, 1]\right)$	$\mathrm{diag}\left([2, 2, 1]\right)$	$\mathrm{diag}\left([0.8, 2, 1]\right)$	$\mathrm{diag}\left([1.6, 2, 1]\right)$	$\mathrm{diag}\left([3, 2, 1]\right)$
$\mathbf{K}_{\boldsymbol{x}_3}$	$\mathrm{diag}\left([30, 5, 30]\right)$	$\mathrm{diag}\left([30, 5, 30]\right)$	$\mathrm{diag}\left([30, 5, 30]\right)$	$\mathrm{diag}\left([30, 5, 30]\right)$	$\mathrm{diag}\left([30, 5, 30]\right)$
$\mathbf{K}_{\mathrm{rm}_{\bar{\boldsymbol{x}}_1}}$	$\mathrm{diag}\left([5, 5]\right)$	$\mathrm{diag}\left([5, 5]\right)$	$\mathrm{diag}\left([2, 2]\right)$	$\mathrm{diag}\left([2, 2]\right)$	$\mathrm{diag}\left([2, 2]\right)$
$\mathbf{K}_{\mathrm{rm}_{\boldsymbol{x}_3}}$	$\mathrm{diag}\left([6, 5, 5]\right)$	$\mathrm{diag}\left([8, 5, 5]\right)$	$\mathrm{diag}\left([6, 5, 5]\right)$	$\mathrm{diag}\left([8, 5, 5]\right)$	$\mathrm{diag}\left([10, 5, 5]\right)$

The controller numbers refer to the different controllers specified in Table 5-1.

For the INCA controller, the control force and moment weighting matrix was defined as

$$\mathbf{Q} = 10 \ \mathrm{diag}\left([m, I_{yy}, 1, 1, 1]\right), \tag{B-13}$$

where the first two factors are scaled so that they are in the same order of magnitude. For the control preference vector, the weighting matrix was defined as

$$\mathbf{W} = \mathrm{diag}\left(\overline{\boldsymbol{u}} - \underline{\boldsymbol{u}}\right)^{-1}, \tag{B-14}$$

which thus scales with the minimum and maximum values of the control inputs. For the power optimization, the weigting matrix is defined as

$$\mathbf{W} = \frac{1}{V_\infty} \mathrm{diag}\left([1, 1, 1, 1, 1, 1]\right), \tag{B-15}$$

which thus scales with the velocity.

B-3 Kalman filter

This section derives the Kalman filter, which is used in the MPC controller to compensate for the actuator dynamics. As discussed in Section 4-4, the actuartor dynamics can be modeled as an LTI system. Therefore, a stationary Kalman gain can be calculated, following the method of [68] which uses the theorem of [72].

Firstly, the unit pulse $\Delta(k)$ is defined as

$$\Delta(k) = \begin{cases} 1, & \text{for } k = 0 \\ 0, & \text{for } k \neq 0 \end{cases} \tag{B-16}$$

Considering the following LTI system

$$\boldsymbol{x}(k+1) = \mathbf{A}\boldsymbol{x}(k) + \boldsymbol{B}\boldsymbol{u}(k)\boldsymbol{w}(k) \tag{B-17a}$$
$$\boldsymbol{y}(k) = \mathbf{C}\boldsymbol{x}(k) + \boldsymbol{v}(k), \tag{B-17b}$$

where $\boldsymbol{w}(k)$ and $\boldsymbol{v}(k)$ are zero-mean random noise values with covariance matrix

$$E\begin{bmatrix} \boldsymbol{w}(k) \\ \boldsymbol{v}(k) \end{bmatrix}\begin{bmatrix} \boldsymbol{w}(j)^{\mathrm{T}} & \boldsymbol{v}(j)^{\mathrm{T}} \end{bmatrix} = \begin{bmatrix} \mathbf{Q} & \mathbf{S} \\ \mathbf{S}^{\mathrm{T}} & \mathbf{R} \end{bmatrix}\Delta(k-j), \tag{B-18}$$

such that

$$\begin{bmatrix} \mathbf{Q} & \mathbf{S} \\ \mathbf{S}^{\mathrm{T}} & \mathbf{R} \end{bmatrix} \geq 0, \text{ and } \mathbf{R} > 0. \tag{B-19}$$

If the pair $(\mathbf{A}, \mathbf{C})$ is observable and the pair $(\mathbf{A}, \mathbf{Q}^{1/2})$ is reachable, then

$$\mathbf{P}(k|k-1) = E\left[(\boldsymbol{x}(k) - \hat{\boldsymbol{x}}(k|k-1))\,(\boldsymbol{x}(k) - \hat{\boldsymbol{x}}(k|k-1))^{\mathrm{T}}\right], \tag{B-20}$$

with $\hat{\boldsymbol{x}}(k|k-1) = E\left[\boldsymbol{x}(k)\right]$, satisfies

$$\lim_{k\to\infty} \mathbf{P}(k|k-1) = \mathbf{P} > 0, \tag{B-21}$$

for any symmetric initial condition $\mathbf{P}(0|k-1) = \mathbf{P} > 0$, where $\mathbf{P}$ satisfies

$$\mathbf{P} = \mathbf{APA}^{\mathrm{T}} + \mathbf{Q} - \left(\mathbf{S} + \mathbf{APC}^{\mathrm{T}}\right)\left(\mathbf{CPC}^{\mathrm{T}} + \mathbf{R}\right)^{-1}\left(\mathbf{S} + \mathbf{APC}^{\mathrm{T}}\right)^{\mathrm{T}}. \tag{B-22}$$

Moreover, such a $\mathbf{P}$ is unique. Using the matrix $\mathbf{P}$ to define the Kalman gain $\mathbf{K}$ gives

$$\mathbf{K} = \left(\mathbf{S} + \mathbf{APC}^{\mathrm{T}}\right)\left(\mathbf{CPC}^{\mathrm{T}} + \mathbf{R}\right)^{-1}, \tag{B-23}$$

the the matrix $\mathbf{A} - \mathbf{KC}$ is stable. This gain $\mathbf{K}$ is used in the innovation predictor model of Eq. (4-59) to give the one-step-ahead prediction of the state.

B-4 General MPC problem formulation

In Section 4-4, it was shown that the optimization function defined in Eq. (4-58) needs to be solved to calculate the optimal control inputs in the MPC formulation. The general MPC optimization problem is defined as [66]

$$\begin{aligned} \min_{\boldsymbol{u}(t)} \quad & J_{N_\mathrm{P}}(\boldsymbol{x}(t, \boldsymbol{u}(t)) \\ \text{subject to} \quad & \boldsymbol{x}(k+1|t) = \boldsymbol{f}(\boldsymbol{x}(k|t), \boldsymbol{u}(k|t)),\; k = 0, 1, ..., N_\mathrm{p} - 1, \\ & x(0|t) = x(t) \\ & x(k|t) \in \mathcal{X},\; \boldsymbol{u}(k|t) \in \mathcal{U},\; k = 0, 1, ..., N_\mathrm{p} - 1, \\ & \boldsymbol{x}(N|t) \in \mathcal{Z}. \end{aligned} \tag{B-24}$$

Here J_{N_p} is the objective function that is to be minimized over the prediction horizon N_p, $\mathcal{M}$ is the state constraint set, $\mathcal{U}$ the input constraint set and $\mathcal{Z}$ the feasible set. the objective function J_{N_p} can be defined in various forms. For the MPC controller implementation is was defined as Eq. (4-58).

B-5 Active set algorithm

The WLS problem is defined as

$$\min_{\boldsymbol{u}} \left\| \begin{pmatrix} \mathbf{QB} \\ \mathbf{W} \end{pmatrix} \boldsymbol{u} - \begin{pmatrix} \mathbf{Q}\boldsymbol{\tau}_{\mathrm{c}} \\ \mathbf{W}\boldsymbol{u}_{\mathrm{p}} \end{pmatrix} \right\|_2^2 \quad \text{subject to } \mathbf{C}\boldsymbol{u} \geq \boldsymbol{U}. \tag{B-25}$$

Algorithm 1 Active set QP optimization for WLS [64], [29]

Let $\boldsymbol{u}_0$ be a feasible starting point so that it satisfies $\mathbf{C}\boldsymbol{u} \geq \boldsymbol{U}$. Let the working set $\boldsymbol{\mathcal{W}}$ contain a subset of the active inequality constraints at $\boldsymbol{u}_0$. Let N be the maximum number of iterations.

for $k = 0, 1, 2, ..., N-1$ **do**

Given $\boldsymbol{u}_k$, find the optimal perturbation $\boldsymbol{p}$, considering the constraints in the working set $\boldsymbol{\mathcal{W}}$ as equality constraints and disregarding the remaining inequality constraints. Solve

$$\min_{\boldsymbol{p}} \left\| \begin{pmatrix} \mathbf{QB} \\ \mathbf{W} \end{pmatrix} (\boldsymbol{u}_k + \boldsymbol{p}) - \begin{pmatrix} \mathbf{Q}\boldsymbol{\tau}_{\mathrm{c}} \\ \mathbf{W}\boldsymbol{u}_{\mathrm{p}} \end{pmatrix} \right\|_2 \quad \text{Subject to } \mathbf{B}\boldsymbol{p} = 0,\ \boldsymbol{p}_i = 0, i \in \boldsymbol{\mathcal{W}} \tag{B-26}$$

if $\boldsymbol{u}_k + \boldsymbol{p}$ is feasible **then**

Set $\boldsymbol{u}_{k+1} = \boldsymbol{u}_k + \boldsymbol{P}$ and compute the Lagrange multiplier $\boldsymbol{\Lambda}$ using Eq. (B-27) where $\boldsymbol{\Lambda}$ is

associated with the active constraints in $\mathbf{C}\boldsymbol{u} \geq \boldsymbol{U}$.

if All $\boldsymbol{\Lambda} \geq 0$ **then**

$\boldsymbol{u}_{k+1}$ is the optimal solution to Eq. (B-25)

else

Remove the constraint associated with the most negative Λ from $\boldsymbol{\mathcal{W}}$.

end if

else

Determine the maximum step length α such that $\boldsymbol{u}_{k+1} = \boldsymbol{u}_k + \alpha\boldsymbol{p}$ is feasible. Add the primary bounding constraint to the working set $\boldsymbol{\mathcal{W}}$.

end if

end for

The Lagrange multiplier $\boldsymbol{\Lambda}$ is determined with

$$\begin{bmatrix} \mathbf{QB} \\ \mathbf{W} \end{bmatrix}^{\mathrm{T}} \left(\begin{bmatrix} \mathbf{QB} \\ \mathbf{W} \end{bmatrix} \boldsymbol{u} - \begin{bmatrix} \mathbf{Q}\boldsymbol{\tau}_{\mathrm{c}} \\ \mathbf{W}\boldsymbol{u}_{\mathrm{p}} \end{bmatrix} \right) = \boldsymbol{C}_0^{\mathrm{T}} \boldsymbol{\Lambda}, \tag{B-27}$$

where $\boldsymbol{C}_0$ contains the rows of $\boldsymbol{C}$ that correspond to the constraints in the active set $\boldsymbol{\mathcal{W}}$

Appendix C

Additional simulation results

C-1 Results INCA high gains controller (4) without MPC

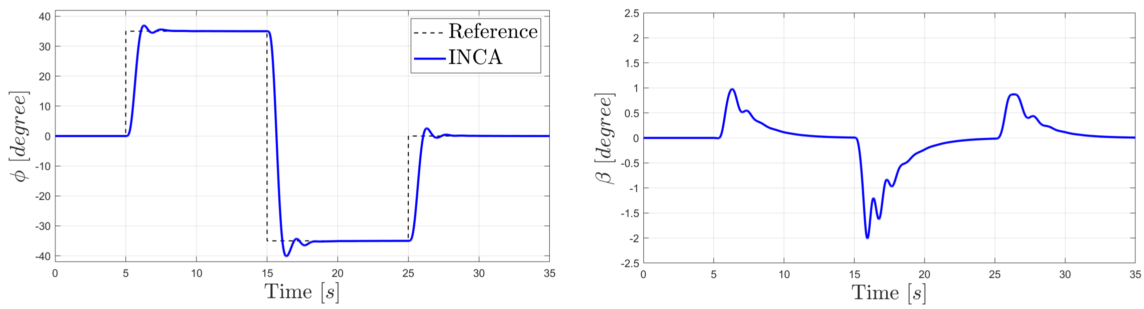

(a) Roll angle ϕ response with the reference signal.

(b) Sideslip angle β, where $\beta_{\text{ref}} = 0°$.

Figure C-1: Time responses of the roll and sideslip angle for the INCA controller (4) with high gains without rate constraints.

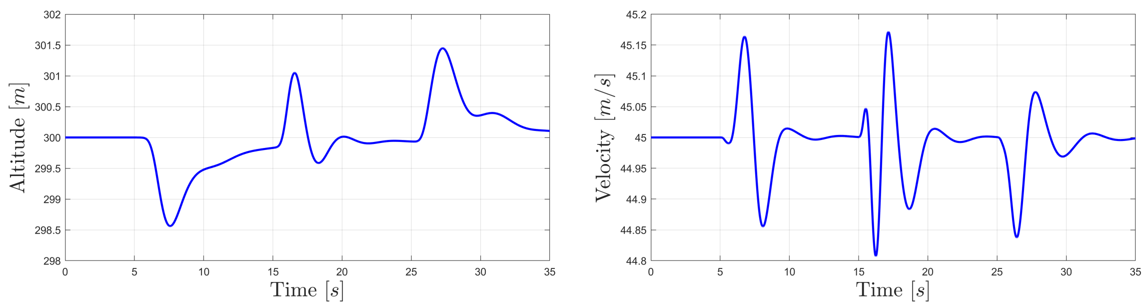

(a) Altitude h response, where $h_{\text{ref}} = 300\ m$.

(b) Velocity V response, where $V_{\text{ref}} = 45\ m/s$.

Figure C-2: Time responses of the altitude and velocity for the INCA controller (4) with high gains without rate constraints.

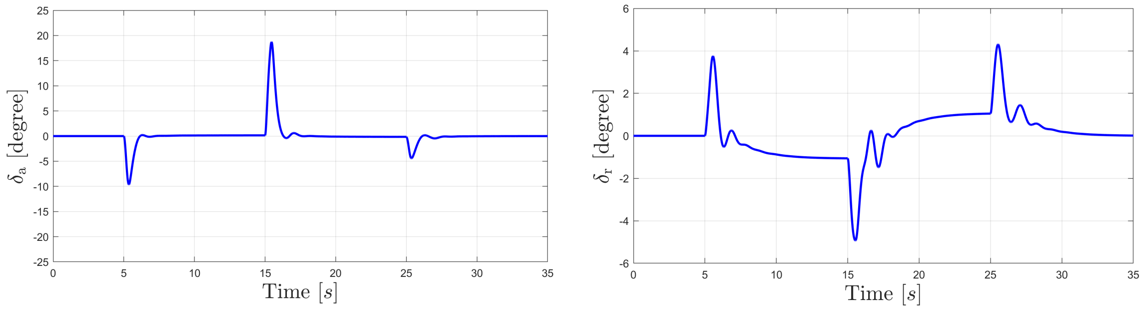

(a) Right aileron deflection δ_{aR} **(b)** Rudder deflection δ_{r}

Figure C-3: Control surface deflections of the INCA controller (4) with high gains without rate constraints.

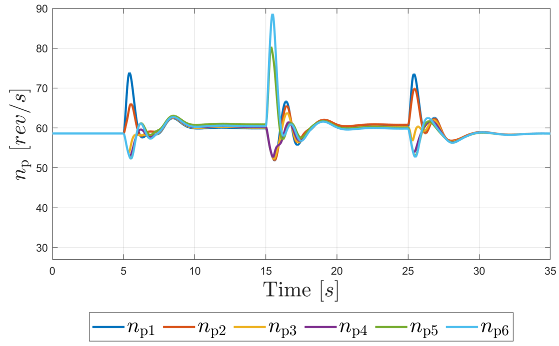

Figure C-4: Rotational velocity of the individual propellers n_{p} for the INCA controller (4) with high gains without rate constraints

C-2 Results INCA MPC power (7) controller for higher cruise velocity

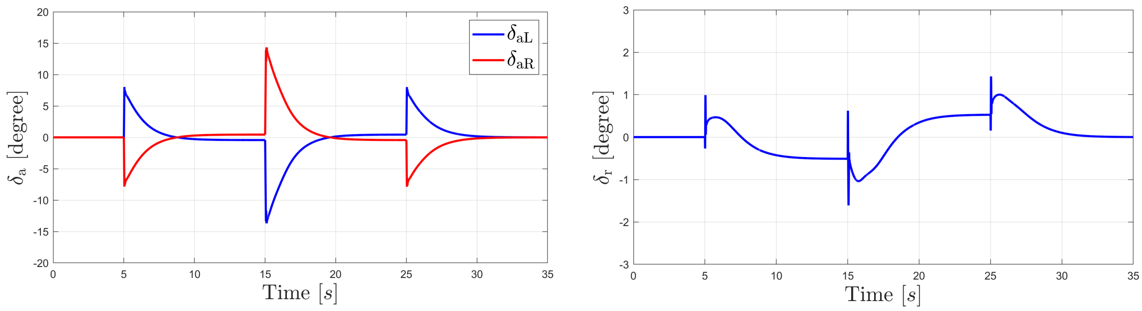

(a) Aileron deflection δ_{aL} and δ_{aR}. **(b)** Rudder deflection δ_{r}.

Figure C-5: Control surface deflection for the INCA power MPC controller (7) with $V_{\mathrm{ref}} = 60$ m/s.

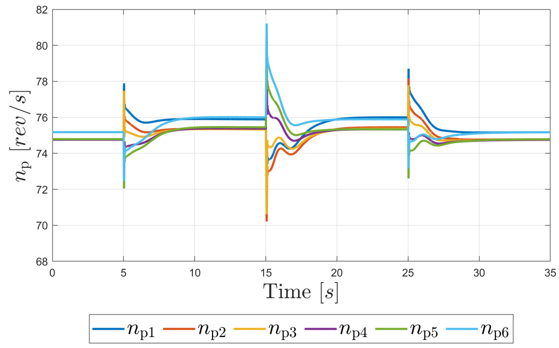

Figure C-6: Rotational velocities of the individual propellers n_{p} for the INCA power MPC controller (7) with $V_{\mathrm{ref}} = 60\ m/s$.

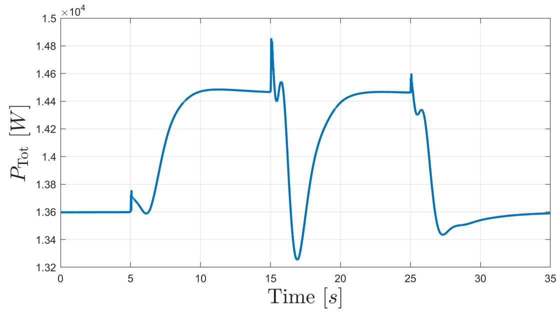

Figure C-7: Total propeller power, defined as $|\boldsymbol{P}_{\mathrm{p}}|_1$, for the INCA power MPC controller (7) and INDI controller (1) with $V_{\mathrm{ref}} = 60\ m/s$.

C-3 Results INCA power without MPC (6) controller

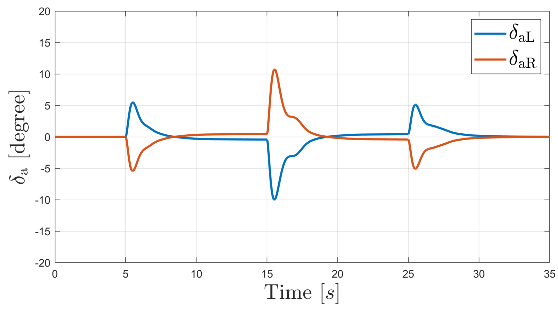

(a) Aileron deflection δ_{aL} and δ_{aR}

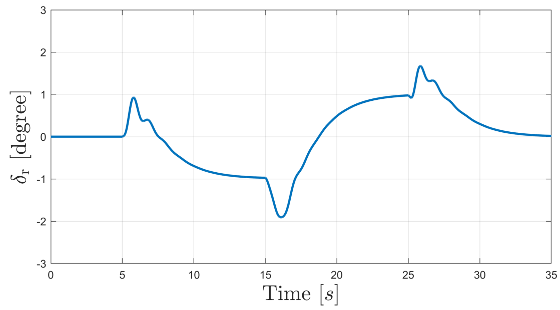

(b) Rudder deflection δ_{r}

Figure C-8: Control surface deflections of the INCA power controller (6) without MPC

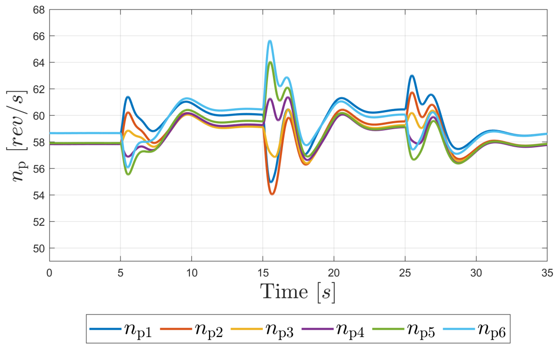

Figure C-9: Rotational velocities of the individual propellers n_{p} for the INCA power controller (6)

h!

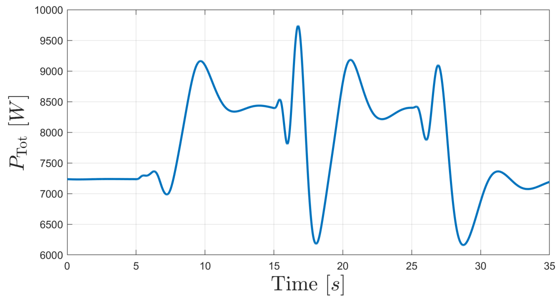

Figure C-10: Total power for INCA power controller (6) defined as $|\boldsymbol{P}_{\mathrm{p}}|_1$

C-4 Results INCA MPC (5) controller with external disturbance

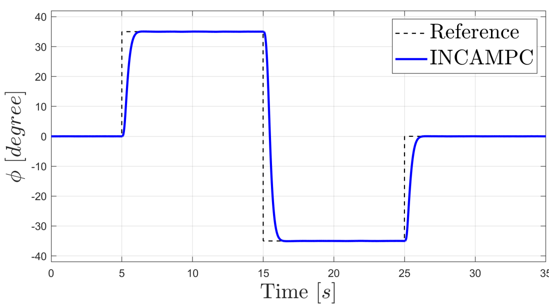

(a) Roll angle ϕ response, with the reference signal.

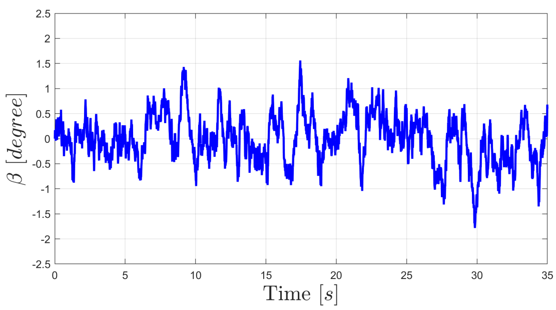

(b) Sideslip angle β response, where $\beta_{\mathrm{ref}} = 0°$.

Figure C-11: Time responses of the roll and sideslip angle for INCA MPC (5) controller with high gains in turbulence.

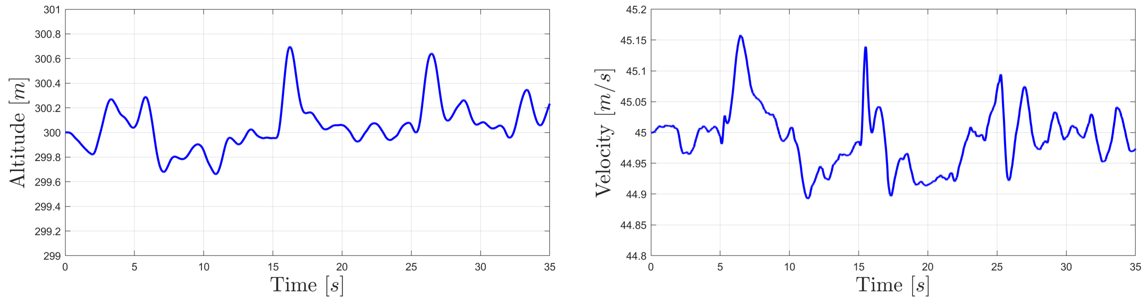

(a) Altitude h response, where $h_{\mathrm{ref}} = 300\ m$. **(b)** Velocity V response, where $V_{\mathrm{ref}} = 45\ m/s$.

Figure C-12: Time responses of the altitude and velocity for INCA MPC controller (5) with high gains in turbulence.

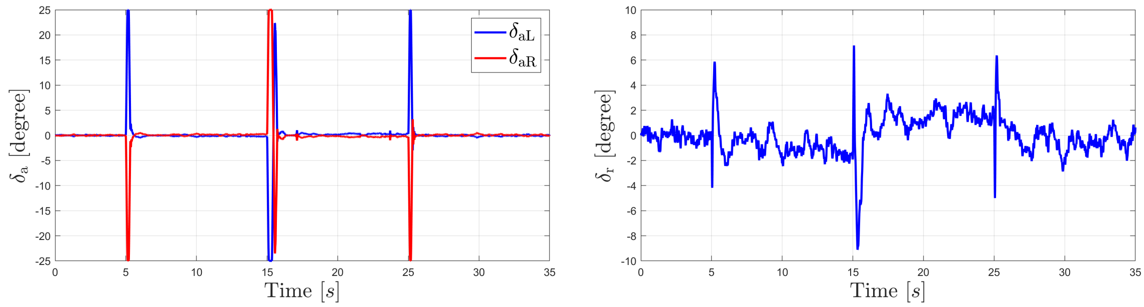

(a) Aileron deflection δ_{aL} and δ_{aR}. **(b)** Rudder deflection δ_{r}.

Figure C-13: Control surface deflection for INCA MPC (5) controller with high gains in turbulence.

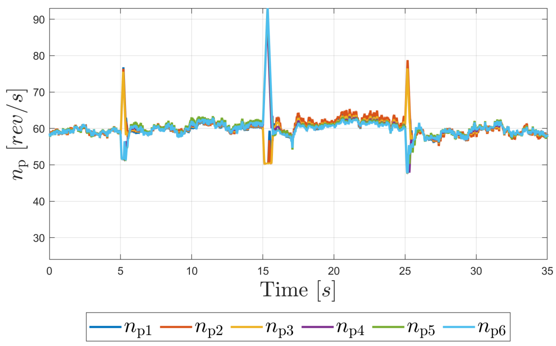

Figure C-14: Rotational velocities of the individual propellers n_{p} for the INCA MPC (5) controller with high gains in turbulence.

Bibliography

[1] DLR, "Strategic research and innovation agenda - The proposed European Partnership on Clean Aviation," tech. rep., DLR, 2020.

[2] EU, "Clean Sky 2 Development Plan Clean Sky 2 Joint Undertaking Development Plan," tech. rep., EU, 2019.

[3] P. Schmollgruber, A. Lepage, F. Bremmers, H. Jentink, N. Genito, A. Rispoli, M. Huhnd, and D. Meissner, "Towards validation of scaled flight testing," in *Aerospace Europe Conference*, pp. 1–10, 2020.

[4] N. K. Borer, M. D. Patterson, J. K. Viken, M. D. Moore, S. Clarke, M. E. Redifer, R. J. Christie, A. M. Stoll, A. Dubois, J. B. Bevirt, A. R. Gibson, T. J. Foster, and P. G. Osterkamp, "Design and performance of the NASA SCEPTOR distributed electric propulsion flight demonstrator," in *16th AIAA Aviation Technology, Integration, and Operations Conference*, pp. 3920–3939, 2016.

[5] K. Pieper, A. Perry, P. Ansell, and T. Bretl, "Design and development of a dynamically, scaled distributed electric propulsion aircraft Testbed," in *2018 AIAA/IEEE Electric Aircraft Technologies Symposium, EATS 2018*, 2018.

[6] N. K. Borer, C. L. Nickol, F. P. Jones, R. J. Yasky, K. Woodham, J. S. Fell, B. L. Litherland, P. L. Loyselle, A. J. Provenza, L. W. Kohlman, and A. G. Samuel, "Overcoming the adoption barrier to electric flight," in *54th AIAA Aerospace Sciences Meeting*, pp. 1022–1035, 2016.

[7] A. M. Stoll, J. B. Bevirt, M. D. Moore, W. J. Fredericks, and N. K. Borer, "Drag reduction through distributed electric propulsion," in *AIAA AVIATION 2014 -14th AIAA Aviation Technology, Integration, and Operations Conference*, pp. 2851–2860, 2014.

[8] H. D. Kim, A. T. Perry, and P. J. Ansell, "A review of distributed electric propulsion concepts for air vehicle technology," in *2018 AIAA/IEEE Electric Aircraft Technologies Symposium, EATS 2018*, pp. 1–21, 2018.

[9] G. T. Klunk, J. L. Freeman, and B. T. Schiltgen, "Vertical tail area reduction for aircraft with spanwise distributed electric propulsion," in *2018 AIAA/IEEE Electric Aircraft Technologies Symposium, EATS 2018*, pp. 5022–5034, 2018.

[10] J. S. E. Soikkeli, "Vertical tail reduction through differential thrust - An initial assessment of aeropropulsive effects on lateral-directional stability and control in engine inoperative conditions," *Master's Thesis, Delft University of Technology, Delft, the Netherlands*, 2020.

[11] J. L. Freeman and G. T. Klunk, "Dynamic flight simulation of spanwise distributed electric propulsion for directional control authority," in *2018 AIAA/IEEE Electric Aircraft Technologies Symposium, EATS 2018*, pp. 1–15, 2018.

[12] A. T. Perry, P. J. Ansell, and M. F. Kerho, "Aero-propulsive and propulsor cross-coupling effects on a distributed propulsion system," *Journal of Aircraft*, vol. 55, no. 6, pp. 2414–2426, 2018.

[13] O. Pfeifle, M. Frangenberg, S. Notter, J. Denzel, D. Bergmann, J. Schneider, W. Scholz, W. Fichter, and A. Strohmayer, "Distributed electric propulsion for yaw control: testbeds, control approach, and flight Testing," in *AIAA Aviation 2021 Forum*, 2021.

[14] P. M. Rothhaar, P. C. Murphy, B. J. Bacon, I. M. Gregory, J. A. Grauer, R. C. Busan, and M. A. Croom, "NASA langley distributed propulsion VTOL tilt-wing aircraft testing, modeling, simulation, control, and flight test development," in *AIAA AVIATION 2014 - 14th AIAA Aviation Technology, Integration, and Operations Conference*, pp. 2999–3012, 2014.

[15] X. Wang, E.-J. van Kampen, Q. Chu, and P. Lu, "Stability analysis for incremental nonlinear dynamic inversion control," *Journal of Guidance, Control, and Dynamics*, vol. 42, no. 5, pp. 1116–1129, 2019.

[16] P. V. M. Simplício, "Helicopter nonlinear flight control - An acceleration measurements-based approach using incremental nonlinear dynamic inversion," tech. rep., Delft University of Technology, 2011.

[17] J. Slotine, *Applied Nonlinear Dynamics*. Prentice-Hall Inc., first ed., 1991.

[18] W. J. Rugh, "Analytical framework for gain scheduling," in *American Control Conference*, pp. 1688–1694, 1990.

[19] P. Apkarian, P. Gahinet, and C. Buhr, "Multi-model, multi-objective tuning of fixed-structure controllers," *2014 European Control Conference, ECC 2014*, pp. 856–861, 2014.

[20] C. Weiser, D. Ossmann, R. O. Kuchar, R. Müller, D. M. Milz, and G. Looye, "Flight testing a linear parameter varying control law on a passenger aircraft," in *AIAA Scitech 2020 Forum*, pp. 1618–1631, 2020.

[21] H. Khalil, *Nonlinear Systems*. Pearson Education Limited, first ed., 2002.

[22] P. Acquatella, E.-J. van Kampen, and Q. P. Chu, "Incremental backstepping for robust nonlinear flight control," in *2nd CEAS Conference on Guidance, Navigation, and Control*, pp. 1444–1463, 2013.

[23] S. Sieberling, Q. P. Chu, and J. A. Mulder, "Robust flight control using incremental nonlinear dynamic inversion and angular acceleration prediction," *Journal of Guidance, Control, and Dynamics*, vol. 33, no. 6, pp. 1732–1742, 2010.

[24] T. Keijzer, G. Looye, Q. Chu, and E. J. van Kampen, "Flight testing of incremental backstepping based control laws with angular accelerometer feedback," in *AIAA Scitech 2019 Forum*, pp. 129–153, 2019.

[25] P. Lu, E. J. van Kampen, C. de Visser, and Q. Chu, "Aircraft fault-tolerant trajectory control using incremental nonlinear dynamic inversion," *Control Engineering Practice*, vol. 57, pp. 126–141, 2016.

[26] T. A. Johansen and T. I. Fossen, "Control allocation - A survey," *Automatica*, vol. 49, no. 5, pp. 1087–1103, 2013.

[27] D. B. Doman and A. G. Sparks, "Concepts for constrained control allocation of mixed quadratic and linear effectors," in *American Control Conference*, pp. 3729–3734, 2002.

[28] M. A. Bolender and D. B. Doman, "Nonlinear control allocation using piecewise linear functions," *Journal of Guidance, Control, and Dynamics*, vol. 27, no. 6, pp. 1017–1027, 2004.

[29] I. Matamoros, "Nonlinear control allocation for a high-performance tailless aircraft with innovative control effectors - An incremental robust approach," *Master's Thesis, Delft University of Technology, Delft, the Netherlands*, 2017.

[30] J. C. Virnig and D. S. Bodden, "Multivariable control allocation and control law conditioning when control effectors limit," in *Guidance, Navigation, and Control Conference, 1994*, pp. 572–582, 1994.

[31] J. M. Buffington and D. F. Enns, "Lyapunov stability analysis of daisy chain control allocation," *Journal of Guidance, Control, and Dynamics*, vol. 19, no. 6, pp. 1226–1230, 1996.

[32] W. C. Durham, "Constrained control allocation," *Journal of Guidance, Control, and Dynamics*, vol. 16, no. 4, pp. 717–725, 1993.

[33] M. Bodson, "Evaluation of optimization methods for control allocation," *Journal of Guidance, Control, and Dynamics*, vol. 25, no. 4, pp. 703–711, 2002.

[34] J. A. Petersen and M. Bodson, "Constrained quadratic programming techniques for control allocation," *IEEE Transactions on Control Systems Technology*, vol. 14, pp. 91–98, 1 2006.

[35] M. W. Oppenheimer and D. B. Doman, "Methods for compensating for control allocator and actuator interactions," *Journal of Guidance, Control, and Dynamics*, vol. 27, no. 5, pp. 922–927, 2004.

[36] Y. S. Luo Andrea and S. Yurkovich, "Model predictive dynamic control allocation with actuator dynamics," in *Proceeding of the 2004 American Control Conference*, pp. 1695–1700, 2004.

[37] M. W. Oppenheimer and D. B. Doman, "A method for including control effector interactions in the control allocation problem," in *AIAA Guidance, Navigation and Control Conference and Exhibit*, pp. 6418–6427, 2007.

[38] I. Matamoros and C. C. de Visser, "Incremental nonlinear control allocation for a tailless aircraft with innovative control effectors," in *2018 AIAA Guidance, Navigation, and Control Conference, 2018*, pp. 1116–1140, 2018.

[39] R. Stolk and C. de Visser, "Minimum drag control allocation for the innovative control effector aircraft," *Master's Thesis, Delft University of Technology, Delft, the Netherlands*, 2017.

[40] J. M. Bakker, "Benchmark flight scenarios for testing fault tolerant control in high performance aircraft," *Master's Thesis, Delft University of Technology, Delft, the Netherlands*, 2019.

[41] O. Pfeifle and W. Fichter, "Energy Optimal Control Allocation for INDI Controlled Transition Aircraft," in *AIAA SciTech Forum*, pp. 1457–1468, 2021.

[42] J. A. Mulder, W. H. J. J. Van Staveren, J. C. Van Der Vaart, E. De Weerdt, C. C. De Visser, A. C. In 't Veld, and E. Mooij, "Lecture notes AE3202 Flight Dynamics," tech. rep., Delft University of Technology, 2013.

[43] R. C. Nelson, *Flight Stability and Automatic Control.* MCgraw-Hill Book Co, second ed., 1998.

[44] M. V. Cook, *Flight Dynamics Principles.* Elsevier Ltd., second ed., 2007.

[45] U.S. Military, "MIL-F-8785C, Military specification: flying qualities of piloted airplanes," tech. rep., Department of Defense, 1980.

[46] G. J. J. Ruijgrok, *Elements of airplane performance.* Delft University Press, second ed., 2009.

[47] L. Veldhuis, *Propeller wing aerodynamic interference.* PhD thesis, Delft University of Technology, 2005.

[48] T. Sinnige, *Aerodynamic and aeroacoustic interaction effects for tip-mounted propellers an experimental study.* PhD thesis, Delft University of Technology, 2018.

[49] R. De Vries, M. Brown, and R. Vos, "Preliminary sizing method for hybrid-electric distributed-propulsion aircraft," *Journal of Aircraft*, vol. 56, no. 6, pp. 2172–2188, 2019.

[50] M. D. Patterson, *Conceptual design of high-lift propeller systems for small electric aircraft.* PhD thesis, Georgia Institute of Technology, 2016.

[51] T. Sinnige, N. Van Arnhem, T. C. Stokkermans, G. Eitelberg, and L. L. Veldhuis, "Wingtip-mounted propellers: Aerodynamic analysis of interaction effects and comparison with conventional layout," *Journal of Aircraft*, vol. 56, no. 1, pp. 295–312, 2019.

[52] W. Durham, *Aircraft Flight Dynamics and Control.* John Wiley & Sons Ltd., second ed., 2013.

[53] V. Klein and E. A. Morelli, *Aircraft System Identification - theory and practice.* American Institute of Aeronautics and Astronautics Inc., first ed., 2006.

[54] C. H. Wolowicz and J. S. Bowman, "Similitude requirements and scaling relationships as applied to model resting," Tech. Rep. August, NASA - National Aeronautics and Space Administration, 1979.

[55] J. Chambers, "Modeling Flight The Role of Dynamically Scaled Free-Flight Models in Support of NASA's Aerospace Programs," tech. rep., National Aeronautics and Space Administration (NASA), 2015.

[56] "Mathworks - findop, steady-state operating point from specifications (trimming) or simulation." https://nl.mathworks.com/help/slcontrol/ug/findop.html. Accessed 05-10-2021.

[57] "Mathworks - linearize, linear approximation of simulink model or subsystem." https://nl.mathworks.com/help/slcontrol/ug/linearize.html. Accessed 05-10-2021.

[58] R. C. van 't Veld, "Incremental nonlinear dynamic inversion flight control - Stability and robustness analysis and improvements," *Master's Thesis, Delft University of Technology, Delft, the Netherlands*, 2016.

[59] C. Schumacher and P. P. Khargonekar, "Stability analysis of a missile control system with a dynamic inversion controller," *Journal of Guidance, Control, and Dynamics*, vol. 21, no. 3, pp. 508–515, 1998.

[60] E. J. Smeur, Q. Chu, and G. C. De Croon, "Adaptive incremental nonlinear dynamic inversion for attitude control of micro air vehicles," *Journal of Guidance, Control, and Dynamics*, vol. 39, no. 3, pp. 450–461, 2016.

[61] F. Grondman, G. H. Looye, R. O. Kuchar, Q. P. Chu, and E. J. van Kampen, "Design and flight testing of incremental nonlinear dynamic inversion based control laws for a passenger aircraft," in *AIAA Guidance, Navigation, and Control Conference, 2018*, pp. 385–409, 2018.

[62] P. Simplício, M. D. Pavel, E. van Kampen, and Q. P. Chu, "An acceleration measurements-based approach for helicopter nonlinear flight control using incremental nonlinear dynamic inversion," *Control Engineering Practice*, vol. 21, no. 8, pp. 1065–1077, 2013.

[63] S. Kim and K. R. Horspool, "Nonlinear controller design for non-minimum phase flight system enhanced by adaptive elevator algorithm," in *AIAA Scitech 2020 Forum*, pp. 1–24, 2020.

[64] O. Härkegård, "Efficient active set algorithms for solving constrained least squares problems in aircraft control allocation," in *41st IEEE Conference on Decision and Control*, pp. 1295–1300, 2002.

[65] E. F. Camacho and C. C. Bordons, *Model predictive control.* Springer, second ed., 2007.

[66] M. A. Müller and F. Allgöwer, "Economic and distributed model predictive control: recent developments in optimization-based control," *SICE Journal of Control, Measurement, and System Integration*, vol. 10, pp. 39–52, 3 2017.

[67] R. Findeisen and F. Allgöwer, "An introduction to nonlinear Model predictive control," in *21st Benelux Meeting on Systems and Control*, pp. 119–141, 2002.

[68] M. M. Verhaegen and V. Verdult, *Filtering and system identification : a least squares approach*. Cambridge University Press, first ed., 2007.

[69] S. Russel and P. Norvig, *Artificial intelligence a modern approach*. Pearson Education Limited, third ed., 2010.

[70] M. A. Skoglund, G. Hendeby, and D. Axehill, "Extended Kalman filter modifications based on an optimization view point," in *18th Conference on Information Fusion*, pp. 1856–1861, 2015.

[71] T. D. Barfoot, *State estimation for robotics*. Cambridge University Press, first ed., 2017.

[72] B. D. O. Anderson and J. B. Moore, *Optimal filtering*. Englewood Cliffs, New Jersey: Prentice Hall, 1979.

[73] "Mathworks - model predictive controller." https://nl.mathworks.com/help/mpc/ref/mpc.html. Accessed 05-10-2021.

[74] C. Cakiroglu, E. J. Van Kampent, and Q. Chu, "Robust incremental nonlinear dynamic inversion control using angular accelerometer feedback," in *AIAA Guidance, Navigation, and Control Conference, 2018*, 2018.

[75] A. Pavlov, N. Van De Wouw, and H. Nijmeijer, "Frequency response functions and Bode plots for nonlinear convergent systems," in *Proceedings of the 45th IEEE Conference on Decision & Control*, pp. 3765–3770, 2006.

[76] J. Mulder, *Design and Evaluation of Dynamic Flight Test Manoeuvres*. PhD thesis, Delft University of Technology, 1986.

[77] J. W. Burrows, "Fuel optimal trajectory computation," *Journal of Aircraft*, vol. 19, no. 4, pp. 324–329, 1982.

[78] C. Edwards, T. Lombaerts, and H. Smaili, *Fault Tolerant Flight Control: A Benchmark Challenge*. Springer, first ed., 2010.

[79] H. J. Karssies, "Extended incremental nonlinear control allocation on the TU Delft Quadplane," *Master's Thesis, Delft University of Technology, Delft, the Netherlands*, 2020.

[80] R. de Vries, M. T. Brown, and R. Vos, "A preliminary sizing method for hybrid-electric aircraft including aero-propulsive interaction effects," in *2018 Aviation Technology, Integration, and Operations Conference*, 2018.

Glossary

List of Acronyms

DEP	Distributed electric propulsion
SFD	Scaled flight demonstrator
NDI	Nonlinear dynamics inversion
INDI	Incremental nonlinear dynamic inversion
INCA	Incremental nonlinear control allocation
FTC	Fault tolerant control
EoM	Equations of motion
PAI	Propulsion airframe interaction
MIMO	Multiple input multiple output
LTI	Linear time-invariant
PID	Proportional-integral-derivative
IMU	Inertial measurement unit
PCH	Pseudo control hedging
MPC	Model predictive control
EU	European union
NLR	Royal Netherlands Aerospace Centre
PCA	Propulsion-controlled aircraft
CFD	Computational fluid dynamics
LPV	Linear parameter varying
BKS	Backstepping
IBKS	Incremental backstepping
NP	Nonlinear programming
QP	Quadratic programming

LP	Linear programming
TSM	Two-step method
WLS	Weighted least squares
FCS	Flight control system
ZOH	Zero-order hold
LQR	Linear-quadratic regulator
SISO	Single-input single-output
KF	Kalman filter
EKF	Extended Kalman filter
IEKF	Iterated extended Kalman filter
DARE	Discrete-time algebraic Riccati equation
CG	Center of gravity
RMSE	Root-mean-square error
FDI	Fault detection and isolation

List of Symbols

$\mathbf{\Omega}$	Mapping of control inputs to power consumption
α	Angle of attack
α_{p}	Angle of attack propeller
β	Sideslip angle
β_{corr}	Finite-slipstream correction factor
$\beta_{0.75}$	Three-quarter chord
χ	Kinematic azimuth angle
Δ	Incremental time step
δ_{a}	Aileron deflection
δ_{e}	Elevator deflection
δ_{r}	Rudder deflection
δ_{s}	Horizontal stabilizer deflection
γ	Flight path angle
$\mathbf{\Phi}$	Nonlinear mapping from control inputs to control forces and moments
μ	Absolute viscosity
∇	Gradient or Jacobian
ω_{a}	Natural frequency actuator
ω_{f}	Natural frequency filter
ϕ	Euler rotation angle
ϕ	Roll angle around x-axis

ψ	Yaw angle around z-axis
ρ	Air density
ρ	Relative degree
θ	Pitch angle around y-axis
$\boldsymbol{\delta}$	Control surface deflection vector
$\boldsymbol{\nu}$	Virtual control input
$\boldsymbol{\Omega}$	Rotational velocity vector
$\boldsymbol{\omega}$	Rotational rates vector in body frame
$\boldsymbol{\tau}$	Control force and moment vector
ζ_{a}	Damping coefficient actuator
ζ_{f}	Damping coefficient filter
$\bar{c}$	Wing mean geometric chord
$\mathcal{B}$	Control effectiveness matrix
$\mathcal{C}$	Controllability matrix
$\mathbf{A}$	State space matrix states
$\mathbf{B}$	Linear mapping from control inputs to control forces and moments
$\mathbf{B}$	State space matrix inputs
$\mathbf{C}$	State space matrix outputs
$\mathbf{D}$	State space matrix direct feedthrough
$\mathbf{F}$	Partial derivative with respect to state
$\mathbf{G}$	Partial derivative with respect to input
$\mathbf{g}$	Control dependent dynamics
$\mathbf{I}$	Mass moment of inertia matrix
$\mathbf{K}$	Diagonal gain matrix
$\mathbf{K}$	Kalman gain
$\mathbf{Q}$	First objective weighting matrix
$\mathbf{Q}$	Tracking weight MPC
$\mathbf{R}$	Control input weight MPC
$\mathbf{W}$	Second objective weighting matrix
$\mathbf{T}$	Transformation matrix
$\boldsymbol{\mathcal{F}}$	Total force vector
$\boldsymbol{\mathcal{M}}$	Total moment vector
$\boldsymbol{\mathcal{W}}$	Working set
$\boldsymbol{F}$	Sate dependent dynamics
$\boldsymbol{f}$	State dynamics
$\boldsymbol{H}$	Moment of impulse
$\boldsymbol{h}$	Output dynamics
$\boldsymbol{R}$	Vector from inertial to moving and rotating frame
$\boldsymbol{r}$	Vector in moving and rotating frame
$\boldsymbol{R}_{\mathrm{P}}$	Arbitrary vector from origin to point P

$\boldsymbol{u}$	Input vector
$\boldsymbol{u}_{\mathrm{a}}$	Actual control input
$\boldsymbol{u}_{\mathrm{c}}$	Commanded control input
$\boldsymbol{u}_{\mathrm{p}}$	Control preference vector
$\boldsymbol{w}$	Process noise
$\boldsymbol{x}$	State vector
$\boldsymbol{y}$	Output vector
$\boldsymbol{z}$	Transformed state
$\boldsymbol{V}$	Linear velocity vector
$A(s)$	Control input transfer function
a_{a}	Axial induction factor at the aileron
a_{p}	Axial induction factor at the propeller
a_{w}	Axial induction factor at the wing leading edge
AR	Aspect ratio
b	Wingspan
c	Speed of sound
c_{f}	Sectional skin friction coefficient
C_l	Sectional wing lift coefficient
C_P	Power coefficient
C_T	Thrust coefficient
D	Drag force
$D(z)$	Discrete time derivative
D_{p}	Propeller diameter
e	Spanwise efficiency factor
$F(s)$	Sensor filtering transfer function
F_{a}	Aerodynamic reference frame
F_{b}	Body-fixed reference frame
F_{E}	Vehicle-carried Earth reference frame
F_{I}	Inertial reference frame
g	Gravitational acceleration
h	Altitude
$H_{\mathrm{ac}}(s)$	Closed loop transfer function incremental control input
J	Advance ratio
L	Lift force
l	Moment around body x-axis
l	Reference length
$L_{\boldsymbol{f}}h$	Lie derivative of h with respect to f
m	Mass of aircraft
m	Moment around body y-axis
M_0	Mach number

n	Geometric scaling factor
n	Moment around body z-axis
N_{c}	Control horizon
N_{p}	Prediction horizon
n_{p}	Rotational velocity propeller
O	Origin
p	Roll rate
P_{p}	Propeller power
q	Pitch rate
q	Dynamic pressure
r	Yaw rate
R_{p}	Radius propeller
R_e	Reynolds number
S	Wing surface area
T_{p}	Propeller thrust
u	Velocity body x-axis
v	Measurement noise
v	Velocity body y-axis
V_{a}	Velocity of slipstream at the aileron
V_{p}	Slipstream velocity at propeller disk
V_∞	True airspeed
w	Velocity body z-axis
X	Force in x-axis
x_{p}	Distance in x-direction of propeller from leading edge wing
Y	Force in y-axis
y_{p}	Distance propeller from CG in y-direction
Z	Force in z-axis
G	Aircraft center of gravity
a	Aerodynamic effect
c	Control effect
d	Atmospheric disturbances effect
g	Gravitational effect
p	Power effect
rm	Reference model
c	Commanded signal
des	Desired commands
D	Drag
h	Hedged signal
L	Lift
ref	Reference commands
p	Position
r	Rate